

UNIVERSITY OF THE
WITWATERSRAND,
JOHANNESBURG

The greening of steel: Modifying a novel open bath furnace (OBF) slag for use in cement

Moise M. Kalenga
(Student No. 2948897)

A dissertation submitted to the
Faculty of Engineering and the Built Environment
In fulfilment of the requirements
For the degree
Master of Science in Engineering

Johannesburg
March 2025

DECLARATION

I declare that this dissertation is my own unaided work. It is being submitted to the University of the Witwatersrand, Johannesburg, for the degree Master of Science in Engineering. It has not been submitted before for any degree or examination to any other university.



……..

(signature of candidate)

Date:01/08/2025

DEDICATION

I dedicate this dissertation to my loving mother (**Kawen Marie**), my best friend, and my fighting angel, the one who saw greatness in me from the beginning and made me believe that I can do anything that I put my mind to. I love you Mama, I am grateful for everything you have taught me, and I will live to make you proud. I would also like to dedicate this dissertation to my father (**Aboubakar Kalenga**) for carrying me through the storms of life. I have to also express my love and appreciation for the support, advice and encouragement from my uncle (**Nkulu Nsanki)**, and my aunt (**Lydia Nsanki)**. Last, but not least, I am grateful to **GOD** for making all of this possible, and for directing me at every stage of my life.

ABSTRACT

In response to the need for lower CO_2 emissions in ironmaking, steelmakers explored alternatives to traditional blast furnace (BF) technology. One such alternative was the Direct Reduced Iron Open Bath Furnace (DRI-OBF). As with BF slag, which has been widely used as a clinker substitute in cement, this study evaluated the potential of DRI-OBF slag for cementitious applications.

OBF slag was produced in a 1 MW prototype furnace, chemically adjusted during smelting, and water-quenched to form a glassy slag comparable to ground granulated blast furnace slag (GGBFS). Two composite OBF slag samples were prepared and compared with BF slags from ArcelorMittal (South Africa) and Thyssenkrupp (Germany), with fineness levels standardized around 275–296 m^2/kg. Mortar and paste mixes were tested for workability, strength development, drying shrinkage, chemical reactivity, and hydration phase evolution.

Cementitious performance was influenced by slag fineness, chemical composition, glass content, and substitution ratio. With similar composition and glass content across samples, performance differences were primarily attributed to fineness. Increased fineness enhanced early strength gain but raised water demand and reduced workability. Slag reactivity—governed by fineness and composition—influenced heat evolution and strength development at later stages of curing.

The hydration phases in slag–cement blends were similar for both BF and OBF slags, forming C-S-H, C-H, and C-A-S-H. Due to its lower sulphur content, OBF slag formed hydrotalcite or hydrogarnet rather than ettringite. Mortar specimens containing OBF slag exhibited a reduced greening effect, consistent with the lower sulphur levels.

Environmentally, OBF slag demonstrated strong potential as a clinker replacement. Its production route via electric smelting offered CO_2 reductions of up to 50% with natural gas, or up to 90% when green hydrogen was used. In cement applications, OBF slag reduced emissions by up to 60% per ton and lowered energy demand associated with clinker production. It also allowed broader use of lower-grade iron ores and aligned with emerging low-carbon steel routes such as DRI–OBF and DRI/Scrap–EAF.

As the availability of fly ash and GGBFS declines, OBF slag and calcined clays were identified as promising supplementary cementitious materials (SCMs). For optimal performance, the slag was recommended to meet key criteria: ≥95% glass content, ≥300 m^2/kg fineness, 80% of particles < 40 μm, and <5% impurities.

To improve refractory lifespan, a second-generation slag (OBF Gen2) was proposed, produced in a slag valorisation furnace (SVF). This MgO-saturated slag was less corrosive and was expected to deliver improved cementitious performance, though further testing was required.

A techno-economic comparison between DRI-OBF and DRI-OBF-SVF routes was also suggested.

In summary, OBF slag proved to be a sustainable SCM with potential benefits for both the steel and cement industries. Continued research was recommended to optimize its chemistry and performance as a viable replacement for conventional GGBFS.

ACKNOWLEDGMENTS

I would first like to acknowledge the support, intellectual guidance, and time investment from all four of my direct supervisors: **Ernst Kleynhans**, **Jeremy Gaylard**, **Paul den Hoed**, and **Janina Kanjee**. I am grateful to you all for making sure that every aspect of this project was successful and completed in the best possible way. You didn't just look at the best interest for the project, but you also paid careful attention to my well-being and you prioritized my best-interests at every step of this journey. I have learnt a lot from each of you, both academically and professionally, and I have gathered a wealth of knowledge on both the steelmaking and cement industries because of all of you. I could not have finished this dissertation within one year without your guidance. I am very grateful to you all.

I would also like to acknowledge the financial and professional support provided by **Metix (Pty) Ltd (SMS Group)** through the sponsorship of this project. A research project of this magnitude could only be undertaken thanks to this sponsorship: from the modification and production of the slag in a first-of-its-kind, 1 MW DC open bath furnace prototype to demonstrate the technology readiness level of this new ironmaking process, to the organization of my participation at an international conference as a presenter (9th International Slag Valorisation Symposium, 2025 in Belgium) in order to share the outcomes of this project with a global audience. It has really been a blessing to work on such a life-changing and interdisciplinary project, this was all possible thanks to the unwavering dedication to excellence from the entire **Metix team**.

I am also very grateful to the whole **Process Engineering team at Metix**. Thank you for making me feel welcomed, loved, and cared for in both professional and personal dimensions. The leadership in the process team, and within Metix at large, is outstanding and inspirational. I have to express my gratitude to **Wynand Moolman** for trailblazing this project and initiating the idea of investing in young talents, and also more directly to **Gerhard Terblanche**, **Stephan Louw**, and **Stefan de Beer** for managing this project from the Metix side. You are all outstanding managers, I am truly inspired in all aspects, and it is a blessing to have had you all by my side throughout this project. I have to mention again my direct manager at Metix, **Ernst Kleynhans**. Thank you for helping me grow not only academically but also professionally. I am grateful for your support in challenging times, for shedding light when I was confused, for helping me understand process engineering at large, and for believing in me in ways that make me believe in myself even more. As part of Metix administration, I would like to express my gratitude to **Cherise du Preez** and **Sibusiso Nyembe**.

Lastly, I would like to express my gratitude to the **pyrometallurgy team at Mintek** for the support during the production of the OBF slag samples, and to all the laboratory technicians at Wits who assisted throughout this project. I have to mention **Thobeka Makhunga** and **Bruce Mothibedi** for their support during the grinding of the slag samples, **Ronny Lambani** for his

unending support during the slag-cement application tests, and **Adam Shnier** for assisting with phase-chemical analyses. Moreover, I would like to thank **Afrimat**, **AfriSam** and **Thyssenkrupp** for providing the BF slag samples. As part of the administration at Wits, I would like to thank the bookkeeper of the School of Chemical and Metallurgical Engineering, **Reghana Khan,** along with the team from **Wits Enterprise** for their administrative support throughout this project. To end, I never thought I would work on a project of such magnitude; I guess “coincidence is indeed **God**’s way of remaining anonymous” ~Albert Einstein.

NOMENCLATURE

AMSA: ArcelorMittal South Africa

AOBFS: Air-cooled open bath furnace slag

ASTM: American Society for Testing and Materials

BF: Blast furnace

BF-grade: Iron ore containing at least 57% iron

BM: Big ball mill

BOF: Basic oxygen furnace

BSE: Backscattered electron

CAPEX: Capital expenditures

Cement types: CEM I, CEM II, CEM III

DC: Direct current

DR-grade: Iron ore containing more than 67% iron

DRI: Direct reduced iron

EAF: Electric arc furnace

EF: Enthalpy flow

FPC: Furnace power consumption

GBFS: Granulated blast furnace slag

GGBFS: Ground-granulated blast furnace slag

GGOBFS: Ground-granulated open bath furnace slag

GHG: Greenhouse gases

GOBFS: Granulated open bath furnace slag

Green materials: Materials produced in an environmentally friendly manner. For example, green steel, green pig iron and green hydrogen

HL: Heat loss

MP: Metallurgical power

OBF Gen 2 slag: Open bath furnace second generation slag

OBF: Open bath furnace

OPEX: Operating expenses

PC: Portland cement

PSD: Particle size distribution

rpm: revolution per minute

RSM: Response surface methodology

SAF: Submerged arc furnace

SANS: South African national standards

SCM: Supplementary cementitious material

SCMs: Supplementary cementitious materials

SDG: Sustainable development goal

SEC: Specific energy consumption

SEM: Scanning electron microscope

SER: Specific energy required

SM: Small ball mill

SVF: Slag valorisation furnace

TkSE: Thyssenkrupp Steel Europe

TRL: Technology readiness level

Table of Contents Page numbers

DECLARATION **I**

DEDICATION **II**

ABSTRACT **III**

ACKNOWLEDGMENTS **V**

NOMENCLATURE **VII**

LIST OF FIGURES **XIII**

LIST OF TABLES **XVII**

CHAPTER 1: INTRODUCTION **1**

1.1. BACKGROUND 1
1.2. PROBLEM STATEMENT 2
1.3. RESEARCH AIM 3
1.4. RESEARCH OBJECTIVES 3
1.5. RESEARCH SIGNIFICANCE 4
1.6. RESEARCH NOVELTY 5
1.7. SCOPE LIMITATION 6
1.8. DISSERTATION FRAMEWORK 6

REFERENCES **7**

CHAPTER 2: LITERATURE REVIEW **12**

INTRODUCTION **12**

2.1. THEME 1: OVERVIEW OF IRONMAKING AND STEELMAKING PROCESSES 12
2.1.1. Global steel production and importance 12
2.1.2. Steel production routes 14
2.1.3. Ironmaking processes 15
2.1.4. Steelmaking processes 22
2.2. THEME 2: SLAGS IN THE IRON AND STEEL INDUSTRY 24
2.2.1. Statistics of slags in the iron and steel industry 24
2.2.2. BOF slag 26
2.2.3. EAF slag 26
2.2.4. BF slag 26
2.2.5. GGBFS recirculation and circular economy 28
2.3. THEME 3: CEMENT MAKING PROCESS AND HYDRATION OF SLAG-CEMENT BLENDS 29
2.3.1. Importance of cement and associated CO_2 emissions 29
2.3.2. Cement making process 30
2.3.3. Hydration of Portland cement 32
2.3.4. Supplementary cementitious materials 34
2.3.5. Hydration of slag-cement blends 36
2.4. THEME 4: DRI-OBF IRONMAKING TECHNOLOGY 39

2.4.1. Impact of climate change and CO_2 emissions *39*
2.4.2. Decarbonization of ironmaking processes *40*
2.4.3. Effect of DRI products in EAF operations *44*
2.4.4. DRI-OBF green ironmaking process and its industrial application *47*
2.4.5. OBF slag modification for cement and summary of research gaps *48*
Conclusions and future outlook of green ironmaking slags **49**
REFERENCES **51**
PART I: DRI-OBF
CHAPTER 3: MATERIALS AND METHODS **64**
3.1. PHASE 1: IN-SITU SLAG MODIFICATION 64
3.1.1. Directly reduced iron (DRI) pellets *64*
3.1.2. Fluxes *65*
3.1.3. Anthracite – used as a reductant *66*
3.1.4. Open Bath Furnace *66*
3.1.5. Slag Granulation *68*
3.1.6. Slag Drying *69*
3.1.7. Sample collection and characterization *70*
3.1.8. Blending of granulated OBF slag taps *71*
3.2. PHASE 2: MILLING OPTIMIZATION AND SLAG SIZE REDUCTION 72
3.2.1. Feed PSD *73*
3.2.2. Equipment *74*
3.2.3. Ball load distribution *75*
3.2.4. Mill setup and feed load adjustment *76*
3.2.5. Optimal milling time and speed *78*
3.3. PHASE 3: CEMENTITIOUS PROPERTIES ASSESSMENT 83
3.3.1. Additional materials *83*
3.3.2. Slag-cement mix design *84*
3.3.3. Preliminary tests of cement and slags *84*
Blended slag-cement mortar tests *85*
3.3.4. Workability (flow test) *85*
3.3.5. Compressive strength *87*
3.3.6. Drying shrinkage *89*
Blended slag-cement paste tests *92*
3.3.7. Evaluation of phases evolution in slag-cement pastes *92*
3.3.8. R^3 Reactivity *96*
REFERENCES **98**
CHAPTER 4: BLENDED SLAG-CEMENT CHARACTERIZATIONS **101**
4.1. INTRODUCTION 101
4.2. COLOUR AND MACROANALYSIS 101
4.3. CHEMICAL COMPOSITION 103
4.3.1. Comparison of OBF slag to conventional BF slag composition *104*

4.3.2. Effect of change in chemical composition on cementitious performance of slag 105
4.4. FINENESS 106
4.4.1. Particle size distribution (PSD) 107
4.4.2. Surface area 109
4.5. GLASS CONTENT 112
4.5.1. Glass content comparison of granulated slags 112
4.5.2. Comparison of air-cooled and granulated OBF slag 113
4.6. CONCLUSIONS AND SLAG PERFORMANCE PREDICTION 115
REFERENCES 115
CHAPTER 5: PERFORMANCE EVALUATION OF SLAG-CEMENT MORTAR 120
5.1. INTRODUCTION 120
5.2. WORKABILITY 120
5.2.1. Importance 120
5.2.2. Workability results 121
5.2.3. Effect of substitution ratio 121
5.2.4. Effect of fineness and glass content 121
5.2.5. Workability and water demand enhancements 123
5.3. COMPRESSIVE STRENGTH 123
5.3.1. Importance 123
5.3.2. Strength tests results 123
5.3.3. Slag activity index 128
5.3.4. Effect of water/binder ratio 129
5.4. DRYING SHRINKAGE 130
5.4.1. Importance 130
5.4.2. Drying shrinkage results 131
5.6. CO_2 EMISSIONS REDUCTION WITH ADDITION OF THE NOVEL OBF SLAG 135
5.7. CONCLUSIONS 136
REFERENCES 137
CHAPTER 6: PERFORMANCE EVALUATION OF SLAG-CEMENT PASTES 141
6.1. INTRODUCTION 141
6.2. DIFFERENCE BETWEEN POZZOLANIC AND HYDRAULIC REACTION 141
6.3. REACTIVITY RESULTS 142
6.3.1. Importance 142
6.3.2. Cumulative heat results 142
6.3.3. Power (rate of heat evolution) 144
6.3.4. Comparison of variations of OBF slags 146
6.3.5. Correlation of R^3 reactivity and compressive strength results 147
6.3.6. Correlation of R^3 reactivity and Blaine fineness 150
6.4. HYDRATED PHASES EVOLUTION IN SLAG-CEMENT PASTES 151
6.4.1. Common phases in slag-cement pastes 151

6.4.2. Hydration products characterization *152*
6.5. CONCLUSION 162

REFERENCES **163**

PART II: DRI-OBF-SVF

Extension of the direct reduced iron (DRI) and open bath furnace (OBF) circuit with a slag valorisation furnace (SVF) stage

CHAPTER 7: OBF-SVF SLAG REFRACTORY DESIGN **168**

7.1. INTRODUCTION 168
7.2. PHASES NOMENCLATURE 168
7.3. DRI GANGUE DISTRIBUTION 168
7.3.1. Short literature survey *168*
7.3.2. Selected gangue distribution for slag design *170*
7.3.3. Fluxing materials *171*
7.4. REFRACTORIES IN IRON AND STEEL PRODUCTION 171
7.4.1. Importance *171*
7.4.2. Types of refractory wear *172*
7.4.3. Properties of refractories *172*
7.4.4. Common refractories in the steel industry *172*
7.4.5. Refractory performance tests *173*
7.4.6. Refractory selection for OBF and SVF *174*
7.5. OBF GEN2 SLAG DESIGN 175
7.5.1. Criteria for selection of slag compositions *175*
7.5.2. Selected slag compositions for each refractory *177*
7.5.3. Evaluation of liquidus temperatures *178*
7.5.4. Process flexibility and slag corrosion assessment *180*
7.6. SVF SLAG DESIGN 183
7.6.1. BF equivalent slag *183*
7.6.2. Feasibility of clinker production in the SVF *184*
7.6.3. High CaO slag (SVF slag) *186*
7.6.4. Selected slag compositions for the SVF *188*
7.7. CONCLUSIONS 188

REFERENCES **189**

CHAPTER 8: SLAG-REFRACTORY DESIGN EVALUATIONS **193**

8.1. INTRODUCTION 193
8.2. SLAG VISCOSITY 193
8.2.1. Measurement *193*
8.2.2. Predictive models *193*
8.2.3. Viscosity models: sensitivity and uncertainty *194*
8.2.4. Viscosities of the selected slag compositions for the OBF and SVF *195*
8.2.5. OBF slag viscosities comparison *196*
8.2.6. SVF product viscosities comparison *196*

8.2.7. Comparison of viscosity model results *196*
8.3. THERMAL CONDUCTIVITY OF THE SLAG 197
8.3.1. Importance *197*
8.3.2. Measurement *198*
8.3.3. Comparison of thermal conductivities of slags *199*
8.4. ELECTRICAL CONDUCTIVITY OF THE SLAG 199
8.4.1. Importance *199*
8.4.2. Measurement *199*
8.4.3. Comparison of electrical conductivity of slags *200*
8.5. TRENDS IN PHYSICAL PROPERTIES OF THE CaO-MgO-Al_2O_3-SiO_2 SLAG 200
8.6. MASS BALANCE 201
8.6.1. Feed materials *201*
8.6.2. Calculation guide *202*
8.6.3. Mass balance for OBF slag type in the SVF *203*
8.6.4. Mass balance for SVF slag 1 type *205*
8.6.5. Mass balance for SVF slag 2 type *206*
8.6.6. Alternative high MgO and low Al_2O_3 slag for the OBF *207*
8.7. ENERGY BALANCE 210
8.7.1. Raw materials compositions and assumptions *211*
8.7.2. Energy balance of selected production cases *212*
8.1.1. Summary of energy balance in selected production cases *218*
8.2. CONCLUSION AND POTENTIAL BENEFITS OF SVF SLAGS 219
8.2.1. Reactivity enhancement and refractory life extension of the OBF *219*
8.2.2. Forecast of supplementary cementitious materials *221*

REFERENCES **222**

CHAPTER 9: CONCLUSIONS AND RECOMMENDATIONS **226**

9.1. SUMMARY OF MAIN FINDINGS 226
9.2. FUTURE OUTLOOK OF IRONMAKING AND SCMS 228
9.3. RECOMMENDATIONS 229

APPENDICES **231**

A. PUBLICATIONS 231
B. EXPERIMENTAL DATA 236

List of Figures Page numbers

Figure 1: Dissertation framework 7
Figure 2: World crude steel production 1950-2023 13
Figure 3: Usage of steel per sector 13
Figure 4: Major producing countries of crude steel production in 2013 and 2023 14
Figure 5: Steelmaking routes and iron source 15
Figure 6: Maturity of ironmaking technologies in 2012 16

Figure 7: Zones and reactions in the blast furnace 17
Figure 8: Order of reduction of iron ore (a), counter current hot gas-charge interactions (b). 18
Figure 9: CO2 emissions for integrated BF-BOF steel plant 19
Figure 10:Comparison of Corex and Finex processes to the Blast furnace process 20
Figure 11: ITmk3 overall process flow 22
Figure 12: Crude steel production by process 23
Figure 13: Solid by-products in iron and steel industry 25
Figure 14: Steel slags (BOF and EAF) utilization per region around the world 25
Figure 15: Distribution of CO2 emissions in the cement industry 30
Figure 16: Global cement production by leading countries for 2018. 30
Figure 17: Cement production process chain 32
Figure 18: Heat released at different stages of hydration 33
Figure 19: Contribution of cement components to strength development 33
Figure 20: Ternary diagram of cementitious phases in the CaO–SiO2–Al2O3 system 34
Figure 21: Global production and consumption of coal fly ash 35
Figure 22: Market size of SCMs 36
Figure 23: CO2 emission reduction from clinker substitution by blast furnace slag 38
Figure 24: Emissions reduction from Midrex technology options 41
Figure 25: Natural gas (NG) Midrex process 41
Figure 26: DRI-EAF steelmaking route 44
Figure 27: Impact of iron content (a), and gangue proportion (b) on EAF productivity 46
Figure 28: Distribution of global iron ore production and grade suitability as EAF and OBF feed 47
Figure 29: Process comparison of BF and DRI-OBF ironmaking process 48
Figure 30: Pathways towards green steel 51
Figure 31: DRI-OBF configuration 63
Figure 32: Typical representation of reduction during the DRI process 65
Figure 33: DRI pellets used in this study 65
Figure 34: Open bath furnace and slag tapping 68
Figure 35: The granulation process 69
Figure 36: Wet granulated OBF slag (GOBFS) 69
Figure 37: Drying oven and dried GOBFS sample 70
Figure 38: Blending of GOBFS taps 72
Figure 39: Flowsheet summary of phase 1 and sample collection 72
Figure 40: Screening process setup 73
Figure 41: Slag Feed PSD curves with bulk density 74
Figure 42: Milling equipment and ball load 75
Figure 43: Ball charge changes during optimization 76
Figure 44: Change in mill setup during optimization 77
Figure 45: Final milling setup and ball charge composition 78
Figure 46: Effect of milling time and speed 79
Figure 47: Close-up look on the impact of speed 80
Figure 48: RSM optimization results 81
Figure 49: Sand used for mortar mixes 84

Figure 50: flow table with mould (left) and mortar sample after table dropping (right) 86
Figure 51: workability test procedure along and mixing table 87
Figure 52: Casting process of cube specimens 88
Figure 53: Images of cube specimen before and after strength testing 88
Figure 54: Water curing tank and compressive strength testing equipment 89
Figure 55: Mortar cube mixes and casting process 89
Figure 56: Casting moulds and prism specimens 90
Figure 57: Mayes DEMEC measuring instrument set and prism specimens in the curing room 91
Figure 58: Mortar Prism mixes and casting procedure 92
Figure 59: Cast disc specimens and de-moulded discs 93
Figure 60: Curing process of disc specimens 93
Figure 61: Hydration arrest process: broken disc pieces in containers (left) and containers covered after the addition of isopropanol (right) 94
Figure 62: Drying and pulverising of broken disc specimens 95
Figure 63: Samples stored in a desiccator before SEM and XRD analyses 95
Figure 64: Calorimeter Equipment setup for R3 reactivity test 96
Figure 65: Reactivity tests procedure and test mix composition table 97
Figure 66: Features responsible for slag's cementitious behaviour 101
Figure 67: Colour of novel granulated OBF slag 102
Figure 68:Greening effect of GBFS compared to GOBFS for 100% PC and 50% PC-Slag blends 103
Figure 69: Conventional BF slag vs novel OBF slag in colour: a) before milling, b) after milling 103
Figure 70: PSD curves of cement and ground slag samples 107
Figure 71: Laboratory scale milling setup 108
Figure 72: PSD of unground slag samples 109
Figure 73: Blaine fineness and relative density (RD) results 110
Figure 74: BET results for slag samples 111
Figure 75: Glass content of slag samples 112
Figure 76: SEM images of AOBFS and GOBFS 114
Figure 77: Workability results 121
Figure 78: Compressive strength results 124
Figure 79: Strength gain results 125
Figure 80: Activity index results 128
Figure 81: Impact of water to binder ratio 130
Figure 82: Drying shrinkage results for all replacement levels 131
Figure 83: Drying shrinkage results for 15% slag substitution 132
Figure 84: Drying shrinkage results for 30% slag substitution 132
Figure 85: Drying shrinkage results for 50% slag substitution 133
Figure 86: greening effect of OBF slag compared to conventional BF slag at 84 days 134
Figure 87: CO_2 emissions reduction with slag addition 135
Figure 88: Cumulative heat release over 72 hours 142
Figure 89: Rate of heat evolution results 144

Figure 90: Effect of chemical composition on the cumulative heat release of slag-cement at 30% 146
Figure 91: Correlation of R3 test results with the 2 days compressive strength results 148
Figure 92: Correlation of R^3 test with the 2 days compressive strength results for OBF slags 149
Figure 93: Correlation of R3 test results with 7 days compressive strength results 150
Figure 94: Correlation of R3 test results with Blaine fineness results 150
Figure 95: pure cement and blended slag-cement microstructure 153
Figure 96: Hydration of 100% cement with curing time (2,7, 28, and 56 days) - SEM 154
Figure 97: Hydration of 100% cement with curing time (2,7, and 28 days) - XRD 155
Figure 98: Original cement-XRD 156
Figure 99: Rate of heat evolution at 20ºC for a typical Portland cement 156
Figure 100: Strength gain of the 100% cement mix 157
Figure 101: Hydration of blended slag-cement with curing time-SEM 158
Figure 102: Hydration of blended slag-cement with curing time (7 – 56 days) - XRD 159
Figure 103: Effect of slag substitution ratio on phase formation at 56 days 160
Figure 104: GGOBFS and GGBFS blended slag-cement hydration-SEM 161
Figure 105: GGOBFS and GGBFS blended slag-cement hydration-XRD 162
Figure 106: DRI-OBF-SVF configuration 167
Figure 107: Names of common phases and typical quaternary diagram, generated at 15% MgO 168
Figure 108: DRI gangue distribution in Al_2O_3-CaO-SiO_2-MgO system 170
Figure 109: Crucible corrosion test 173
Figure 110: (a) Rotating finger test, and (b) Induction furnace heating test 174
Figure 111: Position of old OBF slag with respect to periclase 176
Figure 112: Position of new slag compositions (left: at 15% MgO, right: at 22% MgO) 177
Figure 113:3D quaternary diagram of the new slags 178
Figure 114: Liquidus temperatures of slag 1 to 3 for MgO-rich refractory 179
Figure 115: Liquidus temperatures of slag 4 to 6 for $MgAl_2O_4$ 179
Figure 116: Effect of MgO content at constant temperature for MgO-rich refractory 180
Figure 117: Effect of temperature at constant MgO content for MgO-rich refractory 181
Figure 118: Effect of CaO content at constant temperature for the $MgAl_2O_4$ refractory 182
Figure 119: Effect of temperature at constant CaO for the $MgAl_2O_4$ refractory 183
Figure 120: Quaternary system of clinker at 65% CaO (left: isothermal at 1500°C, right: projections) 184
Figure 121: Isothermal diagram of clinker at 2000°C and 65% CaO 185
Figure 122: Quaternary diagram for 48% CaO at 1500°C 186
Figure 123: Effect of temperature for high CaO slag 187
Figure 124: Effect of increment in CaO content for high CaO slag (SVF slag) 188
Figure 125: OBF and SVF slag design summary 189
Figure 126: Comparison of the Iida and FactSage viscosity models 197
Figure 127: Structure of molten slag glass and physical properties 201
Figure 128: summary of mass balance calculations 203
Figure 129: Selected OBF Gen2 slag compositions for energy balance calculations 209

Figure 130: OBF Gen2 and SVF configuration for energy balance 210
Figure 131: Raw materials compositions for energy balance calculations.....211
Figure 132: Production of Slag 7 in the OBF with valorisation to SVF slag 1 213
Figure 133: Production of Slag 7 in the OBF with valorisation to SVF slag 2 214
Figure 134: Production of Slag 1 in the OBF with valorisation to SVF slag 1 215
Figure 135: Production of Slag 1 in the OBF with valorisation to SVF slag 2 216
Figure 136: Production of Slag 5 in the OBF with valorisation to SVF slag 1 217
Figure 137: Production of Slag 5 in the OBF with valorisation to SVF slag 2 218
Figure 138: Comparison of energy requirement for different production cases in the SVF .219
Figure 139: Reactivity enhancement of slag.....220
Figure 140: Forecast of SCMs consumption in the transition to 2050 carbon neutrality 221

List of Tables Page numbers

Table 1: Main components of cement.....31
Table 2: Comparison of HYL III and Midrex processes 42
Table 3: Comparison of Lump iron ore, BF grade and DR-grade DRI pellets.....46
Table 4: Composition of Direct Reduced Iron (DRI) in the furnace feed 64
Table 5: Composition of fluxes used in the furnace feed 66
Table 6: Anthracite composition.....66
Table 7: On specs GOBFS taps composition.....71
Table 8: Summary of milled granulated slag samples for phase 3 82
Table 9: Mixing proportion of cementitious materials 84
Table 10: Chemical composition of slag samples.....104
Table 11: standard chemical composition specifications.....105
Table 12: Summary of workability, particle size and glass count 122
Table 13: Summary of strength classes 127
Table 14: SANS specifications of activity index and fineness 129
Table 15: cumulative heat released over 72 hours by the main slag samples.....143
Table 16: Common phases in hydrated slag-cement pastes.....152
Table 17: Atomic ratios of hydrated phases in cement pastes 153
Table 18: Typical DRI compositions.....169
Table 19: Selected gangue distribution and proportion for slag design.....171
Table 20: Advantages and disadvantages of corrosion tests.....174
Table 21: Summary of the selected slag composition for the OBF 178
Table 22: Liquidus temperatures of the selected slags 180
Table 23: Activities of calcium silicate system between 1000°C and 1600°C.....185
Table 24: Selected SVF products.....188
Table 25: Calculated viscosities of the selected slags in the OBF and SVF.....195
Table 26: Estimated thermal conductivities of selected slags in the OBF and SVF.....198
Table 27: Electrical conductivity values of selected slags for OBF and SVF 200
Table 28: DRI gangue and Fluxing materials compositions.....202
Table 29: Fluxing requirement for OBF slag.....203
Table 30: Fluxing requirement for SVF slag 1 205

Table 31: Fluxing requirement for SVF slag 2 206
Table 32: Compositions and Physical properties of Slag 7 compared Slag 5 208
Table 33: Mass balance summary of Slag 7 compared Slag 5 208
Table 34: Chemical compositions of Blast furnace slags 210
Table 35: Elements distribution in OBF and SVF products 211
Table 36: PSD data of non-ground granulated slags 236
Table 37: Effect of ball charge composition 236
Table 38: Effect of milling time 237
Table 39: Effect of speed 237
Table 40: Additional tests for statistics 238
Table 41: Effect of milling time-continuation 238
Table 42: Data used for Response Surface Methodology optimization 239
Table 43: PSD data of ground granulated slag samples 240
Table 44: Blaine fineness data 241
Table 45: BET surface area data 241
Table 46: Workability data 241
Table 47: Compressive strength data 1 242
Table 48: Compressive strength data 2 243
Table 49: Summarized cumulative strength data 244
Table 50: Summarized cumulative strength-gain data 244
Table 51: Drying shrinkage data 1 245
Table 52: Drying shrinkage data 2 246
Table 53: Drying shrinkage data 3 247
Table 54: Drying shrinkage data 4 248
Table 55: Shortened reactivity data - heat released rate 249
Table 56: Shortened reactivity data - cumulative heat 249
Table 57: Correlation data - strength to cumulative heat 250

CHAPTER 1: INTRODUCTION

This chapter presents an overview of this study by covering the background, the aim and objectives of the research, the problem statement, the research significance and novelty, and the scope limitation.

1.1. Background

For over a century, conventional blast furnace (BF) slag has been used in the cement industry to partially replace clinker, in an attempt to reduce carbon dioxide (CO_2) emissions from the cement industry (Ahmad et al., 2023; Ehrenberg, 2023). Blast furnace slag is an industrial waste from the pig iron production stage in steelmaking, which is generally granulated from the molten state and ground to a target fineness in order to improve its cementitious performance (Naresh and Saravanan, 2022). Ground granulated BF slag (GGBFS) is the second most abundantly used supplementary cementitious material (SCM) after fly ash (Orozco et al., 2024), followed by silica fume and calcined clays. Furthermore, most SCMs make use of the pozzolanic reaction in which the silica and alumina react with aqueous alkali hydroxides to produce different hydrated binders responsible for strength enhancement, whereas GGBFS can even react in the presence of water alone at a slower pace compared to when it is mixed with alkali hydroxide activators (Kosmatka and Wilson, 2011; Kolani et al. 2012,). This shows that GGBFS possesses both inherent hydraulic properties and pozzolanic properties, hence it is generally referred to as a latent hydraulic material.

SCMs, excluding calcined clay, are waste materials from other production processes, and using SCMs in blended cement also lowers CO_2 emissions in the clinker-making stage, which is responsible for about 90% of CO_2 emissions in the cement production chain (Schneider, 2019; Supriya et al., 2023). Although BF slag has significantly reduced CO_2 emissions in the cement industry, the BF technology is regarded as a carbon-intensive process in the steelmaking industry (Sohn & Mohassab, 2016; Madhavan et al., 2022). Moreover, the steel industry is reported as the second largest industrial CO_2 emitter, accounting for about 7-9% of global greenhouse gas (GHG) emissions, primarily from the ironmaking stage in the blast furnace (BF) and basic oxygen furnace (BOF) steel production route (Cavaliere 2019:36−67; Graupner et al. 2023). The steel industry, as a result, has started implementing measures that reduce CO_2 emissions.

The need to address the impacts of global warming has pushed steelmakers and other industry leaders to reimagine and innovate their processing operations (Levin et al. 2023). Some steelmakers, particularly in Europe, have taken the initiative to replace the old energy-intensive and high CO_2 emitting BF with new eco-friendly production technologies to abide by the 2015 Paris Agreement of achieving net zero carbon emission by 2050 (Eyre & Killip 2019; Glynn et al. 2019; Vogl et al., 2021). The quest for a suitable BF replacement has therefore become central to the decarbonization of the BF-BOF route and integration of the circular economy principle into the steel sector, together with a downstream benefit to the cement sector.

The first innovative decarbonization route for steel that has been implemented, consists of a direct reduced iron (DRI) stage followed by an electric arc furnace (EAF) to produce green

steel (Graupner et al. 2023; Ehrenberg, 2023). The DRI process currently uses natural gas but is flexible for future modification to use green hydrogen, which will further improve its eco-friendliness (Vogl et al. 2021). However, steel production by the DRI-EAF route has iron ore quality constraints as the EAF can only process iron scrap and raw materials with more than 66% iron (DR-grade) to produce steel (Kim and Sohn 2022). In terms of iron ore supply, only 4% of global iron ore exports comprise DR-grade iron ore, and for the last 20 years the grade of iron ores has been decreasing. This makes the DRI-EAF configuration unsustainable for meeting the current and future global steel demand (Nicholas and Basirat 2022a). Alternative technologies are therefore needed that can meet growing demand using lower-grade ores.

The limitation of iron ore quality in the DRI-EAF route has led to the current exploration of the second innovative decarbonization route in steelmaking. This new route has attracted the interests of steelmaking researchers, and it comprises a melting stage between the DRI process and the BOF with the ability to take raw materials containing as little as 57% iron (BF-grade) to produce electric pig iron (Nicholas & Basirat 2022b). Moreover, the melting stage consists of either a submerged arc furnace (SAF), or an open bath furnace (OBF) heated with electrical energy from renewable sources. The main function of the OBF/SAF in this route is to carburize the DRI and remove impurities prior to the BOF process.

This study is focused on the OBF process in the DRI-OBF-BOF steelmaking configuration. The OBF process needs to be optimized in order to generate products that are similar to current BF products, thereby ensuring a smooth transition from the BF to the DRI-OBF technology. The novel OBF slag must therefore possess similar cementitious properties to the conventional BF slag in order to be a suitable clinker substitute in cement. Likewise, the electric pig iron from the OBF must be similar to the conventional pig iron from the BF so that it can be processed in the existing downstream BOF steelmaking units.

1.2. Problem statement

Climate change is one of the most prominent environmental challenges facing the world today, and which can have a drastic impact on the future of human civilization and any other forms of life on the earth. Global warming and climate change are often used interchangeably. According to Lineman et al. (2015), global warming means the increase in the average temperature of the earth's surface, while climate change refers to long-term changes in global or local weather patterns. With the current rise of strict environmental regulations, increased emissions taxes, and implementation of multinational agreements, such as the 2015 Paris agreement, to achieve net zero carbon emission by 2050, every carbon-consuming industry is under pressure to decarbonize its operations in order to stay relevant and competitive in the global market. The steelmaking and cement-making industries, as major consumers of fossil fuels, are not spared from this pressure.

The steelmaking industry, as a result, is currently developing technologies to replace the BF and lower its carbon footprint (Vogl et al., 2021). The DRI-OBF route offers a promising, sustainable alternative to BF technology, producing BF-equivalent products (slag and pig iron) with lower environmental impact. BF technology uses fossil fuel as the energy source, whereas

the novel OBF technology uses electricity. This has the potential for renewable energy utilization in this green energy transition era.

At present, around 66% of conventional BF slag is water-quenched from the molten state and used in the manufacturing of Portland slag cement (Ehrenberg et al., 2020; Tripathy et al., 2020). The usage of cement blended with ground granulated BF slag has been deemed to have significant advantages such as reduction of CO_2 emissions in cement making, and – in cement applications –reduced heat of hydration, reduction of thermal stress, low long-term shrinkage and creep, decreased permeability, and overall improved long-term strength as compared to pure PC (Sakai et al. 1992; Dunne, 2019; Escalante et al. 2001; Kolani et al. 2012; Binici et al. 2007). Moreover, concrete incorporating BF slag generally costs less than concrete made only with Portland cement (PC) as the cementitious component, because the BF slag, as a by-product from steelmaking, is cheaper than PC (Dunne, 2019). The substantial benefits of BF slag in cement, coupled with the need to reduce CO_2 emissions, have driven the steelmaking industry to explore modifying the chemistry of novel OBF slag with the objective of having the same cementitious properties as conventional BF slag. OBF technology is still in development, and no data currently exists on the cementitious performance of its slag.

Several studies have investigated modifying steelmaking slags for use as clinker substitutes to reduce cement industry CO_2 emissions (Criado et al., 2018; Adolfsson et al., 2007; Ryu et al., 2024; Bharati et al., 2022; Kim et al., 2015; Kourounis et al., 2007, Zhang et al., 2024). However, the scope of these studies has not covered the simultaneous CO_2 emissions reduction through the reformulation of the BF slag using a greener production process. This study therefore covers the modification of an OBF slag composition to achieve a BF-equivalent slag so that it can be used as a SCM in the cement industry and a low CO_2 alternative to granulated BF slag (GGBFS).

The expected future volume production of novel OBF slag will be less than that of conventional BF slag due to the low gangue content of the DRI. This demonstrates that although the OBF slag might meet the qualitative requirement of a BF slag replacement, it cannot meet current BF-slag volumes required by the cement industry. The lower quantities of OBF slag could be solved by modifying all the emerging steel slags (BOF slag, EAF slag) in a separate slag valorisation furnace (SVF). Further improvement of the slag's cementitious properties could increase levels of replacement of conventional clinker in the cement industry and improve the feasibility of achieving zero-waste steel production. This will further increase the environmental and economic benefits of steel production by the DRI-OBF-BOF route.

1.3. Research aim

This study aims to establish and understand the relationships between the properties of a novel open bath furnace (OBF) slag and its efficacy as a supplementary cementitious material in the production of eco-friendly cement.

1.4. Research objectives

The objectives of this study are:

- To modify molten OBF slag, in-situ, in order obtain a chemical composition similar to conventional BF slag
- To granulate the molten OBF slag to enhance its cementitious performance, and to characterize it in terms of bulk density, particle size distribution (PSD), glass content, and phase-chemical properties. These properties will be compared with those of industrially produced granulated BF slag.
- To optimize the laboratory-scale ball mill grinding process and grind samples of granulated OBF slag (GOBFS) to a fineness similar to standard production of ground granulated blast furnace slag (GGBFS).
- To compare the cementitious performance of the novel OBF slag with conventional BF slag mortars in terms of workability, strength development, and drying shrinkage tests, conducted at cement replacement levels of 15%, 30%, and 50%, and at age intervals from 2 to 168 days under controlled curing conditions.
- To measure the heat of hydration and determine the evolution of hydrated phases in OBF and BF slag-cement pastes.
- To evaluate the potential to extend the furnace refractory's campaign life by producing a second generation OBF slag (OBF Gen2 slag) that is less corrosive to and more compatible with the refractory lining.
- To assess the possibility of conditioning the molten OBF Gen2 slag in a separate slag valorisation furnace (SVF) to a composition similar to Portland cement clinker, or alternatively to a valorised slag of higher cementitious properties than conventional BF slag.

1.5. Research significance

Most of the past attempts to produce cementitious materials from other steelmaking slags, such as EAF slags, while comparing to BF slag, did not reach the stage of industrial application and commercialization because of less promising outcomes (Andersson et al., 2023; Lee et al., 2019; Hekal et al., 2013). The OBF slag for this study was produced in a 1 MW OBF Metix prototype, which was designed and constructed to de-risk and assess the industrial practicability of this novel DRI-OBF technology by demonstrating its technology readiness level (TRL). In addition, the DRI-OBF-BOF configuration is a green steel production route which is currently under development, particularly in Europe, where some steel producers are actively developing and investing in this route. As an example, Thyssenkrupp Steel Europe (TkSE), has published plans to replace four BFs with new DRI-OBF technologies by 2045, with the first unit being replaced by 2026 (Thyssenkrupp Steel Europe). TkSE will use two 100 MW OBFs designed and constructed by Metix (a South African subsidiary of SMS Group GmbH) to melt the DRI before sending the electric pig iron to an existing BOF. It is intended that the OBF slag arising from this process will be supplied to the cement industry.

If widely adopted, this new green production route will phase out BF slag. Novel OBF slag could then replace clinker in cement, significantly reducing GHG emissions across both industries. This novel production process showcases the combination of the following sustainable development goals (SDGs) as per adjusted descriptions from UN PAGE (2024):

- SDG9: Promote industrial innovation through the adoption of low-emission technologies
- SDG12: Encourage responsible consumption and production by recycling steelmaking by-products
- SDG13: Take climate action by reducing CO_2 emissions in steel and cement industries

Currently, fly ash and GGBFS are the most widely used SCMs (Orozco et al., 2024). However, with declining interest in coal-fired power plants in favour of renewable electricity in this energy transition era, as well as the gradual phasing-out of the BF technology from the steelmaking chain, for low-CO_2 alternative ironmaking technologies, these two SCMs might no longer be part of the cement market in the foreseeable future, thereby leaving a demand deficit. Moreover, there is also rising interest in the production of calcined clays as SCMs due to the abundant clay reserves worldwide, as well as the relatively low temperature and CO_2 emissions associated with the calcination of clays compared to clinker (Overmann et al., 2024). As low-CO_2 alternatives, calcined clays and novel OBF slag are likely to shape the future SCM market.

The success of the DRI-OBF-BOF configuration will enable steel producers to fall in line with the 2015 Paris agreement and meet global climate targets (Olsson et al., 2021). It will further benefit the cement industry if the novel OBF slag possesses similar cementitious properties to conventional BF slag, features that translate into comparable clinker reduction potential and lower CO_2 emissions from cement production. Moreover, if a slag of higher cementitious properties than the BF slag is produced, then the reduction of clinker will potentially be higher for a given cementitious performance, thereby allowing further reduction of energy and CO_2 emissions with clinker production. This study supports steel–cement industry collaboration toward CO_2 reduction by producing and evaluating the novel OBF slag for cementitious use.

1.6. Research novelty

The OBF slag is a novel by-product material, arising from the steel industry decarbonization plans for replacing the old BF technology with new eco-friendly ironmaking technology (DRI-OBF) that can be set up to produce the same products as the BF. Several studies on the DRI process have already been documented in the existing body of knowledge (Muscolino et al., 2016; Hasanbeigi et al., 2014; Cavaliere, 2016; Mohsenzadeh et al., 2019; Jiang et al., 2013). However, the combination of the DRI-OBF production process for green ironmaking purposes is relatively new, and the cementitious properties of the OBF slag have not been studied. This study may provide the first demonstration of OBF slag's cementitious performance, potentially supporting its acceptance as a supplementary cementitious material (SCM) and viable alternative to BF slag. This would position OBF slag as a replacement for the BF slag during the expected phasing-out of the BF technology from the steelmaking process. The DRI-OBF configuration constitutes the first part of this study, which is covered in chapters 3, 4, 5, and 6.

Another novel aspect involves producing a refractory-compatible slag in the OBF, which is subsequently modified in a separate slag valorisation furnace (SVF) to yield a BF-equivalent or higher-performance slag. The exploration of this supplementary process route (DRI-OBF-SVF) could lead to the substantial life-span extension of the OBF's refractory linings and could

enable the steelmaking industry not only to replace the BF slag qualitatively, but also to meet the quantitative demand from the cement industry. This would ensure that once the BF technology is phased out, the new OBF slag could fulfil the role of the BF slag and sustain the volume demand in the cement industry. Additionally, producing a slag with superior cementitious performance may further enhance CO_2 reduction in the cement industry, strengthening the case for the OBF process as a next-generation solution. However, the viability of this supplementary process route requires a feasibility study of slag-refractory interactions for both furnaces (OBF, SVF), which is covered in chapters 7 and 8.

The DRI-OBF-SVF configuration is a recommended improvement from the DRI-OBF configuration, and it constitutes the second part of this study. However, there will be a need to perform detailed techno-economic and emission-reduction evaluations in order to highlight the benefits of the DRI-OBF-SVF slag production compared to the DRI-OBF.

1.7. Scope limitation

The scope of this study is applicable to the following parameters and materials,

Materials:

- Reference Portland cement (AfriSam CEM I: 52.5 R)
- Samples of novel OBF slag, produced by Metix Pty Ltd (6 April to 2 May, 2024)
- Industrial conventional BF slag samples, one produced by ArcelorMittal South Africa (AMSA) and the other produced by Thyssenkrupp Steel Europe (TkSE).

Paste and mortar mix design:

- Water to binder ratio of 0.5 for all the mixes

1.8. Dissertation framework

The layout of this study report is summarized in Figure1. It should be noted that every chapter incorporates an individual reference list with the exception of the concluding chapter (Chapter 9). The study is covered in two parts as follow:

- Part 1: DRI-OBF configuration comprising chapters 3, 4, 5, and 6
- Part 2: DRI-OBF-SVF configuration covered in chapters 7 and 8, which only includes a feasibility study and evaluation of slag properties

Chapter 1 and chapter 2 take into consideration both the DRI-OBF and the DRI-OBF-SVF configurations. Lastly, chapter 9 highlights the main conclusions drawn from this study and provides recommendations for possible further work.

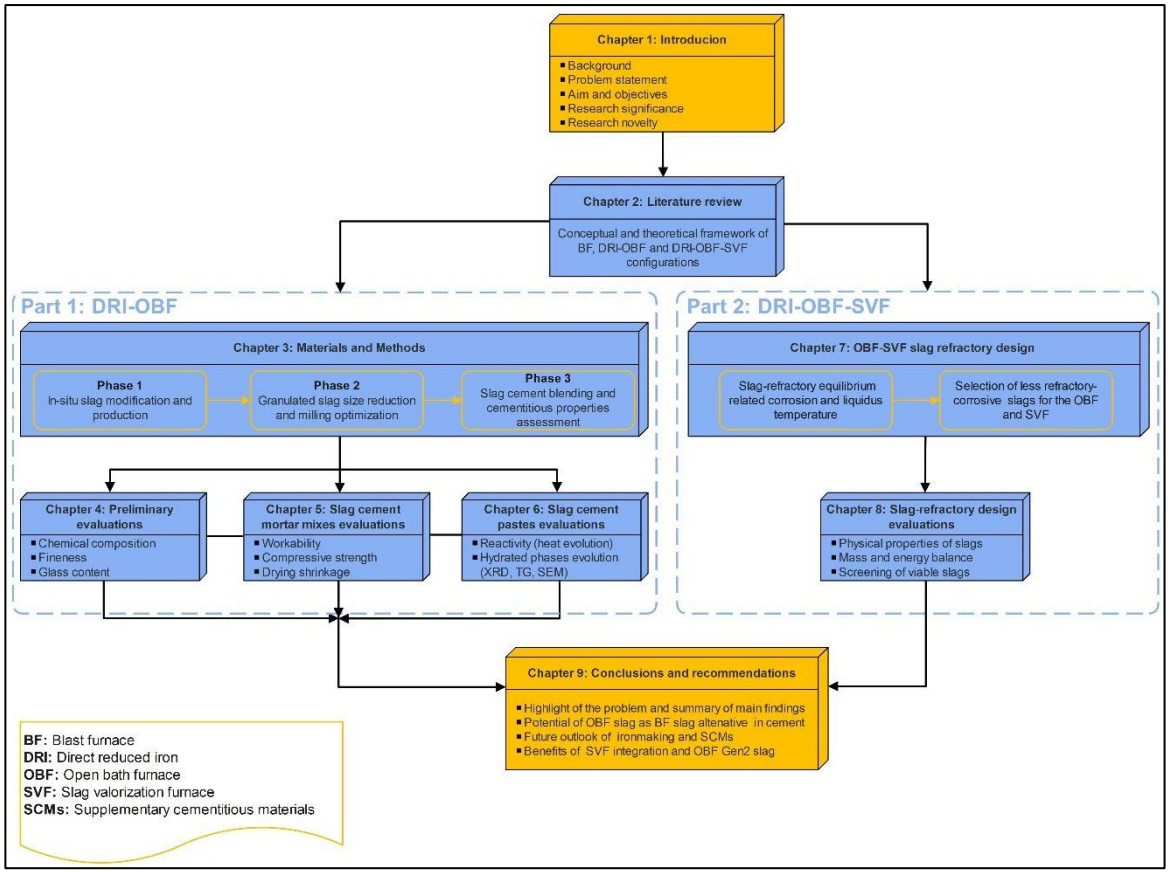


Figure 1: Dissertation framework

References

Adolfsson, D., Menad, N., Viggh, E. and Björkman, B. (2007). Hydraulic properties of sulphoaluminate belite cement based on steelmaking slags. *Advances in Cement Research*, 19(3), pp.133–138. doi:https://doi.org/10.1680/adcr.2007.19.3.133.

Ahmad, M.A., Ranaivomanana, H., Bonnet, S., L'Hostis, V. and Buttin, P. (2023). Study of Hydration Properties for Blast Furnace Slag-Blended Cement: Prediction of Slag Hydration Kinetics. *Rilem bookseries*, pp.165–176. doi:https://doi.org/10.1007/978-3-031-33187-9_16.

Andersson, A., Isaksson, J., Lennartsson, A. and Engström, F. (2023). Insights into the Valorization of Electric Arc Furnace Slags as Supplementary Cementitious Materials. *Journal of Sustainable Metallurgy*, 10(1), pp.96–109. doi:https://doi.org/10.1007/s40831-023-00778-y.

Bharati, S., Sambandam, M. and Lochan, P. (2022). Development of a calcium aluminate cement from steelmaking slag by altering its mineralogical composition. *Advances in Cement Research*, 34(5), pp.187–196. doi:https://doi.org/10.1680/jadcr.19.00160.

Binici, H., Temiz, H. and Köse, M.M. (2007). The effect of fineness on the properties of the blended cements incorporating ground granulated blast furnace slag and ground basaltic pumice. *Construction and Building Materials*, 21(5), pp.1122–1128. doi:https://doi.org/10.1016/j.conbuildmat.2005.11.005.

Cavaliere, P. 2019. *Clean Ironmaking and Steelmaking Processes: Efficient Technologies for Greenhouse Emissions Abatement*. Switzerland: Springer Nature. doi:https://doi.org/10.1007/978-3-030-21209-4.

Cavaliere, P. (2016). *Ironmaking and Steelmaking Processes*. Cham: Springer International Publishing. doi:https://doi.org/10.1007/978-3-319-39529-6.

Criado, M., Bernal, S.A., García-Triñanes, P. and Provis, J.L. (2018). Influence of slag composition on the stability of steel in alkali-activated cementitious materials. *Journal of Materials Science*, 53(7), pp.5016–5035. doi:https://doi.org/10.1007/s10853-017-1919-3.

Dunne, C. A. (2019). *SME mineral processing & extractive metallurgy handbook volume 1*. Englewood, Colorado Society For Mining, Metallurgy & Exploration.

Ehrenberg, A. (2023). Today's and future slags - Potentials and Challenges. ce/papers, 6(6), pp.241–256. doi:https://doi.org/10.1002/cepa.2843.

Ehrenberg, A., Sarcos, N.R., Hart, D., Bornhöft, H. and Deubener, J. (2020). Influence of the Thermal History of Granulated Blast Furnace Slags on Their Latent Hydraulic Reactivity in Cementitious Systems. *Journal of Sustainable Metallurgy*, 6(2), pp.207–215. doi:https://doi.org/10.1007/s40831-020-00269-4.

Escalante, J.I., Gómez, L.Y., Johal, K.K., Mendoza, G., Mancha, H. and Méndez, J. (2001). Reactivity of blast-furnace slag in Portland cement blends hydrated under different conditions. *Cement and Concrete Research*, 31(10), pp.1403–1409. doi:https://doi.org/10.1016/s0008-8846(01)00587-7.

Eyre, N., & Killip, G. (eds). 2019. Shifting the focus: energy demand in a net-zero carbon UK. Centre for Research into Energy Demand Solutions. Oxford, UK. ISBN: 978-1-913299-04-0. Retrieved June 09, 2024 from https://www.creds.ac.uk/publications/shifting-the-focus-energy-demand-in-a-net-zero-carbon-uk/.

Glynn, J., Gargiulo, M., Chiodi, A., Deane, P., Rogan, F. & Gallachóir, B.Ó. 2019. Zero carbon energy system pathways for Ireland consistent with the Paris Agreement. *Climate Policy* **19(1): 30–42.**

Graupner, Y., Weckenborg, C. & Spengler, T. 2023. Low-carbon primary steelmaking using direct reduction and electric arc furnaces: Prospective environmental impact assessment. *Procedia CIRP* **116: 696–701.**

Hasanbeigi, A., Arens, M. and Price, L. (2014). Alternative emerging ironmaking technologies for energy-efficiency and carbon dioxide emissions reduction: A technical review. *Renewable and Sustainable Energy Reviews*, 33, pp.645–658. doi:https://doi.org/10.1016/j.rser.2014.02.031.

Hekal, E.E., Abo-El-Enein, S.A., El-Korashy, S.A., Megahed, G.M. and El-Sayed, T.M. (2013). Hydration characteristics of Portland cement – Electric arc furnace slag blends. *HBRC Journal*, 9(2), pp.118–124. doi:https://doi.org/10.1016/j.hbrcj.2013.05.006.

Jiang, X., Wang, L. and Shen, F.M. (2013). Shaft Furnace Direct Reduction Technology - Midrex and Energiron. *Advanced Materials Research*, 805-806, pp.654–659. doi:https://doi.org/10.4028/www.scientific.net/amr.805-806.654.

Kim, H.-S., Kim, K.-S., Jung, S.S., Hwang, J.I., Choi, J.-S. and Sohn, I. (2015). Valorization of electric arc furnace primary steelmaking slags for cement applications. *Waste Management*, 41, pp.85–93. doi:https://doi.org/10.1016/j.wasman.2015.03.019.

Kim, W. & Sohn, I. 2022. Critical challenges facing low carbon steelmaking technology using hydrogen direct reduced iron. *Joule* **6**(10): 2228–2232.

Kolani, B., Buffo-Lacarrière, L., Sellier, A., Escadeillas, G., Boutillon, L. and Linger, L. (2012). Hydration of slag-blended cements. *Cement and Concrete Composites*, 34(9), pp.1009–1018. doi:https://doi.org/10.1016/j.cemconcomp.2012.05.007.

Kosmatka, S.H. and Wilson, M.L. (2011). *Design and control of concrete mixtures: the guide to applications, methods, and materials*. 15th ed. Skokie, Ill.: Portland Cement Association, pp.67–84.

Kourounis, S., Tsivilis, S., Tsakiridis, P.E., Papadimitriou, G.D. and Tsibouki, Z. (2007). Properties and hydration of blended cements with steelmaking slag. *Cement and Concrete Research*, 37(6), pp.815–822. doi:https://doi.org/10.1016/j.cemconres.2007.03.008.

Lee, J.-Y., Choi, J.-S., Yuan, T.-F., Yoon, Y.-S. and Mitchell, D. (2019). Comparing Properties of Concrete Containing Electric Arc Furnace Slag and Granulated Blast Furnace Slag. *Materials*, 12(9), p.1371. doi:https://doi.org/10.3390/ma12091371.

Levin, K., Fransen, T., Schaumer, C., Davis, C. & Boehm, S. 2023-03-20. What Does "Net-Zero Emissions" Mean? 8 Common Questions, Answered. World Resources Institute: https://www.wri.org/insights/net-zero-ghg-emissions-questions-answered, viewed 2024-06-10.

Lineman, M., Do, Y., Kim, J.Y. and Joo, G.-J. (2015). Talking about Climate Change and Global Warming. *PLOS ONE*, [online] 10(9), p.e0138996. doi:https://doi.org/10.1371/journal.pone.0138996.

Madhavan, N., Brooks, G., Rhamdhani, M.A. and Bordignon, A. (2022). Contribution of CO2 Emissions from Basic Oxygen Steelmaking Process. *Metals*, 12(5), p.797. doi:https://doi.org/10.3390/met12050797.

Mohsenzadeh, F.M., Payab, H., Abedi, Z. and Abdoli, M.A. (2019). Reduction of CO2 emissions and energy consumption by improving equipment in direct reduction ironmaking plant. *Clean Technologies and Environmental Policy*, 21(4), pp.847–860. doi:https://doi.org/10.1007/s10098-019-01672-6.

Muscolino F, Martinis A, Ghiglione M, Duarte P. (2016). Introduction to direct reduction technology and outlook for its use. *Metallurgia Ital*, 108(4): 25–3.

Naresh, B. and Saravanan, M. (2022). Experimental study of replacement of cement with ground granulated blast furnace slag. *Materials Today: Proceedings*, 62, pp.3493–3496. doi:https://doi.org/10.1016/j.matpr.2022.04.302.

Nicholas, S. & Basirat, S. 2022a. Iron ore quality a potential headwind to green steelmaking—Technology and mining options are available to hit net-zero steel-targets. https://ieefa.org/resources/iron-ore-quality-potential-headwind-green-steelmaking-technology-and-mining-options-are, viewed 2024-06-10.

Nicholas, S. & Basirat, S. 2022b. Solving iron ore quality issues for low-carbon steel. https://ieefa.org/resources/solving-iron-ore-quality-issues-low-carbon-steel, viewed 2024-06-10.

Orozco, C., Babel, S., Tangtermsirikul, S. and Sugiyama, T. (2024). Comparison of environmental impacts of fly ash and slag as cement replacement materials for mass concrete and the impact of transportation. *Sustainable Materials and Technologies*, [online] 39, p.e00796. doi:https://doi.org/10.1016/j.susmat.2023.e00796.

Overmann, S., Vollpracht, A. and Matschei, T. (2024). Reactivity of Calcined Clays as SCM—A Review. *Materials*, [online] 17(2), p.312. doi:https://doi.org/10.3390/ma17020312.

Ryu, G.U., Kim, H.J., Yu, H.J. and Pyo, S. (2024). Utilization of steelmaking slag in cement clinker production: A review. *Journal of CO_2 Utilization*, 84, pp.102842–102842. doi:https://doi.org/10.1016/j.jcou.2024.102842.

Sakai, K., Watanabe, H., Suzuki, M., and Hamazaki, K. (1992). Properties of granulated blast-furnace slag cement concrete. *ACI Spec*. Publ. 132:1367–1384.

Schneider, M. (2019). The cement industry on the way to a low-carbon future. *Cement and Concrete Research,* **124**: 105-792.

Sohn, H.Y., Mohassab, Y. (2016). Greenhouse Gas Emissions and Energy Consumption of Ironmaking Processes. In*: Cavaliere, P. (eds) Ironmaking and Steelmaking Processes*. Springer, Cham. pp.427–455. https://doi.org/10.1007/978-3-319-39529-6_25.

Supriya, Chaudhury, R., Sharma, U., Thapliyal, P.C. & Singh, L.P. (2023). Low-CO_2 emission strategies to achieve net zero target in cement sector. *Journal of Cleaner Production*, **417**: 137-466.

Technology and mining options are available to hit net-zero steel-targets. https://ieefa.org/resources/iron-ore-quality-potential-headwind-green-steelmaking-technology-and-mining-options-are, viewed 2024-06-10.

Thyssenkrupp Steel Europe. 2023. Climate-neutral steel—Our strategy. Retrieved from https://www.thyssenkrupp-steel.com/en/company/sustainability/climate-strategy/climate-strategy.html, viewed 2024-06-10.

Tripathy, S.K., Dasu, J., Murthy, Y.R., Kapure, G., Pal, A.R. and Filippov, L.O. (2020). Utilisation perspective on water quenched and air-cooled blast furnace slags. *Journal of Cleaner Production*, 262, p.121354. doi:https://doi.org/10.1016/j.jclepro.2020.121354.

UN PAGE (2024). *Sustainable Development Goals - Partnership for Action on Green Economy*. [online] www.un-page.org. Available at: https://www.un-page.org/sustainable-development/ [Accessed 25 Oct. 2024].

Vogl, V., Olsson, O. and Nykvist, B. (2021). Phasing out the blast furnace to meet global climate targets. *Joule*, 5(10), pp.2646–2662. doi:https://doi.org/10.1016/j.joule.2021.09.007.

Zhang, S., Yao, J., Wu, P., Feng, X., Ban, J., Zhang, S., Sunahara, G. and Ni, W. (2024). A low-carbon cement based on silicomanganese slag and granulated blast furnace slag: hydration process, microstructure, mechanical properties and leaching risks. *Journal of Building Engineering*, pp.109939–109939. doi:https://doi.org/10.1016/j.jobe.2024.109939.

CHAPTER 2: LITERATURE REVIEW

Introduction

This chapter covers the different concepts, processes, and theories that have already been developed and reported in the existing body of knowledge around the topic of this study, which is the greening of steel and the application of slag in cement. It also highlights the challenges which have been encountered and the developed solutions around this topic as well as the research gaps that still need to be uncovered. Furthermore, it also sheds light on the current initiatives taken by the steelmaking and cement industries to mitigate the foreseeable future impacts of global warming. The key factors that are driving the novel technology of melting the DRI (direct reduced iron) in an open bath furnace (OBF) are also critically discussed in this chapter. This chapter is subdivided into 4 themes as follows:

Theme 1: Overview of the ironmaking and steelmaking processes

Theme 2: Slags in the iron and steel industry

Theme 3: Cement making process and hydration of slag-cement blends

Theme 4: DRI-OBF ironmaking technology

2.1. Theme 1: Overview of ironmaking and steelmaking processes

This theme provides information on the steelmaking process by reviewing the conventional steelmaking routes as well as the new innovative technologies in ironmaking. The emphasis is on highlighting the importance of steel and describing blast furnace (BF) technology and recent alternative ironmaking technologies.

2.1.1. Global steel production and importance

The importance of steel and its usage in human activities dates back to the iron age (Verdeja et al., 2020). Steel is the most widely utilised metal in the world, and the production of crude steel has increased by over 1000 million tonnes in the last two decades as illustrated in Figure 2.

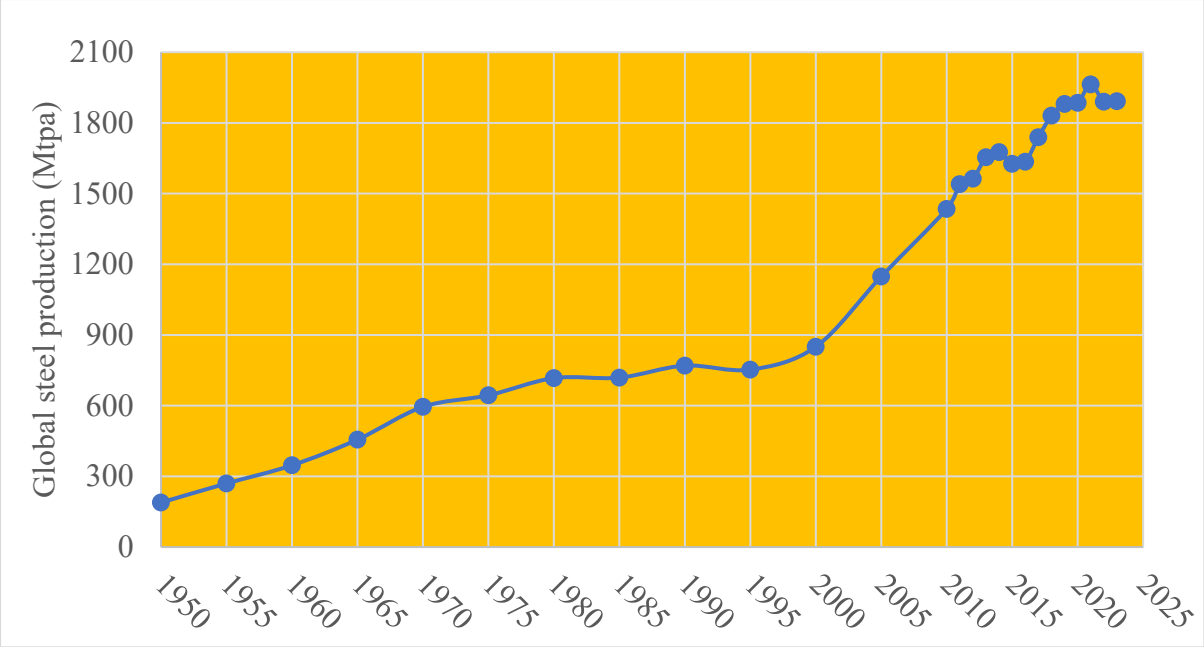


Figure 2: World crude steel production 1950-2023 (World Steel Association, 2024)

The trends in Figure 2 are an indication of the recent peak in the demand for steel by various sectors over the last two decades. Steel has significantly contributed to the modernization of the world and will continue to do so. The majority of steel is consumed in the construction sector for building and infrastructure. The second major consumption sector is in the manufacturing of mechanical equipment, and in the automotive industry. Figure 3 highlights the main sectors that consume steel and their proportions.

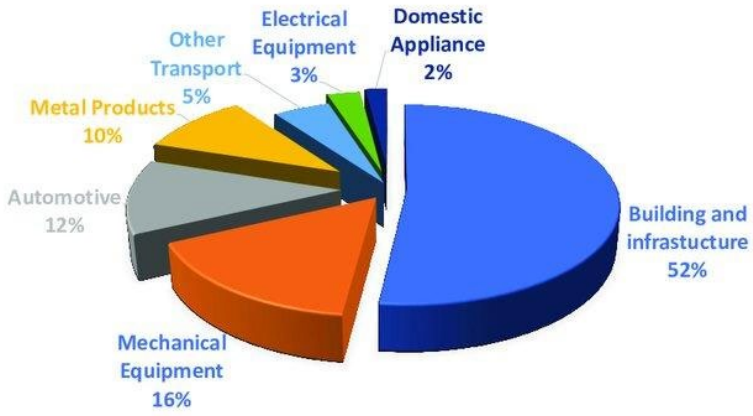


Figure 3: Usage of steel per sector (Mateus et al., 2022)

Mateus et al. (2022) noted that the high demand for steel in the civil construction sector driven partly by the current need for bigger and better buildings, which use increasingly more steel. As the world evolves, the need for infrastructural development increases together with the technology advances, ultimately requiring more steel to sustain that demand. Therefore, the future outlook for steel demand will be controlled by the developments in these major consuming sectors: construction, mechanical equipment, automotive and metal products.

China has been the world's leading producer of crude steel over the last decade, with a 2023 contribution of up to 53.9% to global production as shown in Figure 4. However, most of the iron ores used in China as raw materials for steel production are imported. Australia is the largest global producer of iron ore with a 2022 output totalling 944 Mt, more than 90% of which is exported (World Steel Association, 2024).

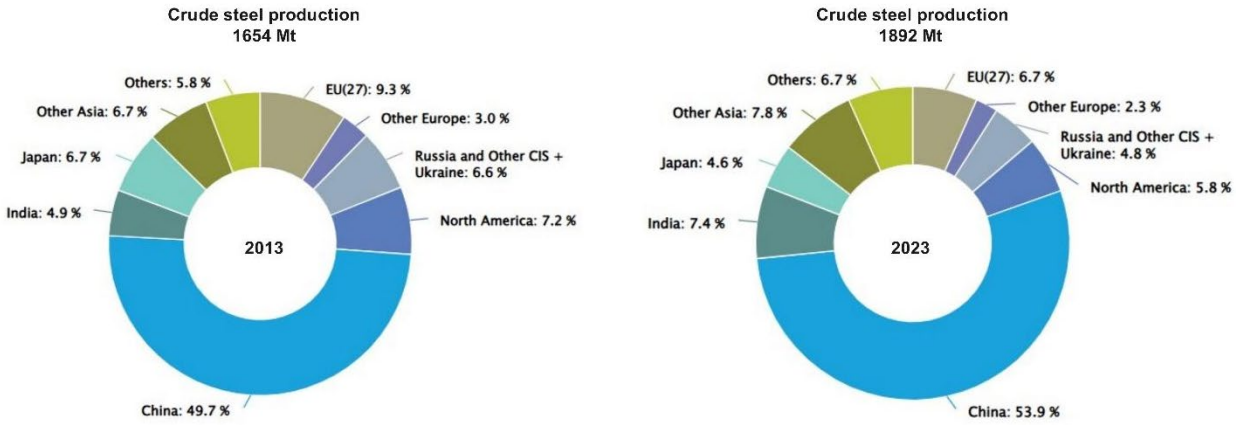


Figure 4: Major producing countries' share of global crude steel production in 2013 and 2023 (World Steel Association, 2024)

2.1.2. Steel production routes

There are two main steelmaking routes: the Blast furnace – Basic oxygen furnace (BF-BOF) route, and the electric arc steelmaking (EAF) route. It should be noted that both routes use iron as raw material, but in different states and with different energy sources. The BF uses iron ore in pelletized, sintered, or lumpy form as charge, with coke as the main reductant and energy source when blasted with hot air. Subsequently, the BOF uses blown-oxygen to reduce the carbon in pig iron, and the energy source is chemical energy from the combustion reaction of carbon and oxygen. On the other hand, the EAF uses metallic iron in the form of scrap, or DRI (direct reduced iron), as charge, with electricity as energy source (Geerdes et al., 2020, pp.1–12). Moreover, the BF-BOF process is considered as the primary source of global steel since it accounts for up to 75% of the total steel output as illustrated in Figure 5 (Lungen and Schmole, 2018; Geerdes et al., 2020).

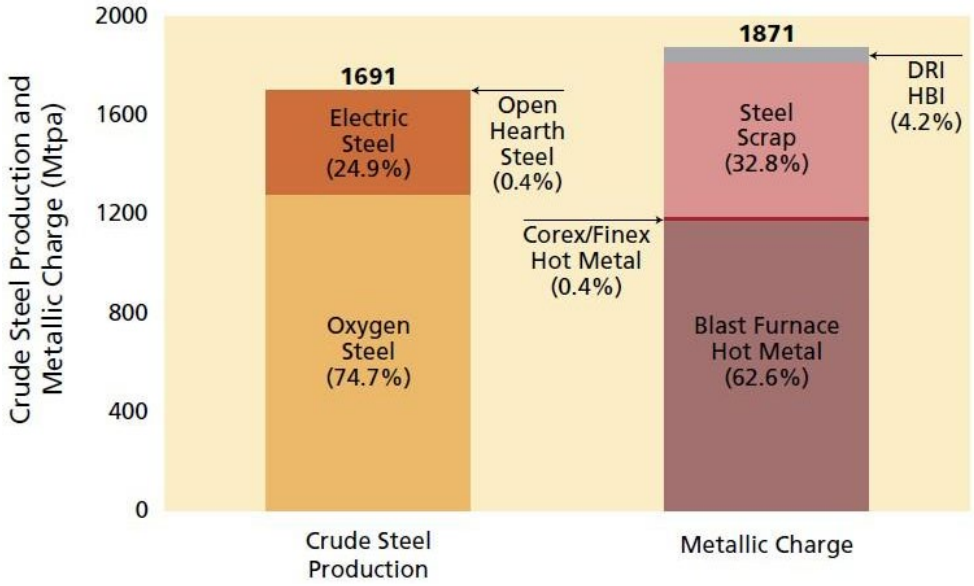


Figure 5: Steelmaking routes and iron source (Lungen and Schmole, 2018)

Figure 5 shows that the BF's hot metal is the major source of metallic iron charge, followed by steel scrap, and finally DRI together with hot briquetted iron (HBI). The hot metal from the Corex/Finex process is part of the innovation in ironmaking and will be briefly described in this chapter.

2.1.3. Ironmaking processes

The ironmaking process is the production of iron, also called hot metal, which is ultimately used as raw material for the production of steel. The hot metal, also called pig iron, is saturated with carbon at approximately 4-5%, which makes it very hard, but brittle, thereby limiting its use (Wang, 2016). The Blast furnace process is the primary production source of hot metal. Recent technological advances have allowed innovative ironmaking technologies such as smelting reduction (Corex process, Finex process, ITmk3 process), and DRI (Energiron process, MIDREX process) to emerge in the ironmaking industrial sector (Hasanbeigi et al, 2014). The main process of this study, the melting of DRI pellets in an open bath furnace (OBF), is also an innovative ironmaking technology (Nicholas and Basirat, 2022).

The primary drivers behind the exploration and development of these alternative ironmaking technologies are the reduction of energy consumption and CO_2 emissions in the BF process to mitigate the foreseeable impact of climate change (Pardo and Moya 2013, Hasanbeigi et al, 2014). In the steelmaking sector, the BF process is both an energy-intensive and CO_2-emitting process (Sohn & Mohassab, 2016; Madhavan et al., 2022).

Schmole et al. (2012) analysed the different factors that affect the path of steel production technologies and noted that the acceptance of technologies is mainly driven by CO_2 emissions policy requirements, and also by technological developments, price, and process efficiency. The reduction of CO_2 emissions is the current main driving factor of steelmaking innovations. A technological performance model, developed by Schmole et al. (2012) to indicate the evolution of major ironmaking processes 10 years ago is shown in Figure 6.

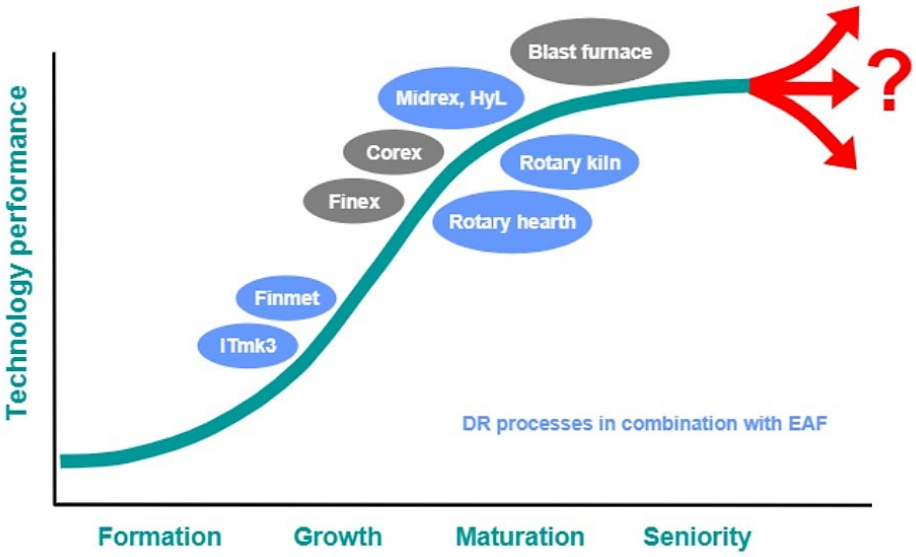


Figure 6: Maturity of ironmaking technologies in 2012 (Schmole et al., 2012)

The main ironmaking processes which will be described in this study together with the BF process are the Corex and Finex processes, the ITmk3 process, and the major DRI processes such as the Midrex process, and Energiron process.

2.1.3.1. Blast furnace (BF) process

The blast furnace process is the conventional route for the production of iron. A BF is a counter-current shaft furnace, where reduction and smelting of iron oxides with coke takes place. Fluxes are added to facilitate the formation of the slag and its separation from the hot metal (Anameric et al, 2019). The furnace is top-fed with the charge mix containing fluxes and the iron ore with mainly hematite (Fe_2O_3) and alternatively magnetite (Fe_3O_4) in pelletized, sintered, or lump form. The charge descends under the influence of gravity, and hot blast air is injected through the tuyeres at the bottom to react with coke from the charge and form carbon monoxide (CO) (Huang and Andrade, 2018). The hot gases rise up the shaft and are utilised in the reduction of iron oxide, as well as heating and melting of the descending charge (Ahmed et al., 2016; Biswas, 2011, p.528). As such, the descending charge and rising hot gases form the counter current working principle of the BF. The hot metal usually contains 4–5% carbon and 0.3–1% silicon and should be suitable for subsequent refining into steel (Anameric et al, 2019). The reaction zones in the BF along with the processes that occur in each zone are summarized in Figure 7 (Ranade and Chaubal, 2004, Ahmed et al., 2016).

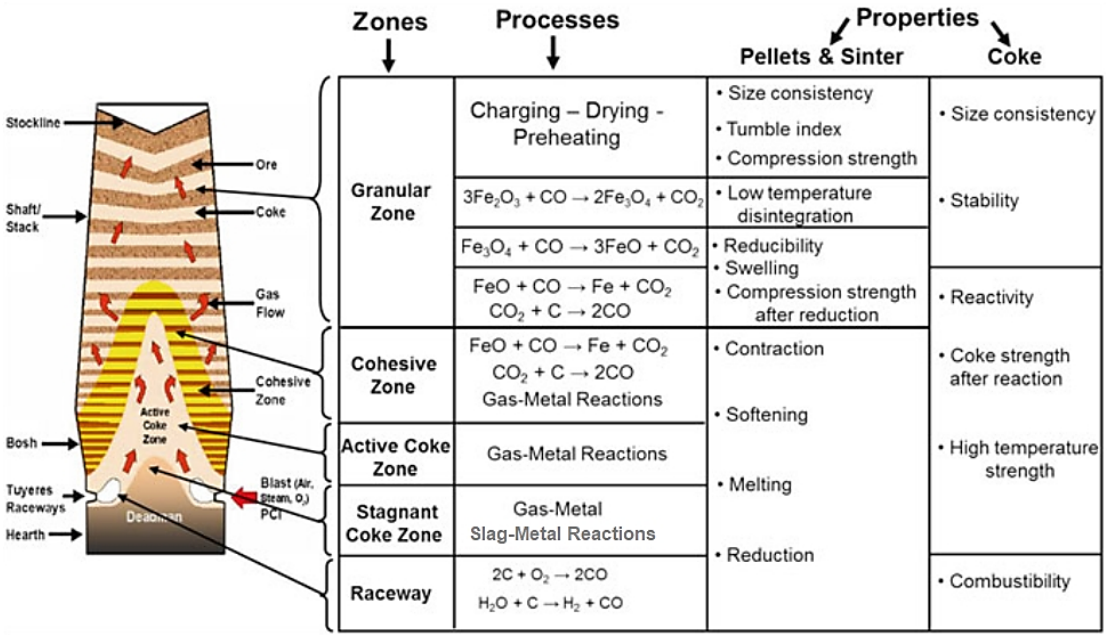


Figure 7: Zones and reactions in the blast furnace (Ranade and Chaubal, 2004)

It can be seen that most of the pre-reduction reactions of iron oxides occur in the granular zone, while the iron metal is formed in the cohesive zone. The charge undergoes various transformations from swelling, contraction, softening and melting. The gasification of coke by the hot blast air occurs in the raceways, where the highest temperature of 1900–2300 °C can be located (Geerdes et al., 2020, pp.1–12). The hot gas ascends through the blast furnace while heating, reducing, and melting the descending charge. Its composition changes through chemical reactions and its temperature decreases to 100–200 °C at the gas exit at the top of the BF. Geerdes et al. (2020, pp.1–12) illustrated the interactions between the ascending hot gas and the descending charge as depicted in Figure 8.

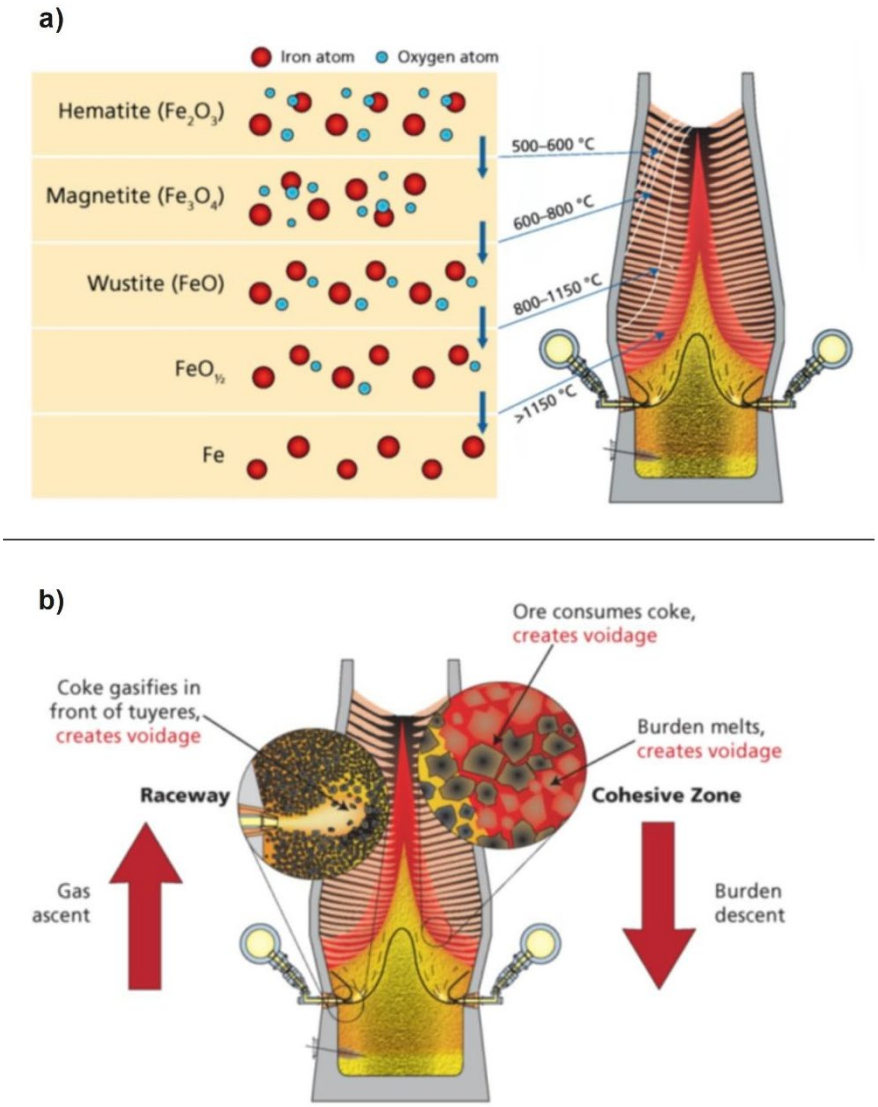


Figure 8: Order of reduction of iron ore (a), counter current hot gas-charge interactions (b) (Geerdes et al. 2020, pp.1–12)

Figure 8 shows that the main process in blast furnace operations is the gasification of coke, generating hot reducing gas that fulfils two purposes: the reduction of the descending charge to Fe and the melting of the reduced charge. Ahmed et al. (2016) stated that the charging system is extremely important in modern BF operation because the distribution of coke and burden materials inside the furnace can significantly impact the overall productivity of the furnace.

Overall, the BF is still the dominant ironmaking process despite the environmental concerns linked to CO_2 emissions that have been raised for the last two decades. Over 500 years, the BF process has seen technological improvements and innovations to abate the emission of greenhouse gases (GHG) of which the major component is CO_2. These efficiency improvements include improvement of the feeding system, alternate fuels injection through the tuyeres, recirculation of waste gases, and heat recovery practices (Cavaliere, 2019). However, the continuous reliance of the BF process on metallurgical coke for fuel and reduction purposes

has raised serious environmental concerns, leading to the exploration of ironmaking technologies that utilise non-coking coal, natural gas, and hydrogen gas as reducing agents. The CO_2 emissions in a typical integrated BF-BOF steel plant are summarized in Figure 9 (Birat and Maizière-lès-Metz, 2010; Hasanbeigi et al, 2014), indicating that the total CO_2 emissions stand at 1815 kg CO_2/t rolled coil with over 1700 kg of CO_2 (94%) associated with coal and about 100 kg of CO_2 associated with the calcination of limestone. Moreover, the BF alone contributes about 69% of CO_2 emissions to the total emissions of the integrated steel plants.

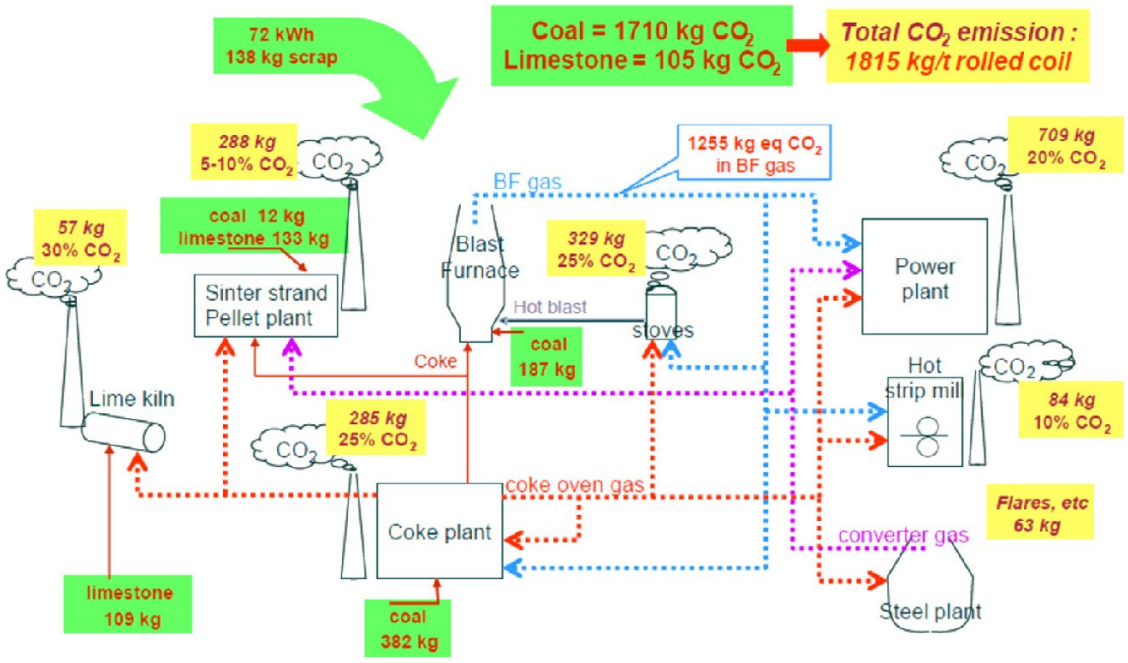


Figure 9: CO2 emissions in a typical integrated BF-BOF steel plant (Hasanbeigi et al, 2014)

2.1.3.2.Corex/Finex processes

The Corex and Finex processes are direct smelting processes that were invented to avoid the reliance of the BF process on metallurgical coke by using non-coking coal. These two processes, developed by Siemens VAI, are industrially proven and commercially available technologies to produce hot metal (Lu et al., 2013; Hasanbeigi et al, 2014). The production of hot metal is achieved through two stages, with the Melter-gasifier being the final stage in both processes. The Melter-gasifier is a fluidized bed chamber resting on liquid slag and hot metal bath, in which coal gasification occurs upon charging of non-coking coal and injection of oxygen through the tuyeres around its circumference (Hasanbeigi et al, 2014). Then, the generated hot reducing gas is used for reduction in the upper unit.

For the Corex process, the upper unit is a shaft furnace in which reduction of iron ore lumps or pellets with the hot gas produces hot DRI that is charged in the Melter-gasifier to ultimately produce hot metal and molten slag (Diez et al., 2023). In comparison, the Finex process utilizes a series of fluidized bed reactors forming a counter-flow system, typically with three to four stages, to reduce fine iron ore into DRI fines. The DRI fines are then agglomerated into hot

compacted iron (HCI), which is charged in the Melter-gasifier to produce hot metal and molten slag (Hasanbeigi et al, 2014).

These processes were deemed cost-effective and environmentally friendly due to their capability of using non-coking coal (coal with less fixed carbon and high ash content) for reduction and smelting operations (Lu et al., 2013). However, a small proportion of coke was also reported to be used alongside non-coking coal for heat generation (Diez et al., 2023). Figure 10 illustrates a generic representation of the Corex and Finex processes in comparison to the blast furnace (Bohm et al., 2009; Hasanbeigi et al, 2014).

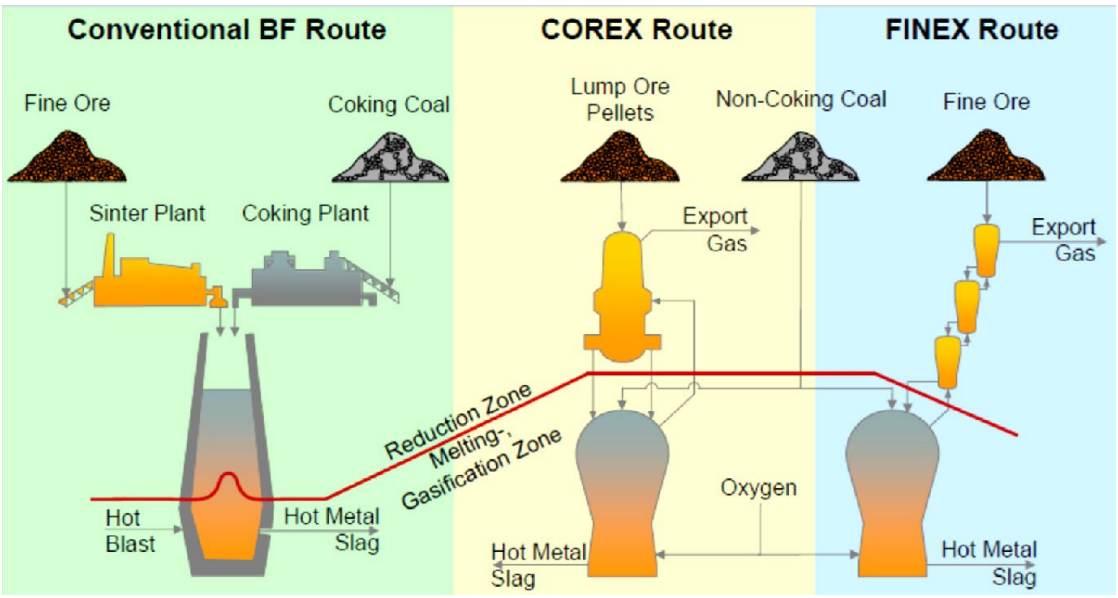


Figure 10:Comparison of Corex and Finex processes to the Blast furnace process (Hasanbeigi et al, 2014)

As can be seen in Figure 10, there is no requirement for sintering and coking plants in the Corex and Finex routes, which is effective in eliminating the CO_2 emissions associated with these additional plants. In addition, the Finex technology can treat fine iron ores directly, and the two processes can produce products similar to the BF (Hasanbeigi et al, 2014). The two routes were claimed to have a lower capital and operational cost compared to the BF routes (Lu et al., 2013). However, these two processes still use carbon-bearing materials for reduction and heat provision, which contribute to high CO_2 emissions. Furthermore, although these processes reached the commercial stage a decade ago, the global adoption rate is very low in the steel industry as noted in Hasanbeigi et al, (2014).

2.1.3.3. DRI processes

DRI technologies are processes used to directly reduce iron ores at solid state to metallic iron using natural gas (NG), or non-coking coal as the energy source. As such, the DRI technology can be either gas-based (NG), or coal-based, depending on the availability of NG and coal in the region where the DRI process is employed (Liu et al., 2021). The DRI process is currently among the most dominant ironmaking technologies, and the gas-based DRI process has

recently attracted a lot of attention due its environmental friendliness and the possibility of using hydrogen as fuel (Ji et al., 2024). Currently, the two leading DRI technologies, and which are commercially available, are the Midrex process and the Energiron process, together contributing up to 82% of the global DRI output (Hamadeh et al, 2018). The remaining proportion is produced using processes such as the Rotary kiln and Rotary hearth. The Midrex process is the leading technology, producing around 65% of global DRI, with 17% produced by the Energiron process (Hamadeh et al, 2018; Bailera et al., 2021).

The Midrex and Energiron DRI processes are similar in that they both use a shaft furnace to directly reduce iron pellets or lumps with NG. They both have the advantages of using gases from other processes such as hydrogen, syngas produced from coke oven gas (COG), or a fossil source (Yilmaz and Turek, 2017; Duarte and Becerra, 2015; Ji et al., 2024). The main difference is that the Energiron process uses an in-situ NG-reformer to generate the reducing gases (H_2 and CO) with capture and reinjection of the CO_2 in the shaft together with the NG, whereas the Midrex process uses an external NG-reformer to generate the reducing gases (H_2 and CO). Moreover, the DRI product in the Energiron process has a relatively higher carbon content (Yilmaz and Turek, 2017; Bailera et al., 2021).

The DRI process plays a major role in this study. As such, further details regarding these two DRI technologies are covered separately in theme 4 of this chapter.

2.1.3.4. ITmk3 process

The ITmk3 (Ironmaking Technology Mark 3) process is a direct reduction ironmaking technology that uses a rotary hearth furnace (RHF) as a stand-alone unit to produce highly-metallized iron nuggets (97% iron and 3% carbon) with no gangue, unlike other RHFs that reduce iron ores to about 80% metallic Fe and require a secondary smelting unit (Hasanbeigi et al, 2014). This process was developed by Kobe Steel and is classified as the third generation of ironmaking following the BF, and DRI technologies, and hence the label “mark 3” (Kikuchi et al., 2010). It is a rapid ironmaking process that combines reduction, carburization, melting of iron and slag separation all at relatively low temperatures. Reactions occur much faster in the ITmk3 process – within 10 minutes – compared to the 8 hours retention time in the BF process and the 6 hours in the Midrex process (Kikuchi et al., 2010). Figure 11 illustrates the process flow in the ITmk3 process.

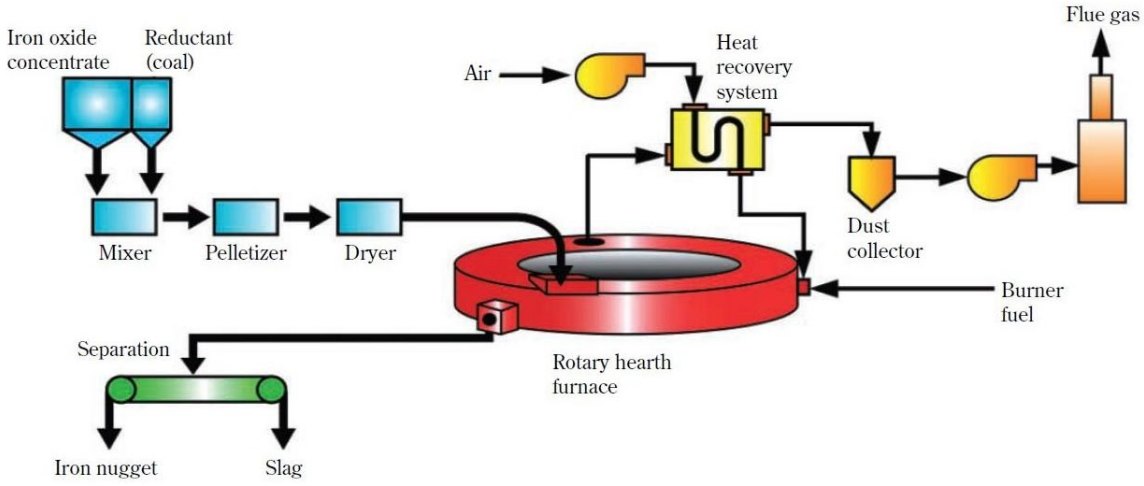


Figure 11: ITmk3 overall process flow (Kikuchi et al., 2010)

This process uses iron ore and non-coking coal as feedstocks. The temperature is raised in the last zone of the RHF to melt the reduced iron ore and separate it from the gangue. The produced iron nuggets can be used directly in the BOF or EAF for refinement to crude steel. This technology offers the same benefits as the smelting reduction technologies in using non-coking coal, as opposed to coke in the BF process, but with a faster production time. Unlike the HBI and DRI, the iron is completely reduced in the ITmk3 process and easily acceptable by EAF operations (Kikuchi et al., 2010). However, like the Corex/Finex processes, the ITmk3 process also uses coal as an energy source and reductant, which results in high CO_2 emissions. An ITmk3 process plant with an annual capacity of 500 000 tons was commissioned in USA in 2010 (Hasanbeigi et al, 2014), but the current commercial status indicates that no additional plants have been built.

2.1.3.5. CO_2 emissions in ironmaking technologies

Overall, DRI processes have a promising future in the ironmaking industry due to their flexibility of accommodating different reducing gases, including carbon-free hydrogen (Ji et al., 2024). This makes DRI processes the possible cornerstones of ironmaking in the future, unlike reduction smelting technologies (Corex, Finex, ITmk3), which rely heavily on carbon-bearing reductant and fuel as shown in the preceding sections. However, the reduction of iron in the DRI process is not 100% complete, and with the process being at solid state means that the gangue is still in the DRI. This requires an extra smelting stage to complete the reduction process and separate the gangue in the form of slag. Hence, DRI products are currently being smelted in electric arc furnaces (EAF) to produce steel.

2.1.4. Steelmaking processes

After ironmaking, the produced hot metal has limited use because it contains 3-4% carbon, making it very hard, brittle, and prone to corrosion during applications (Chen et al., 2022; Wang, 2016). Hence, the requirement of a hot metal refining stage to transform the hot metal into a strong and corrosion resistive material, known as steel. This refining process of the hot metal is known as steelmaking, which produces steel that can be used in major applications as noted in Mateus et al., (2022) and World Steel Association, (2024). Globally, the major

steelmaking processes are basic oxygen furnace (BOF) steelmaking and electric arc furnace (EAF) steelmaking, accounting for 71.1% and 28.6 % of steel production respectively, with the former being the most carbon intensive as shown in Figure 12 (World Steel Association, 2024).

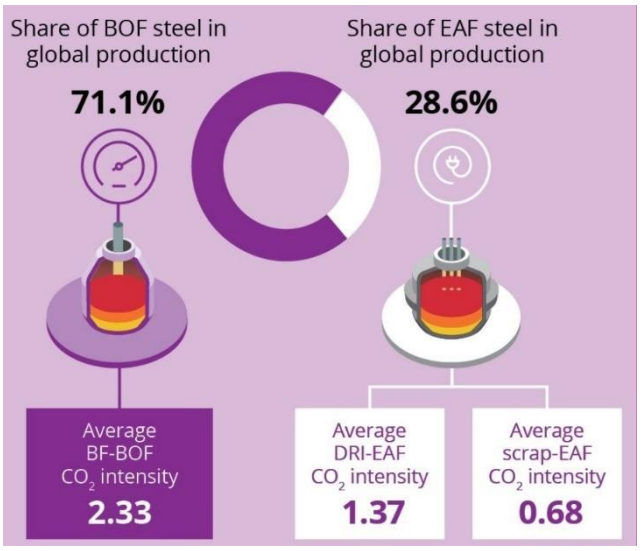


Figure 12: Crude steel production by process (World Steel Association, 2024)

In the final steel product, the carbon is lowered to less than 1% and alloys (secondary metals), such as manganese and chromium, are added to improve the physical and chemical properties (Wang, 2016; Pistorius et al., 2019).

2.1.4.1. Basic Oxygen furnace (BOF)

The BOF is usually charged with hot metal and some steel scrap, and the major operation is the blowing of oxygen through a lance to remove carbon from the hot metal and produce steel. Scrap addition is used to control the temperature of the BOF process, and the level of carbon is reduced from 4% to 0.5%. The reaction of carbon and oxygen results in the release of heat, which keeps the hot metal molten, and the release of CO gas which vigorously mixes the charge as it leaves the vessel (He and Wang, 2017). Therefore, the BOF does not require an additional heating source. Lime (CaO) is added to facilitate slag formation and there is also the occurrence of other oxidation processes for elements such as sulphur, phosphorus, silicon, and manganese (Pistorius et al., 2019).

2.1.4.2. Electric arc furnace (EAF)

EAF steelmaking is the second major steelmaking route after the BF-BOF. It uses an electric arc generated by the electrodes to melt the charge and produce steel. Steel scrap of given grades, and DRI pellets are generally the charge to this furnace, together with the fluxes used to form the slag, thereby enabling its separation from steel (Lee and Sohn, 2014; Pistorius et al., 2019; Kerimov and Shakhov, 2020). It has been noted that carbon powder and CO_2-oxygen mixed gas are also injected to foam the slag and improve the furnace's performance (Li et al., 2023). It can be seen that the furnace requires electrical energy to generate the arc depending on whether it is a direct current (DC) furnace or an alternate current (AC) furnace. For AC

furnaces, the arcing occurs between the electrodes, whereas for DC furnaces, arcing occurs between the electrode (cathode) and a conductive hearth (anode) at the bottom (Kleinschmidt et al., 2010).

2.1.4.3. CO_2 emissions in steelmaking routes

Overall, steelmaking via an EAF using scrap, or DRI, is the most promising steelmaking route for the future due to the lower CO_2 emissions compared to BF-BOF steelmaking as shown in Figure12. In addition, Figure12 shows that the scrap-based EAF is the most environmentally friendly with a CO_2 intensity of 0.68 compared to the 1.37 CO_2 intensity in the DRI-based EAF. However, the EAF-scrap route heavily depends on the availability of scrap. It should be noted that the CO_2 intensity is the ratio of tons of CO_2 per ton of steel produced (World Steel Association, 2024). The BOF process in itself does not release a substantial amount of CO_2, it is the raw material (pig iron) from the BF process which contributes significantly to the total emissions in the BF-BOF route, as previously shown in Figure 9.

Another factor that contributes to the CO_2 emissions in EAF operations is the practice of slag foaming, which is critical in providing exceptional performance such as enhanced heating efficiency, and protection of electrodes and refractory lining materials (de Almeida et al., 2017, Zhu et al., 2012). Slag foaming results in the release of CO gas from the bath, which then contributes to the overall CO_2 emissions of the EAF process (Liu and Yan, 2024).

2.2. Theme 2: Slags in the iron and steel industry

During the ironmaking and steelmaking processes mentioned in theme 1, slags are formed as by-products, which are discussed in this theme. The emphasis is on the BF slag, however other steelmaking slags, such as the BOF and EAF slags, are also briefly discussed.

2.2.1. Statistics of slags in the iron and steel industry

Slags are molten oxide by-products from either ironmaking or steelmaking, arising from a mixture of gangue and fluxing materials during the process (Pistorius et al., 2019). The addition of fluxing materials enables the removal of gangue materials (impurities) from the iron ore, or DRI, in the form of slag that is lighter than the liquid metal, hence it floats on top of the metal and can easily be separated. In 2023, the global iron slag production was estimated to be between 330 million and 390 million tons, and steel slag production (EAF + BOF) was estimated to be between 190 million and 290 million tons (Callaghan, 2024). These figures are influenced by the global production patterns of crude iron and steel. Moreover, slags are among the largest solid by-products from the iron and steel industry, by mass, as shown in Figure 13 (World Steel Association, 2021). Hence, slags necessitate careful management, including recovery and re-use, and handling procedures to avoid landfill and risks associated with waste disposal.

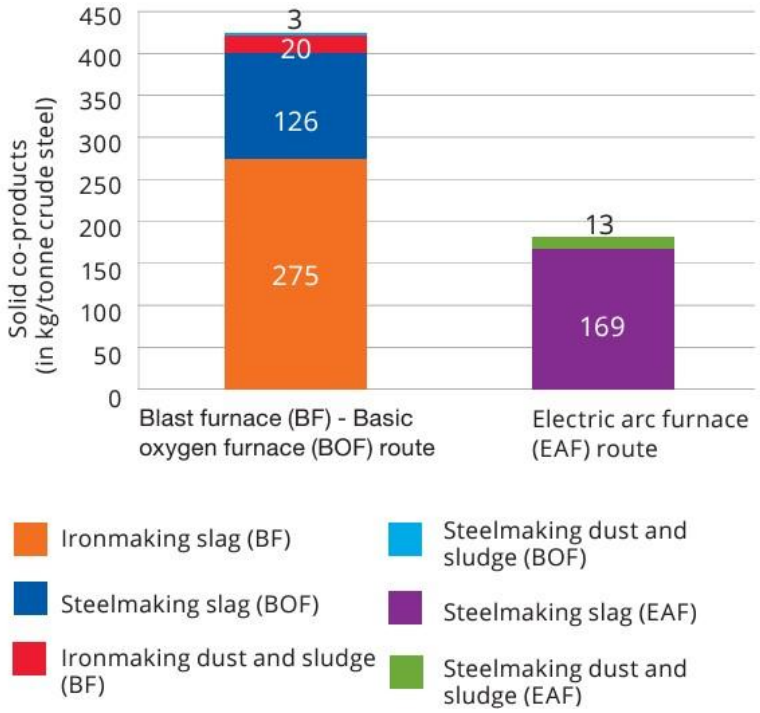


Figure 13: Solid by-products in iron and steel industry (World Steel Association, 2021)

The molten slags are either air-cooled or water-granulated, which affects their downstream uses (Tripathy et al., 2020). The major application of slags is in the construction industry as aggregate and supplementary cementitious materials, while other applications include road paving and asphalting, road bases, and inert fillers (World Steel Association, 2021). The usage as aggregates in concrete is at a low level compared to natural aggregates, such as crushed stone, sand and gravels which are widely available. Callaghan (2024) highlighted that 90% of the value from the total slag output comes from BF slag, mostly the granulated slag. Hence, the granulated BF slag is the most valuable solid by-product from the iron and steel industry. The extended application of granulated BF slag in the cement industry will increase the global value of slag, especially with the emerging ironmaking technologies that are planned to produce lower CO_2 products (hot metal and slag). The types of utilization of steel slags (BOF + EAF) in Europe and major steel producing countries are shown in Figure 14.

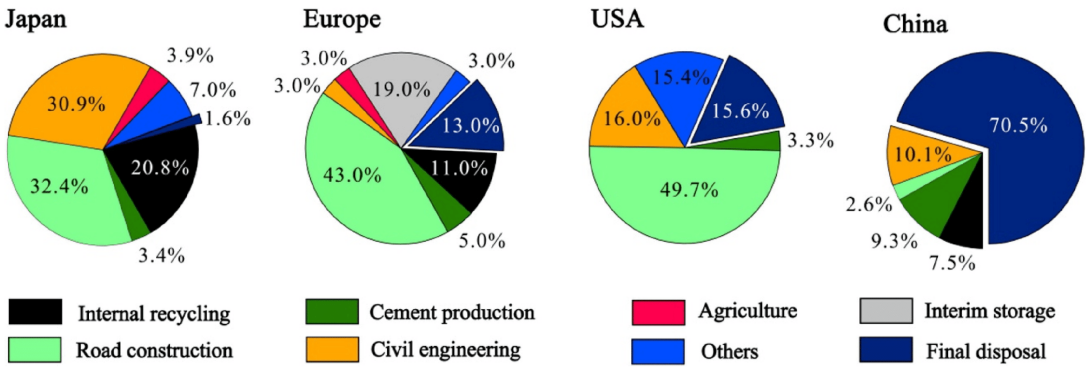


Figure 14: Steel slags (BOF and EAF) utilization per region around the world (Guo et al., 2018)

With the exception of China, it can be seen that the main use of steel slags is in road construction as aggregates. Japan has almost a 100% utilization rate compared to China, which disposes about 70% of its steel slags. A higher disposal rate of steel slags leads to excessive land occupation and environmental risks linked to the leaching toxicity of heavy metals like Mn and Cr (Sun et al., 2024).

In recent years, there has been increasing interest in valorising the BOF and EAF slags as clinker substitutes in the cement industry due to the higher CO_2 emissions associated with the BF technology. However, these steelmaking slags have limited application in the cement industry due to their higher content of free CaO, free MgO, and heavy metals (Pistorius et al., 2019, Horii et al., 2017; Sun et al., 2024). According to Das et al. (2007), 50 to 90% of steel slags have a high concentration of sulphur and phosphorus, thereby limiting their direct recycling to the ironmaking and steelmaking industries. Hence, steel slags are mostly re-used to recover the lost iron during recycling, with the resulting slag recycled to other industries. Granulation of steel slags is not widely practised while hot-stage slag engineering is sometimes employed to improve the properties of steel slags (Pistorius et al., 2019).

2.2.2. BOF slag

The BOF process, as a major contributor to the global output of steel, also generates a substantial amount of slag. Based on data summarized by Yildirim and Prezzi (2011), the chemical composition of BOF slags is in the range of CaO (35 - 55%), FeO/Fe_2O_3 (10 - 38%), SiO_2 (8 - 20%), Al_2O_3 (1 - 6%), and MgO (1 - 15%). The high CaO content is due to the addition of lime for slag formation with the oxidized silica during oxygen blowing, while the Fe loss to the slag depends on the efficiency of the given BOF process. The content of free CaO can go up to 12% while Horii et al. (2015) noted that hydration of free CaO and MgO leads to poor volume stability, thereby limiting the usage of BOF slag in construction work, for example: road construction.

2.2.3. EAF slag

EAF slag is similar to BOF slag, except that the BOF slag has high alkalinity (MgO +CaO) and the EAF slag has higher heavy metals content (Horii et al. 2015). The chemical composition of EAF slags varies widely depending on the type of steel produced. The typical composition is in the range of CaO (22 - 55%), FeO/Fe_2O_3 (10 - 35%), SiO_2 (8 - 20%), Al_2O_3 (5 - 13%), MgO (3 - 15%), and MnO (3 - 8%) as per the data gathered by Yildirim and Prezzi (2011). EAF slag may also contain chromium and other heavy metals if stainless steel is produced (Shen et al., 2004).

The problems with recycling steelmaking slags (EAF and BOF) in the cement industry whether as a raw material addition in clinker production, or for blending with a cement product are linked to the high iron content and the presence of leachable heavy metals, which can pose environmental risks.

2.2.4. BF slag

2.2.4.1. Importance and chemical composition

The BF slag is the highest value solid by-product from the entire iron and steel industry, particularly as granulated BF slag, due to its cementitious application (Callaghan, 2024). The chemical composition of the BF slag varies widely depending on the region and the composition of the raw materials used. The reported chemical composition range is Al_2O_3 (8 - 24%), CaO (30 - 50%), MgO (1 - 18%), and SiO_2 (28 - 38%) (Dom et al., 2022; Shetty and Jain, 2019). Unlike steel slags, the BF slag generally contains trace levels of heavy metals, and the iron content is usually less than 2% (Pistorius et al., 2019). Hence, the leaching of heavy metals is comparatively low in BF slag.

2.2.4.2. Glass structure

The main components of the BF slag form the Al_2O_3-CaO-SiO_2-MgO glass structure, in which SiO_2 is a network former while basic components, such as CaO and MgO modify the glass network. Al_2O_3, on the other hand, displays amphoteric behaviour by acting either as acidic, or basic depending on the concentration of the basic components (Blotevogel et al., 2020). Generally, glass structures that are more modified, or depolymerized, dissolve faster when mixed with water, thereby allowing the slag to display higher reactivity (Zhang et al., 2022). Therefore, the degree of depolymerization increases as the proportion of network modifiers (CaO, MgO) increases. Moreover, the significant presence of other elements, such as in EAF and BOF slags, decreases the total proportion of the network formers and modifiers in the slag, thereby affecting the overall reactivity of glass. Hence, the EAF and BOF slags are not widely employed in cementitious applications, only the BF slag possesses viable reactivity due to its chemical composition when finely milled.

The theories behind glass formation play a very important role in the slag designing process and are further covered in chapter 7. The degree of depolymerization is commonly measured using the basicity (CaO+MgO)/SiO_2 value. In a more precise way, it is measured by calculating the number of non-bridging oxygen atoms per silicate tetrahedron (NBO/T) as reported by Blotevogel et al. (2024). Silica forms the silicate tetrahedron (SiO_4^{4-}) through covalent bonds, whereas basic cations (Ca^{2+} and Mg^{2+}) react with the oxygen through ionic bonds to depolymerize the glass (Mills et al., 2012). The NBO/T ranges between 0 (complete 3D tectosilicate network) to 4 (no bridging oxygen - nesosilicate network). Therefore, the lower the NBO/T, the lower the proportion of basic cations, the less depolymerized the glass structure, and the lower the corresponding reactivity of the BF slag.

2.2.4.3. Thermophysical properties

The main thermophysical properties of the molten BF slag which are generally important during smelting operations are the liquidus temperature, the viscosity, the thermal conductivity, and the electrical conductivity. These properties are also dependent on the structure of the silicate network, which in turn rely on the chemical composition of the slag. The liquidus temperature is the temperature above which the slag becomes 100% liquid, or the temperature at which the first solids form on cooling (Mills et al., 2012). The viscosity is the measure of the fluidity, or flowability of the slag. The slag should be fluid enough so that it can be separated from the metal and easily tapped from the blast furnace.

The thermal conductivity highlights the heat transfer capability of the slag. Mills (1993) stated that the thermal conductivity of the slag at the liquidus temperature decreases almost linearly as the silicate network becomes more depolymerized, demonstrating that thermal conduction in the slag favours covalent bonds. It was further noted that it is the opposite effect for electrical conductivity. The slag conducts electricity through the motion of cations, and the more cations present in the slag, the more depolymerized the glass structure, and the higher the electrical conductivity (Mills et al., 2012). Therefore, all the physical properties of the slag depend on the chemical composition, a more depolymerized glass structure at liquidus temperature will lead to reduced viscosity and thermal conductivity, with increased electrical conductivity.

2.2.4.4. Granulation and uses

According to Tripathy et al. (2020), air-cooled BF slag contains more than 50% of crystalline phases, while water-quenched or granulated BF slag contains more than 90% amorphous or glass phases. Crystalline phases are inert and do not possess hydraulic properties (Escalante et al., 2001; Tripathy et al. 2020). Hence, the more glass content, the higher the reactivity of the slag, provided that the degree of depolymerization is constant. Currently, over 66% of conventional BF slags are granulated to form granulated BF slag GBFS and used in the manufacturing of Portland slag-cement blends (Ehrenberg et al., 2020). Moreover, air-cooled slags are mainly used as aggregates in the construction industry, and other applications such as asphalting and road paving.

Temperature and viscosity are the main factors that affect the final glass content of the slag (Escalante et al., 2001). The slag needs to be molten and fluid enough before water granulation to ensure sufficient glass formation. Hence, granulation units are generally installed next to the furnace to avoid major temperature drops. Moreover, GBFS is the only solid by-product with a high monetary value in the iron and steel industry (Callaghan, 2024). It can be seen that water granulation is the most valuable route for the valorisation of the BF slag into a cementitious material that can be used in the cement industry in a sustainable application which contributes to decarbonization.

2.2.4.5. Size reduction

Prior to the application in the manufacturing of slag-cement blends, GBFS is ground to a fine particle size in order to improve its reactivity. This is because the hydration of coarser particles is slower, leading to inferior cementitious performance for both slag and cement (Binici et al., 2007). Industrially, the grinding of GGBFS is done using ball mills, or the more energy efficient vertical roller mills (Tamashige et al., 1991). However, the cement industry is still widely using the ball mill technology because of its simplicity of operations, and comparatively lower investment cost (Xu et al., 2015). Moreover, when granulated blast furnace slag (GBFS) is ground, it is known as ground granulated blast furnace slag (GGBFS), which is the final product that is mixed with Portland cement to produce a range of slag-cement blends that are commercially available in the market, for example: CEM II B (21 – 35% slag) and CEM III A (36 – 65% slag).

2.2.5. GGBFS utilisation and circular economy

The utilisation of granulated BF slag to the cement industry prevents massive landfilling of waste slags, reduces the requirement of the CO_2-intensive clinker in cement by replacing it with slag, allows conservation of natural resources, and reduces the overall energy requirement associated with clinker production. These are attributes that will contribute to sustainability and the achievement of zero-waste steel production. In 2023, cement producers in the European Union and Great Britain reduced the emission of 12Mt of CO_2 through the substitution of clinker with granulated blast furnace slag(Global Slag, 2024). Moreover, up to 42% of embodied energy and 59% embodied CO_2 emissions can be saved by replacing Portland cement with slag-cement blends in concrete without counting the CO_2 emissions associated with slag production (Skyway Slag Cement, 2024; World Steel Association, 2021).

It can be seen that the utilisation of slag is also pivotal to the current transition towards a greener and circular economy in the iron and steel industry. Furthermore, it is the development of innovative technologies and the synergy with the cement industry to utilize slags that can bring the steel industry closer to its goal of zero-waste and green production (World Steel Association, 2021). Therefore, the untapped potential of slags arising from these emerging new technologies in the steelmaking industry needs to be explored, studied, and improved for efficient utilization.

2.3. Theme 3: Cement making process and hydration of slag-cement blends

This theme highlights the importance of cement in human civilization as a building and construction material. It further shows the current environmental challenge related to CO_2 emissions from the cement industry as well as the solutions taken to reduce these emissions. Lastly, it includes a brief description of the cement making process, the hydration of cement, and the contribution of BF slag to the cement industry as a supplementary cementitious material.

2.3.1. Importance of cement and associated CO_2 emissions

The binding properties of ordinary Portland cement (PC) has made concrete (a mixture of cement, sand, aggregates, and water) the most widely used material in the world aside from water (Gagg, 2014). Moreover, the ability of concrete to withstand severe environmental conditions and support heavy compressive loads has made it the most consumed product in the civil and construction sector (Antunes et al., 2021). However, the CO_2 emissions associated with the production process of PC have raised serious environmental concerns. In 2022, around 4158 Mt of cement was produced with a CO_2 intensity 0.58 t CO_2/t cement, bringing the overall annual CO_2 emissions to 2411 Mt (IEA, 2024). Currently, the cement industry contributes 6-8% of global CO_2 emissions (Ahmad et al., 2023), very close to the global CO_2 emissions from the iron and steel industry. Hence, the cement industry is currently seeking ways to reduce its CO_2 emissions with a projected CO_2 intensity of 0.45 in 2030 for net-zero emission scenarios (IEA, 2024) and fulfilment of the 2015 Paris agreement to achieve carbon neutrality by 2050. The distribution of CO_2 emissions in the cement industry is shown in Figure 15.

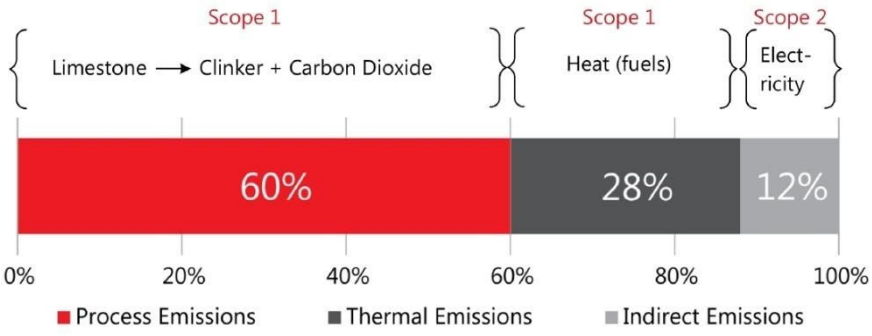


Figure 15: Distribution of CO2 emissions in the cement industry (Cement Industry Federation, 2023)

It can be seen that the majority of the CO_2 emissions comes from the calcination of limestone. The share of global cement production by leading producing countries, in 2022, is summarized in Figure 16.

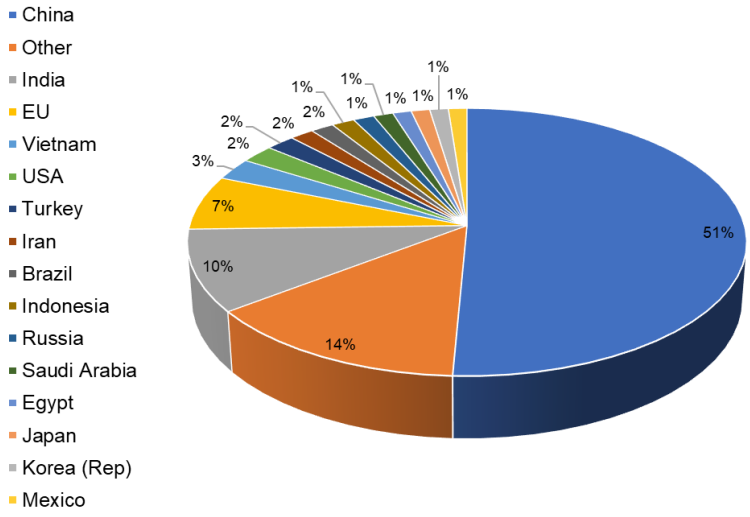


Figure 16: Global cement production by leading countries for 2022 (USGS, 2024; Cembureau, 2023).

It can be seen that China is the biggest producer with a contribution of 53% to the total global output of cement, followed by India with a contribution of 8%. The World Cement Association (2024) further stated that the global production of cement has increased by 30 times since 1950 due to increased urbanisation and economic development across the world.

2.3.2. Cement making process

Cement is the main binding material in concrete, typically making up 10 to 15% of the mix by volume (Gagg, 2014). The preparation of raw materials for PC consists of calcining limestone and clay in a kiln at temperatures up to 1450ºC to produce clinker, the main component of cement (Nicolas et al., 2019). The mixing raw materials require careful proportioning to control the quality of the clinker produced. Clinker is primarily made up of four constituents: Tricalcium silicate (alite) $3CaO.SiO_2$; Dicalcium silicate (belite) $2CaO.SiO_2$; Tricalcium aluminate $3CaO.Al_2O_3$; Tetracalcium aluminoferrite $4CaO.Al_2O_3.Fe_2O_3$. In cement notations,

CaO, SiO_2, Al_2O_3, H_2O, SO_3, Na_2O, and CO_2 are represented as C, S, A, H, $\bar{S}$, N, and $\bar{C}$ respectively (Hewlett and Liska, 2019). Therefore, the main components of clinker in cement notations are C_3S, C_2S, C_3A, C_4AF respectively. Table 1 summarizes the main components of cement as well as their impact during hydration.

Table 1: Main components of cement (Sahin, 2023)

	Name	Phase (compound)	Shorthand notation	Effect	Amount	
Aluminates		Tricalcium aluminate	C_3A	• Liberates a large amount of heat • Can cause early stiffening and flash set • Prone to sulfate attack	5%–10%	Clinker
	Ferrite	Tetracalcium aluminoferrite	C_4AF	• Contributes little to strength • Contributes to gray color	5%–15%	
Silicates	Alite	Tricalcium silicate	C_3S	• Hydrates and hardens rapidly • Largely responsible for initial set and early strength	50%–70%	
	Belite	Dicalcium silicate	C_2S	• Hydrates and hardens slowly • Contributes to strength increase after one week • Contributes to low concrete permeability	15%–30%	
Sulfates	Gypsum*	Calcium sulfate	$C\bar{S}$	• Controls the hydration of C_3A	3%–5%	Gypsum

After calcination, the clinker is cooled, finely ground together with a small amount of gypsum to form Portland cement (Gagg, 2014). Nicolas et al. (2019) added that PC can also contain some minor inclusions of unreacted (free) lime (CaO) and magnesia (MgO), also some alkali sulphates. A typical Portland cement chemical analysis comprises by weight CaO (60 – 67%), SiO_2 (17 – 25%), Al_2O_3 (3 – 8%), Fe_2O_3 (0.5 – 6%), MgO (0.1 – 4%), SO_3 (1 – 3%), and lasty $Na_2O + K_2O$ (0.2 – 1.3%) as noted by (Sahin, 2023).

A flow diagram highlighting the calcination process which results in clinker production, as well as the milling of clinker together with gypsum to produce cement is illustrated in Figure 17.

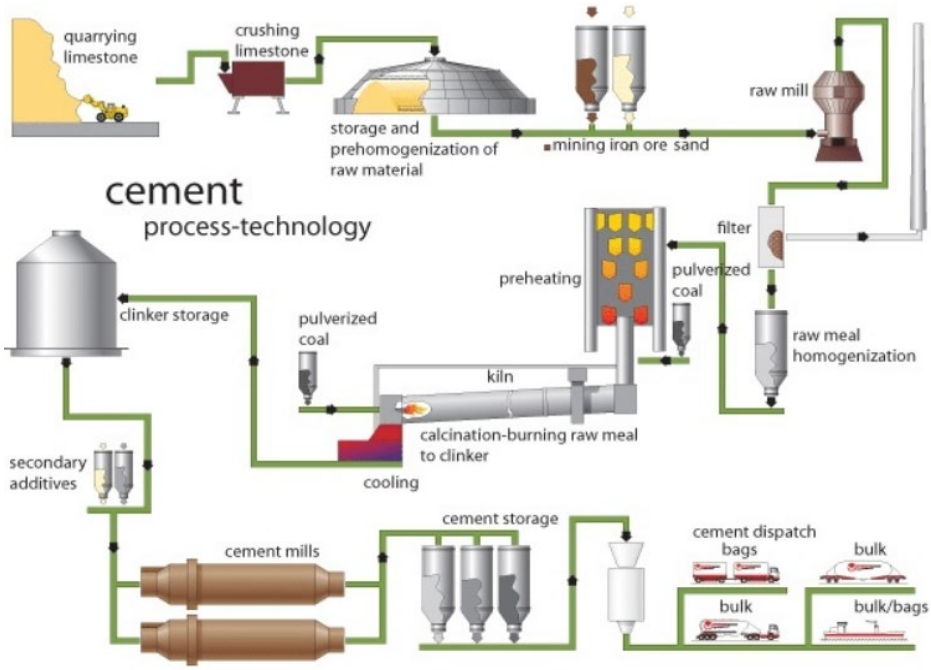


Figure 17: Cement production process chain (Sahin, 2023)

Traditionally, closed-circuit ball mills have been used to grind the clinker after production. However, vertical roller mills (VRMs) have recently become the standard milling equipment for clinker and more than 80% of new plants are using VRMs (Nicolas et al., 2019; Harder, 2010).

2.3.3. Hydration of Portland cement

The main hydrate that provides all the beneficial properties of cement is C-S-H, which is generated along with portlandite (CH) through the hydraulic reaction of C_3S and C_2S as shown in Equation 1 (Nicolas et al., 2019).

(C_3S, C_2S) from Portland cement + H = Primary C-S-H + CH (1)

Using the CaO-SiO_2 system, the possible phases and their polymorphs that are likely to form are alite (C_3S), belite (C_2S), rankinite (C_3S_2), and wollastonite (CS) in decreasing CaO content. Moreover, only alite and belite are hydraulically active with alite presenting higher hydration kinetics (Antunes et al., 2021). It can be seen that as the SiO_2 content increases, the crystal structure becomes more compact and ultimately decreases the hydraulic reactivity of the calcium-silicate phases, as per the notions of depolymerization elaborated earlier in this chapter. This has further been attributed to the organization and spatial distribution Ca atoms and SiO_x units in the crystal structure (Freitas et al., 2015).

Pure Portland cement contains around 95% clinker and 5% gypsum. The other types of cements are made by substituting a certain proportion of clinker with supplementary cementitious materials (SCMs). It should be noted that this only applies when the SCMs are added at the clinker milling stage. In practice, SCMs are usually separately milled and then mixed with Portland cement.

Other phases, such as the alumina-ferrite-trisulphate (AFt), sometimes called ettringite, and mono-sulphate (AFm) also formed through the hydration of C_3A, C_4AF (Nicolas et al., 2019). However, these hydrated phases do not contribute to strength development. Moreover, alite (C_3S) makes up 50 to 70% of PC and its hydration is the primary early strength inducer up to 28 days. Belite, on the other hand, only contributes to strength development at later ages and makes up 15 to 30% of PC (Chatterjee, 1996). The hydration of PC is exothermic and the usage of supplementary cementitious materials (SCMs) as replacement of PC helps reduce the heat of hydration as one of the benefits (Wang et al., 2023; Hewlett and Liska, 2019). The main stages of the hydration process along with the heat released are illustrated in Figure 18.

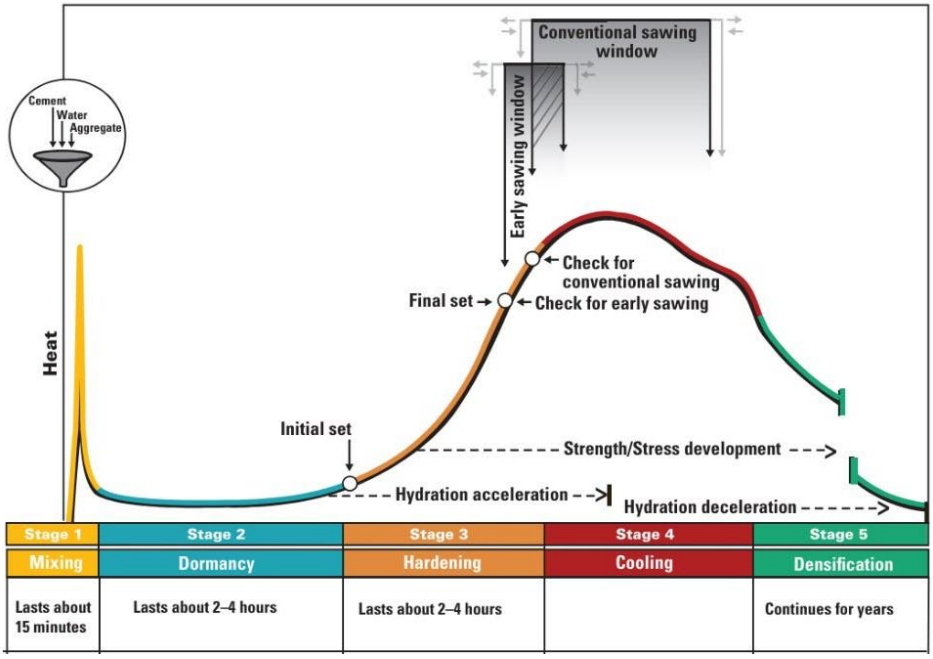


Figure 18: Heat released at different stages of hydration (Sahin, 2024)

The strength contribution of every major clinker component is summarized in Figure 19.

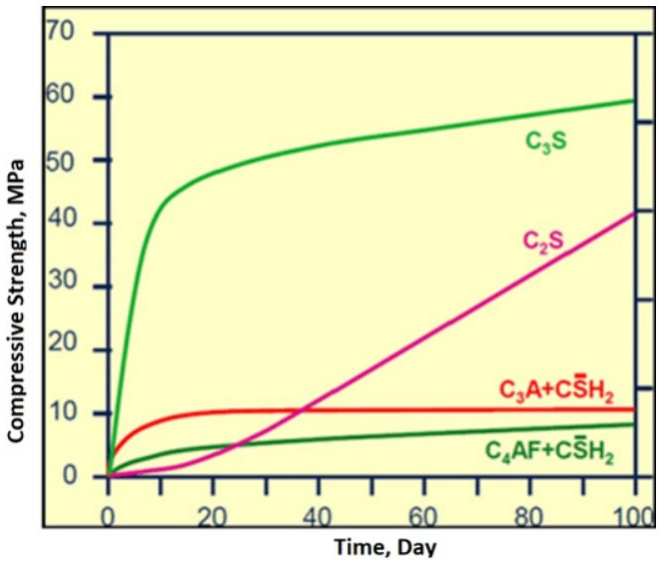


Figure 19: Contribution of cement components to strength development (Sahin, 2023)

It is clear that alite (C_3S) and belite (C_2S) are the components that strongly contribute to strength development of cement specimens. Alite strongly contributes to the early while belite's contribution is only significant at later ages.

2.3.4. Supplementary cementitious materials

From the total CO_2 emissions in the cement industry, 90% arises solely from the clinker making process (Supriya et al., 2023; Benhelal et al., 2021). Moreover, in the total CO_2 emissions from the clinker production stage, around 60% is associated with the decomposition of limestone ($CaCO_3$) and 40% with the combustion of the fuel used for kiln firing (Imbabi et al., 2012). The usage of SCMs is one way to minimize CO_2 emissions by using industrial by-products, such as fly ash, silica fume, and GGBF slag, as well as calcined clay, as partial replacements for PC. Some SCMs are also known as pozzolanic materials, which are described as materials with active silica (SiO_2), or alumina (Al_2O_3) that react with external hydrated lime (CH) to form secondary calcium silicate hydrates (C-S-H) or calcium aluminate gel (C-A-H), as well as C-A-S-H gel as shown in Equations 2 and 3 (Wang et al., 2023).

SiO_2 from pozzolanic materials + CH = Secondary C-S-H (2)

Active SiO_2 and active Al_2O_3 + CH = C-A-S-H (3)

While comparing the rate of the hydraulic reaction to the pozzolanic reaction in blended cements, the hydraulic reaction of PC is faster than the pozzolanic reaction. It is the occurrence of the hydraulic reaction that generates free hydrated lime, which then activates the pozzolanic reaction as shown in Equations 1–3 (Sun and Zhang, 2021; Chen and Brouwers, 2006). None the less, the addition of pozzolanic materials to cement enhances the durability of concrete and the resistance to chemical attack since the generated secondary C-S-H gel and other gels fill the pores created by cement grains, which ultimately improves the overall mechanical properties of concrete (de Brito and Kurda, 2020). The ternary diagrams incorporating the different SCMs before and after hydration are shown in Figure 20.

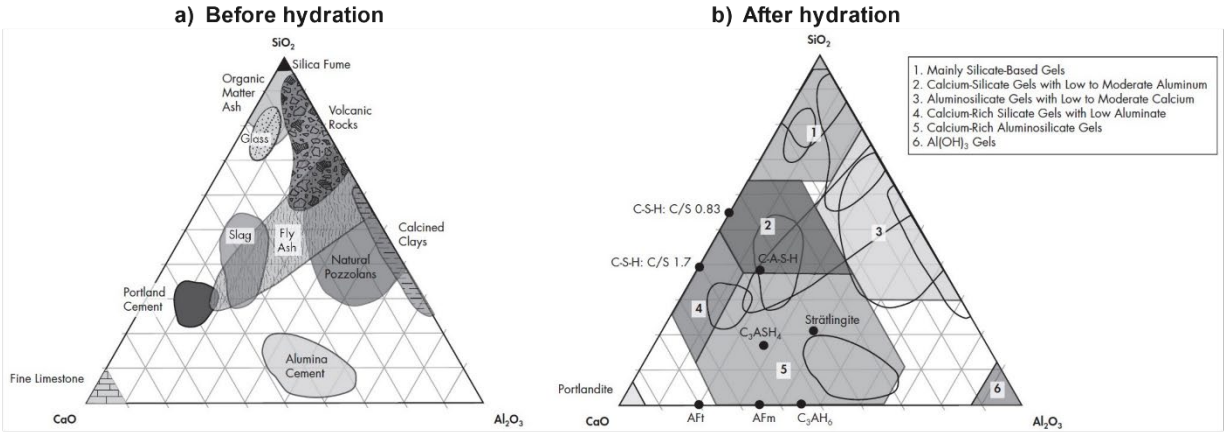


Figure 20: Ternary diagram of cementitious phases in the CaO–SiO2–Al2O3 system (Nicolas et al., 2019)

Fly ash and GGBF slag are among the most widely used SCMs (Orozco et al., 2024) and are included in the list of standard blended cements that are used globally (CEM II, CEM III, CEM

IV) as per the common cements in SANS 50197-1. However, with the declining interest in coal-fired power plants and preference for renewable electricity in this energy transition era, together with the phase-out of the BF technology from the steelmaking chain for low-CO_2 alternative ironmaking technologies, these two SCMs might no longer be part of the cement market in the foreseeable future. The production of coal fly ash (CFA) is already significantly reduced in countries that are mostly using electricity from non-carbon sources, for example, in Europe as shown in Figure 21.

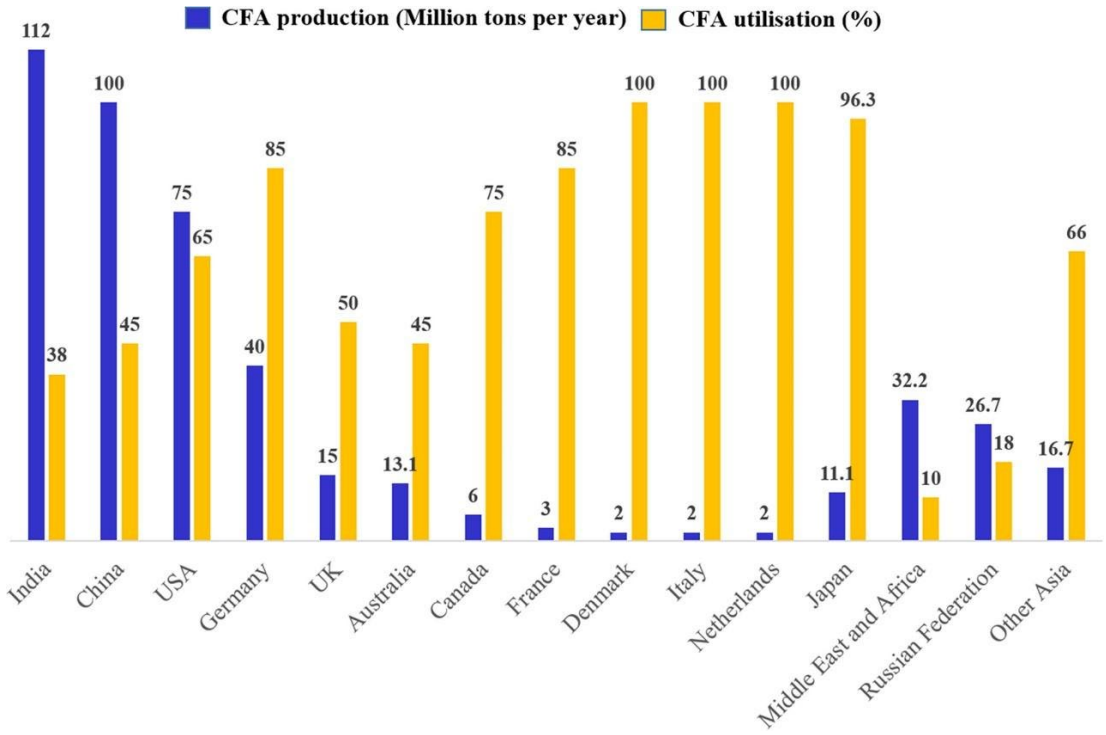


Figure 21: Global production and consumption of coal fly ash (Gollakota et al., 2019)

The same scenario is likely to happen to GBFS during the transitional phase to green iron and steel production. There is also rising interest in the production of calcined clays as SCMs due to the abundant clay reserves worldwide, and the relatively low temperature and CO_2 emissions associated with the calcination of clays compared to clinker (Overmann et al., 2024). The focus of this study is on slag; therefore, it is only the hydration properties of slag-cement blends that will be discussed in detail.

Market Research Future (2023) predicted that the market share of fly ash, BF slag, and silica fume will increase in the next decade are shown in Figure 22. However, the future marketing trends will also be driven by the current global challenges linked to CO_2 emissions for all the SCMs.

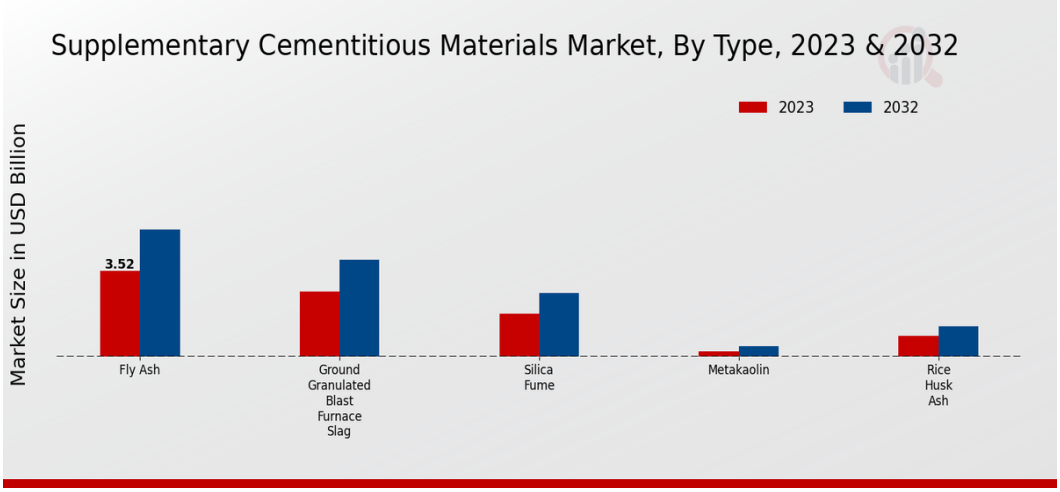


Figure 22: Market size of SCMs (Market Research Future, 2023)

2.3.5. Hydration of slag-cement blends

2.3.5.1. Hydrated phases evolution

Unlike other SCMs such as silica fume and calcined clays, the granulated BF slag is latent hydraulic because it possesses inherent hydraulic properties that can be activated either with the addition of Portland cement to form a slag/cement blend (CEM II or CEM III), or with alkali activators to form what is known as alkali-activated cement (Nicolas et al., 2019; Ahmad et al., 2023).

Alkali-activated cements with BF slag have been demonstrated in various projects but are still not yet commercially available in the cement market (Nicolas et al., 2019). The most widely used alkali activator is sodium silicate (Na_2SiO_4) which forms another hydration product, N-A-S-H by substituting CaO in the main hydration product from blended slag-cement, C-A-S-H. This study focuses mainly on the activation of slag with the addition of pure PC to produce blended slag-cement.

In slag-cement blends, the MgO content leads partial accommodation of Mg^{2+} into the C-A-S-H gel (Nicolas et al., 2019; Kolani et al. 2012). Moreover, other secondary Mg-Al phases known as hydrotalcite (magnesium-aluminium hydroxycarbonate ($Mg_6Al_2CO_3(OH)_{16}.4H_2O$)), fitting the M-A-H and M-A-$\bar{C}$-S structures also form during hydration depending on the availability of magnesia in the slag and carbonate (Hewlett and Liska, 2019). Hence, these hydration reactions can also be expected from a blend of cement with a slag of similar chemical composition to the BF slag. The hydration of slag-cement blends is further discussed in chapter 6 of this study.

It should be noted that the hydration process needs to be stopped in order to study the evolution of phase. The hydration stoppage is done by removing the free water at a given curing age thereby preventing further hydration. According to Snellings et al. (2018), the common methods of hydration stoppage are: oven drying at 105ºC, freeze drying at low temperature and pressure (-78ºC and <0.3 Pa), vacuum drying at low temperature and pressure (-78ºC and <0.3 Pa), and lastly, solvent extraction using an organic solution. Ideally, the best hydration stoppage

method is the one that preserves the original hydration assemblage, and solvent extraction by isopropanol solution was the best recommended method (Snellings et al. 2018).

2.3.5.2. Cementitious properties of slag

According to Nicolas et al. (2019), the cementitious reactivity of slag is dependent on the degree of depolymerization of the aluminosilicate framework and on the particle size distribution (PSD). The degree of depolymerization is directly linked to the chemical composition of the slag and the phases present in the slag as shown in the previous sections of this chapter. Amorphous or glassy phases tend to display higher reactivity than crystalline phases (Tripathy et al., 2020), and the more depolymerized the glass structure, the higher the reactivity (Zhang et al., 2022). The degree of depolymerization increases with increasing proportion of network modifiers (CaO, MgO) in the Al_2O_3-CaO-SiO_2-MgO slag system (Blotevogel et al., 2024). The PSD of milled slag helps gauge the fineness of the slag, and finer slag particles tend to display higher reactivity by dissolving faster due to the large surface area (Binici et al., 2007).

The other main parameter that determines the cementitious properties is the replacement level of PC by the slag, which can affect the degree of hydration since the reaction of slag depends on the hydraulic reaction of PC for activation (Hewlett and Liska, 2019). Therefore, it can be stated that the cementitious properties, or the overall reactivity of the slag is defined by the combined effect of:

- Slag properties: the chemical composition, the glass content, and the fineness
- The mixing ratio of PC and slag

2.3.5.3. Cementitious performance tests

Several tests are generally conducted to evaluate the cementitious performance of slag-cement blends. These tests can use various types of cement specimens, including concretes (mix of slag-cement, sand, aggregates, and water), mortars (mix of slag-cement, standard sand, and water), and pastes (mix of slag-cement, and water). This study will use mortar and paste specimens to avoid variations in the test results that may be caused by the variability of aggregate materials. The use of a standard sand in the mortar tests enables comparison with a larger test database. The main tests include workability, compressive strength, drying shrinkage for mortar specimens, and heat of hydration along with the analysis of hydrated phase evolution for paste specimens (Hewlett and Liska, 2019). It should be noted that these performance tests will be defined and fully described in chapter 3 of this study.

2.3.5.4. Slag reactivity enhancement

The reactivity of the slag can be increased by modifying the cementitious performance-defining parameters, such as the chemical composition, the glass content and the fineness of the slag. In this study, the enhancement of cementitious performance will be done by modifying the chemical composition of the slag in ways that increase the degree of depolymerization of the aluminosilicate glass network for improved dissolution rate of the glass during hydration. The improvement of the degree of depolymerization of the glass will make the slag more reactive

than conventional BF slag, thereby increasing the potential substitution ratio of the new slag for a given cementitious performance requirement (Blotevogel et al., 2024). Moreover, further reduction in clinker proportion implies that the CO_2 emissions and energy consumption associated with the production of clinker is reduced. A typical CO_2 emission reduction diagram by substitution levels of clinker with BF slag is shown in Figure 23.

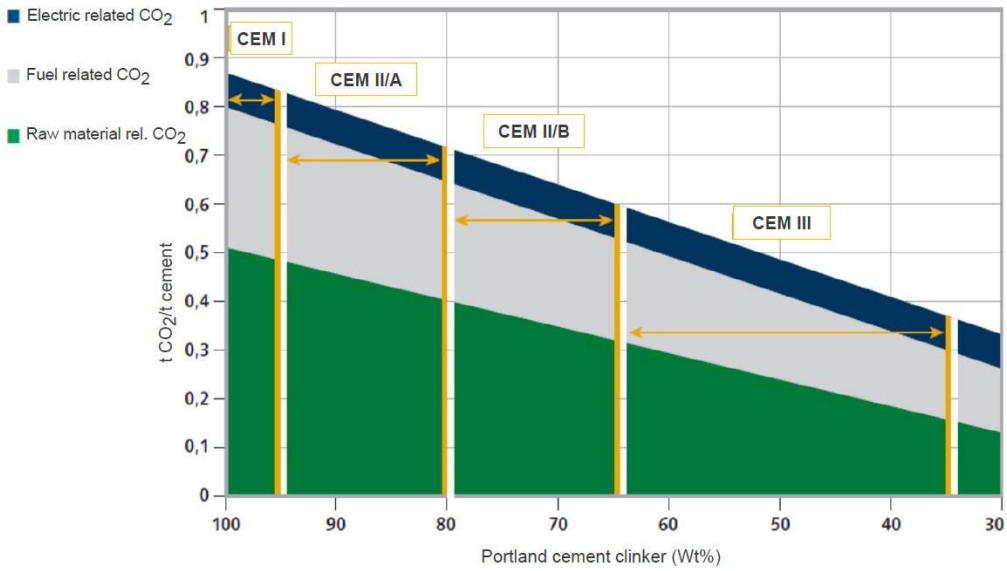


Figure 23: CO2 emission reduction from clinker substitution by blast furnace slag (Bolte et al, 2023)

As per SANS 50197-1:2013, these common slag cements have the following proportions:

- CEM II/A = 6-20% slag and 94-80% clinker
- CEM II/B = 21-35% slag and 79-65% clinker
- CEM III/A = 36-65% slag and 64-35% clinker
- CEM III/B = 66-80% slag and 34-20% clinker

From Figure 23, it can be seen that CO_2 emissions from cement clinker production are reduced progressively as the proportion of clinker replaced by blast furnace slag increases. However, the increment in replacement levels of clinker corresponds with a reduction of Portland cement in cement-slag blends, which reduces the early strength development and affects the degree of hydration of the slag. This is because it is the hydration of clinker phases such as alite and belite that releases portlandite, which then activates the reactivity of slag as noted earlier in this theme. Therefore, a balance between the required strength development and the level of clinker substitution by the slag must be found and investigated.

The ideal scenario is producing a slag that can substitute clinker at higher levels yet providing similar cementitious performance to the BF slag at lower clinker substitution. Therefore, production of such slags will increase the CO_2 emissions-reduction potential in the cement industry and allow the cement industry to further lower its global CO_2 emissions.

The CO_2 intensity in the cement industry is currently around 0.58 t CO_2/t cement and the projected CO_2 intensity in 2030 is around 0.45 for net-zero emission scenarios (IEA, 2024).

The making of green cement can only be achieved through the development of clinker-free binders, or the production of clinker in an environmentally friendly manner. The use of oxygen enriched fuel for combustion during calcination, and subsequent capture of generated CO_2 is one way of making the clinker production green as currently being explored by Thyssenkrupp Polysius GmbH (2024) using oxy-fuel. The currently utilized way of reducing CO_2 emissions in the cement industry is through the valorisation of wastes from other industries as SCMs, which includes GGBFS and fly ash. However, the production processes of these waste materials are not environmentally friendly due to their high CO_2 emissions. Hence, the focus has now shifted towards utilizing SCMs that emanate from greener production methods.

The novel slag modification using the green ironmaking path of this study is covered in the upcoming theme.

2.4. Theme 4: DRI-OBF ironmaking technology

This theme describes the incentives behind the current exploration of smelting the DRI in an open bath furnace (OBF). It provides a brief evolution of ironmaking technologies from the BF to DRI-OBF technology together with the current global crisis that is driving these technological changes in the iron and steel industry. It further provides details regarding the designing process of the novel OBF slag.

2.4.1. Impact of climate change and CO_2 emissions

Climate change is one of the most prominent environmental challenges facing the world today, which can have a drastic impact on the future human civilization on earth. Global warming and climate change are often used interchangeably. According to Lineman et al. (2015), global warming means the increase in the average temperature of the earth's surface, while climate change refers to long-term changes in global or local weather patterns. The impact of climate change on society and the economy at large has been intensified by the increase in global GHG emissions, with CO_2 emissions making up the major portion, and the recent occurrences of extreme weather-related events (IPCC, 2023; Zhang et al., 2024). Many countries are therefore seeking to achieve net-zero CO_2 by implementing the 2015 Paris agreement (United Nations, 2015).

The rise of strict environmental regulations, increased emissions taxes, and the foreseeable danger of climate change have put every carbon-consuming industry under pressure to decarbonize its operations in order to stay relevant and competitive in the global market. The steelmaking and cement-making industries as the two major industrial consumers of fossil fuels, are not spared from this pressure. Ahmad et al. (2022) reported that the global CO_2 emissions from the cement industry range approximately between 7-9%. Similarly, the steelmaking industry globally contributes about 8% of CO_2 emissions, the majority of which arises solely from the BF technology (IEA, 2020; Graupner et al. 2023). Therefore, it has become a strategic imperative for the iron and steel industry to reduce its CO_2 emissions.

It is clear that climate change is a global challenge, and thus its impact can only be mitigated through collaborative efforts among the different sectors that contribute to global CO_2 emissions. This study focuses mainly on the reduction of CO_2 emissions during ironmaking

and the valorisation of the associated slag as a viable supplementary cementitious material. The production of a low-CO_2 pig iron will help the steelmaking industry to reduce its global CO_2 emission share by using an innovative and less carbon-consuming process. The slag will be modified to resemble the BF slag so that it can be utilised in the cement industry to lower its CO_2 emission share by substituting clinker. This shows the dual impact of this study in these two industries.

2.4.2. Decarbonization of ironmaking processes

The generation of CO_2 emissions is mainly associated with the usage of carbon-based materials. The conventional blast furnace ironmaking process has seen a number of innovations throughout its industrial application (Cavaliere, 2019). The pursuit of process efficiency of the BF has been the top priority in the industry, and Kim et al. (2022) noted that decarbonization in the iron and steel industry through process efficiency alone is limited, since current iron and steelmaking processes have been efficiently operated close to their thermodynamic limits. This indicates that the exploration of alternative ironmaking technologies is necessary in order to achieve a significant level of decarbonization in the iron and steelmaking industry.

The awareness of the environmental impact of BF technology has been raised more than two decades ago and there have been process developments that focused on replacing the BF process. Some of these processes, such as the Corex and Finex processes, were commercialized and contributed to the total global output of iron and steel. However, the global acceptance and adoption rate of these technologies is still very low (Hasanbeigi et al., 2014). Currently, the only ironmaking technology that has seen a significant rise in acceptance rate is the DRI process, due to its flexibility of using different reducing agents. The DRI process also has the potential to use carbon-free gas, such as hydrogen (Ji et al., 2024). As noted in theme 1 of this chapter, the two major DRI processes are the Midrex process with 65% share in total global DRI output, and the Energiron process with a global output share of 17%.

2.4.2.1. Midrex process

The Midrex process is the global leading DRI technology, using a shaft furnace with an external gas reformer. The process was originally developed by Midrex (USA) and then acquired by Kobe Steel in 1984 (Atsushi et al, 2010). The flexibility of using different reducing gases, even up to 100% hydrogen, has the potential to make the Midrex process one of the positive factors in the decarbonization of the ironmaking step within the steelmaking industry (Midrex Technologies, 2024). Moreover, the quality of DRI products can easily be adjusted and Midrex currently provides three technology options:

- MXCoL: using syngas (a mixture of CO, CO_2 and H_2) from gasification of carbon-bearing fuel as the reducing agent, this technology option is not carbon-free and is mainly applied in regions where natural gas (NG) availability is low.
- MIDREX-Flex: using NG containing more than 50% H_2, with easy future adjustment once hydrogen becomes available, so that it can operate at 100% H_2. MIDREX-Flex is currently the most widely applied Midrex technology with favourable acceptance rate by steelmakers.

- MIDREX-H_2: is the future of MIDREX technologies and will be fully operational once the transition from carbon-bearing fuel to green hydrogen becomes viable.

The three Midrex technology options are further summarized in Figure 24 together with their potential reduction in CO_2 emissions, compared to conventional BF ironmaking (Midrex Technologies, 2024). When these technologies are implemented in combination with Carbon capture, utilization and storage (CCUS) technologies, the CO_2 emission reduction potential is even higher (Toan Vu et al., 2024).

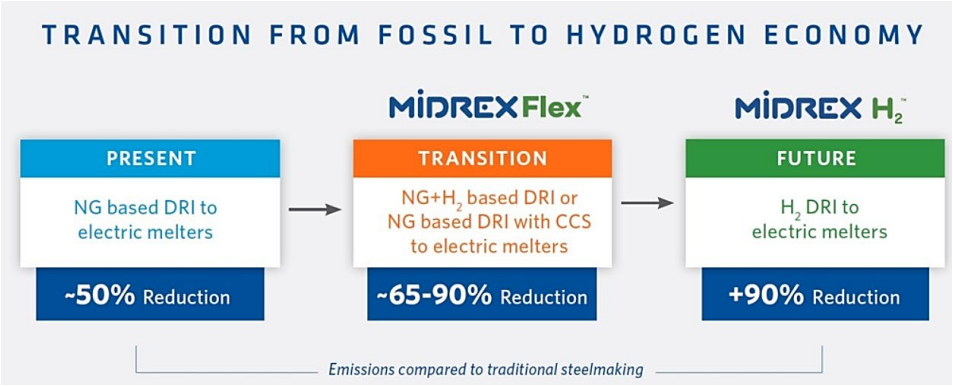


Figure 24: Emissions reduction from Midrex technology options (Midrex Technologies, 2024)

A process flowsheet of the natural gas based Midrex process to produce cold DRI (CDRI), Hot DRI (HDRI) and hot briquetted iron (HBI) with more than 90% metallization is shown in Figure 25 (Midrex Technologies Inc., 2018; Atsushi et al, 2010). Moreover, HBI is obtained by compacting the DRI for easy handling, storage, and transportation (Dutta and Sah, 2016).

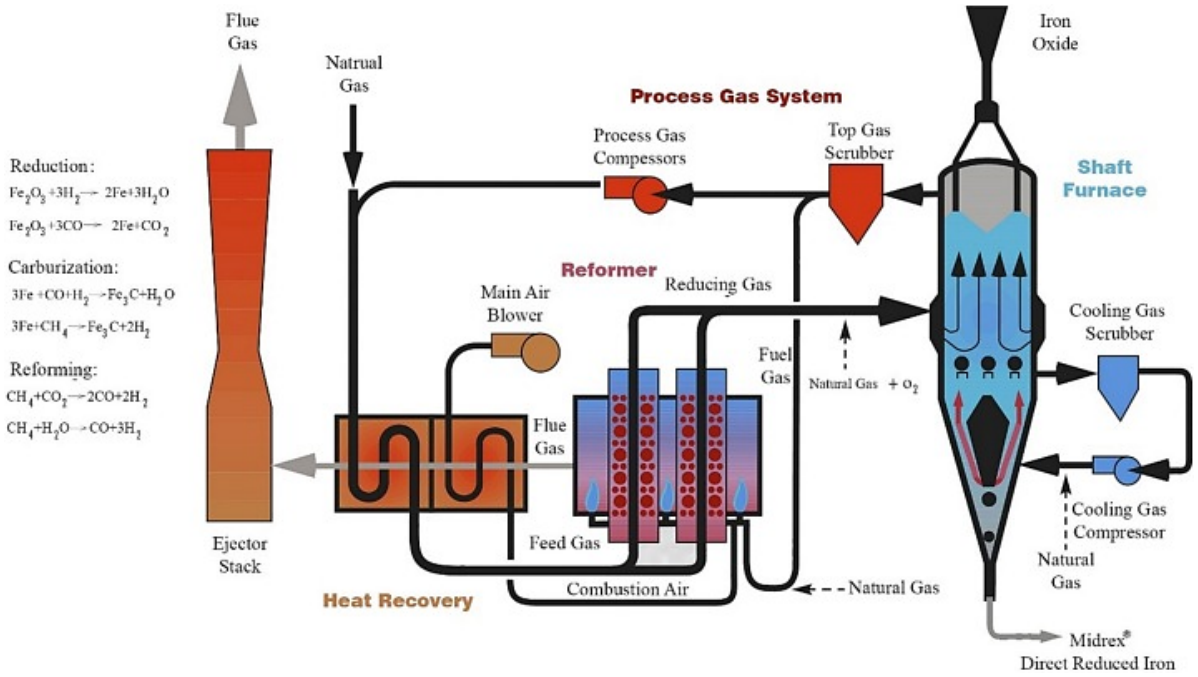


Figure 25: Natural gas (NG) Midrex process (Midrex Technologies Inc., 2018)

As can be seen, the main processes in the NG-based DRI process are gas reforming, iron reduction and carburization. The NG consists mostly of methane (CH_4), the iron is present in both the metallic (Fe) and carbide (Fe_3C) phases, while most of the carbon is associated with the carbide phase (Atsushi et al, 2010). Zecca et al. (2023) stated that the main source of emissions in the NG-based Midrex process is the flue gas from the reformer. However, this can be equipped with CCUS facilities in order to improve the emission reduction potential of this process (Toan Vu et al., 2024).

2.4.2.2. Energiron process

The Energiron process is the second global DRI products contributor (World Steel Association, 2024). The process was originally developed by HYLSA, known as the HYL process and it matured from HYL I to HYL III. Then, Techint Group, a combination of Tenova and Danieli, acquired the HYL III process in 2006 and rebranded it as the Energiron process (Sui et al., 2023; Duarte et al., 2010). Similar to the Midrex process, the HYL/Energiron process is also versatile in reducing agents and can use NG, gas from coal gasification, coke oven gas (COG), and green hydrogen (Ji et al., 2024; Tenova, 2020). Unlike the Midrex process, the Energiron process uses an internal NG-reformer to produce H_2 and CO with reinjection of CO_2, the reducing gas has a higher molar% of H_2, and the DRI products have a relatively higher carbon content (Yilmaz and Turek, 2017; Bailera et al., 2021). Table 2 further shows a comparison of operating parameters between the HYL III and Midrex DRI processes (Liu et al., 2021).

Table 2: Comparison of HYL III and Midrex processes (Liu et al., 2021)

Technology	Midrex	HYL III
Operation pressure	0.23 MPa	0.4–0.6 MPa
Cracking agent	Top gas	Steam
Reducing gas composition	About 24–36% CO, 40%–60% H_2, 12–15% N_2	About 14% CO and 75% H_2
Raw material requirements	TFe > 64%, gangue < 4%, S < 0.05%, P < 0.05%	TFe > 64%, gangue < 4%, P < 0.05%
Energy consumption	Gas consumption: 10.2–11 GJ/t Power consumption: 100Kw·h/t	Gas consumption: 10–11.3 GJ/t Power consumption: 90 kW h/t
Gas temperature	850–900 °C	900–960 °C

It can be seen that both DRI processes currently have a global standing, and their futures rely strongly on their abilities to use hydrogen as fuel.

2.4.2.3. Hydrogen metallurgy and green production

The future of decarbonization and sustainability of the steelmaking industry lies in the metallurgy of H_2-based productions aside from the implementation of CCUS technologies. The application of hydrogen is the key aspect that makes DRI ironmaking technologies future-proof in terms of sustainability in this decarbonisation era, and transition to environmentally friendly ironmaking (Vogl et al. 2021). Liu et al., (2021) noted that hydrogen is considered as the most promising clean energy in the 21st century because of its high calorific value and high reaction rate, which makes it a good substitute for carbon in the steel industry, and even the entire global energy system for deep decarbonization (Parra et al., 2019). Therefore, the exploration of hydrogen fuel technologies can reduce the reliance on fossil fuel in the iron and steel industries.

The quest for green hydrogen metallurgy has been boosted by the looming impact of climate change and the decarbonization requirements in different industries. Currently, hydrogen is produced through CH_4 reforming, coal gasification, and coke oven gas (COG) reforming from DRI ironmaking processes, which are not completely carbon-free (Li and Cheng, 2020; Liu et al., 2021; Chen et al., 2022). Recently developed and green hydrogen production technologies include water electrolysis using renewable energy (Boretti, 2020), biomass gasification (Doranehgard et al., 2017), and hydrogen production using nuclear energy (Karaca et al., 2020). However, these emerging green technologies barely contribute to the current global production output of hydrogen due to the poor balance between the overall cost of the process, and profitability of hydrogen application (IEA, 2019; Parra et al., 2019). A significant amount of hydrogen, around 99%, is still produced using carbon-based production methods, 76% using CH_4, 23% using coal, and the remainder using biomass and water electrolysis (Elaouzy and El Fadar, 2024; IEA, 2019).

It can be seen that the green nature of hydrogen, or iron, is defined by the intensity of carbon utilization during the production process: the less carbon involved in the production process, the greener the resulting hydrogen or iron. Moreover, the development of green hydrogen metallurgy still has a very long way to go, and the continued reliance on carbon in alternative ironmaking technologies is what has made the BF ironmaking process keep its position as the dominant ironmaking process until today (Elaouzy and El Fadar, 2024; Schmole et al, 2012).This section has further shown that the use of green hydrogen is the ideal solution to carbon neutrality in ironmaking, and it is the development pace of green hydrogen technologies that will dictate the speed of decarbonization of ironmaking processes. Therefore, the complete success of ironmaking decarbonization plans partly depends on the success of carbon-free (green) hydrogen production technologies, and the application of CCUS.

The current availability of flexible technologies, such as Midrex-Flex and Energiron, can still challenge the BF technology since they can use varied proportions of hydrogen, up to 75%. These technologies seem very good alternatives in this decarbonization transition until green hydrogen becomes sufficiently available at a competitive price (Midrex Technologies, 2024; Tenova, 2020). However, these DRI processes only produce metallized iron at solid state with inherent gangue materials as previously shown in theme 1 of this chapter. Therefore, there is a requirement to develop a subsequent downstream process that can convert the DRI or HBI into pig iron and slag similar to the BF technology. Moreover, the subsequent process should ideally emit minimal CO_2 in order to ensure lower overall CO_2 emissions and keep decarbonization patterns of the DRI production route.

2.4.2.4. Processing of DRI products

The majority of the DRI products (CDRI, HDRI, HBI) are currently processed using Electric arc furnaces (EAF) to produce steel and form what is known as the DRI-EAF steelmaking route as shown in Figure 26 for the Midrex DRI.

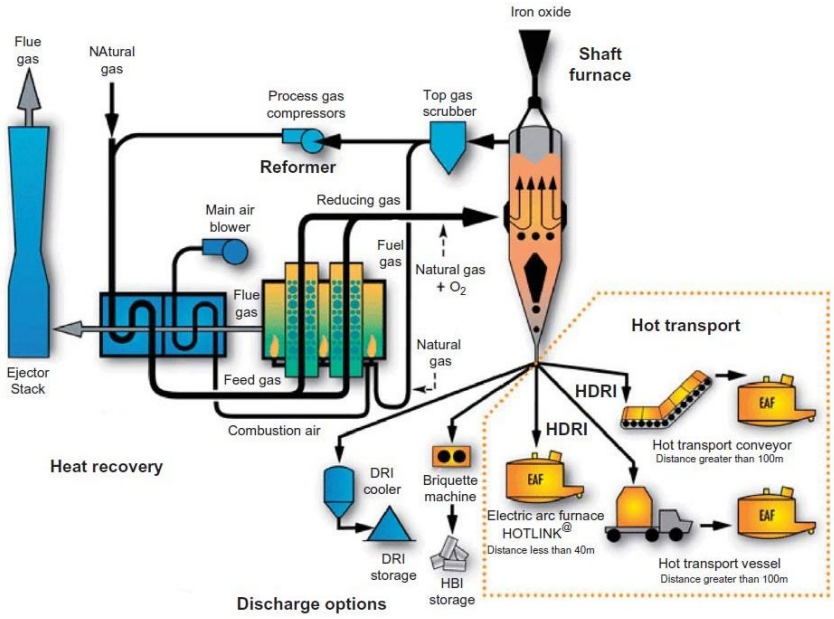


Figure 26: DRI-EAF steelmaking route (Dutta and Sah, 2016)

2.4.3. Effect of DRI products in EAF operations

2.4.3.1. DRI to scrap ratio

The EAF usually takes blended feedstocks of steel scrap and DRI/HBI, and the CO_2 intensity increases with increasing proportion of DRI (Kirschen et al., 2011). The scrap-based EAF is the best decarbonization route with a CO_2 intensity of 0.68 compared to the 1.37 CO_2 intensity in the DRI-based EAF, as shown in Figure 12. It should be noted that the CO_2 intensity is the ratio of tons of CO_2 per ton of steel produced (World Steel Association, 2024). Moreover, the metal yield (tapped steel/charged metal) is lower in DRI-based electric arc furnaces (87–92%), due to the presence of gangue materials and unreduced Fe, compared to a higher metal yield (90–94%) observed in scrap-based electric arc furnaces with high or medium quality steel (Kirschen et al., 2021). This ultimately increases the overall energy demand of EAF operations (Conejo and Cárdenas, 2006). Therefore, a seasoned charge of DRI and steel scrap to the EAF is preferable to counteract these effects.

2.4.3.2. Metallization degree of DRI

The degree of metallization of the DRI is another important parameter that affects DRI-based EAF operations. According to Kirschen et al. (2011) the best operational conditions are obtained when the degree of metallization is between 94 to 96%. The remaining FeO in the DRI is important since its reduction releases CO gas upon carbon injection, which helps agitate the bath, increase the heat transfer efficiency, and lower the energy requirement. This also assists with slag foaming and protection of refractory materials, although carbon and oxygen injections are usually employed in an EAF for the same purpose (Liu and Yan, 2024). Moreover, the carbon in the DRI also has the same beneficial effect of slag foaming in EAF operations. However, a lower degree of metallization implies that more FeO will have to be reduced in the EAF, which can also adversely affect the efficiency of operations. Hence, the degree of metallization must be controlled to ensure optimal EAF operation.

2.4.3.3. Grade of DRI

The grade of DRI is crucial in EAF operation as it affects the volume of the EAF slag produced and impacts the process at large. The grade of DRI can be broadly categorized by the iron (Fe) content in the DRI, which is defined by the type of iron ore used during the DRI process and the gangue content. Generally, the grade can be defined:

In terms of iron ore quality (Yang, 2014),

- High grade iron ores: +65% Fe
- Medium grade iron ores: 62 to 65% Fe
- Low grade iron ores: less than 62% Fe

In terms of DRI products (Kim and Sohn, 2022),

- DR-grade DRI products contain +66% Fe
- BF-grade DRI contains less than 66% Fe

These grade nomenclature of DRI products have been determined because medium/high grade iron ores are used in BF ironmaking, while DRI processes only use high grade iron ore (Yang, 2014). Moreover, the overall iron content of the DRI is also dictated by the type of mineral hosting iron in the ore. Hematite (Fe_2O_3) and Magnetite (Fe_3O_4) are the only minerals with a higher inherent Fe content (> 69% Fe) and therefore capable of producing DR-grade DRI products. Other iron minerals, such as limonite and goethite, can only be used to produce BF-grade DRI products due to their mineralogy.

According to Liu et al. (2021), the total Fe content required in the raw materials for the Midrex and Energiron processes is greater than 64% Fe, to produce DR-grade and BF-grade DRI as previously shown in Table 3. This requirement by the DRI plants is mainly driven by the downstream application of the DRI products. As previously shown, the majority of DRI products are used in the EAF to produce steel, and the EAF technology can viably take only DR-grade products with 66 to 67% Fe. This is because the gangue composition of the DRI is usually acidic, requiring more basic fluxes to reach the target slag composition. This results in high slag volume, high Fe loss to the slag, high energy consumption, and decreased operational efficiency (Kim and Sohn, 2022). The generic chemical properties of DR-grade and BF-grade DRI are summarized in Table 3.

Table 3: Comparison of Lump iron ore, BF grade and DR-grade DRI pellets (Linklater, 2021)

DR-Grade Pellets	Blast Furnace Grade Pellets	Lump Iron Ore
High Iron Content Fe, total iron > 67%.	Fe, total iron 63 - 65%.	Fe, total iron > 67%. (becoming more difficult to source)
Acidic Gangue: Silica SiO_2 1.0 - 3.0 Alumina Al_2O_3 0.2 – 3.0	Acidic Gangue Silica SiO_2 2.5 – 5.3 Alumina Al_2O_3 0.4	Acidic Gangue: Silica SiO_2 1.0 - 3.0 Alumina Al_2O_3 0.2 – 3.0
Basicity 4 (CaO+MgO) (SiO_2+Al_2O_3) Magnesia MgO 0.2 – 0.9 Lime CaO 0.4 – 1.2	Basicity 4 (CaO+MgO) (SiO_2+Al_2O) Magnesia MgO 0.3 – 1.5 Lime CaO 0.6 – 3.6	Basicity 4 (CaO+MgO) (SiO_2+Al_2O_3) Magnesia MgO 0.2 – 0.9 Lime CaO 0.4 – 1.2 Usually required to be added in steelmaking process

The impact of iron content and DRI gangue proportions on EAF productivity are further highlighted in Figure 27.

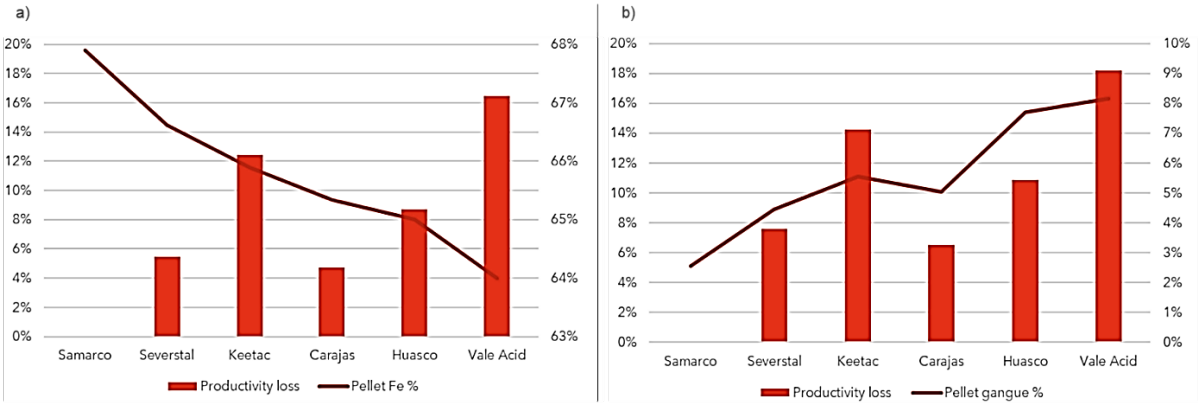


Figure 27: Impact of iron content (a), and gangue proportion (b) on EAF productivity (Barrington , 2022)

It can be seen that the higher the gangue content, the higher the productivity loss. Moreover, higher gangue content indirectly implies lower iron content. Therefore, the lower the iron content in the DRI, the higher the productivity loss of EAF operations to produce steel.

2.4.3.4. Solutions to iron ore quality limitation

Nicholas and Basirat (2022) stated that the iron ore quality limitation can be solved by developing iron ore mines to produce high quality ores, further improving the beneficiation stage of iron, or developing innovative technologies that can treat low grade iron ores to produce steel, or iron. Currently, only 4% of global iron ore exports comprise DR-grade iron ore, and for the last 20 years the grade of iron ores has been decreasing (Nicholas and Basirat, 2022). Moreover, further improvement of the beneficiation process will require extra energy and investment costs, which makes the overall beneficiation process expensive (Linklater, 2021). The development of innovative technologies is therefore seen as the best option to address the limitation arising from the availability of DR-grade iron ore.

The current global steel demand is around 1900 Mtpa, and EAF steel plants currently contribute only 28.6% to the total production output (World Steel Association, 2024). This is an indication that the DRI-EAF technology, although being the most environmentally friendly steelmaking process at present, cannot solely replace the BF technology to meet the current and future global steel demand. Therefore, it is necessary for steelmakers to explore additional technologies that are capable of sustaining the rising global steel demand, without requiring high quality iron ores as raw materials.

An example of novel technology that is being explored in the steelmaking industry is the melting of DRI in an electrically heated furnace to produce iron, which is subsequently converted to steel using existing BOF infrastructure. The usage of electricity in this novel ironmaking process contrasts it from the smelting reduction technologies (Corex, Finex, ITmk3) since electricity has the potential to originate from green sources, such as solar, wind, or hydroelectric power (Wei et al., 2019), unlike non-coking coal that still generates CO_2. Moreover, the electrically operated furnace is labelled as "open bath furnace (OBF)" because it operates in open arc, or brushed arc mode, whereby the electrode is not submerged in the burden. The OBF has the capability to take DRI products with as little as 57 - 58% Fe to produce electric pig iron similar to the BF (Nicholas & Basirat, 2022). It can be seen that the usage of the OBF will bring a solution to the iron ore quality limitation and will allow DRI plants to use low grade iron ores, which are abundantly available at a relatively cheaper price.

The comparison of the OBF with the EAF in terms of iron content of the raw materials, as well as the global production of different grades of iron ore, is shown in Figure 28.

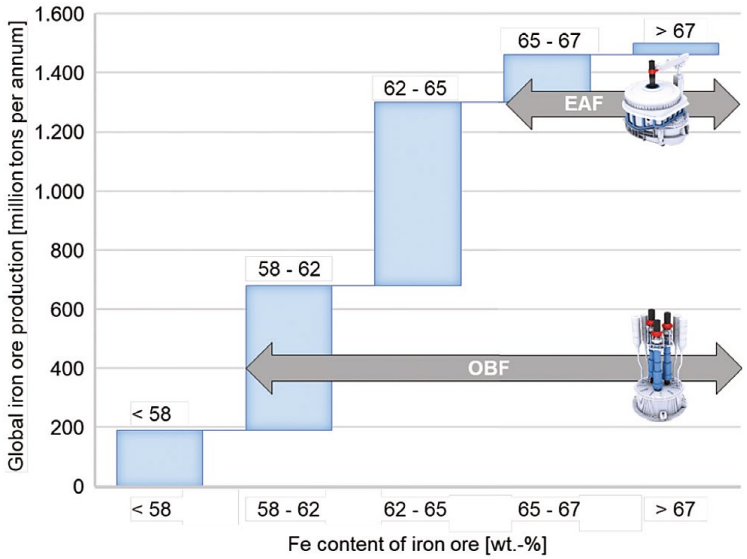


Figure 28: Distribution of global iron ore production and grade suitability as EAF and OBF feed (SMS group, 2022)

Figure 28 highlights that the majority of iron ores produced globally have 58 to 65% Fe and the OBF is very flexible in handling a wide range of iron ore grades (58 to +67%) compared to the EAF, which can only handle iron ores with 65 to +67% Fe.

2.4.4. DRI-OBF green ironmaking process and its industrial application

The DRI-OBF technology is part of the main topic of this study. The OBF process needs to be optimized in order to generate products that are similar to current BF products in order to ensure a seamless transition from the BF to the DRI-OBF technology and smooth integration of the OBF process in the DRI-OBF-BOF steelmaking configuration. The novel OBF slag must therefore possess similar, or better cementitious properties than the conventional BF slag in order to be a suitable clinker substitute in cement. Likewise, the electric pig iron from the OBF must be similar to the conventional pig iron from the BF so that it can be processed in the existing downstream BOF steelmaking units. The DRI process is already a matured, industrially proven, and commercially available technology worldwide, with a rising adoption rate as shown throughout this chapter. Hence, the main focus of this study is on the novel OBF process, particularly the modification of the OBF slag for cementitious applications.

Thyssenkrupp, a major steelmaking company in Europe, has already invested in this new technology and the comparison of this new ironmaking route to the conventional BF route is shown in Figure 29.

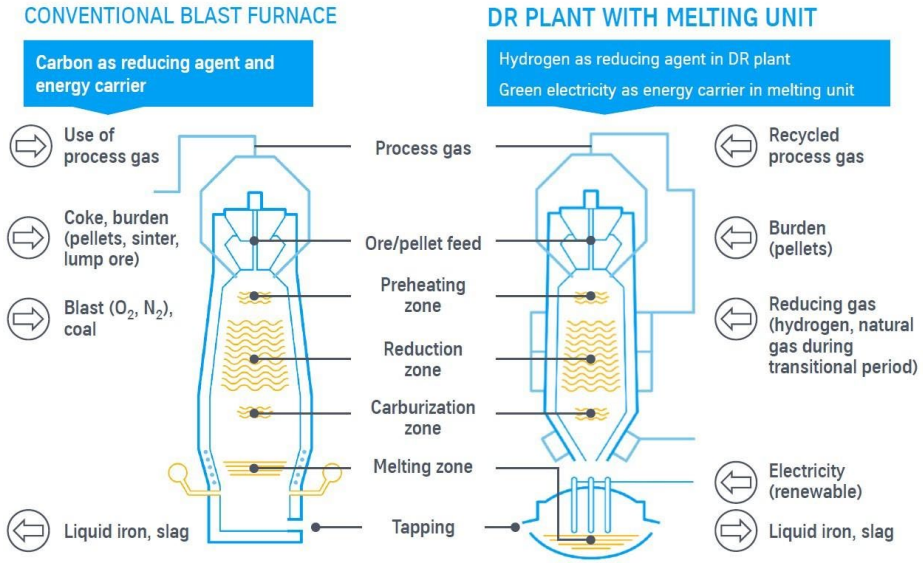


Figure 29: Process comparison of BF and DRI-OBF ironmaking process (Thyssenkrupp, 2022)

The OBF process has been designed and manufactured by Metix (Pty) Ltd, a South African subsidiary of the SMS Group GmbH. A semi-industrial scale furnace is being used to de-risk the DRI-OBF technology and demonstrate its technology readiness level. Samples of slag for this study have been sourced from the modified OBF slag produced as part of this demonstration.

2.4.5. OBF slag modification for cement and summary of research gaps

The modification of the slag will directly affect the selection of refractory for the novel OBF process, the slag designing process should therefore be done in consideration of the type of refractory to be used and the potential impacts on the refractory. Blast furnace slag, in granulated form, has proven cementitious properties as shown throughout this chapter:

modifying the OBF slag to a BF slag-equivalent composition is therefore seen as a good starting point. The composition of the novel OBF slag is given in Table 10, section 4.3.

In-situ modification of the slag will have limitations due to the complex slag-metal-refractory interactions that restrict how far the slag can be changed without affecting the overall furnace operations. However, the extent of in-situ modification should be assessed while guided by the furnace operational conditions (slag-metal immiscibility, energy consumption efficiency), and the slag-refractory interactions. The extent of achievable OBF slag modification, the evaluation of related refractory performance, and the cementitious performance of the novel slag as well as special slag features can only be established through well-defined practical experiments.

The ideal scenario is the production of a slag with comparable cementitious properties to the conventional BF slag, while still prioritizing the furnace operational efficiency and minimizing the corrosion of the furnace refractory by the slag. This will allow a smooth transition from the BF process to the OBF process since both the pig iron and the slag will be similar for these two processes. In case the in-situ modification of the slag is met with process efficiency bottlenecks, an alternative option will be producing a less corrosive slag in the OBF and integrating a separate slag valorisation furnace (SVF) to subsequently valorise the slag into a cementitious product. In this respect, the resulting slag production path will be: DRI-OBF-SVF.

This new slag modification path would increase control over the slag modification process, and a SVF slag with improved cementitious properties compared with BF slag can potentially be produced. This will increase the overall sustainability of the OBF route in terms of waste valorisation and circular economy application compared to the BF route.

Due to the OBF process being a novel ironmaking process, the physical and cementitious properties of the OBF slag are unknown at this stage. Properties of the slag and refractory go hand in hand as shown through this chapter, and the best refractory material for the OBF process has not been identified. In addition, the possible SVF integration into the OBF process is a novel slag valorisation route, and the properties of the corresponding SVF slags require study and investigation to assess their potential values in the cement industry. Finally, a study of the environmental and economic benefits of these novel slags is also required.

These are the research gaps that this dissertation plans to address and also to add to the existing body of knowledge within the cement and steelmaking industries.

Conclusions and future outlook of green ironmaking slags

The application of the OBF technology will increase the overall production output of DRI, lessen the requirement of iron ore quality restriction in DRI processes, and thereby increase the market share of low-grade iron ores, which are readily available.

The current quest for green energy and green production processes is causing declining interest in coal-fired power plants in favour of renewable electricity, and planning for phasing out of BF technology from the steelmaking chain with replacement by low-CO_2 alternative ironmaking technologies. This will result in reduced availability of fly ash and GGBFS, which are currently the most widely utilised SCMs in the cement industry. Materials that are most

likely to emerge and become dominant as SCMs in the future are calcined clays and the novel granulated OBF slag, due to their relatively lower associated CO_2 emissions.

If the OBF slag has a higher CO_2 reduction potential than BF slag, its demand from the cement industry will increase as well. This will enable the OBF process to achieve an unprecedented milestone by supplying a slag that can further lower CO_2 emissions compared to conventional BF slag.

The BF technology will, however, remain the dominant ironmaking technology for a number of years until the adoption rate of the new ironmaking technologies becomes significant enough to outweigh the BF's dominance. The rate of adoption will be boosted significantly by successful development of green hydrogen production, at a competitive price, that will be profitable to the hydrogen users. This is because the application of hydrogen in this new ironmaking route increases its environmental friendliness in terms of CO_2 emissions (Thyssenkrupp, 2024).

The implementation of carbon capture, utilization and storage (CCUS) facilities will also be a strong asset to the growth of these new technologies by further increasing their carbon neutrality. The new pathways for green steel production as per SMS Group, (2024) include both the DRI-EAF and the DRI-OBF technologies which are shown in Figure 30. It can be seen that the ideal pathway for the iron and steel industries to achieve carbon neutrality is summarized by three points:

- DRI processes: fully using green hydrogen as fuel and reductant to produce DR-grade and BF-grade DRI products, even from low grade iron ores
- EAF and OBF processes: fully using green electricity from renewable sources
- CCUS facilities implementation: to capture, store and re-use any excess CO_2 gas

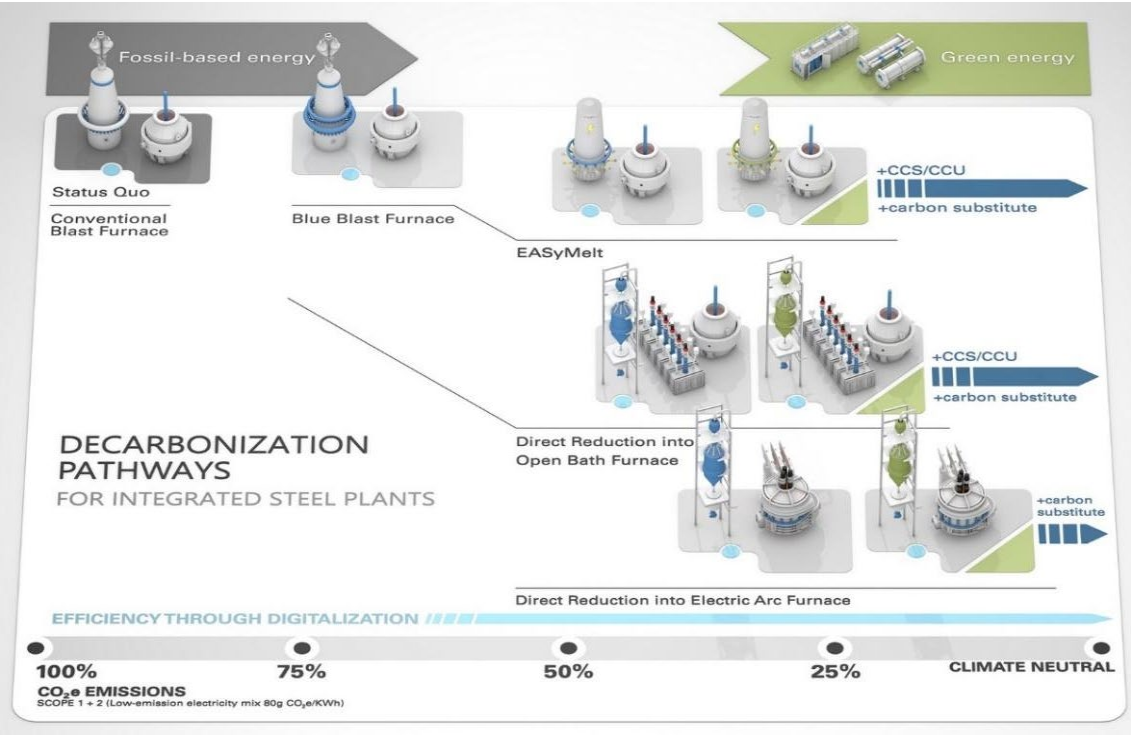


Figure 30: Pathways towards green steel (SMS Group, 2024)

References

Ahmad, J., Kontoleon, K.J., Majdi, A., Naqash, M.T., Deifalla, A.F., Ben Kahla, N., Isleem, H.F. and Qaidi, S.M.A. (2022). A Comprehensive Review on the Ground Granulated Blast Furnace Slag (GGBS) in Concrete Production. *Sustainability*, 14(14), p.8783. doi:https://doi.org/10.3390/su14148783.

Ahmad, M.A., Ranaivomanana, H., Bonnet, S., L'Hostis, V. and Buttin, P. (2023). Study of Hydration Properties for Blast Furnace Slag-Blended Cement: Prediction of Slag Hydration Kinetics. *Rilem bookseries*, pp.165–176. doi:https://doi.org/10.1007/978-3-031-33187-9_16.

Ahmed, H.M., Mousa, E.A., Larsson, M. and Viswanathan, N.N. (2016). Recent Trends in Ironmaking Blast Furnace Technology to Mitigate CO2 Emissions: Top Charging Materials. *In: Cavaliere, P. (eds) Ironmaking and Steelmaking Processes.* Springer, Cham, pp.101–124. doi:https://doi.org/10.1007/978-3-319-39529-6_6.

Anameric, B., Rohaus, D. and Riebeiro, T.R. (2019). Ironmaking. *In: Dunne, C. (eds) SME mineral processing & extractive metallurgy handbook.* Englewood, Colorado Society For Mining, Metallurgy & Exploration, pp.1781–1797.

Antunes, M., Santos, R.L., Pereira, J., Rocha, P., Horta, R.B. and Colaço, R. (2021). Alternative Clinker Technologies for Reducing Carbon Emissions in Cement Industry: A Critical Review. *Materials*, 15(1), p.209. doi:https://doi.org/10.3390/ma15010209.

Atsushi, M., Uemura, H. and Sakaguchi, T. (2010). MIDREX processes. *Kobelco Technol Rev*, [online] pp.50–57. Available at: https://www.kobelco.co.jp/english/ktr/pdf/ktr_29/050-057.pdf [Accessed 26 Dec. 2024].

Bailera, M., Lisbona, P., Peña, B. and Romeo, L.M. (2021). A review on CO2 mitigation in the Iron and Steel industry through Power to X processes. *Journal of CO2 Utilization*, 46, p.101456. doi:https://doi.org/10.1016/j.jcou.2021.101456.

Barrington , C. (2022). *Future DRI Production and Iron Ore Supply* . [online] International Iron Metallics Association (IIMA). Available at: https://www.metallics.org/assets/files/Public-Area/Decarbonisation/Paper3_DRIProduction.pdf [Accessed 9 Jan. 2025].

Benhelal, E., Shamsaei, E. and Rashid, M.I. (2021). Challenges against CO2 abatement strategies in cement industry: A review. *Journal of Environmental Sciences*, 104, pp.84–101. doi:https://doi.org/10.1016/j.jes.2020.11.020.

Binici, H., Temiz, H. and Köse, M.M. (2007). The effect of fineness on the properties of the blended cements incorporating ground granulated blast furnace slag and ground basaltic pumice. *Construction and Building Materials*, 21(5), pp.1122–1128. doi:https://doi.org/10.1016/j.conbuildmat.2005.11.005.

Birat, J. and Maizière-lès-Metz, D. (2010). "Steel sectoral report-Contribution to the UNIDO roadmap on CCS1-fifth draft." Global Technology Roadmap for CCS in Industry. United Nations Industrial Development Organization, Vienna, Austria.

Biswas, A.K. (2011). *Principles of blast furnace ironmaking : theory and practice*. Calcutta India: Sba Publications, p.528.

Blotevogel, S., Doussang, L., Poirier, M., André, L., Canizarès, A., Simon, P., Montouillout, V., Judit Kaknics, Cédric Patapy and Cyr, M. (2024). The influence of Al2O3, CaO, MgO and TiO2 content on the early-age reactivity of GGBS in blended cements, alkali-activated materials and supersulfated cements. *Cement and Concrete Research*, 178, pp.107439–107439. doi:https://doi.org/10.1016/j.cemconres.2024.107439.

Blotevogel, S., Ehrenberg, A., Steger, L., Doussang, L., Kaknics, J., Patapy, C. and Cyr, M. (2020). Ability of the R3 test to evaluate differences in early age reactivity of 16 industrial ground granulated blast furnace slags (GGBS). *Cement and Concrete Research*, 130, pp.105998–105998. doi:https://doi.org/10.1016/j.cemconres.2020.105998.

Bohm, C., Wieder, K., Schmidt, U. and Grill, W. (2009). Simetalcis Corex / Finex Prepared For Present And Future Iron Making Challenges. *ABM Proceedings*. doi:https://doi.org/10.5151/2594-357x-15664.

Bolte, G., Schade, T. and Bullerjahn, F. (2023). Synergies of steel and cement industry: how to replace declining GBFS quantities by scrap based, engineered EAF-slag. In: *Proceedings of*

the 8th International Slag Valorisation Symposium. Mechelen, Belgium: KU Leuven Institute for Sustainable Metals and Minerals.

Boretti, A. (2020). Production of hydrogen for export from wind and solar energy, natural gas, and coal in Australia. *International Journal of Hydrogen Energy*, 45(7), pp.3899–3904. doi:https://doi.org/10.1016/j.ijhydene.2019.12.080.

Callaghan, R.M. (2024). *Iron and steel slags*. [online] USGS Publications Warehouse. Available at: https://pubs.usgs.gov/periodicals/mcs2024/mcs2024-iron-steel-slag.pdf.

Cavaliere, P. (2016). *Ironmaking and Steelmaking Processes*. Cham: Springer International Publishing, pp doi:https://doi.org/10.1007/978-3-319-39529-6.

Cavaliere, P. (2019). Blast Furnace: Most Efficient Technologies for Greenhouse Emissions Abatement. *Springer eBooks*, pp.167–273. doi:https://doi.org/10.1007/978-3-030-21209-4_4.

Cembureau (2023). *Activity report 2023*. [online] Cembureau. Available at: https://cembureau.eu/media/dnbf4xzc/activity-report-2023-for-web.pdf [Accessed 13 Jul. 2025].

Cement Industry Federation (2023). *Cement Industry & Emissions – Cement*. [online] Cement Industry Federation. Available at: https://cement.org.au/sustainability/climate-change/ [Accessed 3 Jan. 2025].

Chatterjee, A.K. (1996). High belite cements—Present status and future technological options: Part I. *Cement and Concrete Research*, 26(8), pp.1213–1225. doi:https://doi.org/10.1016/0008-8846(96)00099-3.

Chen, W. and Brouwers, J. (2006). The hydration of slag, part 2: reaction models for blended cement. *Journal of Materials Science*, 42(2), pp.444–464. doi:https://doi.org/10.1007/s10853-006-0874-1.

Chen, Y., Fang, Y., Feng, W., Zhang, Y. and Zhao, G.X. (2022). How to minimise the carbon emission of steel building products from a cradle-to-site perspective: A systematic review of recent global research. *Journal of Cleaner Production*, [online] 368, p.133156. doi:https://doi.org/10.1016/j.jclepro.2022.133156.

Conejo, A. and Cárdenas, J. (2006). Energy Consumption in the EAF with 100% DRI. *In Proceedings of the Iron & Steel Technology Conference*, Cleveland, OH, USA, pp. 1-4.
Das, B., Prakash, S., Reddy, P.S.R. and Misra, V.N. (2007). An overview of utilization of slag and sludge from steel industries. *Resources, Conservation and Recycling*, 50(1), pp.40–57. doi:https://doi.org/10.1016/j.resconrec.2006.05.008.

de Almeida, R.A.M., Vieira, D., Bielefeldt, W.V. and Vilela, A.C.F. (2017). Slag Foaming Fundamentals - A Critical Assessment. *Materials Research*, [online] 20(2), pp.474–480. doi:https://doi.org/10.1590/1980-5373-mr-2016-0059.

de Brito, J. and Kurda, R. (2020). The past and future of sustainable concrete: A critical review and new strategies on cement-based materials. *Journal of Cleaner Production*, 281, p.123558. doi:https://doi.org/10.1016/j.jclepro.2020.123558.

Diez, M.A., Centeno, T.A. and Fierro, A.A. (2023). Coal use for iron and steel production in low-carbon transition scenarios. *Elsevier eBooks*, pp.493–546. doi:https://doi.org/10.1016/b978-0-12-824327-5.00010-7.

Dom, A.A.M., Jamaluddin, N., Hamid, N.A.A. and Hoon, C.S. (2022). A Review: GGBS as a Cement Replacement in Concrete. *IOP Conference Series: Earth and Environmental Science*, 1022(1), p.012044. doi:https://doi.org/10.1088/1755-1315/1022/1/012044.

Doranehgard, M.H., Samadyar, H., Mesbah, M., Haratipour, P. and Samiezade, S. (2017). High-purity hydrogen production with in situ CO 2 capture based on biomass gasification. *Fuel*, 202, pp.29–35. doi:https://doi.org/10.1016/j.fuel.2017.04.014.

Duarte, P. and Becerra, J., 2015. High-carbon DRI with Energiron DR technology. *Stahl und Eisen*, *135* (11), pp.153-160.

Duarte, P.E., Becerra, J., Lizcano, C. and Martinis, A. (2010). Energiron direct reduction ironmaking - Economical, flexible, environmentally friendly. *Steel Times International*, 34(3), pp.25–30.

Ehrenberg, A., Sarcos, N.R., Hart, D., Bornhoft, H. and Deubener, J. (2020). Influence of the Thermal History of Granulated Blast Furnace Slags on Their Latent Hydraulic Reactivity in Cementitious Systems. *Journal of Sustainable Metallurgy*, 6(2), pp.207–215. doi:https://doi.org/10.1007/s40831-020-00269-4.

Elaouzy, Y. and El Fadar, A. (2024). Water-energy-carbon-cost nexus in hydrogen production, storage, transportation and utilization. *International journal of hydrogen energy*, 53, pp.1190–1209. doi:https://doi.org/10.1016/j.ijhydene.2023.12.114.

Escalante, J.I., Gómez, L.Y., Johal, K.K., Mendoza, G., Mancha, H. and Méndez, J. (2001). Reactivity of blast-furnace slag in Portland cement blends hydrated under different conditions. *Cement and Concrete Research*, 31(10), pp.1403–1409. doi:https://doi.org/10.1016/s0008-8846(01)00587-7.

Freitas, A., Santos, R.L., Rogério Colaço, R. Bayão Horta and Lopes, J.H. (2015). From lime to silica and alumina: systematic modeling of cement clinkers using a general force-field. *Phys. Chem*, 17(28), pp.18477–18494. doi:https://doi.org/10.1039/c5cp02823j.

Gagg, C.R. (2014). Cement and concrete as an engineering material: An historic appraisal and case study analysis. *Engineering Failure Analysis*, [online] 40(40), pp.114–140. doi:https://doi.org/10.1016/j.engfailanal.2014.02.004.

Geerdes, M., Chaigneau, R., Lingiardi, O., Molenaar, R., Opbergen, R. van, Sha, Y. and Warren, P. (2020). *Modern Blast Furnace Ironmaking*. *IOS Press eBooks*, IOS Press, pp.1–12. doi:https://doi.org/10.3233/stal9781643681238.

Global Slag (2024). *EuroSlag hosts European Ferrous Slag Conference 2024*. [online] Globalslag.com. Available at: https://www.globalslag.com/news/item/369-euroslag-hosts-european-ferrous-slag-conference-2024 [Accessed 29 Dec. 2024].

Gollakota, A.R.K., Volli, V. and Shu, C. (2019). Progressive utilisation prospects of coal fly ash: A review. *Science of The Total Environment*, 672, pp.951–989. doi:https://doi.org/10.1016/j.scitotenv.2019.03.337.

Graupner, Y., Weckenborg, C. & Spengler, T. 2023. Low-carbon primary steelmaking using direct reduction and electric arc furnaces: Prospective environmental impact assessment. *Procedia CIRP,* 116: 696–701.

Guo, J., Bao, Y. and Wang, M. (2018). Steel slag in China: Treatment, recycling, and management. *Waste Management*, 78, pp.318–330. doi:https://doi.org/10.1016/j.wasman.2018.04.045.

Hamadeh, H., Mirgaux, O. and Patisson, F. (2018). Detailed Modeling of the Direct Reduction of Iron Ore in a Shaft Furnace. *Materials*, 11(10), p.1865. doi:https://doi.org/10.3390/ma11101865.

Harder, J. (2010). Grinding trends in the cement industry - Cement Lime Gypsum. *ZKG (Zement Kalk Gips)*, 3(4), pp.46–58.

Hasanbeigi, A., Arens, M. and Price, L. (2014). Alternative emerging ironmaking technologies for energy-efficiency and carbon dioxide emissions reduction: A technical review. *Renewable and Sustainable Energy Reviews*, 33, pp.645–658. doi:https://doi.org/10.1016/j.rser.2014.02.031.

He, K. and Wang, L. (2017). A review of energy use and energy-efficient technologies for the iron and steel industry. *Renewable and Sustainable Energy Reviews*, 70, pp.1022–1039. doi:https://doi.org/10.1016/j.rser.2016.12.007.

Hewlett, P.C. and Liska, M. (Eds) (2019). *Lea's Chemistry of Cement and Concrete*, 5th Edition, Elsevier Science & Technology, Butterworth-Heinemann, Oxford, UK.

Horii, K., Sugahara, K., Kitano, Y., Kato, T. and Tsutsumi, N. (2015). Overview of Iron / Steel Slag Application and Development of New Utilization Technologies. *Nippon Steel Sumitomo Met Tech Rep*, 109, pp.5–11.

Huang, D. and Andrade, M. (2018). Optimizations of blast furnace oxygen enrichments. *Iron & Steel Technology*,15(9), pp.78–87.

IEA (2019). *The Future of Hydrogen*. [online] IEA. Available at: https://www.iea.org/reports/the-future-of-hydrogen [Accessed 26 Dec. 2024].

IEA (2020). Iron and Steel Technology Roadmap – Analysis. IEA. Available at: https://www.iea.org/reports/iron-and-steel-technology-roadmap, viewed 12-07-2024.

IEA. (2024). *Direct emissions intensity of cement production in the Net Zero Scenario, 2015-2030 – Charts – Data & Statistics*. [online] Available at: https://www.iea.org/data-and-statistics/charts/direct-emissions-intensity-of-cement-production-in-the-net-zero-scenario-2015-2030-2 [Accessed 31 Dec. 2024].

Imbabi, M.S., Carrigan, C. and McKenna, S. (2012). Trends and developments in green cement and concrete technology. *International Journal of Sustainable Built Environment*, [online] 1(2), pp.194–216. doi:https://doi.org/10.1016/j.ijsbe.2013.05.001.

IPCC (2023). Climate Change 2023: Synthesis Report, Summary for Policymakers. Contribution of Working Groups I, II and III to the Sixth Assessment Report of the Intergovernmental Panel on Climate Change [Core Writing Team, H. Lee and J. Romero (eds.)]. IPCC, Geneva, Switzerland. *IPCC*, [online] pp.1–34. doi:https://doi.org/10.59327/ipcc/ar6-9789291691647.001.

Ji, Y., Chi, Z., Yuan, S., Chen, Y., Li, Y., Jiang, T., Liu, X. and Zhang, W. (2024). Development and Application of Hydrogen-Based Direct Reduction Iron Process. *Processes*, 12(9), pp.1829–1829. doi:https://doi.org/10.3390/pr12091829.

Kerimov, R.I. and Shakhov, S.I. (2020). Use of Metallized Raw Materials in Electric Furnace Steelmaking. *Metallurgist*, 64(1-2), pp.128–135. doi:https://doi.org/10.1007/s11015-020-00974-1.

Kikuchi, S., Kobayashi, I., Ito, S., Tsuge, O. and Tokuda, K. (2010). *ITmk3 Process*. [online] KOBELCO TECHNOLOGY REVIEW. Available at: https://www.kobelco.co.jp/english/products/ironunit/itmk3.htm [Accessed 24 Dec. 2024].

Kim, J., Sovacool, B.K., Bazilian, M., Griffiths, S., Lee, J., Yang, M. and Lee, J. (2022). Decarbonizing the iron and steel industry: A systematic review of sociotechnical systems, technological innovations, and policy options. *Energy Research & Social Science*, [online] 89(2214-6296), p.102565. doi:https://doi.org/10.1016/j.erss.2022.102565.

Kim, W. and Sohn, I. (2022). Critical challenges facing low carbon steelmaking technology using hydrogen direct reduced iron. *Joule*, 6(10), pp.2228–2232. doi:https://doi.org/10.1016/j.joule.2022.08.010.

Kirschen, M., Badr, K. and Pfeifer, H. (2011). Influence of direct reduced iron on the energy balance of the electric arc furnace in steel industry. *Energy*, 36(10), pp.6146–6155. doi:https://doi.org/10.1016/j.energy.2011.07.050.

Kirschen, M., Hay, T. and Echterhof, T. (2021). Process Improvements for Direct Reduced Iron Melting in the Electric Arc Furnace with Emphasis on Slag Operation. *Processes*, 9(2), p.402. doi:https://doi.org/10.3390/pr9020402.

Kleinschmidt, G., Koneke, M., Degel, R. and Oterdoom, H. (2010). AC- And DC- Smelter Technology For Ferrous Metal Production . *The Twelfth International Ferroalloys Congress Sustainable Future.* Helsinki, Finland, pp.825–838.

Kolani, B., Buffo-Lacarrière, L., Sellier, A., Escadeillas, G., Boutillon, L. and Linger, L. (2012). Hydration of slag-blended cements. *Cement and Concrete Composites*, 34(9), pp.1009–1018. doi:https://doi.org/10.1016/j.cemconcomp.2012.05.007.

Lee, B. and Sohn, I. (2014). Review of Innovative Energy Savings Technology for the Electric Arc Furnace. *JOM*, 66(9), pp.1581–1594. doi:https://doi.org/10.1007/s11837-014-1092-y.

Li, J. and Cheng, W. (2020). Comparative life cycle energy consumption, carbon emissions and economic costs of hydrogen production from coke oven gas and coal gasification. *International Journal of Hydrogen Energy*, 45(51), pp.27979–27993. doi:https://doi.org/10.1016/j.ijhydene.2020.07.079.

Li, J., Wei, G. and Han, C. (2023). Fundamental Study on Electric Arc Furnace Steelmaking with Submerged Carbon Powder Injection with CO2-O2 Mixed Gas. *Metals*, 13(9), pp.1602–1602. doi:https://doi.org/10.3390/met13091602.

Lineman, M., Do, Y., Kim, J.Y. and Joo, G.-J. (2015). Talking about Climate Change and Global Warming. *PLOS ONE*, [online] 10(9), p.e0138996. doi:https://doi.org/10.1371/journal.pone.0138996.

Linklater, J. (2021). *Adapting to Raw Materials Challenges: Part 1 - Operating MIDREX Plants With Lower Grade Pellets & Lump Ores*. [online] Midrex Technologies, Inc. Available at: https://www.midrex.com/tech-article/adapting-to-raw-materials-challenges-part-1-operating-midrex-plants-with-lower-grade-pellets-lump-ores/ [Accessed 27 Dec. 2024].

Liu, W., Zuo, H., Wang, J., Xue, Q., Ren, B. and Yang, F. (2021). The Production and Application of Hydrogen in Steel Industry. *International Journal of Hydrogen Energy*, [online] 46(17). doi:https://doi.org/10.1016/j.ijhydene.2020.12.123.

Liu, X. and Yan, W. (2024). Current advances in slag foaming processes toward reduced CO2 emission for electric arc furnace steelmaking. *Journal of CO2 Utilization*, 90, p.102979. doi:https://doi.org/10.1016/j.jcou.2024.102979.

Lu, L., Devasahayam, S. and Sahajwalla, V. (2013). Evaluation of coal for metallurgical applications. *The Coal Handbook: Towards Cleaner Production*, pp.352–386. doi:https://doi.org/10.1533/9781782421177.3.352.

Lungen, H.B., Schmole, P. (2018). Comparison of Blast Furnace Operation Modes in the World. *Proceedings of the 8th International Congress on Science and Technology of Ironmaking*, Vienna, Austria, pp. 1054–1063.

Madhavan, N., Brooks, G., Rhamdhani, M.A. and Bordignon, A. (2022). Contribution of CO2 Emissions from Basic Oxygen Steelmaking Process. *Metals*, [online] 12(5), p.797. doi:https://doi.org/10.3390/met12050797.

Market Research Future (2023). *Supplementary Cementitious Materials Market Size, Growth Drivers 2032*. [online] Marketresearchfuture.com. Available at: https://www.marketresearchfuture.com/reports/supplementary-cementitious-materials-market-25457 [Accessed 4 Jan. 2025].

Mateus, B.C., Mendes, M., Paulo, J., Ismael, A., Assis, R. and da, M. (2022). Forecasting Steel Production in the World—Assessments Based on Shallow and Deep Neural Networks. *Applied Sciences*, 13(1), pp.178–178. doi:https://doi.org/10.3390/app13010178.

Midrex Technologies Inc. (2018). *The MIDREX Process - the world's most reliable and productive Direct Reduction Technology*. [online] Available at: https://www.midrex.com/wp-content/uploads/MIdrex_Process_Brochure_4-12-18.pdf [Accessed 26 Dec. 2024].

Midrex Technologies. (2024). *MIDREX® Process*. [online] Midrex Technologies, Inc. Available at: https://www.midrex.com/technology/midrex-process/ [Accessed 26 Dec. 2024].

Mills, K., Yuan, L., Li, Z., Zhang, G. and Chou, K. (2012). A Review of the Factors Affecting the Thermophysical Properties of Silicate Slags. *High Temperature Materials and Processes*, 31(4-5). doi:https://doi.org/10.1515/htmp-2012-0097.

Mills, K.C. (1993). The Influence of Structure on the Physico-chemical Properties of Slags. *ISIJ International*, 33(1), pp.148–155. doi:https://doi.org/10.2355/isijinternational.33.148.

Nicholas, S. & Basirat, S. 2022. Solving iron ore quality issues for low-carbon steel. https://ieefa.org/resources/solving-iron-ore-quality-issues-low-carbon-steel, viewed 2024-06-10.

Nicolas, R.S., Walkley, B. and van Deventer, J.S.J. (2019). Portland and Other Cements. In: C. Dunne, ed., *SME mineral processing & extractive metallurgy* . Englewood: Colorado Society For Mining, Metallurgy & Exploration, pp.2013–2029.

OEC (2022). *Granulated Slag (HS: 2618) Product Trade, Exporters and Importers | The Observatory of Economic Complexity*. [online] The Observatory of Economic Complexity. Available at: https://oec.world/en/profile/hs/granulated-slag [Accessed 28 Dec. 2024].

Orozco, C., Babel, S., Tangtermsirikul, S. and Sugiyama, T. (2024). Comparison of environmental impacts of fly ash and slag as cement replacement materials for mass concrete and the impact of transportation. *Sustainable Materials and Technologies*, [online] 39, p.e00796. doi:https://doi.org/10.1016/j.susmat.2023.e00796.

Overmann, S., Vollpracht, A. and Matschei, T. (2024). Reactivity of Calcined Clays as SCM—A Review. *Materials*, [online] 17(2), p.312. doi:https://doi.org/10.3390/ma17020312.

Pardo, N. and Moya, J.A. (2013). Prospective scenarios on energy efficiency and CO2 emissions in the European Iron & Steel industry. *Energy*, 54, pp.113–128. doi:https://doi.org/10.1016/j.energy.2013.03.015.

Parra, D., Valverde, L., Pino, F.J. and Patel, M.K. (2019). A review on the role, cost and value of hydrogen energy systems for deep decarbonisation. *Renewable and Sustainable Energy Reviews*, 101, pp.279–294. doi:https://doi.org/10.1016/j.rser.2018.11.010.

Parra, D., Valverde, L., Pino, F.J. and Patel, M.K. (2019). A review on the role, cost and value of hydrogen energy systems for deep decarbonisation. *Renewable and Sustainable Energy Reviews*, 101, pp.279–294. doi:https://doi.org/10.1016/j.rser.2018.11.010.

Pistorius, P.C., Gao, X., Holappa, L., Matsuura, H., Park, J. and Guo, M. (2019). Steelmaking. *In: Dunne, C. (eds) SME mineral processing & extractive metallurgy handbook.* Englewood, Colorado Society For Mining, Metallurgy & Exploration, pp.2091–2105.

Ranade M, Chaubal P (2004) An intensive course—blast furnace ironmaking. McMaster University, Hamilton, pp 9–1

Sahin, F.G. (2023). *What is hydration? How Does Cement Hydration Take Place?* [online] CIMSA. Available at: https://cimsa.com.tr/en/what-is-hydration-how-does-cement-hydration-take-place/ [Accessed 8 Feb. 2025].

Sahin, F.G. (2024). *What are the Hydration Stages? How is Durable Concrete Created Based on the Stages of Hydration?* [online] CIMSA. Available at: https://cimsa.com.tr/en/what-are-the-hydration-stages-how-is-durable-concrete-created-based-on-the-stages-of-hydration/ [Accessed 8 Feb. 2025].

SANS 50197-1:2013. South African National Standard for Cement Part 1: Composition, Specifications and Conformity Criteria for Common Cements, South African Bureau of Standards, Pretoria, South Africa

Schmole, P., Lungen, H.B. and Noldin, J.H. (2012). New ironmaking technologies: Will the dominance of the blast furnace be ever challenged? *6th International Congress on the Science and Technology of Ironmaking*, 3(6), pp.2093–2104.

Shen, H., Forssberg, E. and Nordström, U. (2004). Physicochemical and mineralogical properties of stainless-steel slags oriented to metal recovery. *Resources, Conservation and Recycling*, 40(3), pp.245–271. doi:https://doi.org/10.1016/s0921-3449(03)00072-7.

Shetty, M.S. and Jain, A.K. (2019). *Concrete technology theory and practice*. New Delhi S. Chand Publishing.

Skyway Slag Cement (2024). *Sustainability - Skyway Cement Company*. [online] Skyway Cement Company. Available at: https://www.skywaycement.com/sustainability/ [Accessed 29 Dec. 2024].

SMS group (2022). *Sustainable Steel Strategies Summit, September 2022*. [online] Available at:https://issuu.com/quartzbusinessmedia/docs/sustainable_steel_strategies_summit_september_2022 [Accessed 29 Dec. 2024].

SMS group (2024). *Green steel*. [online] Sms-group.com. Available at: https://www.sms-group.com/innovation/turning-metals-green/green-steel [Accessed 27 Dec. 2024].

Snellings, R., Chwast, J., Cizer, Ö., De Belie, N., Dhandapani, Y., Durdzinski, P., Elsen, J., Haufe, J., Hooton, D., Patapy, C., Santhanam, M., Scrivener, K., Snoeck, D., Steger, L., Tongbo, S., Vollpracht, A., Winnefeld, F. and Lothenbach, B. (2018). Report of TC 238-SCM: hydration stoppage methods for phase assemblage studies of blended cements—results of a round robin test. *Materials and Structures*, 51(4). doi:https://doi.org/10.1617/s11527-018-1237-5.

Sohn, H.Y. and Mohassab, Y. (2016). Greenhouse Gas Emissions and Energy Consumption of Ironmaking Processes. *In: Cavaliere, P. (eds) Ironmaking and Steelmaking Processes.* Springer, Cham, pp.427–455. doi:https://doi.org/10.1007/978-3-319-39529-6_25.

Sun, J. and Zhang, P. (2021). Effects of different composite mineral admixtures on the early hydration and long-term properties of cement-based materials: A comparative study. *Construction and Building Materials*, 294, p.123547. doi:https://doi.org/10.1016/j.conbuildmat.2021.123547.

Sun, J., Hou, S., Guo, Y., Cao, X. and Zhang, D. (2024). Feasibility of Preparing Steel Slag–Ground Granulated Blast Furnace Slag Cementitious Materials: Synergistic Hydration, Fresh, and Hardened Properties. *Buildings*, 14(3), pp.614–614. doi:https://doi.org/10.3390/buildings14030614.

Supriya, Chaudhury, R., Sharma, U., Thapliyal, P.C. and Singh, L.P. (2023). Low-CO2 emission strategies to achieve net zero target in cement sector. *Journal of Cleaner Production*, [online] 417, p.137466. doi:https://doi.org/10.1016/j.jclepro.2023.137466.

Tamashige, T., Obana, H. and Hamaguchi, M. (1991). Operational results of OK series roller mill. *IEEE Transactions on Industry Applications*, 27(3), pp.416–424. doi:https://doi.org/10.1109/28.81821.

Tenova (2020). *ENERGIRON | Tenova*. [online] Available at: https://tenova.com/technologies/energiron [Accessed 26 Dec. 2024].

Thyssenkrupp (2022). *Charts on Q1 FY2021/22.* [online] Available at: https://d2zo35mdb530wx.cloudfront.net/_binary/UCPthyssenkruppAG/21da5310-dbe3-4c6b-

9b6d-989c8eb1075f/20220316_Charts-on-Q1_21_22_Prasentation_March_FINAL_.pdf [Accessed 27 Dec. 2024].

Thyssenkrupp (2024). *Climate-neutral steel - Our strategy | thyssenkrupp Steel*. [online] thyssenkrupp. Available at: https://www.thyssenkrupp-steel.com/en/company/sustainability/climate-strategy/climate-strategy.html [Accessed 27 Dec. 2024].

Thyssenkrupp Polysius GmbH (2024). *polysius® pure oxyfuel | thyssenkrupp Polysius*. [online] Thyssenkrupp-polysius.com. Available at: https://www.thyssenkrupp-polysius.com/en/green-technologies/polysius-pure-oxyfuel [Accessed 8 Feb. 2025].

Toan Vu, T., Seo, J., Kim, E., Ryoo, S.G., Park, B.C. and Song, D. (2024). Techno-economic analysis of integrated MIDREX process with CO2 capture and storage: Evaluating sustainability and viability for iron production. *Process Safety and Environmental Protection*, 189, pp.1314–1322. doi:https://doi.org/10.1016/j.psep.2024.07.005.

Tripathy, S.K., Dasu, J., Murthy, Y.R., Kapure, G., Pal, A.R. and Filippov, L.O. (2020). Utilisation perspective on water quenched and air-cooled blast furnace slags. *Journal of Cleaner Production*, 262, p.121354. doi:https://doi.org/10.1016/j.jclepro.2020.121354.

United Nations (2015). Transforming our world: The 2030 agenda for sustainable development. *New York: United Nations, Department of Economic and Social Affairs*, *1*, p.41.

USGS (2024). Cement - Mineral Commodity Summaries 2024. [online] USGS Publications Warehouse. Available at: https://pubs.usgs.gov/periodicals/mcs2024/mcs2024-cement.pdf [Accessed 13 Jul. 2025].

Verdeja, I., González, D.F. and Felipe, L. (2020). Raw Materials. *Topics in mining, metallurgy and materials engineering*, pp.1–14. doi:https://doi.org/10.1007/978-3-030-54606-9_1.

Vogl, V., Olsson, O. and Nykvist, B. (2021). Phasing out the blast furnace to meet global climate targets. *Joule*, [online] 5(10), pp.2646–2662. doi:https://doi.org/10.1016/j.joule.2021.09.007.

Wang, G.C. (2016). Ferrous metal production and ferrous slags. *The Utilization of Slag in Civil Infrastructure Construction*, pp.9–33. doi:https://doi.org/10.1016/b978-0-08-100381-7.00002-1.

Wang, H., Liu, X. and Zhang, Z. (2023). Pozzolanic activity evaluation methods of solid waste: A review. *Journal of cleaner production*, 402, pp.136783–136783. doi:https://doi.org/10.1016/j.jclepro.2023.136783.

Wei, M., McMillan, C.A. and de la Rue du Can, S. (2019). Electrification of Industry: Potential, Challenges and Outlook. *Current Sustainable/Renewable Energy Reports*, 6(4), pp.140–148. doi:https://doi.org/10.1007/s40518-019-00136-1.

World Cement Association. (2024). *WCA-About Cement*. [online] Available at: https://www.worldcementassociation.org/about-cement [Accessed 28 Dec. 2024].

World Steel Association (2021). *Steel industry co-products Fact sheet*. [online] Available at: https://worldsteel.org/wp-content/uploads/Fact-sheet-Steel-industry-co-products.pdf [Accessed 28 Dec. 2024].

World Steel Association (2024). *World Steel in Figures 2024*. [online] worldsteel.org. Available at: https://worldsteel.org/data/world-steel-in-figures-2024/ [Accessed 23 Dec. 2024].

Xu, D., Cui, Y., Li, H., Yang, K., Xu, W. and Chen, Y. (2015). On the future of Chinese cement industry. *Cement and Concrete Research*, 78, pp.2–13. doi:https://doi.org/10.1016/j.cemconres.2015.06.012.

Yildirim, I.Z. and Prezzi, M. (2011). Chemical, Mineralogical, and Morphological Properties of Steel Slag. *Advances in Civil Engineering*, 2011, pp.1–13. doi:https://doi.org/10.1155/2011/463638.

Yilmaz, C. and Turek, T. (2017). Modeling and simulation of the use of direct reduced iron in a blast furnace to reduce carbon dioxide emissions. *Journal of Cleaner Production*, 164, pp.1519–1530. doi:https://doi.org/10.1016/j.jclepro.2017.07.043.

Zecca, N., Cobden, P.D., Lücking, L. and Giampaolo Manzolini (2023). SEWGS integration in a direct reduction steelmaking process for CO2 mitigation. *International journal of greenhouse gas control*, 130, pp.103991–103991. doi:https://doi.org/10.1016/j.ijggc.2023.103991.

Zhang, X., Zhong, J., Zhang, X., Zhang, D., Miao, C., Wang, D. and Guo, L. (2024). China Can Achieve Carbon Neutrality in Line with the Paris Agreement's 2 °C Target: Navigating Global Emissions Scenarios, Warming Levels, and Extreme Event Projections. *Engineering*. [online] doi:https://doi.org/10.1016/j.eng.2024.11.023.

Zhang, Y., Zhang, S., Chen, Y. and Çopuroğlu, O. (2022). The effect of slag chemistry on the reactivity of synthetic and commercial slags. *Construction and Building Materials*, 335, p.127493. doi:https://doi.org/10.1016/j.conbuildmat.2022.127493.

Zhu, T.X., Coley, K.S. and Irons, G.A. (2012). Progress in Slag Foaming in Metallurgical Processes. *Metallurgical and Materials Transactions B*, 43(4), pp.751–757. doi:https://doi.org/10.1007/s11663-012-9654-2.

PART I: DRI-OBF

The first part of this project focuses on meeting both the metallurgical and cementitious requirements in one furnace (OBF), the corresponding slag production configuration is DRI-OBF. The materials and methods will be covered in chapter 3, the preliminary characterizations of the OBF slag are covered in Chapter 4, the performance of slag-cement blends are covered in chapter 5 for mortar mixes, and in chapter 6 for paste mixes. The summary of this first part is illustrated in Figure 31.

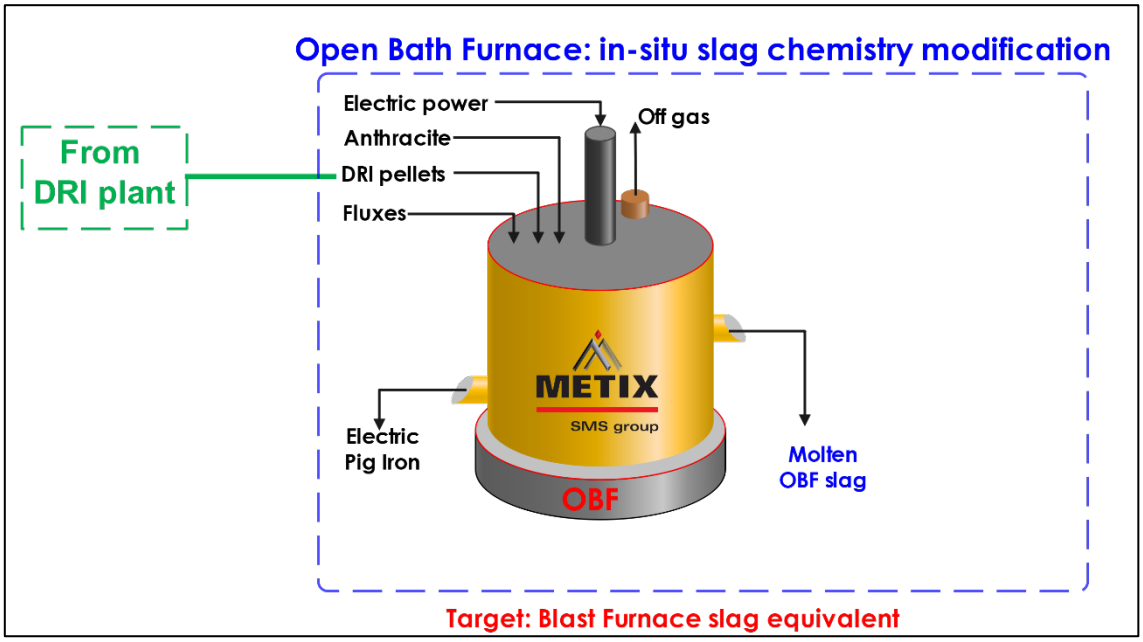


Figure 31: DRI-OBF configuration

CHAPTER 3: MATERIALS AND METHODS

This chapter provides detailed information regarding the materials and the methods employed to fulfil the objectives of part one of this study, which can be broadly divided into three consecutive phases as follows:

- In-situ slag modification and production
- Slag particle size reduction and milling optimization
- Slag cement blending and cementitious properties assessment

3.1. Phase 1: In-situ slag modification

The gangue composition of the DRI selected for use was not aligned with the specifications of a blast furnace slag composition. As a result, other materials, known as fluxes, were added during smelting to modify the OBF slag composition so as to reach a BF slag equivalent composition. Control of slag chemical composition was based on meeting target values for the following ratios: CaO/SiO_2; $(CaO+MgO)/SiO_2$; MgO/CaO.

The work entailed in this phase was conducted at Mintek South Africa. The following materials and equipment were employed.

3.1.1. Directly reduced iron (DRI) pellets

Iron ore pellets of a BF grade quality (64% Fe) for use as furnace feed, were reduced at solid state through the Midrex process under H_2 and CO atmospheres (Sarkar et al., 2017). These pellets had hematite (Fe_2O_3) as the main iron mineral phase, representing 92% of the pellet mass, and the remainder being the gangue materials. This resulted in the production of DRI pellets with 94% iron metallization (abbreviated as Met) while the remaining 6% of Fe was still present as wustite (FeO) along with the other gangue materials. The DRI process does not produce any slag; however, there is a slight enrichment in terms of gangue proportion since most of the oxygen is removed from hematite to produce solid metallic iron. The composition of the DRI used in this study is summarised in Table 4. It should be noted that this project used cold DRI (CDRI), fed to the furnace at ± 25 °C.

Table 4: Composition of Direct Reduced Iron (DRI) in the furnace feed

Composition	C	Fe met	FeO	SiO_2	MgO	Al_2O_3	CaO	TiO_2	MnO	V_2O_5	P	S	Total
Wt%	2,5	83,94	6,61	4,25	1,03	0,31	0,52	0,152	0,127	0,132	0,04	0,016	99,63

A brief and typical description of reduction in the DRI process is illustrated in Figure 32. However, it should be noted that this is not a complete representation since Fe_3C along with other complex phases also form during the DRI process.

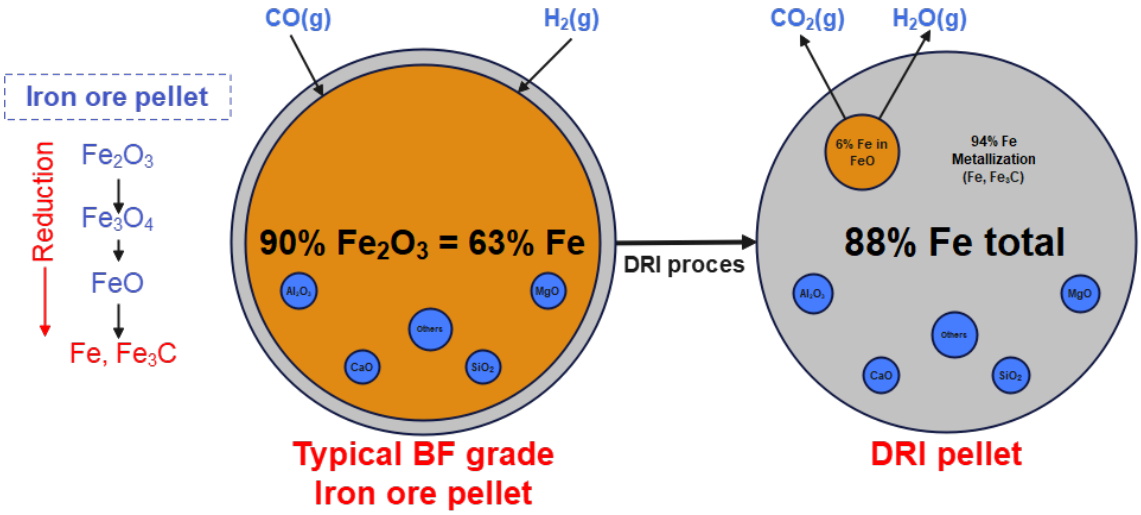


Figure 32: Typical representation of reduction during the DRI process

An illustration of the DRI pellets used in this study is shown in Figure 33.



Figure 33: DRI pellets used in this study

3.1.2. Fluxes

Fluxing materials play a very important role in conditioning and modifying the behaviour of the slag. These materials react with the gangue components of the DRI to form low melting-point compounds that can easily be separated from the liquid metal at lower processing temperature, thereby saving energy. Moreover, the amount and the types of fluxes used depend upon the gangue composition of the DRI, the required final slag composition, as well as the key performance indicators of the furnace operations. The fluxes used in the smelting campaign of this study were:

- Bauxite to supplement the Al_2O_3 content
- Burnt lime to control the CaO content
- Burnt dolomite to adjust the MgO and CaO content of the slag
- Quartzite to control the SiO_2 content of the slag

The main goal of fluxes addition was to obtain a slag with BF equivalent composition. Table 5 summarizes the compositions of all the fluxing materials.

Table 5: Composition of fluxes used in the furnace feed

FLUXES (%)	MgO	Al_2O_3	SiO_2	CaO	TiO_2	MnO	Fe_2O_3	SO_3	CO_2	Total
Burnt dolomite	37,49	0,31	1,52	52,48	0,08	1,57	1,28	0,05	4,03	98,81
Burnt lime	0,97	0,48	0,93	92,60	0,08	0,95	0,74	0,10	2,28	99,13
Bauxite	0,76	81,75	6,42	0,16	3,37	0,06	5,18	0,00	0,00	97,70
Quartz	0,08	1,14	93,23	0,07	0,08	0,06	0,72	0,00	0,00	95,38

3.1.3. Anthracite – used as a reductant

As previously mentioned, the DRI pellets were 94% metallized. In order to achieve complete reduction of the remaining FeO to metallic Fe, anthracite was added, and this reduction occurs at liquid state as opposed to the DRI process where solid-state reduction takes place. Table 6 contains the ash composition together with the proximate analysis of the anthracite used in this study, and the corresponding caloric value was 29.71 MJ/kg.

Table 6: Anthracite composition

			Combined
Anthracite (%)	C	78,80	78,80
	H	2,18	2,18
	S	1,99	1,99
	N	1,83	1,83
	O	0,22	0,22
	Ash	11,90	
	Moisture	3,00	3,00
	Total	99,92	
Ash (%)	SiO_2	47,00	5,59
	Al_2O_3	35,40	4,21
	Fe_2O_3	7,91	0,94
	CaO	2,18	0,26
	MgO	0,82	0,10
	K_2O	1,73	0,21
	Na_2O	1,47	0,17
	P_2O_5	0,87	0,10
	TiO_2	1,45	0,17
	SO_3	1,09	0,13
	Total	99,92	99,91

3.1.4. Open Bath Furnace

The smelting tasks of this study were carried out in a 1 MW DC arc furnace designed and constructed by Metix (Pty) Ltd at Mintek South Africa. The furnace was set up to operate in an open arc mode, where arcing occurs above a molten bath as opposed to the well-known submerged arc mode where arcing occurs within the slag bath for slag foaming practices. This novel furnace has therefore been named as “Open Bath Furnace” (OBF) and the resulting slag is labelled similarly as “Open Bath Furnace Slag”. The pilot-scale OBF prototype was a one-electrode circular furnace, using electrical energy, in contrast to conventional blast furnaces

that operate on fossil fuel energy resulting in excessive emissions of CO_2 coupled with adverse environmental impacts. The use of electric energy, however, has the potential for utilisation of greener sources in line with the current global transition towards greener energy.

The smelting process objectives were to:

- Melt the metallized Fe in the DRI pellets
- Reduce the remaining FeO to metallic Fe with the addition of anthracite (reductant)
- Modify the molten slag composition
- Separate the molten slag from the hot metal

A limited volume of slag was produced, relative to the volume of the hot metal, since the DRI typically contains less than 15% of gangue materials. This led to a very low slag to metal ratio, making the control of the slag properties more difficult. Consequently, a greater quantity of fluxing materials was utilised to effectively manage the properties of the slag. This proved to be one of several challenges that were overcome during the smelting campaign, and the semi-industrial experience of this novel ironmaking route (DRI-OBF) provided a learning opportunity extending beyond the scope of this study.

From a process and equipment perspective, for Metix, the overall purpose of the campaign was mainly to de-risk this novel iron processing route as well as to assess its industrial stability and viability. Key factors in the success of the campaign were the innovative pyrometallurgical approach and the skills displayed in furnace operation. Overall, a total of 150 slags and hot metals was tapped during the smelting campaign.

In parallel with the test campaign, the first full scale industrial implementation of this novel technology has commenced at Thyssenkrupp Steel Europe (TkSE), where two major 100 MW OBFs are currently being constructed. These are scheduled to replace two existing BFs by 2026, and this programme will continue until all the remaining BFs are replaced by 2030 as per TkSE's decarbonisation plans (Thyssenkrupp Steel Europe).

The Open bath furnace and slag tapping are shown in Figure 34.



Figure 34: Open bath furnace and slag tapping

3.1.5. Slag Granulation

The granulation process was done after the tapping of the molten slag. Around 75 slag taps were granulated, and at each slag tap, up to 5 scoops (approximately 1 kg) of the molten slag were quenched in a small wet granulation unit that was installed next to the OBF. The granulation unit was a circular tank fitted with spray water pipes and valves to control the flow rate of the water jets. The molten slag was poured into a conical receiver, stationed above the tank, which controlled the flow rate of the molten slag. From the cone outlet, the controlled molten slag dropped at the intersection of water jets, resulting in rapid cooling and the formation of brittle, glassy solid particles in the form of granulated OBF slag (GOBFS).

This is aligned with the conventional process for granulating blast furnace slag and which is known to improve the reactivity of the slag in comparison with slow air cooling of the slag (Pal et al., 2003). It should be noted that the efficiency of the granulation process is dictated by the degree of vitrification as compared to crystallisation, which takes place when the molten slag is cooled slowly in air (Tripathy et al., 2020). The granulation process and setup are depicted in Figure 35.



Figure 35: The granulation process

The physical appearance of samples of granulated OBF slags is shown in Figure 36.



Figure 36: Wet granulated OBF slag (GOBFS)

3.1.6. Slag Drying

The wet granulated OBF slag samples were dried in an oven dryer at 120°C to remove the adsorbed and unbound water from the slag particles. This made the milling, and further handling process of the slag easier by eliminating particle agglomeration. All of the 75 GOBFS

samples were dried individually. The drying oven along with a dried GOBFS sample are shown in Figure 37.



Figure 37: Drying oven and dried GOBFS sample

3.1.7. Sample collection and characterization

The chemical composition of each slag tap was determined using inductively coupled plasma-optical emission spectroscopy (ICP-OES). From the 75 GOBFS samples, only 30 samples met the chemical composition requirement of a BF-equivalent slag composition. Three ratios were used as criteria to classify the slag taps as follows:

- CaO/SiO_2 should be in the 1.05 to 1.25 range
- Basicity $(CaO+MgO)/SiO_2$ should be greater than 1.3
- MgO/CaO should be in a range of 0.17 to 0.18

The chosen slag taps had to meet at least two of these selection criteria, and 30 samples were therefore categorized as GOBFS according to these specifications. The remaining 45 GOBFS samples did not fully meet the composition requirements and were categorized as off-spec GOBFS samples. The compositions of the 30 on-spec GOBFS samples are set out in Table 7, arranged in order of meeting the basicity and the MgO/CaO requirements.

Table 7: On specs GOBFS taps composition

On Specs	MgO	Al2O3	SiO2	CaO	TiO2	V2O5	FeO	CaO/SiO2	Basicity	MgO/CaO
Tap No	6-8	10.7-11.3	35.0-35.9	42.0-44.9	1.1-1.25	-	<0.5	1.05-1.25	>1.3	0.17-0.18
132	9,66	10,00	35,3	39,2	1,80	0,09	1,75	1,111	1,385	0,246
85	8,15	15,25	34,9	39,7	0,69	0,09	0,42	1,138	1,371	0,205
144	7,52	9,96	35,5	42,3	1,45	0,09	2,69	1,193	1,405	0,178
63	8,33	11,50	34,9	43,0	0,84	0,09	0,00	1,232	1,471	0,194
65	8,40	11,70	36,8	41,7	0,92	0,09	0,00	1,133	1,361	0,201
66	8,15	11,60	35,7	41,3	0,97	0,09	0,00	1,157	1,385	0,197
80	8,39	11,10	36,0	42,6	0,97	0,09	0,00	1,184	1,417	0,197
89	8,77	11,00	35,0	43,3	1,00	0,09	0,54	1,237	1,488	0,202
94	8,71	10,85	35,9	43,0	0,67	0,09	0,51	1,201	1,444	0,202
95	8,30	10,20	35,3	42,3	0,80	0,09	0,35	1,197	1,432	0,196
100	8,98	10,10	36,2	42,1	0,90	0,09	0,46	1,164	1,412	0,213
75	9,59	11,54	35,7	40,4	1,09	0,09	1,12	1,132	1,401	0,237
78	9,77	10,55	36,0	41,5	1,01	0,09	0,89	1,155	1,427	0,235
102	9,73	10,60	37,5	41,4	0,97	0,09	0,15	1,105	1,364	0,235
88	8,33	9,64	35,2	42,4	1,00	0,09	0,90	1,204	1,440	0,197
101	9,58	9,69	36,3	40,8	1,00	0,09	0,45	1,125	1,389	0,235
104	8,77	9,66	35,1	43,7	0,97	0,09	0,32	1,245	1,495	0,201
134	8,52	9,67	36,2	41,9	1,74	0,09	0,44	1,159	1,394	0,203
131	7,74	9,54	36,4	44,5	1,27	0,09	0,49	1,224	1,436	0,174
115	6,69	11,20	35,7	42,5	0,69	0,09	0,84	1,190	1,377	0,158
126	7,77	10,00	35,5	44,1	1,67	0,09	0,30	1,242	1,461	0,176
127	7,78	10,60	34,9	44,1	1,96	0,09	0,41	1,263	1,486	0,177
128	7,79	10,10	35,2	44,1	2,05	0,09	0,36	1,251	1,473	0,177
129	7,46	10,20	36,8	42,5	2,02	0,09	0,40	1,155	1,357	0,176
130	7,84	10,45	37,4	41,6	1,63	0,09	0,42	1,113	1,323	0,189
138	7,51	9,84	36,4	44,4	0,43	0,09	0,06	1,220	1,426	0,169
140	7,48	10,90	35,8	43,9	0,63	0,09	0,18	1,227	1,436	0,170
142	7,62	10,30	34,5	42,6	1,50	0,09	0,00	1,235	1,456	0,179
143	7,54	10,20	36,1	42,2	1,18	0,09	0,54	1,170	1,379	0,178
145	7,65	10,90	37,7	42,5	1,67	0,09	0,02	1,127	1,330	0,180

As can be seen in Table 7, all the selected slag-tap samples met the basicity and CaO/SiO_2 ratio requirements as highlighted in light green colour. However, only a few highlighted tap samples met the defined MgO/CaO ratio requirement for BF slag composition.

3.1.8. Blending of granulated OBF slag taps

The average mass of each selected GOBFS sample was about 1 kg, which was not sufficient for the required slag cement testing. Based on the similarity of some of the slag compositions as well as smelting conditions, some of the individual GOBFS samples were combined and blended as composite samples to increase the total mass available for milling and cement tests. The selection of samples for combination was done using the difference in MgO/CaO ratio. This resulted in two composite samples of more than 10 kg each, one with higher MgO levels labelled GOBFS1 and the other with lower MgO levels labelled GOBFS2 as shown in Figure 38. It should be noted that GOBFS samples that contained the highest Al_2O_3, the highest MgO, as well as the least MgO were not blended: they were, however, classified as a group of Outliers. These three samples namely, Tap 85, Tap 132, and Tap 144 as highlighted in red in Table 7 were evaluated separately (only for reactivity and setting time tests) as will be elaborated further in phase 3 of this chapter.

Label	Tap No	CaO/SiO2	MgO/CaO
Outliers	85	1,138	0,205
	132	1,111	0,246
	144	1,193	0,178
GOBFS1	63	1,232	0,194
	65	1,133	0,201
	66	1,157	0,197
	80	1,184	0,197
	89	1,237	0,202
	94	1,201	0,202
	95	1,197	0,196
	100	1,164	0,213
	75	1,132	0,237
	78	1,155	0,235
	102	1,105	0,235
	88	1,204	0,197
	101	1,125	0,235
	104	1,245	0,201
	134	1,159	0,203
	131	1,224	0,174
GOBFS2	115	1,190	0,158
	126	1,242	0,176
	127	1,263	0,177
	128	1,251	0,177
	129	1,155	0,176
	130	1,113	0,189
	138	1,220	0,169
	140	1,227	0,170
	142	1,235	0,179
	143	1,170	0,178
	145	1,127	0,180

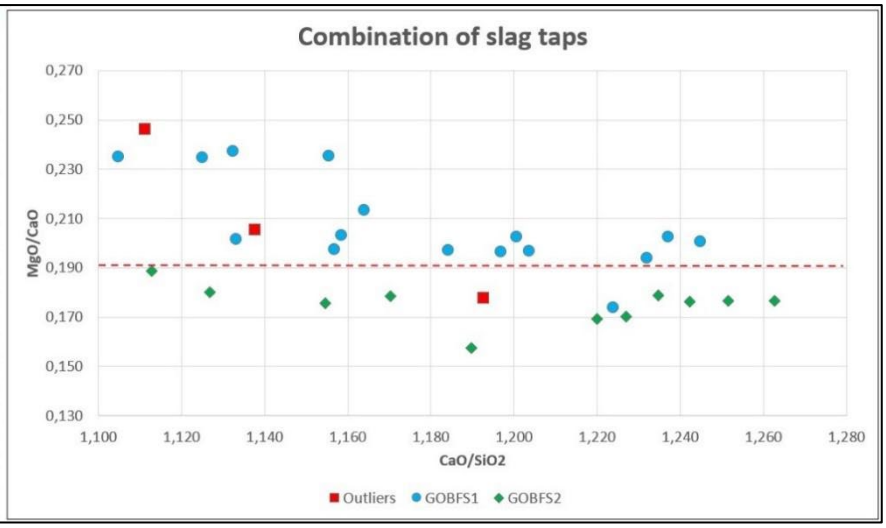


Figure 38: Blending of GOBFS taps

The Phase 1 flowsheet summary in Figure 39 illustrates the origins and processing of the three outliers (Taps 85, 132 and 144), the composite samples, GOBFS1 and GOBFS2, and the two industrial granulated BF slag samples, Thyssenkrupp Steel Europe (TkSE) and ArcelorMittal South Africa (AMSA). In addition, two samples from the air-cooled slag (AOBFS1 and AOBFS2) were also selected for analysis of the difference in morphology between granulated and air-cooled samples of the novel slag. AOBFS1 was taken from the top of the air-cooled slag ladle and AOBFS2 was taken from the bottom, expected to have cooled relatively slower.

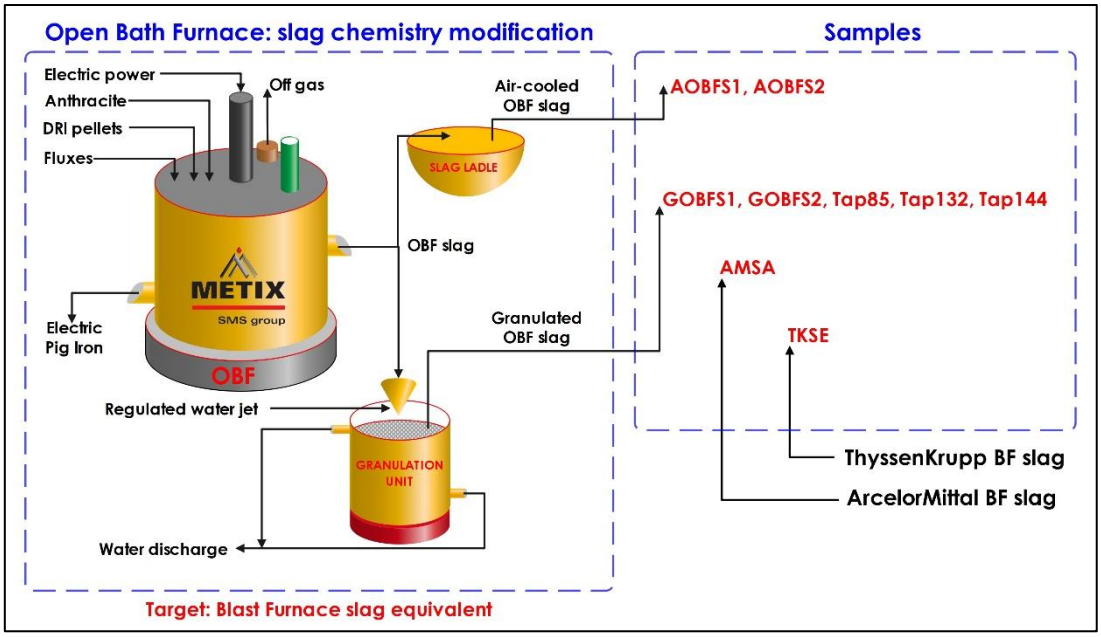


Figure 39: Flowsheet summary of phase 1 and sample collection

3.2. Phase 2: Milling optimization and slag size reduction

The processing of the slag by fine grinding was done with the intention to assess the potential valorisation of the novel OBF slag as a supplementary cementitious material (SCM). Tests of cementitious properties require really fine particle sizes for activation of granulated slag,

similar to or even finer than the particle size of Portland cement. The particle size distribution of the dried granulated OBF slag was coarser than the commercial BF slag samples (TkSE and AMSA) with 40 – 50% finer than 1000 µm as illustrated in Figure 41. In addition, the granulated OBF slag is a novel material with unknown milling properties and SCM behaviours.

The identification of the minimum required target fineness of GBFS (m^2/kg) when used as a supplementary cementitious material has been discussed in the Literature Review (He et al., 2022) together with the correlation between fineness and PSD. The milling of the granulated OBF slag samples was conducted in the Mineral Processing Laboratory at the School of Chemical and Metallurgical Engineering. Taking account of the minimum fineness of 275 m^2/kg for milled GBFS (as specified in SANS 55167-1:2011) and using the particle size vs m^2/kg data from He et al (2022), the particle size distribution targets for laboratory mill operation were defined as 100% passing 90µm and 75% passing 45µm. It was considered essential to avoid over-grinding the OBF slag in order to conduct tests of cementitious properties at a fineness level which would permit realistic commercial evaluation.

3.2.1. Feed PSD

The particle size distribution (PSD) of the feed materials is a very important parameter in any size reduction process, as it helps determine the amount of energy as well as the type of equipment that can adequately handle the size of the feed (Hlabangana et al., 2018; Khumalo et al., 2006). All the selected samples for this study were screened using bigger laboratory screens of about 45 cm in diameter. The stacked set of screens set up for automatic shaking is illustrated in Figure 40.



Screening equipment & procedure

Bulk Screening: granulated slag PSD

Screen diameter (45 cm)

Screen mesh sizes used (6700, 3350, 2360, 1700, 422, 212, 106 µm)

Screening time: 15 minutes

Test Screening: milled slag PSD

Screen diameter (20 mm)

Screen mesh sizes used (212, 180, 125, 90, 75, 63, 45 µm)

Screening time (15 minutes)

Figure 40: Screening process setup

The PSD curves of the feed slags along with their bulk densities are highlighted in Figure 41. It should be noted that the bulk density was measured using a plastic measuring cylinder by recording the weight and volume occupied by each slag sample. This was done just to get an indication of the density since the packing requirement was not taken into account.

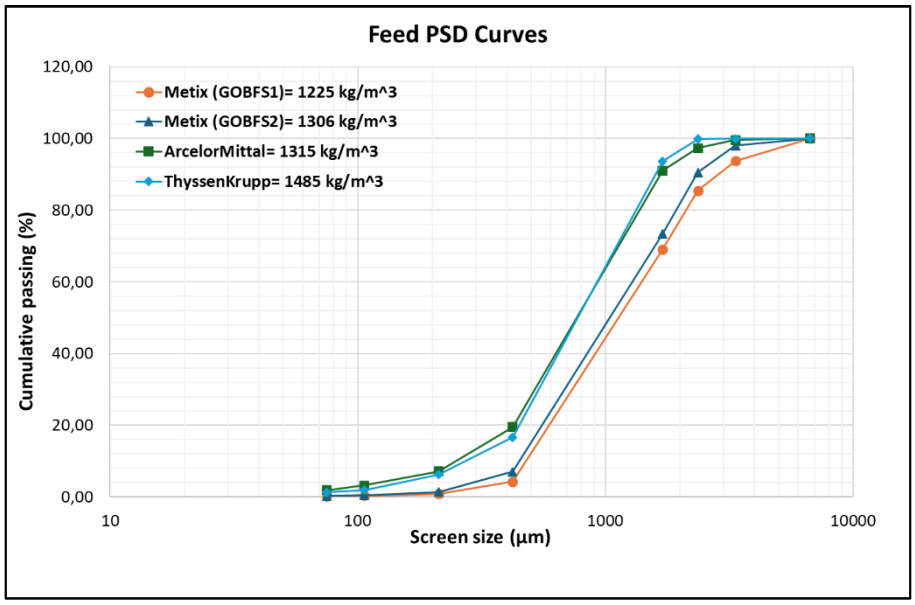


Figure 41: Slag Feed PSD curves with bulk density

3.2.2. Equipment

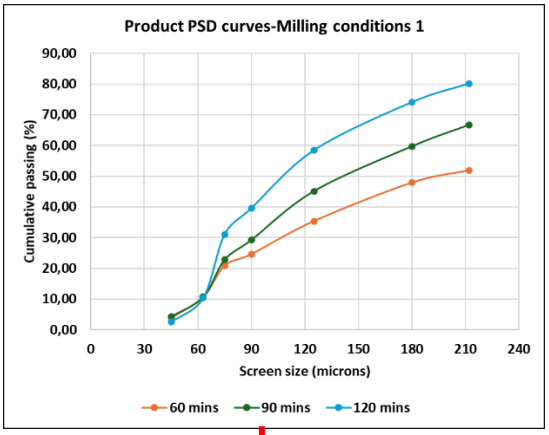
From the feed PSD and the target fineness of the product (100% passing 90 µm and 75% passing 45 µm), a ball mill was the best suited type of mill that can fulfil such a task on a laboratory scale from the equipment available at the Mineral Processing Laboratory (Wits). It should be noted that ball mills are used even on industrial scale for size reduction of cementitious materials together with vertical roller mills, with the latter described as more energy efficient (Tamashige et al., 1991). However, ball milling technology is still widely used by the cement industry owing to its simplicity of operations, and comparatively lower investment cost (Xu et al., 2015). In this study, an Eriez Macsalab roller-driven, single chamber ball mill was used as per Figure 42.



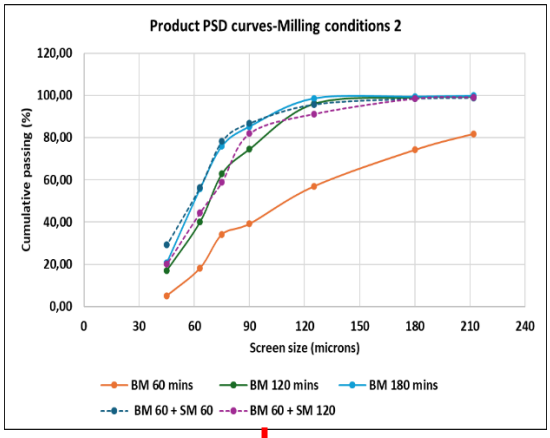
Figure 42: Milling equipment and ball load

3.2.3. Ball load distribution

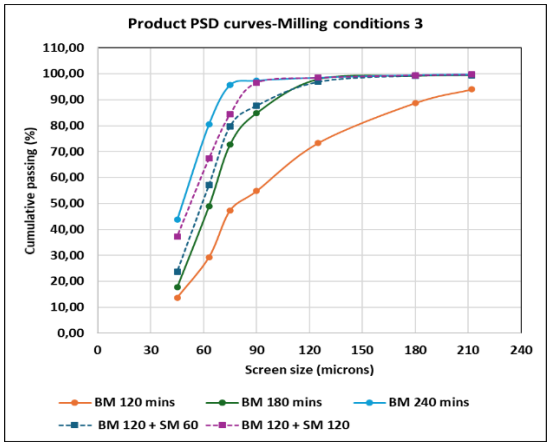
The composition of the mill grinding media is generally customized based on the hardness and PSD of the feed materials as well as the intended fineness of the milled products. The size of the spherical steel ball is commonly measured using the diameter. Steel balls with bigger diameters will ideally induce more impact on bigger particles, leading to the quick breakage of bigger particles but with less impact zone, especially for smaller particles, due to the higher proportion of voids that is created by bigger steel balls. Likewise, smaller diameter steel balls will break smaller particles and have more impact zone, however, they cannot break bigger particles due to their relatively lower weight (Kabezya and Motjotji, 2015). Hence, a balanced charge with a range of ball sizes is generally preferred during milling in order to reduce the size of both bigger and smaller particles simultaneously and efficiently. In this study, in order to obtain the optimal ball charge composition, the milling speed, and the slag load were kept constant while the ball load composition was changed as per Figure 43. It should be noted that to avoid wasting the limited quantity of on-spec GOBFS samples, the 45 off-spec GOBFS samples were used for all the milling optimization tasks since they are expected to have similar milling properties to the on-spec GOBFS.



Ball charge 1	30% fill		
Ball size (mm)	Weight (g)	%	No of balls
30	3 192	26,7	30
25	3 506	29,3	59
20	3 922	32,8	97
15	1 326	11,1	129
Total	11 946	100	315
Average weight (g/ball)			37,9



Ball charge 2	30% fill		
Ball size (mm)	Weight (g)	%	No of balls
40	216	1,8	1
30	4 626	37,7	43
25	3 506	28,6	59
20	3 922	32,0	97
Total	12 270	100	200
Average weight (g/ball)			61,4



Ball charge 3	50% fill		
Ball size (mm)	Weight (g)	%	No of balls
40	2 398	12,1	10
35	2 147	10,8	13
30	7 677	38,7	71
25	3 506	17,7	59
20	4 099	20,7	102
Total	19 827	100	255
Average weight (g/ball)			77,8

Figure 43: Ball charge changes during optimization

3.2.4. Mill setup and feed load adjustment

The milling setup was also changed as part of the optimization process, in the following steps:

i. Single mill operation: one bigger mill (BM) with a chamber volume of 10 litres (30 x 20 cm)
ii. Two mills operating in series: one BM followed by a smaller mill (SM) with a chamber volume of 5 litres (20 x 15 cm)
iii. Two mills operating in parallel: two BM (with optimized ball charge composition)

For the operation of two mills in series, the slag feed was first ground in the BM. After the required milling time, the milled slag was removed and transferred to the SM for the final grinding stage.

The BM could take a feed material load up to 2 kg maximum while the SM could take up to 1 kg maximum. The ball charge occupied 50% of the mill volume while the slag charge occupied 25% and the remaining 25% was left free to allow sufficient movement and interaction between the grinding media and the slag feed for effective grinding. It was observed that either increasing or decreasing the slag load from the 2 kg led to poor milling performance regardless of the milling time and speed. This is because any change in the feed charge weight directly affects the effective interaction between the milling media and feed material, ultimately affecting the milling performance. Furthermore, the decision to run BMs in parallel was taken in order to increase the throughput to 4 kg per run, and also because the BM and SM generated products with relatively similar PSDs. Moreover, having two milling units operating in parallel decreased the required milling time by 50% compared to either single mill operation (one BM), or two mills operating in series (one BM + one SM). The change in mill setup is depicted in Figure 44.

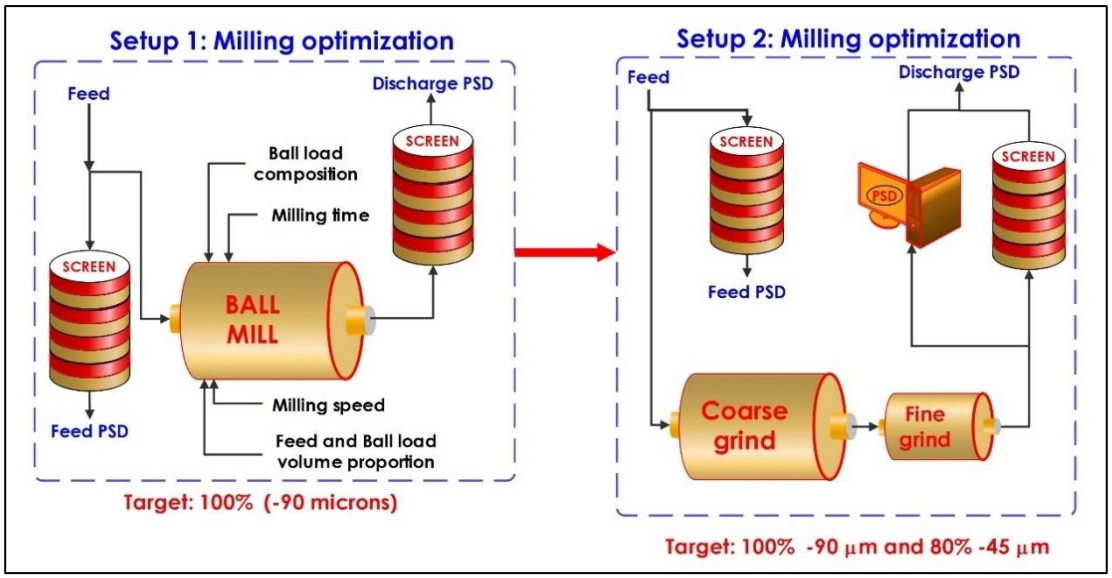


Figure 44: Change in mill setup during optimization

The final ball load composition along with the final mill setup are shown in Figure 45.

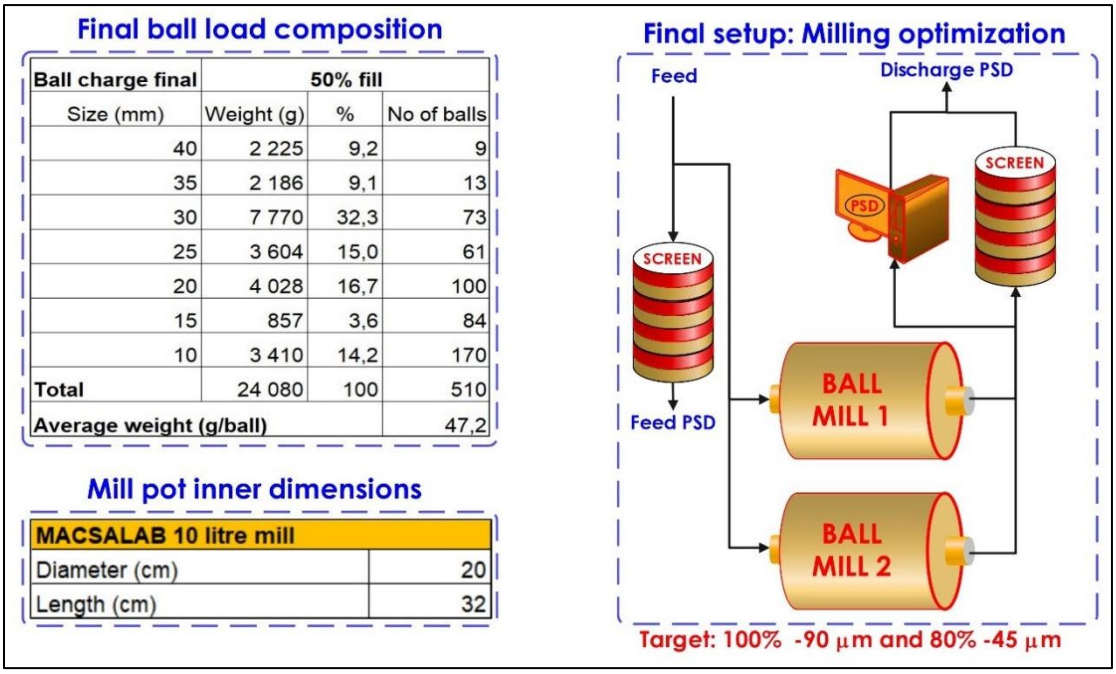


Figure 45: Final milling setup and ball charge composition

3.2.5. Optimal milling time and speed

After the milling setup, the ball charge composition, as well as the slag load weight were optimized. The effect of time and speed were also evaluated in order to improve the milling performance. The main observation as per Figure 46. was that the milling time could be decreased by increasing the milling speed. However, a further increment in the milling speed past an indicated optimum level is expected to limit the interaction between the slag particles and the grinding media thereby decreasing the milling performance.

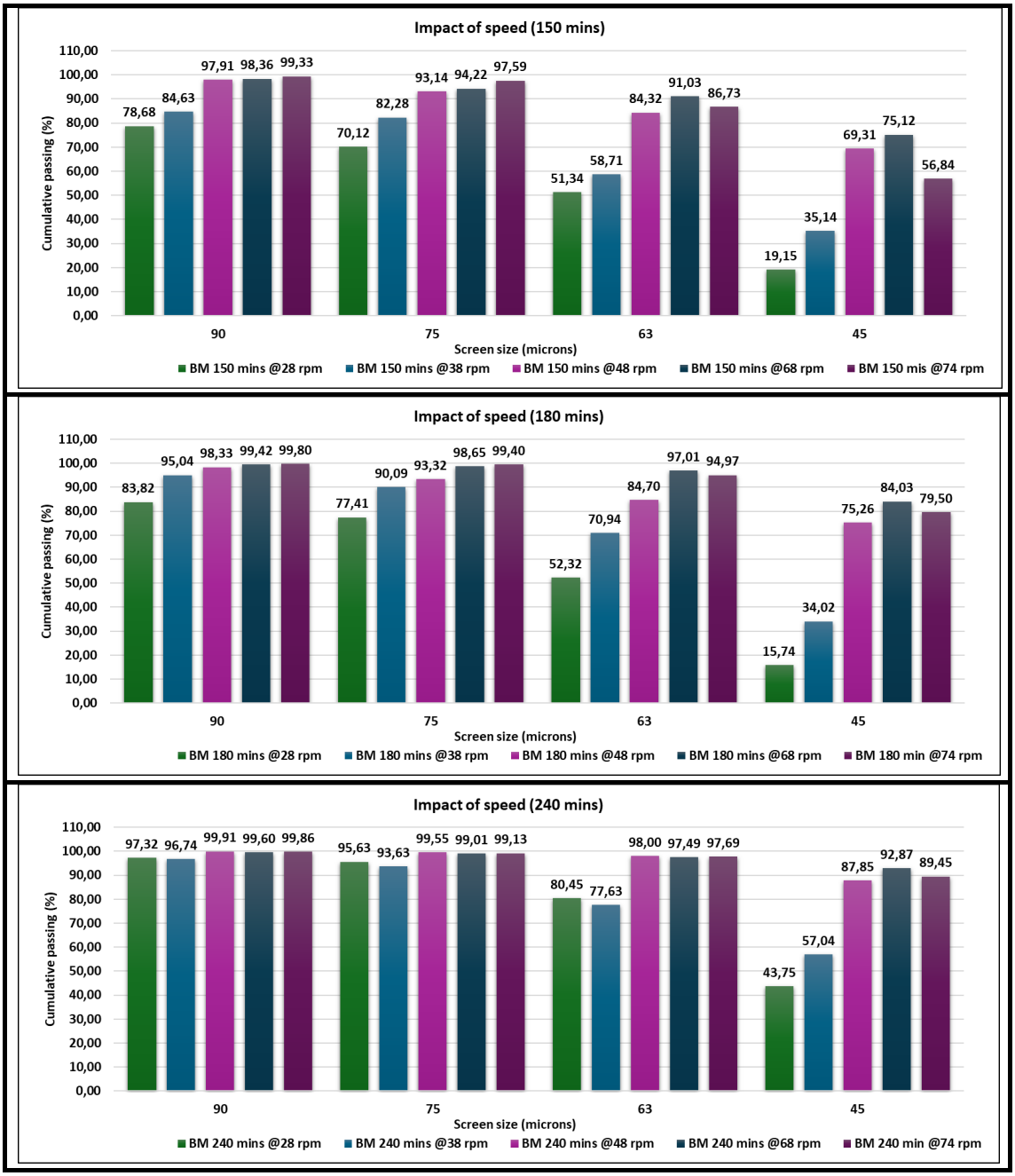


Figure 46: Effect of milling time and speed

The main goals of the milling tests were to reduce the milling time and increase the production capacity, while maintaining the required fineness. The setup of 2 BM in parallel alleviated the capacity problem. With the aim of minimizing the overall milling time for processing the granulated slag samples, 68 rpm was established as the optimal speed that can yield the target fineness of 99.9% passing 90 µm and 80% passing 45 µm in just 3h, as shown by the results in Figure 46. The milling time could, however, be extended to 3h30 in order to accommodate variability in the slag taps' properties. An increase in mill rotation speed had a significant impact on the finer particles, as indicated by the increase from 16% to 84% cumulative passing at 45 µm, for 180 mins milling time, following a speed change from 28 rpm to 68 rpm. The impact of speed on the milling performance has further been highlighted in Figure 47.

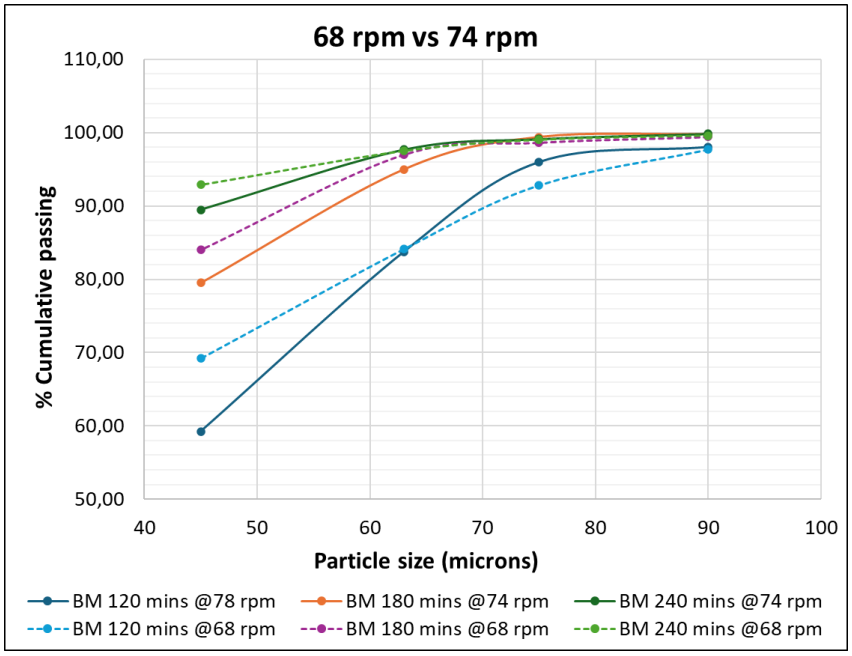


Figure 47: Close-up look on the impact of speed

As shown in Figure 47, the milling speed of 74 rpm displayed poor results compared to the 68 rpm speed. For instance, on the 45 µm screen, 84% passing was observed at 68 rpm as opposed to the 79% passing at 74 rpm. This may be due to less impactful attrition as the fast speed keeps the balls into suspension, thereby preventing gravity from having its full effect during attrition and abrasion as per the breakage mechanisms that occur during milling (Hogg, 1999; Parapari et al., 2020). The balls in these laboratory mills is in oscillation and rolling motions as compared to the rotational motion (lifting and cataracting) that is observed in industrial mills; hence, compression and impact breakage mechanisms are less dominant in these laboratory mills without internal lifter bars.

This effect is more noticeable, especially in the finer fractions demonstrating how the higher speed begins to slightly limit the interaction between the balls and the particles as they get finer in size. Moreover, the milling experimental results were further run using response surface methodology (RSM) tools in order to approximate predictions of optimal milling speed and time, and also to further confirm the impact of higher speed. The results obtained from RSM tools are summarized in Figure 48.

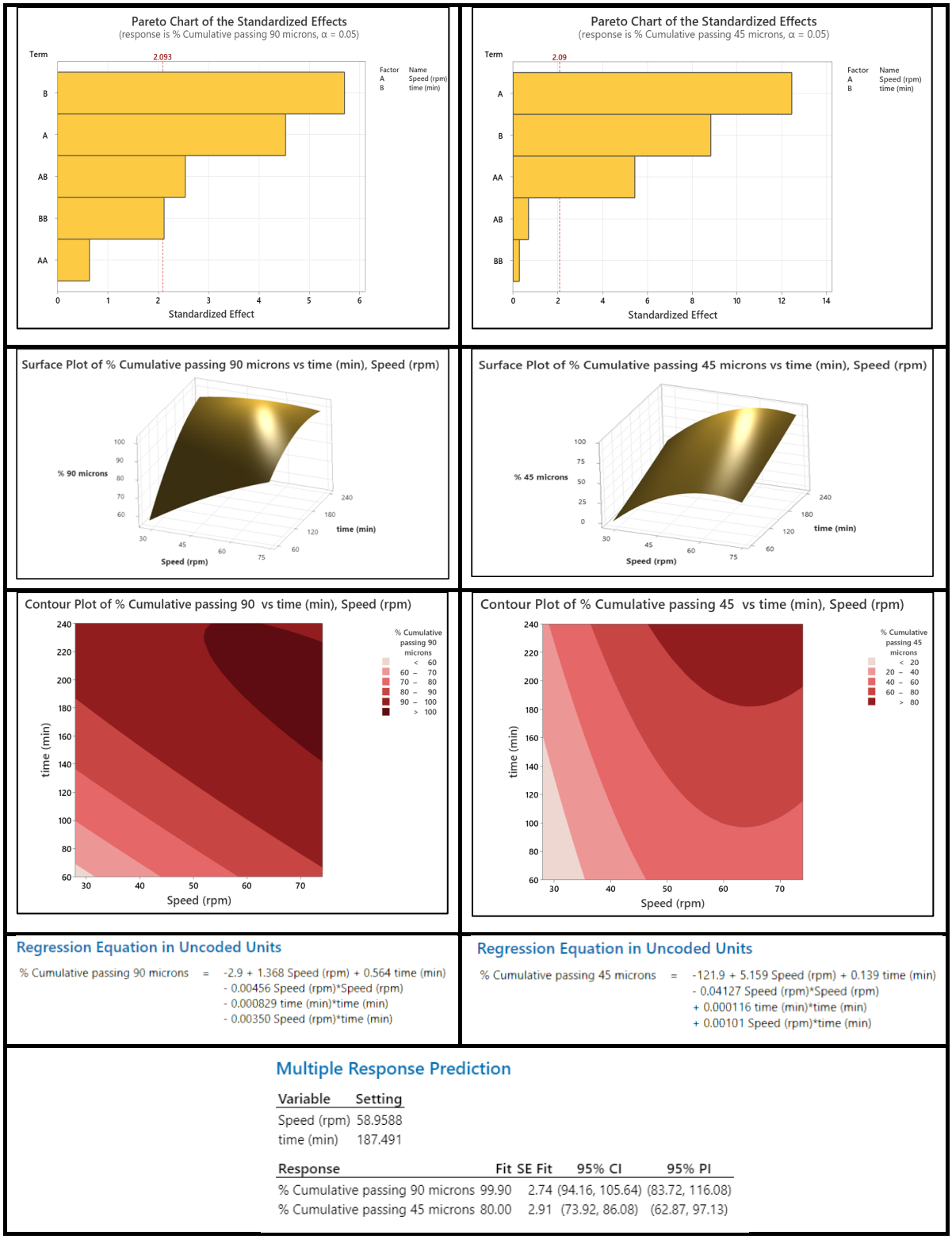


Figure 48: RSM optimization results

The pareto charts display the input factor that has the most impact on the given response (ref). As per Figure 48, for 90 µm, it is the time whereas for the ultrafine particles (45 µm), it is the speed. This implies that the 90 µm target can be reached simply by prolonging the milling time at the same speed, while to achieve the 45 µm target, the speed needs to be adjusted for a given duration. Therefore, the change in milling speed has more impact on the size reduction of

particles under 45 µm in size, whereas for particles under 90 µm, the milling time has the greatest influence.

The surface plots highlight the maximum values for the different responses, which can be seen in the lighter coloured zones. If the aim is to maximize the response value, these lighter coloured areas represent the optimal condition zones. As per Figure…. from both the -90 µm and -45 µm surface plots, the conditions for maximization are around 68-70 rpm and 180-240 minutes. However, in the same Figure 48, the contour plots highlight that any further increase in speed from 68 rpm will start deteriorating the milling performance, and this affirms what has been discussed in Figure 47.

As per the statistically predicted milling conditions in Figure 48, a milling time of 187 minutes at 58 rpm of milling speed is sufficient to achieve the target fineness, which are close to the manually suggested milling conditions of 3h30 at 68 rpm for the accommodation of variabilities among the different slag taps. Therefore, the selected conditions for milling experiments were 3h30 at 68 rpm.

This optimization process enabled the duration of this phase to be reduced from 16 working days to 8 working days, for milling 30 kg of on-spec GOBFS samples on a 4 kg per run basis. Moreover, it has provided insightful information regarding the milling of this novel slag on a laboratory scale. However, the expected milling behaviour would differ on an industrial scale since the milling mechanisms are different, depending on the type of mill used: ball mill or vertical roller mill. For a ball mill application, other applicable parameters such as the number of compartments, and the use of classifying liners, for example, become important (Muanpaopong et al., 2022).

It should be noted that the five slag samples from Metix (GOBFS1, GOBFS2, Tap85, Tap132, Tap144) along with the slag supplied by Thyssenkrupp Steel Europe (TkSE) were all milled at these selected optimal conditions in the Mineral Processing Laboratory at Wits University. On the other hand, the slag supplied by ArcelorMittal South Africa (AMSA) was milled using an industrial ball mill at Afrimat. Table 8 summarizes the different slag samples that will be used as supplementary cementitious materials (SCMs) in the following phase 3 of this chapter.

Table 8: Summary of milled granulated slag samples for phase 3

Slag sample type	Amount (kg)	Milling location
GOBFS1	10	Wits
GOBFS2	14	Wits
TkSE	10	Wits
AMSA	10	Afrimat
Tap 85	1	Wits
Tap 132	1	Wits
Tap 144	1	Wits

Two air cooled slag samples were also taken from one ladle (Tap 138), one sample, labelled AOBFS1 was taken from the top of the ladle, and the other labelled, AOBFS2 was taken from the bottom of the ladle. The air-cooled samples were taken in order to evaluate the efficiency of the granulation process and identify the possible crystalline phases that formed.

3.3. Phase 3: Cementitious properties assessment

This phase comprises all the tests that were conducted to evaluate the performance of the novel OBF slag as a supplementary cementitious material (SCM). Three types of specimens were cast in this slag cement testing campaign:

- Mortar cubes for compressive strength evaluation,
- Mortar prisms for drying shrinkage evaluation,
- Cement paste discs for thermogravimetric, morphology, and phase formation assessments at different aging intervals.

Three additional tests, namely R^3 reactivity test (Rapid, Reliable and Relevant test), workability (flow test), and setting time were also conducted to further evaluate the cementitious performance of the OBF slag and the industrial BF slags.

3.3.1. Additional materials

3.3.1.1. Portland cement

The reference Portland cement used in this study for the cementitious tests is the high early strength AfriSam 52.5R Rapid Hard Cement.

3.3.1.2. Standard sand

Unlike concrete tests that generally incorporate aggregates from different sources, mortar tests make use of only a standard sand that is manufactured in France. This makes the reproducibility of the results more precise on a global basis. The standard sand used in this study together with the reference cement are shown in Figure 49.



Figure 49: Sand used for mortar mixes

3.3.2. Slag-cement mix design

The cementitious performance was assessed by blending the two samples of the novel slag (GOBFS1 and GOBFS2) with Portland cement in various cement/slag proportions as per Table 9. The same blending ratios were used with the two industrial BF slags in order to observe performance of the novel slag in comparison to the conventional BF slags. The mixing proportions fall within CEM II, and CEM III/A international standards for blast furnace slag cement (SANS 50197-1:2013).

Table 9: Mixing proportion of cementitious materials

Mix label	Mix proportion	Abbreviation of mixing materials
M1	100 PC	AfriSam 52.5 R (Reference Cement) = **PC** Metix 1 – OBF Slag = **GOBFS1** Metix 2 – OBF Slag = **GOBFS2** Thyssenkrupp - BF Slag = **TKSE** ArcelorMittal – BF Slag = **AMSA**
M2	50/50 PC/GOBFS1	
M3	50/50 PC/GOBFS2	
M4	50/50 PC/TKSE	
M5	50/50 PC/AMSA	
M6	85/15 PC/GOBFS1	
M7	85/15 PC/GOBFS2	
M8	85/15 PC/TKSE	
M9	85/15 PC/AMSA	
M10	70/30 PC/GOBFS1	
M11	70/30 PC/GOBFS2	
M12	70/30 PC/TKSE	
M13	70/30 PC/AMSA	

3.3.3. Preliminary tests of cement and slags

3.3.3.1. Fineness (specific surface area)

The specific surface area, or fineness was measured using two methods:

- **Blaine fineness test:** It is the conventional measurement of fineness in the cement industry. It applies the air permeability method by passing a flow of air through a compacted bed of cement or another ground material. The equipment is usually calibrated using a material of known Blaine fineness, known as the NIST Standard Reference Material No. 114. Then, subsequent values are calculated based on the value of the calibrated materials (ASTM C204-23). The Blaine fineness tests of the reference cement and slags of this study were conducted and computed at Afrimat South Africa.
- **BET test:** The Brunauer, Emmett and Teller (BET) method involves the adsorption of Nitrogen gas on the surface of the solid. This technique calculates the amount of gas adsorbed, corresponding to a monomolecular layer on the surface. Unlike the Blaine fineness, it does not make assumptions about the shape of the particles. A procedure known as outgassing is essential prior to the BET test and the BET values reporting procedure is described in the study (Sing, 1985).

3.3.3.2. PSD measurement

The particle size distribution of all the cementitious materials were measured using a Malvern Panalytical Mastersizer 2000 particle size analyser.

3.3.3.3. Chemical and mineralogical characterization

The chemical compositions of the milled slag samples were analysed using inductively coupled plasma-optical emission spectroscopy (ICP-OES) while the total sulphur was determined using LECO combustion infrared analyser. The mineralogical characterizations were performed using X-ray diffraction (XRD). Furthermore, the morphology of the air-cooled and granulated OBF slags were determined using scanning electron microscopy-energy dispersive spectroscopy (SEM-EDS).

3.3.3.4. Glass count

The glass count was determined by microscopic analysis at AfriSam South Africa, a point counting method was used to approximated the proportion of glassy, or amorphous phases. This involves preparing a polished sample, observing it under a microscope with a refractive index liquid, and identifying and counting the glassy, crystalline, and opaque phases.

Blended slag-cement mortar tests

3.3.4. Workability (flow test)

3.3.4.1. Sample preparation

The workability tests were conducted according to ASTM/C1437−20 to determine the flow of the reference Portland cement and blended slag cement mortars. The flow test experiments of this study were carried out on a flow table complying with the ASTM C230M – 20 specifications. Firstly, the flow table and mould were thoroughly cleaned, wiped, and allowed to dry. Then, the flow mould with top and bottom diameters of 70mm and 100mm respectively)

was placed at the centre of the flow table (with a diameter of 255mm). Each mix for workability tests, was composed of 165 g cement/blended slag cement, 495 g standard sand, and 83 g water. In this way the ratio of 1 cement, 3 sands, and 0.5 water was maintained as per the mixing table in Figure 51. After the mortar sample was thoroughly mixed for 3 minutes, the first layer of mortar, of about 400 g, was placed in the mould and tamped 20 times to allow uniform filling. Thereafter, the mould was completely filled with the second layer of mortar and tamped again 20 times using a metallic tamper. Then, the mortar at the top of the mould was struck off to create a flat surface parallel to the top of the mould. Any water around the bottom edge of the mould was wiped off, and then the mould was lifted off 1 minute after completing the mixing. The flow table was promptly dropped 25 times in 15s. The flow table and mould along with the sample after dropping the table are shown in Figure 50.



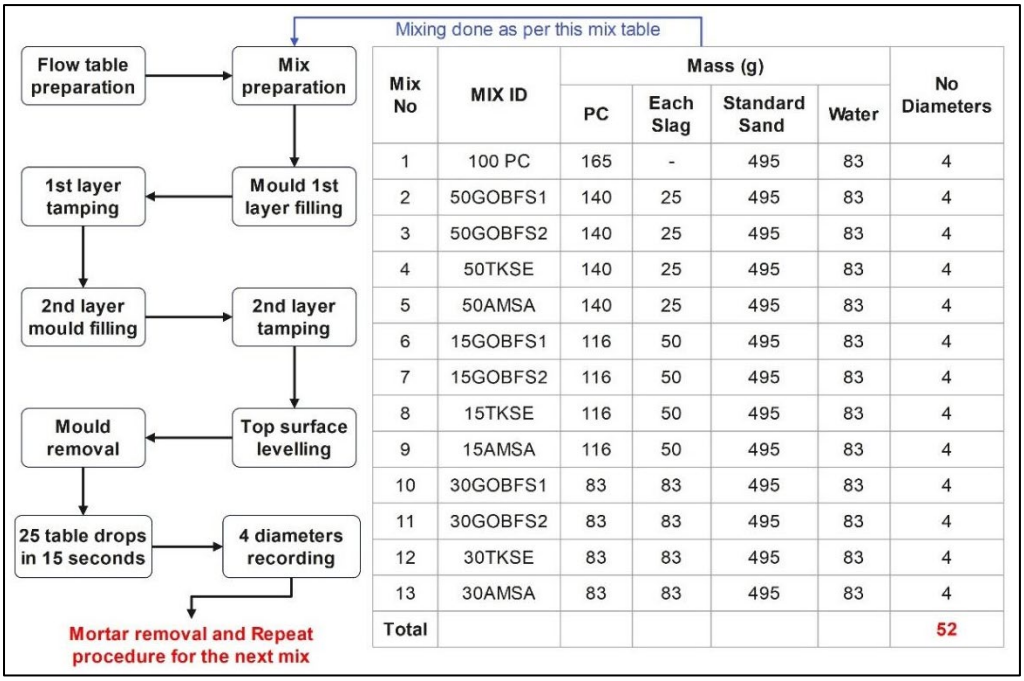
Figure 50: flow table with mould (left) and mortar sample after table dropping (right)

3.3.4.2.Measurement

After the flow table was dropped 25 times, 4 diameter readings were taken using the scribed lines on the flow table. Priorities were given to the longest observed diameters first. Then, the average of the measured diameter was calculated and the percentage difference between the measured average flow and the bottom diameter of the mould was also calculated as per the formula in Equation 4.

$$Workability\ (\%) = \frac{Measured\ average\ diameter - Bottom\ mould\ diameter}{Bottom\ mould\ diameter} * 100 \qquad (4)$$

The workability (flow measurement) test procedure along with the mixing table is summarized in Figure 51.



Mix No	MIX ID	Mass (g)				No Diameters
		PC	Each Slag	Standard Sand	Water	
1	100 PC	165	-	495	83	4
2	50GOBFS1	140	25	495	83	4
3	50GOBFS2	140	25	495	83	4
4	50TKSE	140	25	495	83	4
5	50AMSA	140	25	495	83	4
6	15GOBFS1	116	50	495	83	4
7	15GOBFS2	116	50	495	83	4
8	15TKSE	116	50	495	83	4
9	15AMSA	116	50	495	83	4
10	30GOBFS1	83	83	495	83	4
11	30GOBFS2	83	83	495	83	4
12	30TKSE	83	83	495	83	4
13	30AMSA	83	83	495	83	4
Total						52

Figure 51: workability test procedure along and mixing table

3.3.5. Compressive strength

3.3.5.1. Casting

The mix design was adopted according to SANS 55167-1:2011 and BS EN 196:2016 standards, and compressive strength tests were performed on mortar cubes of dimensions 50x50x50 mm cubes. The mortar mix was cast into cube moulds assembled on two steel frames, each holding a set of 16 moulds. After assembling the moulds, a single layer of motor oil was applied to the internal surfaces of each mould in order to lubricate and facilitate the demoulding of the mortar cube specimens.

The mixing was done manually in a mixing bowl, with each mix consisting of 1 part of cement (blended cement), 0.5 part of water, and 3 parts of standard sand. The total mix amount was calculated at 110% in order to accommodate some wastage. For blended cement (slag + cement), the slag and cement were weighed separately and then mixed for 5 minutes, then the standard sand was added to the batch and mixed again for 5 minutes until a homogeneous mixture was obtained. Lastly, water was added and the resulting mortar was mixed again for an additional 5 minutes. Thereafter, the mortar was transferred into the 32 prepared moulds on the two steel frames. The frames with the mould sets were then placed on a vibrating table and the mortar cube specimens were vibrated to remove the air bubbles and allow homogeneous filling. The vibration process was repeated until the moulds were fully filled with mortar and, and there were no signs of significant air bubbles formation. The mortar at the top of the mould was then struck off to create a flat surface parallel to the top of the mould.

The mould sets were then removed from the vibrating table and covered with a plastic sheet for 24 hours of initial curing at the controlled laboratory temperature (23 ± 2°C). This allows setting of the mortar cube specimens prior to demoulding. This procedure was repeated for all

13 mixes (M1 – M13), and a total of 412 mortar specimens were cast. The steel moulds along with a picture of specimens after 24 hours of hardening are shown in Figure 52.



Figure 52: Casting process of cube specimens

3.3.5.2.Curing and strength measurement

After the 24 hours of setting and hardening, the specimens were demoulded, labelled, and placed in a water curing tank held at 23 ±2 °C. Compressive strength tests were conducted at the following aging intervals: 2, 7, 28, 56, 84, 112, 140, and 168 days of curing. The compressive strength of 4 specimens was determined at each aging interval for every mix, and the average value was considered as the compressive strength for that age. The measurement was done as per ASTM C109-23 using stress testing, which is a destructive test that measures how strong a material is when compressed. The mortar cube specimens were placed under increasing compressive load until they broke, with the force (measured in kN) applied at a constant loading rate (40 kN/min). The compressive strength (expressed in MPa) was calculated using the mortar cube cross-section area. Figure 53 illustrates a mortar cube before and after completion of strength testing. The water curing tank, with mortar test cubes in the foreground, and the compressive strength testing equipment are shown in Figure 54.

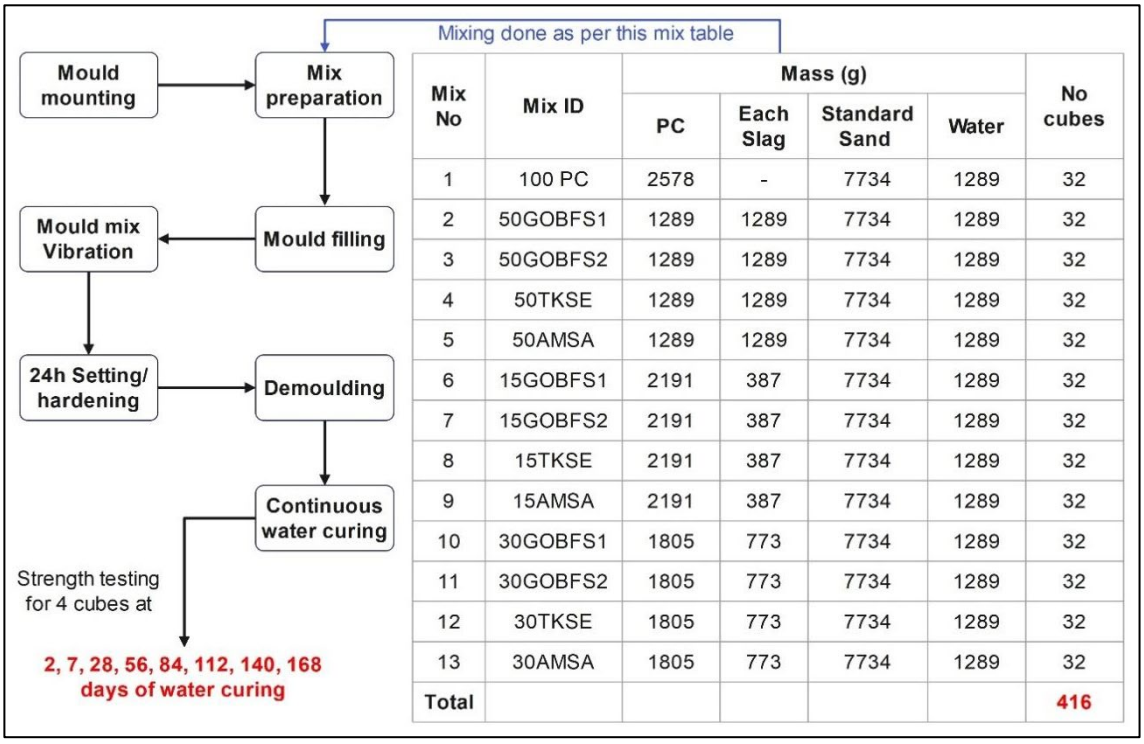


Figure 53: Images of cube specimen before and after strength testing



Figure 54: Water curing tank and compressive strength testing equipment

The cube casting procedure is also schematically represented Figure 55 together with the amount of each mixing material.



Mix No	Mix ID	Mass (g)				No cubes
		PC	Each Slag	Standard Sand	Water	
1	100 PC	2578	-	7734	1289	32
2	50GOBFS1	1289	1289	7734	1289	32
3	50GOBFS2	1289	1289	7734	1289	32
4	50TKSE	1289	1289	7734	1289	32
5	50AMSA	1289	1289	7734	1289	32
6	15GOBFS1	2191	387	7734	1289	32
7	15GOBFS2	2191	387	7734	1289	32
8	15TKSE	2191	387	7734	1289	32
9	15AMSA	2191	387	7734	1289	32
10	30GOBFS1	1805	773	7734	1289	32
11	30GOBFS2	1805	773	7734	1289	32
12	30TKSE	1805	773	7734	1289	32
13	30AMSA	1805	773	7734	1289	32
Total						416

Figure 55: Mortar cube mixes and casting process

3.3.6. Drying shrinkage

3.3.6.1. Casting

The casting of mortar prisms, and drying shrinkage determination were done as per ASTM/C596 – 23. Mortar prisms with dimensions 40x40x160mm were prepared for the drying shrinkage tests. The casting procedure of the prisms was identical to the procedure used for mortar cubes, from mixture preparation to vibration of specimens. However, after vibrating the mortar prisms for compaction, the specimens were covered with a plastic sheet for an extended time of 48h to allow for sufficient hardening and to facilitate the handling after demoulding. The prisms casting moulds were mounted on two steel plates, each comprising 8 moulds. A total of 39 mortar prisms were cast, with 3 specimens produced per mix, for all 13 mixes. An illustration of the casting moulds together with some demoulded prism specimens is shown in Figure 56.



Figure 56: Casting moulds and prism specimens

3.3.6.2.Curing and drying shrinkage measurement

After demoulding, the prisms specimens were marked and then placed directly in the water curing tank held at 23 ±2 °C. After a 24-hours curing period, the specimens were removed from the curing tank and wiped off to remove moisture. Thereafter, 4 steel targets were attached on both sides of each prism specimen, with 2 targets on opposite faces (bigger area sides). The attachment of the steel targets was done using a specialized glue, and all the targets were separated by a distance of 100 mm. The specimens with attached targets were stored on specimen holders in a curing room with a controlled room temperature of 23 ±2 °C. The first measurement of shrinkage was taken right after the targets were fully glued to the specimens. Two measurements were taken per prism, with 6 measurements per mix. For 13 mixes, a total of 78 measurements were taken at each measurement time. Measurements were completed at the following aging intervals in the curing room: 0, 1, 2, 3, 4, 5, 6, 13, 20, 27, and 55 days.

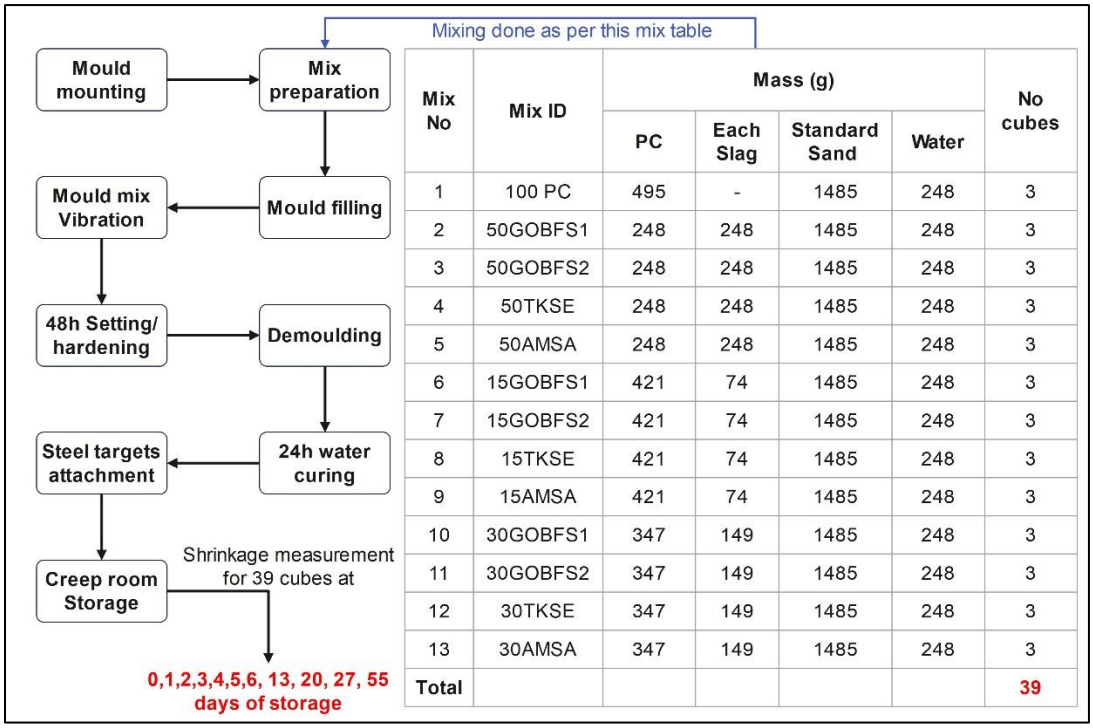
A DEMEC mechanical strain gauge was used for the drying shrinkage measurements. It was developed as a reliable and accurate way of taking strain measurements at different points on a structure using a single instrument (Mayes Group, UK). In this study, the gauge length was 100 mm, and 1 division on the dial gauge corresponded to 16 micro-strains. Moreover, the reference reading was 943 divisions, and this value remained constant throughout the entire test procedure, demonstrating the accuracy of the measurements taken.

An illustration of the Mayes drying shrinkage measurement equipment together with the prism specimens in the curing room is shown in Figure 57.



Figure 57: Mayes DEMEC measuring instrument set and prism specimens in the curing room

A block flow diagram of the casting and curing of prism specimens together with the mixing table is shown in Figure 58.



Mix No	Mix ID	Mass (g)				No cubes
		PC	Each Slag	Standard Sand	Water	
1	100 PC	495	-	1485	248	3
2	50GOBFS1	248	248	1485	248	3
3	50GOBFS2	248	248	1485	248	3
4	50TKSE	248	248	1485	248	3
5	50AMSA	248	248	1485	248	3
6	15GOBFS1	421	74	1485	248	3
7	15GOBFS2	421	74	1485	248	3
8	15TKSE	421	74	1485	248	3
9	15AMSA	421	74	1485	248	3
10	30GOBFS1	347	149	1485	248	3
11	30GOBFS2	347	149	1485	248	3
12	30TKSE	347	149	1485	248	3
13	30AMSA	347	149	1485	248	3
Total						39

Figure 58: Mortar Prism mixes and casting procedure

Blended slag-cement paste tests

3.3.7. Evaluation of phases evolution in slag-cement pastes

3.3.7.1. Casting

The cement paste specimens were cast into small plastic containers as per Figure 59. with the intention to produce a small disc specimen for every mix. The mixing was done using a water to cement, or blended cement, ratio of 0.5. The slags and cement were mixed in accordance with the composition of the 13 mixes of this study. Water was added to each mix and the mixed paste was then used to fill the small plastic containers for hardening. Each batch of containers with cement paste was covered with a plastic sheet for a 24-hours hardening and setting period. A total of 208 discs were cast for the 13 mixes (16 discs per mix) as shown in Figure 59.

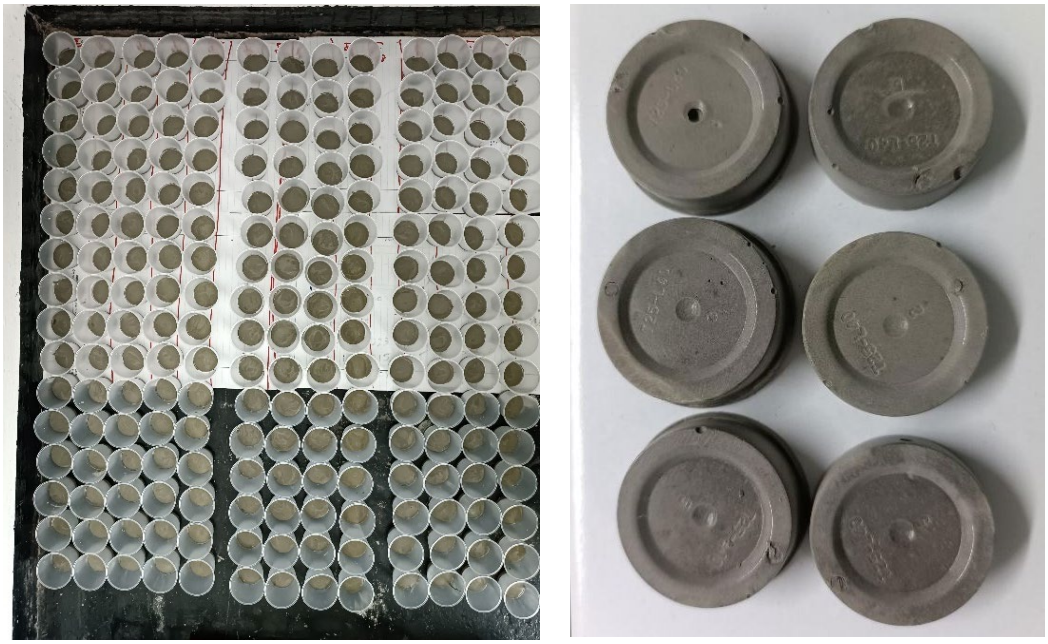


Figure 59: Cast disc specimens and de-moulded discs

3.3.7.2.Curing

After 24 hours of setting, the discs were removed from the moulds and placed in lime saturated solution (2 g of lime per litre of water) chambers held at 23 ±2 °C for curing as per the test procedure. A total of 13 chambers was used – one for each mix – with 16 discs in each chamber, as shown in Figure 60.

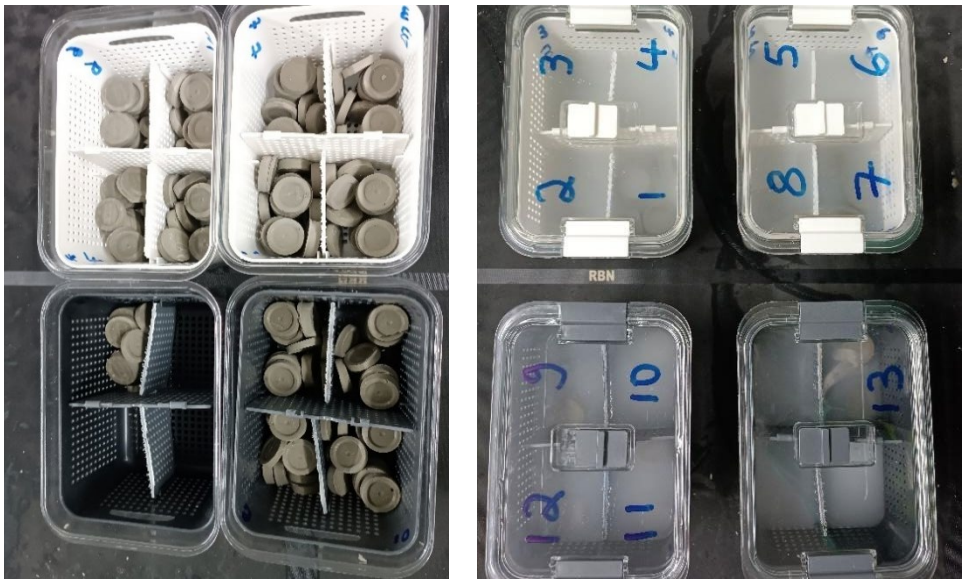


Figure 60: Curing process of disc specimens

3.3.7.3.Hydration arrest

In order to make a comparative assessment of hydration progress, the hydration process in the cement paste discs was stopped after several different curing ages: this was done using the alcohol method. In this method, 2 disc-specimens from each mix were removed from the curing chambers at the following aging intervals: 2, 7, 28, 56, 84, 112, 140, and 168 days. The disc-

specimens were broken into smaller pieces using a mortar and pestle, and then put into the same casting plastic containers. Isopropanol (Isopropyl alcohol, C_3H_7OH) was then added to remove the remaining water from the specimens. Isopropanol and water are both polar molecules. Isopropanol is hygroscopic: can absorb moisture to reach an equilibrium of 65% isopropanol and 35% water. Hence, Isopropanol was added to the broken discs in the plastic containers and removed quite a few times in order to completely absorb the moisture as shown in Figure 61. In the research (Snellings et al., 2018), it was highlighted that among the four methods that were tested, solvent exchange by isopropyl alcohol gave the best results in terms of preservation as previously discussed in Chapter 2. In this study, the plastic containers were closed with a lid to prevent the evaporation of isopropanol, with isopropanol added and replaced in the following sequence:

i. Isopropanol was added and allowed to react for 24 hours
ii. The used isopropanol solution was removed, replaced with fresh isopropanol and allowed to react for a further 24 hours
iii. Repeat of step ii: isopropanol removed and replaced; reaction proceeded for 24 hours
iv. Second repeat of step ii: isopropanol removed and replaced; reaction proceeded for 24 hours
v. A further 72 hours was allowed to ensure complete removal of water to end the hydration process
vi. The used isopropanol solution was finally removed, after which the broken disc pieces (in containers) were placed in an oven set at 49 ±1°C for a 72-hour drying period



Figure 61: Hydration arrest process: broken disc pieces in containers (left) and containers covered after the addition of isopropanol (right)

3.3.7.4.Measurement of hydration phases evolution

After stoppage of the hydration process and drying of the broken disc specimens, 2 broken pieces were removed from each paste mix sample for Scanning Electron Microscopy (SEM) analysis to examine the surface morphology and to determine the extent of hydration products formation at the different curing ages. The remaining broken disc pieces were pulverised and taken for X-ray diffraction (XRD) analysis as per Figure 62. Prior SEM and XRD analyses the samples were placed and stored in a desiccator to prevent carbonation as shown in Figure 63.



Figure 62: Drying and pulverising of broken disc specimens

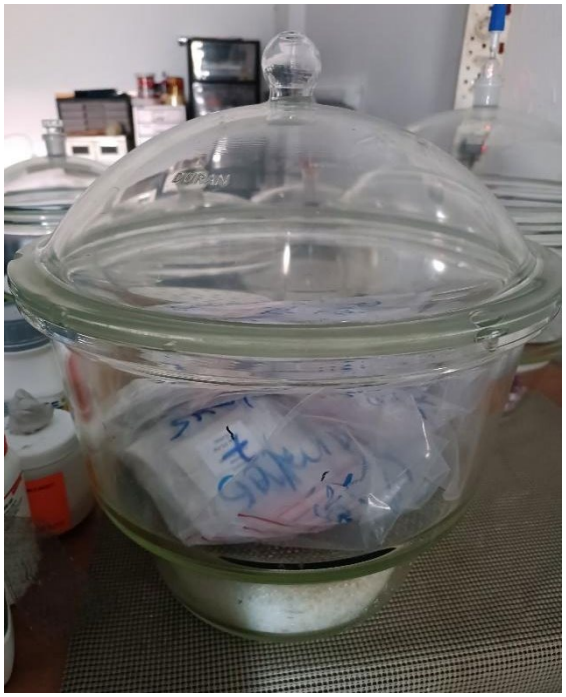


Figure 63: Samples stored in a desiccator before SEM and XRD analyses

3.3.8. R^3 Reactivity

3.3.8.1. Computer and sample preparation

The R^3 reactivity test (Rapid, Reliable and Relevant test) is used for determining the chemical reactivity of supplementary cementitious materials (SCM's). This test does not distinguish between hydraulic and pozzolanic reactivity, it provides information of the combined reactivity (Londoño-Zuluaga et al., 2022; Avet et al., 2016). In this study, reactivity tests were conducted as per ASTM/C1897 – 20 to assess the chemical reactivity (hydraulic and pozzolanic) of the novel OBF slag in comparison to the conventional BF slags by measuring the heat released over a hydration period of 7 days. A Calmetrix I-Cal 4000H 4-chamber isothermal Calorimeter, connected to a digital computer, was used to perform the tests, as illustrated in Figure 64.

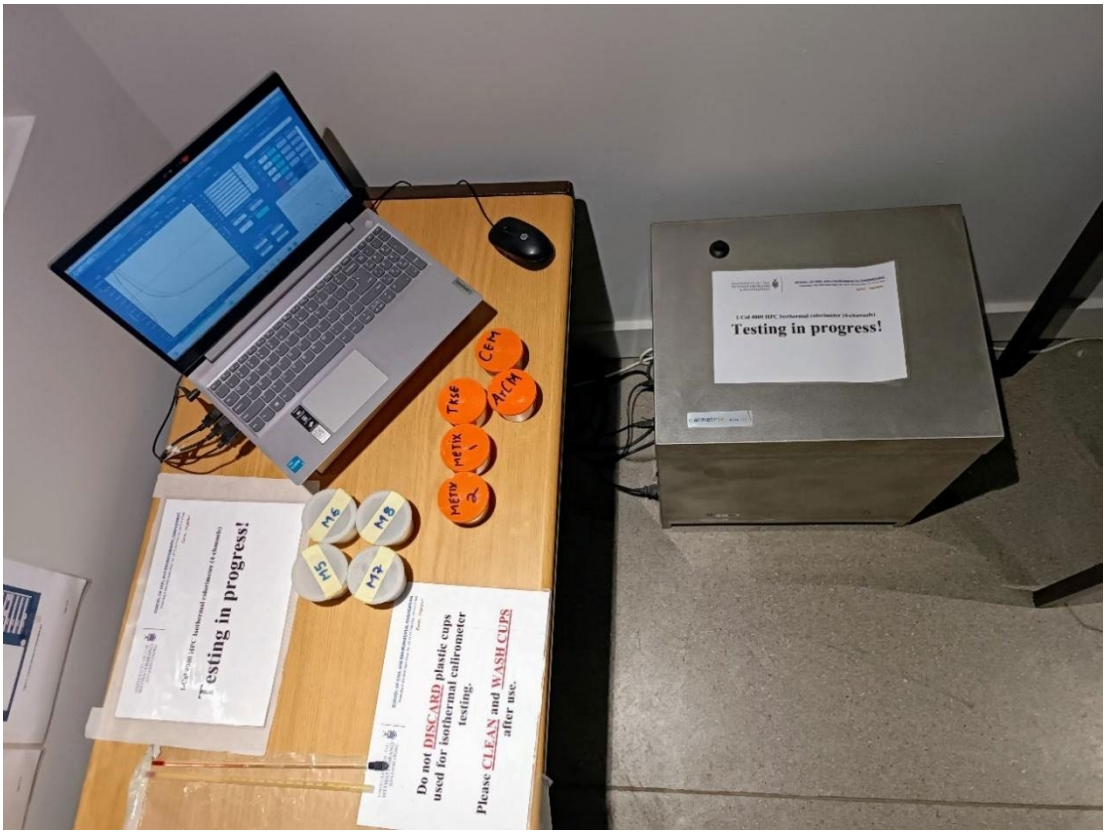


Figure 64: Calorimeter Equipment setup for R3 reactivity test

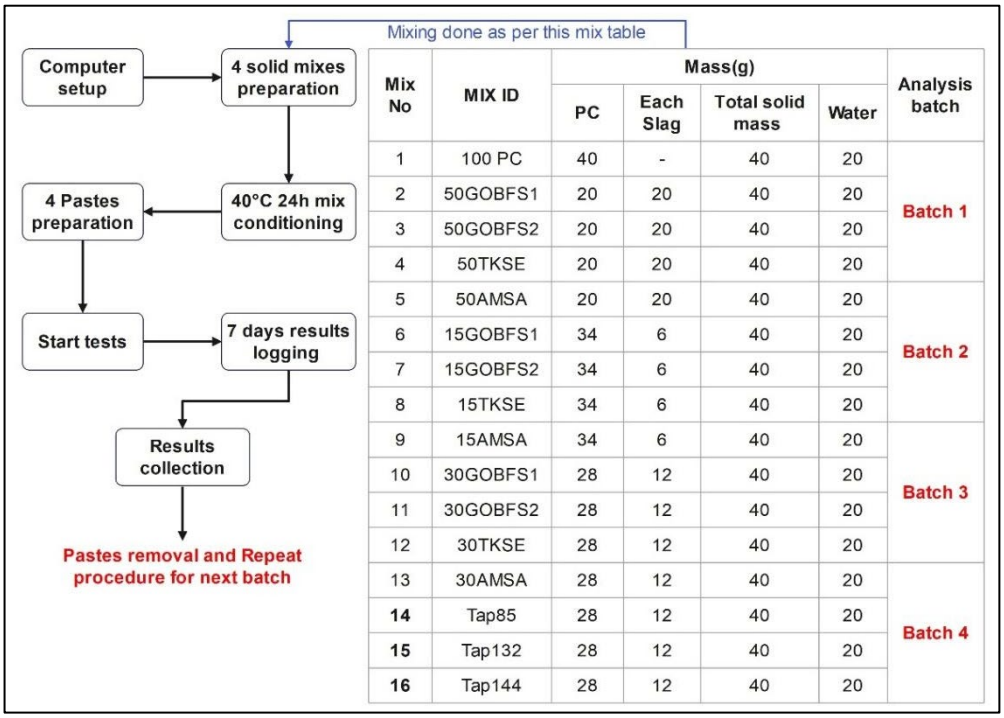
The hydration tests were conducted under isothermal conditions, at 40 ±0.5ºC, in order to accelerate the rate of reaction of otherwise slowly reactive slags. The preparation for the R^3 test required the following steps:

i. The computer was set up for testing at 40°C by selecting the calibration file for this temperature.
ii. The required calorimeter environment temperature was set to 40°C.
iii. Four identical sample holders, suitable for fitting the calorimeter chambers, were selected for the simultaneous testing of four cement paste mixes.

For the hydration test mixes, the cementitious binder mass was 40 g at an effective water to binder ratio of 0.5, giving a water mass of 20 g. The cementitious binder was prepared as per the mixing table in Figure 65. In the first 4 mixes, the control mix (M1) was prepared using 100% cement, hence 40 g of reference cement was used, and no slag was added to the mix. Then for M2, M3, and M4, 20 g of the reference cement was weighed and mixed with 20 g of GOBFS 1, GOBFS2, and TKSE, respectively. The mixing was done thoroughly until a homogeneous colour was obtained. Then the four samples were placed in the calorimeter and held at 40 ºC for 24 hours in order to condition the temperature of the mixes along with the mix holders to 40 ºC. After the 24-hour conditioning time, 20 g of water, prepared at 40 ºC, was added to each conditioned sample. A thermometer was used to make sure the water was at 40 ±2 ºC before mixing. The mixing was done continuously for 2 minutes and the 4 samples were swiftly placed back in the calorimeter chambers.

3.3.8.2. Measurement

After the mix of water and binder were placed back in the calorimeter, each calorimeter chamber was relabelled in the computer using the mix IDs. The type and the amount of reference cement and slag were entered for each mix ID. The logging of results was done automatically on the computer. The time of contact between water and the binder in each mix, was set as the start time for that mix ID. The results were set to be recorded after every 15 seconds for the first 45 minutes, and thereafter they were recorded after every minute for the overall test duration of 7 days, or 168 hours. On conclusion of the 7-day hydration time, the cumulative heat release, along with the heat release per unit time, by each mix was recorded and plotted. This procedure was repeated for the remaining mixes until all the heat release data by each mix was recorded and plotted. The R^3 reactivity test procedure, along with the mixing table, are also summarized in Figure 65.



Mix No	MIX ID	Mass(g)				Analysis batch
		PC	Each Slag	Total solid mass	Water	
1	100 PC	40	-	40	20	Batch 1
2	50GOBFS1	20	20	40	20	
3	50GOBFS2	20	20	40	20	
4	50TKSE	20	20	40	20	
5	50AMSA	20	20	40	20	Batch 2
6	15GOBFS1	34	6	40	20	
7	15GOBFS2	34	6	40	20	
8	15TKSE	34	6	40	20	
9	15AMSA	34	6	40	20	Batch 3
10	30GOBFS1	28	12	40	20	
11	30GOBFS2	28	12	40	20	
12	30TKSE	28	12	40	20	
13	30AMSA	28	12	40	20	Batch 4
14	Tap85	28	12	40	20	
15	Tap132	28	12	40	20	
16	Tap144	28	12	40	20	

Figure 65: Reactivity tests procedure and test mix composition table

References

ASTM C109/C109M – 23. Standard Test Method for Compressive Strength of Hydraulic Cement Mortars (Using 50 mm [2 in.] Cube Specimens). DOI: 10.1520/C0109_C0109M-23.

ASTM C204-23, "Standard Test Method for Fineness of Hydraulic Cement by Air Permeability Apparatus," West Conshohocken, PA: ASTM International. DOI: 10.1520/C0204-23.

ASTM/C1437 – 20. Standard Test Method for Flow of Hydraulic Cement Mortar. DOI:10.1520/C1437–20.

ASTM/C1897 – 20. Standard Test Methods for Measuring the Reactivity of Supplementary Cementitious Materials by Isothermal Calorimetry and Bound Water Measurements. DOI:10.1520/C1897-20.

ASTM/C191 – 21. Standard Test Methods for Time of Setting of Hydraulic Cement by Vicat Needle. DOI:10.1520/C0191-21.

ASTM/C230M – 20. Standard Specification for Flow Table for Use in Tests of Hydraulic Cement. DOI:10.1520/ C230M – 20.

ASTM/C596 – 23. Standard Test Method for Drying Shrinkage of Mortar Containing Hydraulic Cement, ASTM International, West Conshohocken, PA, USA. DOI:10.1520/C0596-23.

Avet, F., Snellings, R., Alujas Diaz, A., Ben Haha, M. and Scrivener, K. (2016). Development of a new rapid, relevant and reliable (R3) test method to evaluate the pozzolanic reactivity of calcined kaolinitic clays. *Cement and Concrete Research*, 85, pp.1–11. doi:https://doi.org/10.1016/j.cemconres.2016.02.015.

BS EN 196-1:2016. European Standard, Methods of testing cement Determination of strength.

BS EN 196-6:2018. Methods of testing cement Determination of fineness. European Committee for Standardization. British Standards Institution, London.

DEMEC mechanical strain gauge, Mayes Group, Windsor, UK. Available at http://www.mayes.co.uk/6.html.

EN 15167-1:2006. Ground granulated blast furnace slag for use in concrete, mortar and grout - Part 1: Definitions, specifications and conformity criteria.

He, T., Xu, Z., Li, Z., Zhao, X., Zhao, S. and Liu, Y. (2022). Study on the relationship between the particle size distribution characteristics of ground granulated blast furnace slag and its mortar properties. *Frontiers in Materials*, 9. doi: https://doi.org/10.3389/fmats.2022.962279.

Hlabangana, N., Danha, G. and Muzenda, E. (2018). Effect of ball and feed particle size distribution on the milling efficiency of a ball mill: An attainable region approach. *South African Journal of Chemical Engineering*, 25, pp.79–84. doi: https://doi.org/10.1016/j.sajce.2018.02.001.

Hogg, R. (1999). Breakage mechanisms and mill performance in ultrafine grinding. *Powder Technology*, 105(1-3), pp.135–140. doi:https://doi.org/10.1016/s0032-5910(99)00128-x.

Kabezya, K.M. and Motjotji, H. (2015). The Effect of Ball Size Diameter on Milling Performance. *Journal of Material Science & Engineering*, 04(01). doi: https://doi.org/10.4172/2169-0022.1000149.

Khumalo, N., Glasser, D., Hildebrandt, D., Hausberger, B. and Kauchali, S. (2006). The application of the attainable region analysis to comminution. *Chemical Engineering Science*, 61(18), pp.5969–5980. doi: https://doi.org/10.1016/j.ces.2006.05.012.

Londoño-Zuluaga, D., Gholizadeh-Vayghan, A., Winnefeld, F., Avet, F., Haha, M.B., Bernal, S.A., Çizer, Ö., Cyr, M., Dolenec, M., Durdzinski, P., Haufe, J., Hooton, D., Kamali-Bernard, S., Li, X., Marsh, A., Marroccoli, M., Mrak, M., Muy, Y., Patapy, C. and Pedersen, M.K. (2022). Report of RILEM TC 267-TRM phase 3: vaIidation of the R3 reactivity test across a wide range of materials. *Materials and Structures,* 55(5). doi:https://doi.org/10.1617/s11527-022-01947-3.

Muanpaopong, N., Davé, R. and Bilgili, E. (2022). Impact of ball size distribution, compartment configuration, and classifying liner on cement particle size in a continuous ball mill. *Minerals Engineering*, 189, p.107912. doi: https://doi.org/10.1016/j.mineng.2022.107912.

Pal, S.C., Mukherjee, A. and Pathak, S.R. (2003). Investigation of hydraulic activity of ground granulated blast furnace slag in concrete. *Cement and Concrete Research*, 33(9), pp.1481–1486. doi: https://doi.org/10.1016/s0008-8846(03)00062-0.

Parapari, P.S., Parian, M. and Rosenkranz, J. (2020). Breakage process of mineral processing comminution machines – An approach to liberation. *Advanced Powder Technology*, 31(9), pp.3669–3685. doi: https://doi.org/10.1016/j.apt.2020.08.005.

SANS 50197-1:2013. South African National Standard for Cement Part 1: Composition, Specifications and Conformity Criteria for Common Cements, South African Bureau of Standards, Pretoria, South Africa

SANS 55167-1:2011. Ground granulated blast furnace slag for use in concrete, mortar and grout Part 1: Definitions, specifications and conformity criteria. South African Bureau of Standards, Pretoria, South Africa

Sarkar, S., Bhattacharya, R., Roy, G.G. and Sen, P.K. (2017). Modeling MIDREX Based Process Configurations for Energy and Emission Analysis. *steel research internatio*nal, 89(2), p.1700248. doi: https://doi.org/10.1002/srin.201700248.

Sing, K.S.W. (1985). Reporting physisorption data for gas/solid systems with special reference to the determination of surface area and porosity (Recommendations 1984). *Pure and Applied Chemistry*, [online] 57(4), pp.603–619. doi:https://doi.org/10.1351/pac198557040603.

Snellings, R., Chwast, J., Cizer, Ö., De Belie, N., Dhandapani, Y., Durdzinski, P., Elsen, J., Haufe, J., Hooton, D., Patapy, C., Santhanam, M., Scrivener, K., Snoeck, D., Steger, L.,

Tongbo, S., Vollpracht, A., Winnefeld, F. and Lothenbach, B. (2018). RILEM TC-238 SCM recommendation on hydration stoppage by solvent exchange for the study of hydrate assemblages. *Materials and Structures*, 51(6). doi:https://doi.org/10.1617/s11527-018-1298-5.

Tamashige, T., Obana, H. and Hamaguchi, M. (1991). Operational results of OK series roller mill. *IEEE Transactions on Industry Applications*, 27(3), pp.416–424. doi: https://doi.org/10.1109/28.81821.

Tripathy, S.K., Dasu, J., Murthy, Y.R., Kapure, G., Pal, A.R. and Filippov, L.O. (2020). Utilisation perspective on water quenched and air-cooled blast furnace slags. *Journal of Cleaner Production*, 262, p.121354. doi: https://doi.org/10.1016/j.jclepro.2020.121354.

Xu, D., Cui, Y., Li, H., Yang, K., Xu, W. and Chen, Y. (2015). On the future of Chinese cement industry. *Cement and Concrete Research*, 78, pp.2–13. doi: https://doi.org/10.1016/j.cemconres.2015.06.012.

CHAPTER 4: BLENDED SLAG-CEMENT CHARACTERIZATIONS

4.1. Introduction

This chapter provides a critical discussion of the characterization results of the novel OBF slag in comparison to the conventional BF slags. The following features of the slag and their effects on slag performance are discussed:

- Chemical composition
- Fineness
- Glass content

In combination, these parameters induce unique cementitious behaviour to the slag particles and can serve as predictive measures of the slag's performance when blended with Portland cement. An illustration of the combined effect of these parameters is shown in Figure 66. It should be noted that the mixing of the cement and slag is discussed in Chapter 5 for mortar mixes, and in chapter 6 for paste mixes.

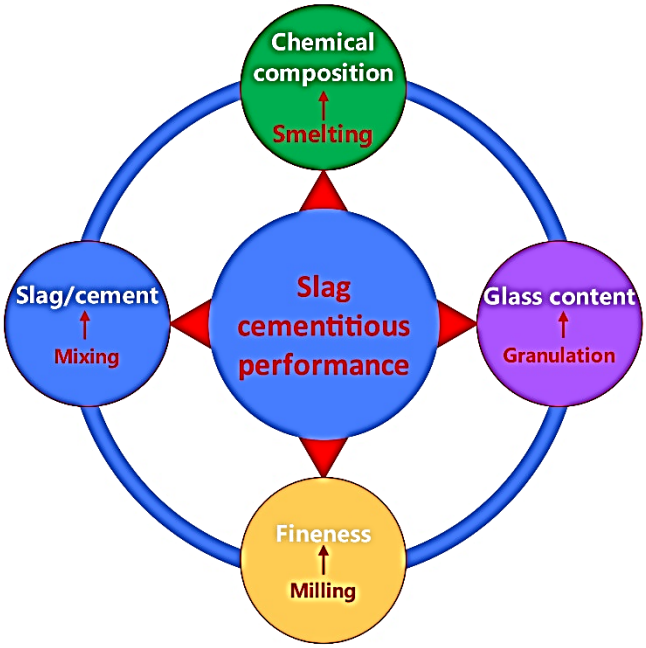


Figure 66: Features responsible for slag's cementitious behaviour

4.2. Colour and macroanalysis

Different colours of the granulated OBF slag (GOBFS) were obtained during the smelting campaign due to the slight changes in chemical composition of some slag taps. The colour observed in most slag taps is a blend of dark and white-grey hues with glassy grains as seen in Tap 64 in Figure 67. However, there was a variation of colours, sometimes to a darker colour, or to a brownish colour for a number of slag taps. Tap 124 and Tap 132 are good illustrations of this colour variation. The change in the colour of the OBF slag might be attributed to the change in chemical composition of the batch mix for each furnace tap as well as the final slag composition of each tap during the smelting campaign. Based on chemical composition of

major slag components in Figure 67, the change in colour seems to be directly proportional to a decrease in CaO content and an increase in the MgO, Al_2O_3 and SiO_2 contents of the slag. This can be seen by the 48,1 % CaO in Tap 124 that led to a brownish colour of GOBFS compared to the 39,2% CaO in Tap 132 that led to a darker colour of GOBFS.



	Tap 124	Tap 64	Tap 132
MgO %	7,22	8,15	9,66
Al_2O_3 %	9,65	11,40	10,00
SiO_2 %	33,5	35,1	35,3
CaO %	48,1	42,0	39,2
TiO_2 %	1,10	0,84	1,80
S %	0,22	0,25	0,20

Figure 67: Colour of novel granulated OBF slag

It should be noted that the top and bottom images of each Tap represent the normal and milled slag samples, respectively. The general colour of the glassy grains from the conventional granulated BF slag (GBFS) is a light brownish colour, a bit similar to brown sugar, as shown in Figure 69a. Arguments can be made about the TiO2 content affecting the colour, however, the trends are still not making sense since the other components are also changing for the three samples. Hence, further experimental work is need to fully evaluate the true cause of colour differences between the granulated BF slag and OBF slag. Furthermore, another potential factor that can assist with understanding the colour differences might be the degree of greening effect of slag-cement mixes (Couvidat et al., 2021; Le Cornec et al., 2017; Chaouche et al., 2017). The greening effect is a commonly observed temporary discolouration of the BF slag-cement mix when the surface is exposed to air after hydration, linked to its sulphur content. This concept is shown in Figure 68 for broken disc specimens and will be discussed in chapter 5. Nonetheless, both the GOBFS and the GBFS take on a very light grey colour after milling, which almost makes the two slags indistinguishable as shown in Figure 69b.

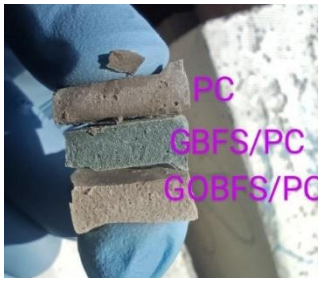


Figure 68:Greening effect of GBFS compared to GOBFS for 100% PC and 50% PC-Slag blends

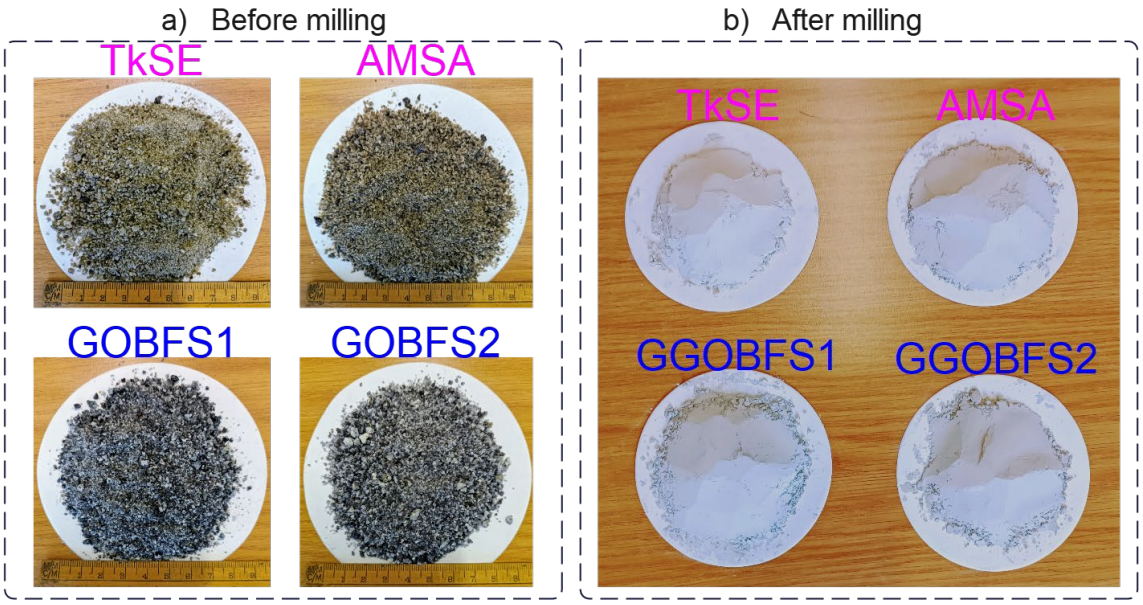


Figure 69: Conventional BF slag vs novel OBF slag in colour: a) before milling, b) after milling

4.3. Chemical composition

The chemical compositions of the slag samples were determined using inductively coupled plasma-optical emission spectroscopy (ICP-OES) while the total sulphur was determined using LECO Infrared Combustion Analyzer, and the results are summarized in Table 10.

Table 10: Chemical composition of slag samples

Oxides(%)	Al_2O_3	CaO	SiO_2	MgO	TiO_2	FeO	S	Total
GOBFS1	10,56	42,26	35,88	8,75	1,01	0,41	0,24	99,11
GOBFS2	10,43	43,10	36,00	7,56	1,40	0,32	0,19	99,00
TkSE	11,14	42,76	37,07	6,07	0,54	0,28	1,14	99,00
AMSA	16,60	35,65	35,13	9,07	0,81	0,50	1,31	99,06
	Other variations of OBF slag							
AOBFS1	9,84	44,40	36,40	7,51	0,43	0,06	0,15	98,79
AOBFS2	9,84	44,40	36,40	7,51	0,43	0,06	0,15	98,79
Tap 85	15,25	39,70	34,90	8,15	0,69	0,42	0,23	99,34
Tap 132	10,00	39,20	35,30	9,66	1,80	1,75	0,20	97,91
Tap 144	9,96	42,30	35,50	7,52	1,45	2,69	0,18	99,60

4.3.1. Comparison of OBF slag to conventional BF slag composition

From the results in Table 10, it is evident that the OBF slags' composition is roughly similar to the composition of conventional BF slags from Thyssenkrupp and ArcelorMittal. However, the relatively lower CaO and higher Al_2O_3 content of the AMSA slag can be noted as well as the slightly higher TiO_2 in novel OBF slags. Generally, the composition of the BF slags varies depending on the source of iron ore and the fluxing materials as well as the ash in the coke used for energy provision and reduction purposes (Hewlett and Liska, 2019). The range of composition for a BF slag for the main oxides as reported in (Dom et al., 2022; Jonczy et al., 2023; Shetty and Jain, 2019; Snellings et al., 2012) is as follows

- Al_2O_3 = 8 - 24%
- CaO = 30 - 50%
- MgO = 1 - 18%
- SiO_2 = 28 - 38%

It also can be seen that the composition of the main novel OBF slag (GGOBFS1, GGOBFS2) falls within the reported composition ranges of the main oxide components. Furthermore, the chemical composition of the novel OBF slag is in agreement with the SANS 55167-1:2011 and the BS-EN 197-1:2011 as per Table 11. From a chemical composition perspective, GOFBS1, GOBFS2, TkSE, and AMSA have roughly similar compositions. Therefore, similar cementitious performances can be expected from these slags.

Table 11: standard chemical composition specifications

Standard	$CaO + MgO + SiO_2$ (%)	$(CaO + MgO)/ SiO_2$
SANS 55167-1: 2011 BS-EN 197-1:2011	> 66	> 1
Novel OBF slags		
GOBFS1	86.89	1.42
GOBFS2	86.66	1.41
Reference slags		
GBFS1	85.96	1.32
GBFS2	79.85	1.27

4.3.2. Effect of change in chemical composition on cementitious performance of slag

It is important to highlight the expected effects on the cementitious performance when there is a significant difference in chemical composition of major components in the Al_2O_3-CaO-SiO_2-MgO system as well as other minor components such as, TiO_2 that is usually associated with BF slags and in this case, the novel OBF slag. Several studies (Zhang et al., 2022; Blotevogel et al., 2020a; Haha et al., 2011) are in agreement that the reactivity of the slag is higher when the proportion of network modifiers (CaO, MgO) is higher than the proportion of network formers (SiO_2) in the glass structure. The reason for this conclusion is attributed to the degree of depolymerization of the glass network, with more depolymerized glass dissolving faster, and thus increasing the reactivity of the slag. However, Al_2O_3 can display mixed effects since the presence of more Al_2O_3 in the slag can lead to higher early strength development with low long-term strength in cement blended with slag (Wang et al., 2004; Kucharczyk et al., 2016; Blotevogel et al., 2024). In this study, the OBF slag sample, labelled Tap 85 Table 10 can be expected to experience the above-mentioned alumina effect since it contains about 15,25% of Al_2O_3 as well as the AMSA slag.

Sulphur is commonly present in slag as sulfide (S^{2-}), and the sulphur content of the OBF slags is relatively low (<0,30%) compared to the commonly observed sulphur content of 1 – 2% in conventional BF slags (Roy, 2009). According to Couvidat et al. (2020), sulphur in GGBFS does not affect the cementitious performance, but it does contribute to the greening of hydrated slag-cement specimens, and the degree of this greening effect is proportional to the amount of GGBFS used to replace Portland cement. This further explains the observations in Figure 68, and it can be seen that the low sulphur content of the novel OBF slag did not lead to excessive greening of slag-cement specimens, unlike the conventional BF slag.

TiO_2 is a trace compound commonly found in modern GGBF slags and even in the novel GGOBF slags. TiO_2 has been reported to have a negative effect on the compressive strength in blended slag cements when the concentration exceeds 1% for low Al_2O_3 slag (Blotevogel et al., 2020b; Wang et al., 2004). The introduction of TiO_2 into the slag might either come from the iron ore, or the fluxing materials used during smelting operations. Blotevogel et al. (2022) suggested that the negative effect of Ti might be due to the fact that Ti stabilizes the glass structure, and there is formation of an amorphous, Ti-bearing gel layer around the slag grains

during hydration, thereby obstructing the hydration process. The latter suggestion aligns with the observation made during the smelting campaign of this study, whereby high TiO_2 led to the formation of popcorn-like glassy slag particles after water quenching of the molten slags. The OBF slag variations which are most likely to display the effect of TiO_2 are the Tap 132 and 144 samples with 1,8% and 1,45% TiO_2 respectively, as per Table 10. It should be noted that the TiO_2 in the novel OBF slags originated from bauxite, where it was a major impurity, and bauxite was used to supplement the Al_2O_3 content of the slags as discussed in chapter 3.

Other minor elements commonly found in GGBFS such as barium (Ba), cerium (Ce), chromium (Cr), vanadium (V), zirconium (Zr), manganese (Mn), ceasium (Cs), potassium (K), and strontium (Sr) have a negligible effect on the reactivity of the slag, as long as these elements are present in trace amounts. However, their impacts start becoming significant when their concentrations in the slag are significantly higher, possibly above 2%. Several investigations (Brown et al., 1995; Blotevogel et al., 2020b; Bunker, 1994) have shown that the presence of network modifiers such as, Sr, Ba, K, Cs in GGBFS increased the slag reactivity as is the case for Mg and Ca. On the other hand, the presence of the other listed elements, including Ce, Cr, V, and Zr, had either no impact, or significant negative effects on GGBFS reactivity. Just as in the case of TiO_2, the presence of network-forming elements stabilizes the glass structure, leading to a low slag dissolution rate, decreased formation of C-(A)-S-H binder, and ultimately low strength development.

Manganese has also been found to reduce the early strength development while increasing the long-term strength after 28 days, but slags with high MnO content (more that 15% by weight) were described as unsuitable for cementitious applications since the proportion of other essential compounds will be lower, at less than 85% (Péra et al., 1999; Rai et al., 2002). This is most likely one of the major problems that other steelmaking and ferroalloy slags displayed during cementitious applications, since the presence of heavy metals is significant in those slags and the likelihood for leaching is very high. The study conducted by Proctor et al. (2000) highlighted that the metal leaching from GGBFS is low, demonstrating that the minor proportion of metals present in the slag is directly included in the glass matrix. Hence, this contributes to the predominant preference of using GGBFS in blended cements.

The OBF slag, on the other hand, is similar to GGBFS in composition, in terms of the four major components (Al_2O_3, CaO, SiO_2, MgO) as per Table 1, with all the minor elements discussed above being significantly lower, except for Ti. Therefore, the only potential difference in cementitious performance, caused by the variation in chemical composition, might arise from the TiO_2 content, as well as the Al_2O_3 content, especially for the Tap 85 sample.

4.4. Fineness

It has been widely reported that slags with the same properties and finer particles hydrate faster, leading to improved cementitious performance, whereas when the particle size is coarser, the hydration is slower, leading to sluggish cementitious performance of the slag (Binici et al., 2007; Nakamura et al., 1992; Wang et al., 2005), this applies even to cement as reported by Celik (2009). It can be seen that the fineness of the slag plays a crucial role in the hydration of

blended cements since finer particles typically display higher reaction kinetics due to the larger exposed surface area. Industrially, the fineness of the ground slag is generally determined using the Blaine air permeability test, while particle size distribution (PSD) measurements, and the Brunauer-Emmett-Teller (BET) method also provide good indications of fineness. The samples from this study were analysed using PSD tests, together with both the Blaine fineness test and the BET test.

4.4.1. Particle size distribution (PSD)

The PSD of the four major samples of this study were analysed using a Malvern Panalytical Mastersizer 2000 particle size analyser, and the results are summarized in Figure70. It should be noted that the instrument also determined the surface area of each slag by calculation, with these results also included in Figure 70.

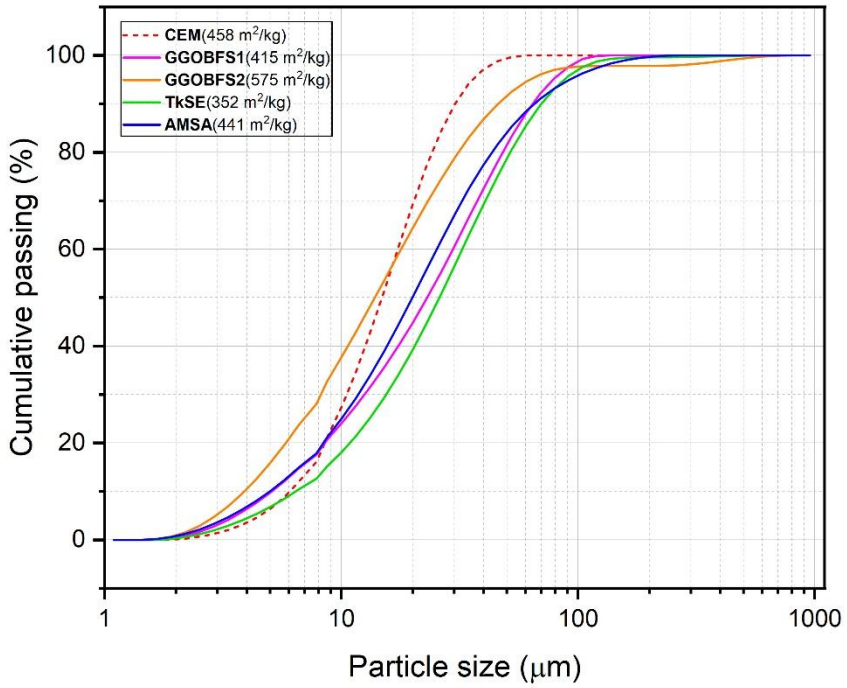


Figure 70: PSD curves of cement and ground slag samples

As per the results in Figure 70, on an 80% cumulative passing basis, the corresponding size for the reference cement (CEM) is 25 µm; for GGOBFS2 it is 32 µm, while for TkSE it is 52 µm. This shows that the reference cement sample (CEM) is finer than all the slag samples in this study, among which, GGOBFS2 is the finest slag sample. This is followed by the AMSA and GGOBFS1 slags, with TkSE being the slag sample with coarsest particles.

In terms of the sharpness of the curve and narrow range for the particle size distribution (PSD), the cement sample, CEM, has the narrowest distribution, with more than 80% of particles passing 30 µm. This is particularly important with regard to displaying consistent behaviour during hydration, with more particles reacting at a similar rate, due to the size range of the majority of particles. It should be noted that the reference cement sample is CEM I 52.5R which is ground to a high fineness to counteract the lower earlier strength that occurs when used in

blends with slag. The steepness of the distribution is also affected by the grindability of the clinker, which is crystalline and easier to grind than the glassy slag (Hewlett and Liska, 2019). Hence, the milling behaviour of the CEM sample cannot be compared to the slag samples.

A comparison of the slags' PSD shows that GGOBFS2 is finer among the slag samples tested in this study, but its PSD is very broad. Moreover, GGOBFS2 has a mixed amount of finer and coarser particles, with 37% of particles less than 10 µm, and with 60% of particles between 10 and 100 µm. If the sample is not well homogenized, there will be some variations in cementitious performance between different portions of the same sample since the finer particles will tend to hydrate faster, whereas the coarser particles will tend to hydrate slowly. As a result, it is the proportion of finer and coarser particles involved in a particular test for this slag that will dictate its cementitious performance. Therefore, the homogenization of the sample is very important for consistent cementitious performance, especially for slag samples that have wide PSD.

The TkSE slag, similar to the GGOBFS2 slag, was milled at the optimized milling conditions established for GGOBFS1 as described in phase 2 of chapter 3 in this study. The optimal milling conditions were 3h30mins at 68 rpm, and the laboratory scale milling setup along with the mill charge composition are shown in Figure 71. The AMSA and CEM samples were milled on an industrial scale under standard production conditions at Afrimat and AfriSam South Africa, respectively. The slightly coarser grain size observed for TkSE slag sample might be because its feed PSD is relatively finer from the feed PSD of GGOBFS1 as shown in Figure 72, and thus affecting the overall milling efficiency. The other potential reason might be the difference in the grindability of the TkSE slag compared to the GGOBFS1 slag. The grindability of the novel OBF slag compared to the conventional BF slag has not been covered in this study and remains another key parameter that needs to be explored.

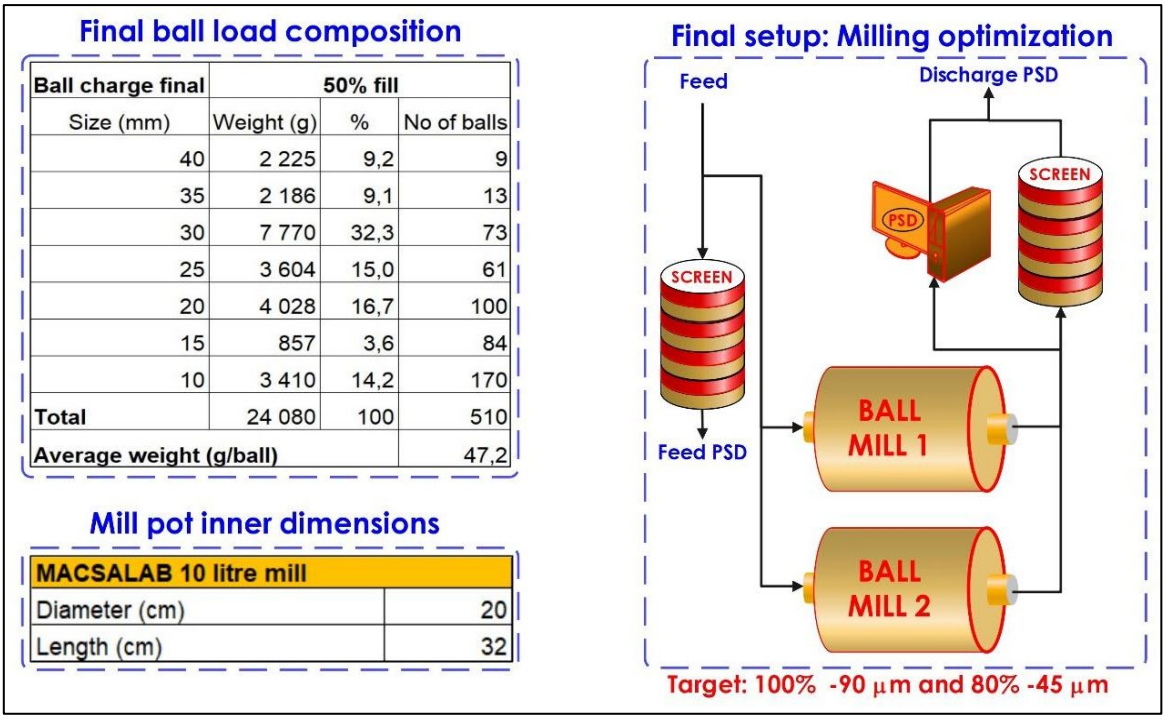


Figure 71: Laboratory scale milling setup

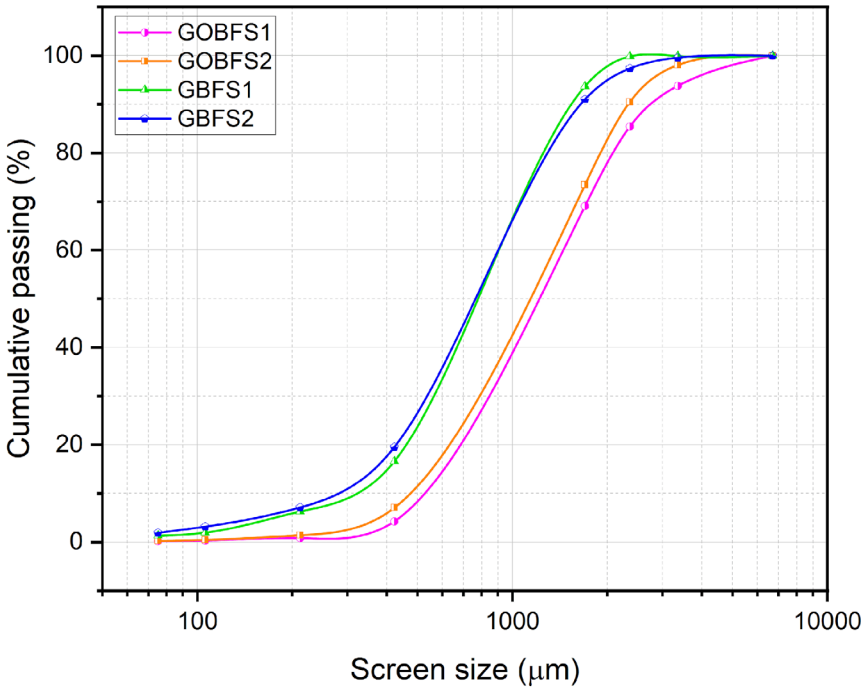


Figure 72: PSD of unground slag samples

Wang et al., (2005) pointed out that GBFS should be ground to at least < 40 µm, and slag particles with grain size > 20 µm only significantly contribute to strength development at later stage (after 7 days), whereas for high early strength development, or faster hydration process, slag particles of size < 20 µm are very important, especially the < 5 µm particles. This observation supports the view that slag samples with a greater proportion of finer particles are likely to display high early strength development and better cementitious performance overall. From the results in Figure 70, using the 20 µm cut-size, the slag sample that can be expected to perform at its best is GGOBFS2 with approximately 65% passing 20 µm, followed by AMSA with roughly 50% passing 20 µm.

4.4.2. Surface area

Surface area and PSD are usually employed interchangeably to describe the fineness of the sample. As per Figure 70, the PSD trends were also confirmed using the calculated particle surface areas from the equipment, with GGOBFS being finer with 575 m^2/kg and TkSE having 352 m^2/kg as specific surface area as the coarsest sample. However, the surface area measurements determined by the Mastersizer assume spherically shaped particles, which is not always the case for the materials, especially with slag particles. Hence, some degree of uncertainty should be considered for the fineness measurements.

4.4.2.1. Blaine fineness method

Blaine fineness is the conventional measurement of fineness in the cement industry and is also the reference method for determining the fineness of ground granulated blast furnace slag (GGBFS) in standard specification SANS 55167-1: 2011. It applies the air permeability method by passing a flow of air through a compacted bed of cement or another ground material. The equipment is usually calibrated using a material of known Blaine fineness. The relative

densities were also approximated throughput this measurement. The Blaine fineness results of the cement and slag samples aloμng with the relative densities are summarized in Figure 73.

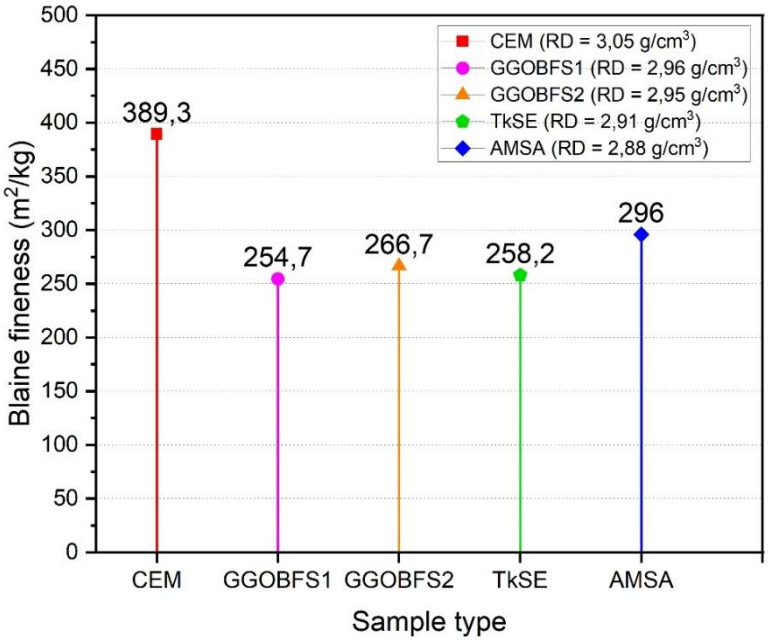


Figure 73: Blaine fineness and relative density (RD) results

The AMSA sample is shown to be the finest milled slag sample, with a Blaine fineness of 296 m^2/kg. In comparison, the reference cement has a Blaine fineness of 389.9 m^2/kg. Unlike the trend observed in the PSD results, the Blaine fineness results show that the TkSE sample has a fineness of 258.2 m^2/kg which is slightly higher compared to the 254.7 m^2/kg of the GGOBFS1 sample. In addition, the relative density (RD) results show that the CEM sample has the highest RD of 3.05 g/cm^3 , while for the slag samples, the AMSA sample has the lowest RD of 2.88 g/cm^3. Nevertheless, the RD values of all the slag samples are very close, with a deviation of 0.08 g/cm^3, making the possible impact of RD insignificant on the individual cementitious performance of the slags in this study.

Ideally, the fineness of the slag should either be the same as that of the reference cement (Ogirigbo and Black, 2016), or even higher for improved cementitious performance (Yang et al., 2023; Dom et al., 2022). Therefore, the results from this study will be slightly conservative since the analysed Blaine fineness is a bit lower than the industry minimum recommended limit of 275 m^2/kg (BS EN 196-6:2018; SANS 55167-1:2011). The conservative approach is good since overgrinding the slag, especially for first experimental trials of a novel material (OBF slag), will lead to unrealistic results that can never be viably achieved on an industrial scale. Moreover, when the slag is ground to a higher fineness than 275 m^2/kg in industrial operations, the performance will definitely be better than in this study since higher fineness translates to improved cementitious performance provided that the other properties, such as the chemical composition and glass count are kept constant.

Overgrinding of supplementary cementitious materials (SCMs) is also practiced in the cement industry. This can be of benefit to materials that are not naturally cementitious since they can

accomplish what is known as the filler effect when overground to ultrafine sizes in order to stimulate nucleation of the calcium silicate hydrate (C-S-H) binder (Berodier and Scrivener, 2014). However, overgrinding can also lead to excessive energy consumption, which can accumulate to the overall process costs, and it can also decrease the workability of the blended cement mix whether it is used in concrete, or mortar.

While the Blaine fineness test has been characterized as a quick and simplistic method, it also has some degree of uncertainties, especially when analysing materials other than cement, in this case, the slags. In the studies (Arvaniti et al., 2014a, Arvaniti et al., 2014b), it was highlighted that for highly accurate Blaine fineness tests, the reference material should have the same particle size distribution (PSD), and shape as the material of interest. Additionally, forming a well-compacted bed with a specific porosity for supplementary cementitious materials (SCMs) is particularly challenging.

4.4.2.2. Brunauer, Emmett and Teller (BET) method

The specific surface area was also determined using the nitrogen adsorption Brunauer, Emmett and Teller (BET) method for the slag samples, for comparison with the observed trends in the Blaine fineness test. The BET results are shown in Figure 74.

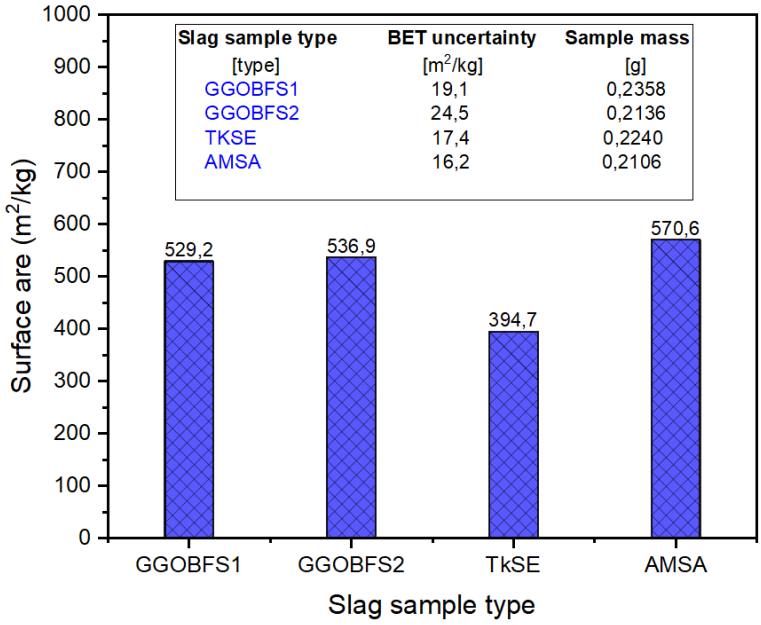


Figure 74: BET results for slag samples

As per Figure 74, the AMSA milled slag has the highest BET surface area of 570.6 m^2/kg. In comparison, the TkSE sample has the lowest BET surface area of 394.7 m^2/kg, demonstrating that its expected cementitious performance is more likely to be the lowest among all the slag samples. The measure of uncertainty reported with each test result ranges from 16.2 to 24.5 m^2/kg. Unlike the Blaine fineness, the BET test does not make an assumption about the shape of the particles. However, the BET test also has some drawbacks since the possibilities of micropore filling or penetration into cavities of molecular size are not considered in the measurement (Arvaniti et al., 2014a; Sing, 1985).

Although the BET surface area results (in m^2/kg) are higher than the values determined in the Blaine fineness measurements, the trends in fineness levels have been confirmed. For the GGOBFS1 and TkSE samples, the BET test confirmed the trend observed in the surface area determined from the PSD results in Figure 70, but not the result from the Blaine fineness measurements in Figure 73. Therefore, the expected ranking of cementitious performance of the slags based upon the overall fineness results is as follows: the GGOBFS2 and AMSA samples are more likely to perform better overall, followed by GGOBFS1 and lastly, TkSE.

4.5. Glass content

The glass count was analysed using a microscopic technique, a point counting method was used to approximated the proportion of glassy, or amorphous phases; the results are summarized in Figure 75.

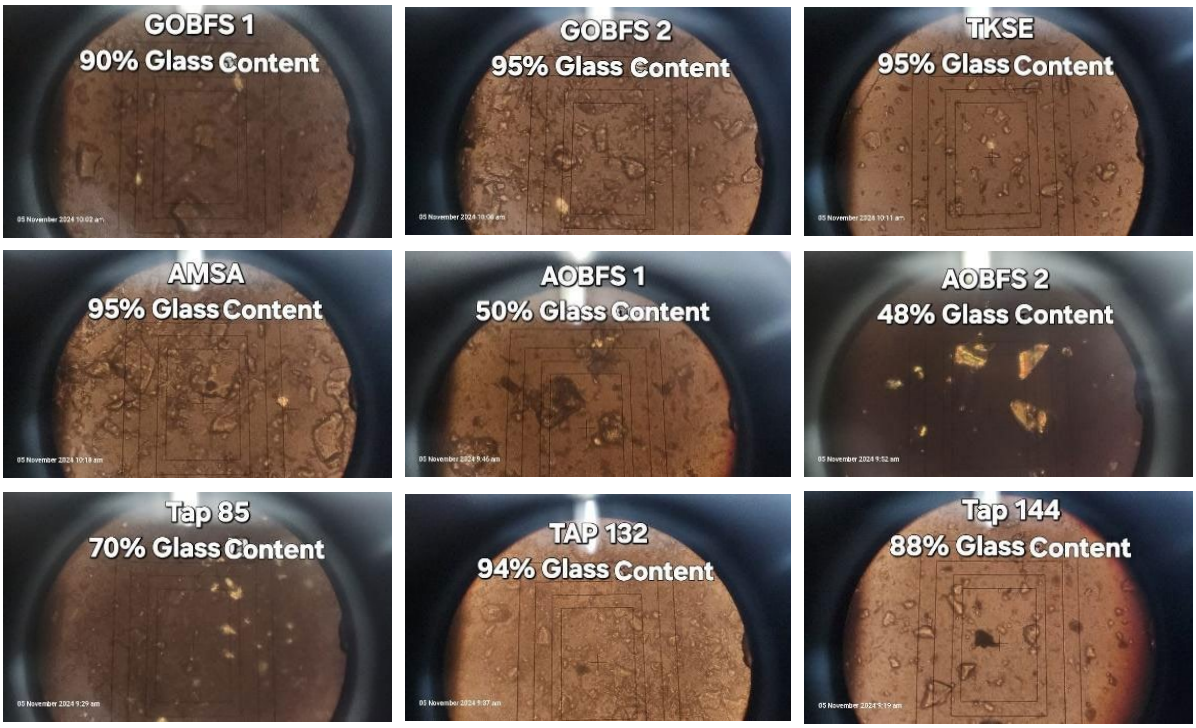


Figure 75: Glass content comparison of slag samples

4.5.1. Glass content comparison of granulated slags

Based on the glass count results in Figure 75, all the main granulated slag samples are expected to perform equally since they have more than 95% glass, with the exception of GOBFS1, which has a glass count of 90%. The difference in glass content is minimal; however, the increase in crystalline proportion 5 to 10% can affect the overall cementitious performance of GOBFS1 (Escalante et al., 2001; Hewlett and Liska, 2019). On the other hand, the other variations of OBF slag (Tap 85, Tap132, and Tap 144) displayed different glass content results since they exhibit differences in chemical composition compared to the main OBF slag samples (GOBFS1, GOBFS2).

Tap 85 has the lowest glass count of 70%, which is most likely linked to its significantly higher Al_2O_3 content, of 15.25 %. The alumina effect has been discussed in the studies reported by Wang et al., (2004) and Kucharczyk et al., (2016). In addition, a further possible reason might

be due to the fact that an increase in Al_2O_3 content leads to increased viscosity of the slag, which can ultimately affect the sizes of the granules after water quenching. Larger slag granules are prone to crystallization, especially within the core of the granules where the temperature gradient might still be high. For the Tap 132 and 144 samples, the glass count is considerable at 94% and 88%, respectively. The slight difference, particularly for Tap 144, might be due to the high Fe_2O_3 content as well as the level of TiO_2.

It has been widely reported that the more vitreous (glassy) the slag, the higher the reactivity (Escalante et al., 2001; Tripathy et al., 2020). This is because crystalline phases that form during slag cooling are inert and do not contribute to slag reactivity. However, Wedding et al., (1981) highlighted that the chemical durability of the slag glass is also a very important parameter to consider, as for strength development, GGBFS glass needs to dissolve and then re-precipitate as cementitious phases. The latter information was also confirmed in (Blotevogel et al., 2020a), where a strong link between the dissolution rate of slag glass to chemical composition has been highlighted. Although the degree of depolymerization of the glass is not quantified in this study, the slag samples from this study are expected to have the same degree of depolymerization since their chemical compositions are almost identical as per Table 10. Therefore, the quantified amount of amorphous (glassy) phases in Figure 75, can be used as an additional aspect for comparison of the different slag samples in this study.

4.5.2. Comparison of air-cooled and granulated OBF slag

The glass count measurements in Figure 75 show further that the air-cooled OBF slags (AOBFS) have not more than 50% glass, whereas the granulated OBF slags have more than 90% glass, making GOBFS samples more reactive than AOBFS samples, and highlighting the importance of water quenching. This observation is also in agreement with results observed in the study by Tripathy et al., (2020), in which air-cooled BF slags are classified as slags with more than 50% crystalline phases, while granulated BF slags typically have more than 90% amorphous phases. Moreover, it should be noted that the AOBFS1 sample was taken on top of a ladle filled with air-cooled slag and AOBFS2 was taken at the bottom of the ladle. AOBFS2 had 48% glass while AOBFS2 had 50% glass, demonstrating that the difference in cooling position is not that significant. The small difference in glass count of the air-cooled slags can be explained by the fact that the cooling rate, between the slag and air at the top of the ladle, would be expected to be higher than the cooling rate between the slag and the refractory at the bottom of the ladle.

To further analyse the difference between the air-cooled and granulated OBF slag, SEM images of each sample are shown in Figure 76.

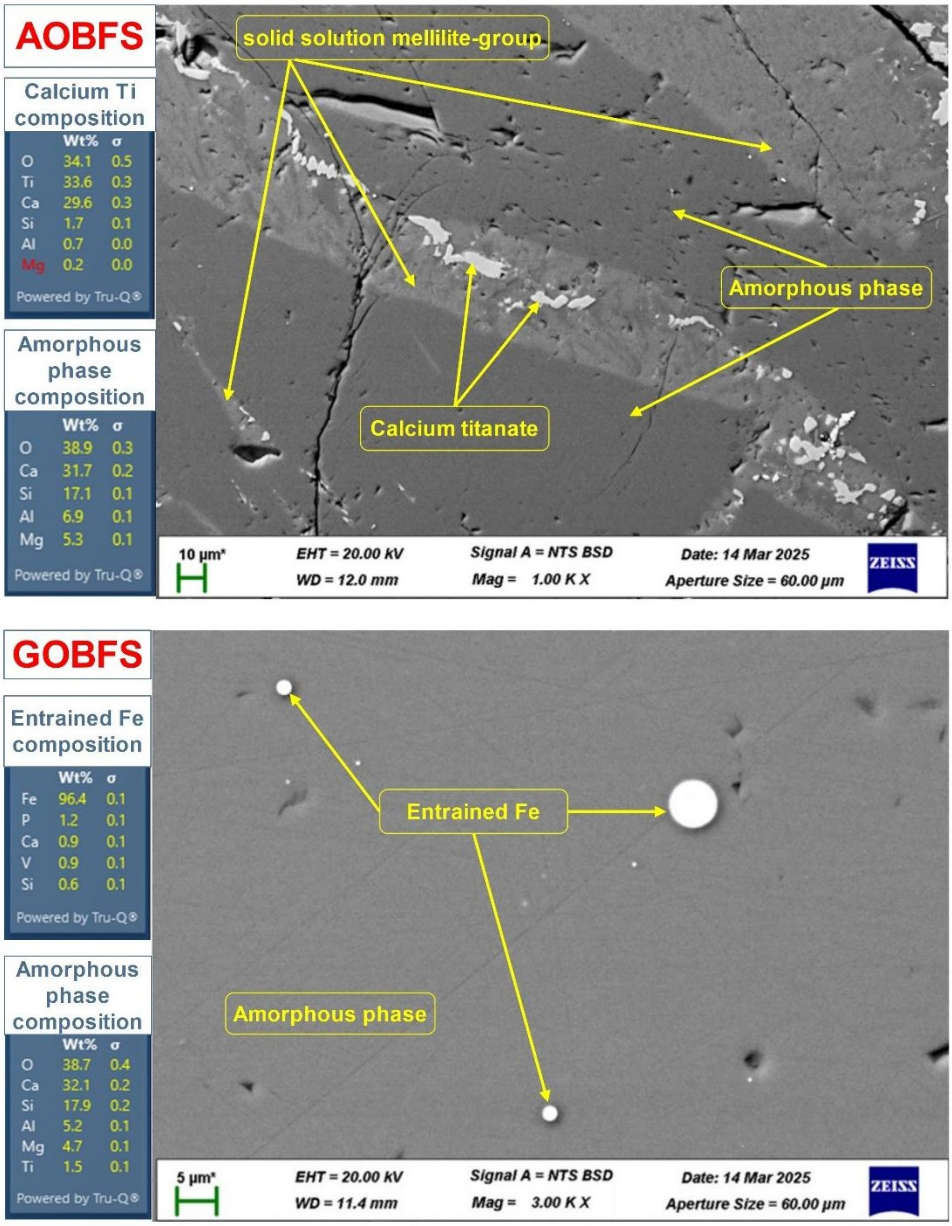


Figure 76: SEM images of AOBFS and GOBFS

As per Figure 76, the main crystalline phases found in AOBFS are calcium titanate and melilite group phases (calcium silicates of magnesium and aluminium), such as gehlenite and akermanite. These are common phases that are generally found in the conventional BF slags (Grubb and Berggren, 2018). The SEM results are in agreement with the XRD results for AOBFS, wherein a solid solution of akermanite (calcium magnesio-silicate, ($Ca_2Mg(Si_2O_7)$) and gehlenite (calcium alumino-silicate, ($Ca_2Al_2SiO_7$)) is identified as the main phase. The presence of titanium (1.5%) in the amorphous phase of GOBFS is what differentiates it from the amorphous phase in AOBFS (0%). This is unsurprising since the composition of GOBFS has more than 90% amorphous phase and its composition should closely resemble the composition of the original molten slag before water-granulation. Moreover, the presence of Fe droplets in the granulated slag is also noted as per Figure 76. This is most likely entrained Fe that could not drop down to the hot metal zone during smelting. It should be noted that the

SEM image of the GOBFS sample is at a higher magnification of 3000x in order to highlight the Fe droplets, compared to the AOBFS image which is at a lower magnification of 1000x.

4.6. Conclusions and slag performance prediction

From the overall characterization results discussed in this chapter, the following conclusions and recommendations can be considered.

The novel OBF slag has roughly similar chemical composition to the conventional BF slags: chemical composition will therefore not be a factor in any observed variation in cementitious performance in a comparison of the slag samples. With similar chemical composition, the degree of depolymerization of the OBF slag glass can be assumed to be the same as the degree of depolymerization of the conventional BF slag glass, since the proportions of network formers and network modifiers are the same. Although, the novel OBF slag composition falls within the generic BF slag compositions, the relatively lower CaO and higher Al_2O_3 content of the AMSA slag can be noted as well as the slightly higher TiO2 in novel OBF slags. Furthermore, the glass count of the GOBFS2, AMSA, and TkSE samples is 95% while GOBFS1 has a lower glass count, of 90%. Therefore, GOBFS1 might underperform slightly in comparison to the other slags.

Fineness is mostly likely to be the parameter that dictates the trends in the cementitious performance of the slags, since the other important parameters such as the chemical composition and the glass count, are roughly similar for the four main slag samples in this study (GGOBFS1, GGOBFS2, AMSA, TkSE). The trends in fineness rank the AMSA and GGOBFS2 milled slags on the same scale as the best slags, but GGOBFS2 slag has a wider PSD, requiring proper homogenization for consistent performance. The third-ranked slag in terms of fineness is most likely to be GGOBFS1, followed by the TkSE slag. However, the order of these two slags might be switched because the glass count of TkSE is slightly higher, at 95%, compared to that of GGOBFS1, at 90%.

Based on the characterization results from this study in conjunction with the information from the literature, a narrow PSD with at least 80% passing 40 μm is recommended for consistent results as the AMSA slag sample and less requirement of sample homogeneity (Wang et al., 2005), while the chemical composition must be within the specified range, preferably with a major proportion of network modifiers (CaO, MgO) in order to have a more depolymerized glass structure, which in turn will favour fast hydration of the slag. The slag should have at least 95% glass to counteract the effect of the inert crystalline phases, and the level of prominent impurities, including TiO_2, must be controlled to less than 2%. The presence of titanium leads to the crystallization of calcium titanate if the slag is air-cooled.

References

Arvaniti, E., Juenger, M., Bernal, S.A., Duchesne, J., Courard, L., LeRoy, S.F., Provis, J.L., Klemm, A.J. and De Belie, N. (2014a). Physical characterization methods for supplementary cementitious materials. *Materials and Structures*, 48(11), pp.3675–3686. doi:https://doi.org/10.1617/s11527-014-0430-4.

Arvaniti, E.C., Juenger, M.C.G., Bernal, S.A., Duchesne, J., Courard, L., Leroy, S., Provis, J.L., Klemm, A. and De Belie, N. (2014b). Determination of particle size, surface area, and shape of supplementary cementitious materials by different techniques. *Materials and Structures*, 48(11), pp.3687–3701. doi:https://doi.org/10.1617/s11527-014-0431-3.

Berodier, E. and Scrivener, K. (2014). Understanding the Filler Effect on the Nucleation and Growth of C-S-H. *Journal of the American Ceramic Society*, [online] 97(12), pp.3764–3773. doi:https://doi.org/10.1111/jace.13177.

Binici, H., Temiz, H. and Köse, M.M. (2007). The effect of fineness on the properties of the blended cements incorporating ground granulated blast furnace slag and ground basaltic pumice. *Construction and Building Materials*, 21(5), pp.1122–1128. doi:https://doi.org/10.1016/j.conbuildmat.2005.11.005.

Blotevogel, S., Doussang, L., Poirier, M., André, L., Canizarès, A., Simon, P., Montouillout, V., Kaknics, J., Patapy, C. and Cyr, M. (2024). The influence of Al2O3, CaO, MgO and TiO2 content on the early-age reactivity of GGBS in blended cements, alkali-activated materials and supersulfated cements. *Cement and Concrete Research*, 178, pp.107439–107439. doi:https://doi.org/10.1016/j.cemconres.2024.107439.

Blotevogel, S., Ehrenberg, A., Steger, L., Doussang, L., Kaknics, J., Patapy, C. and Cyr, M. (2020a). Ability of the R3 test to evaluate differences in early age reactivity of 16 industrial ground granulated blast furnace slags (GGBS). *Cement and Concrete Research*, 130, pp.105998–105998. doi:https://doi.org/10.1016/j.cemconres.2020.105998.

Blotevogel, S., Poirier, M., Vantelon, D., Chesneau, E., Dutoit, C.-E., Montouillout, V., Fayon, F., Kaknics, J., Landrot, G., Saldi, G.D., Schott, J., Vezin, H., Patapy, C. and Cyr, M. (2022). Titanium in GGBS-like calcium-magnesium-aluminosilicate glasses: Its role in the glass network, dissolution at alkaline pH and surface layer formation. *Journal of Non-Crystalline Solids*, 591, pp.121708–121708. doi:https://doi.org/10.1016/j.jnoncrysol.2022.121708.

Blotevogel, S., Steger, L., Hart, D., Doussang, L., Judit Kaknics, Poirier, M., Bornhöft, H., Deubener, J., Patapy, C. and Cyr, M. (2020b). Effect of TiO_2 and 11 minor elements on the reactivity of ground-granulated blast-furnace slag in blended cements. *Journal of the American Ceramic Society*, 104(1), pp.128–139. doi:https://doi.org/10.1111/jace.17431.

Brown Jr., G., Farges, F. and Calas, G. 1995. Chapter 9. X-RAY SCATTERING AND X-RAY SPECTROSCOPY STUDIES OF SILICATE MELTS. In: Stebbins, J., McMillan, P. and Dingwell, D. ed. *Structure, Dynamics, and Properties of Silicate Melts*. Berlin, Boston: De Gruyter, pp. 317-410. https://doi.org/10.1515/9781501509384-011

BS EN 196-6:2018. Methods of testing cement Determination of fineness. European Committee for Standardization. British Standards Institution, London.

BS EN 197-1: 2011. Cement. Composition, Specifications and Conformity Criteria for Common Cements. European Committee for Standardization. British Standards Institution, London.

Bunker, B.C. (1994). Molecular mechanisms for corrosion of silica and silicate glasses. *Journal of Non-Crystalline Solids*, 179, pp.300–308. doi:https://doi.org/10.1016/0022-3093(94)90708-0.

Celik, I.B. (2009). The effects of particle size distribution and surface area upon cement strength development. *Powder Technology*, 188(3), pp.272–276. doi:https://doi.org/10.1016/j.powtec.2008.05.007.

Chaouche, M., Gao, X.X., Cyr, M., Cotte, M. and Frouin, L. (2017). On the origin of the blue/green colour of blast-furnace slag-based materials: Sulphur K-edge XANES investigation. *Journal of the American Ceramic Society*, 100(4), pp.1707–1716. doi:https://doi.org/10.1111/jace.14670.

Couvidat, J., Diliberto, C., Meux, E., Cotelle, S., Bojic, C., Izoret, L. and Lecomte, A. (2021). Greening effect of slag cement-based concrete: Environmental and ecotoxicological impact. *Environmental Technology & Innovation*, 22, p.101467. doi:https://doi.org/10.1016/j.eti.2021.101467.

Couvidat, J., Diliberto, C., Meux, E., Izoret, L. and Lecomte, A. (2020). Greening effect of concrete containing granulated blast-furnace slag composite cement: Is there an environmental impact? *Cement and Concrete Composites*, 113, p.103711. doi:https://doi.org/10.1016/j.cemconcomp.2020.103711.

Dom, A.A.M., Jamaluddin, N., Hamid, N.A.A. and Hoon, C.S. (2022). A Review: GGBS as a Cement Replacement in Concrete. *IOP Conference Series: Earth and Environmental Science*, 1022(1), p.012044. doi:https://doi.org/10.1088/1755-1315/1022/1/012044.

Dom, A.A.M., Jamaluddin, N., Hamid, N.A.A. and Hoon, C.S. (2022). A Review: GGBS as a Cement Replacement in Concrete. *IOP Conference Series: Earth and Environmental Science*, 1022(1), p.012044. doi:https://doi.org/10.1088/1755-1315/1022/1/012044.

Escalante, J.I., Gómez, L.Y., Johal, K.K., Mendoza, G., Mancha, H. and Méndez, J. (2001). Reactivity of blast-furnace slag in Portland cement blends hydrated under different conditions. *Cement and Concrete Research*, 31(10), pp.1403–1409. doi:https://doi.org/10.1016/s0008-8846(01)00587-7.

Grubb, D.G. and Berggren, D.R.V. (2018). Air-Cooled Blast Furnace Slag. I: Characterization and Leaching Context. *Journal of Hazardous, Toxic, and Radioactive Waste*, 22(4). doi:https://doi.org/10.1061/(asce)hz.2153-5515.0000411.

Haha, M.B., Lothenbach, B., Le Saout, G. and Winnefeld, F. (2011). Influence of slag chemistry on the hydration of alkali-activated blast-furnace slag — Part I: Effect of MgO.

Cement and Concrete Research, 41(9), pp.955–963. doi:https://doi.org/10.1016/j.cemconres.2011.05.002.

Hewlett, P.C. and Liska, M. (Eds) (2019). *Lea's Chemistry of Cement and Concrete*, 5th Edition, Elsevier Science & Technology, Butterworth-Heinemann, Oxford, UK.

Jonczy, I., Grzesik, B., Wieczorek, A., Gerle, A., Nuckowski, P. and Staszuk, M. (2023). Characteristics of the phase and chemical composition of blast furnace slag in terms of the possibility of its economic use. *Gospodarka Surowcami Mineralnymi*, 38(4). doi:https://doi.org/10.24425/gsm.2022.143625.

Kucharczyk, S., Deja, J. and Zajac, M. (2016). Effect of Slag Reactivity Influenced by Alumina Content on Hydration of Composite Cements. *Journal of Advanced Concrete Technology*, 14(9), pp.535–547. doi:https://doi.org/10.3151/jact.14.535.

Le Cornec, D., Wang, Q., Galoisy, L., Renaudin, G., Izoret, L. and Calas, G. (2017). Greening effect in slag cement materials. *Cement and Concrete Composites*, 84, pp.93–98. doi:https://doi.org/10.1016/j.cemconcomp.2017.08.017.

Nakamura, N., Saki, M. and Swamy, N. (1992). Effect of Slag Fineness on the Development of Concrete Strength and Microstructure. *'SP-132: Fly Ash, Silica Fume, Slag, and Natural Pozzolans and Natural Pozzolans in Concrete - Proceedings Fourth Interna'*, 132, pp.1343–1366. doi:https://doi.org/10.14359/1231.

Ogirigbo, O.R. and Black, L. (2016). Influence of slag composition and temperature on the hydration and microstructure of slag blended cements. *Construction and Building Materials*, 126, pp.496–507. doi:https://doi.org/10.1016/j.conbuildmat.2016.09.057.

Péra, J., Ambroise, J. and Chabannet, M. (1999). Properties of blast-furnace slags containing high amounts of manganese. *Cement and Concrete Research*, 29(2), pp.171–177. doi:https://doi.org/10.1016/s0008-8846(98)00096-9.

Proctor, D.M., Fehling, K.A., Shay, E.C., Wittenborn, J.L., Green, J.J., Avent, C., Bigham, R.D., Connolly, M., Lee, B., Shepker, T.O. and Zak, M.A. (2000). Physical and Chemical Characteristics of Blast Furnace, Basic Oxygen Furnace, and Electric Arc Furnace Steel Industry Slags. *Environmental Science & Technology*, 34(8), pp.1576–1582. doi:https://doi.org/10.1021/es9906002.

Rai, A., Prabakar, J., Raju, C.B. and Morchalle, R.K. (2002). Metallurgical slag as a component in blended cement. *Constr Build Mater*, 16(8), pp.489–494. doi:https://doi.org/10.1016/s0950-0618(02)00046-6.

Roy, A. (2009). Sulphur speciation in granulated blast furnace slag: An X-ray absorption spectroscopic investigation. *Cement and Concrete Research*, 39(8), pp.659–663. doi:https://doi.org/10.1016/j.cemconres.2009.05.007.

SANS 55167-1:2011. Ground granulated blast furnace slag for use in concrete, mortar and grout Part 1: Definitions, specifications and conformity criteria.

Shetty, M.S. and Jain, A.K. (2019). *Concrete technology theory and practice*. New Delhi S. Chand Publishing.

Sing, K.S.W. (1985). Reporting physisorption data for gas/solid systems with special reference to the determination of surface area and porosity (Recommendations 1984). *Pure and Applied Chemistry*, [online] 57(4), pp.603–619. doi:https://doi.org/10.1351/pac198557040603.

Snellings, R., Mertens, G. and Elsen, J. (2012). Supplementary Cementitious Materials. *Reviews in Mineralogy and Geochemistry*, 74(1), pp.211–278. doi:https://doi.org/10.2138/rmg.2012.74.6.

Tänzer, R., Buchwald, A. and Stephan, D. (2014). Effect of slag chemistry on the hydration of alkali-activated blast-furnace slag. *Materials and Structures*, 48(3), pp.629–641. doi:https://doi.org/10.1617/s11527-014-0461-x.

Tripathy, S.K., Dasu, J., Murthy, Y.R., Kapure, G., Pal, A.R. and Filippov, L.O. (2020). Utilisation perspective on water quenched and air-cooled blast furnace slags. *Journal of Cleaner Production*, 262, p.121354. doi:https://doi.org/10.1016/j.jclepro.2020.121354.

Wang, P.Z., Rudert, V., Lang, E. and Trettin, R., 2002. Influence of the TiO2 content on the reactivity of granulated blast furnace slags. *Cem Int*, 1(1), pp.120-128.

Wang, P.Z., Trettin, R. and Rudert, V. (2005). Effect of fineness and particle size distribution of granulated blast-furnace slag on the hydraulic reactivity in cement systems. *Advances in Cement Research*, 17(4), pp.161–167. doi:https://doi.org/10.1680/adcr.2005.17.4.161.

Wang, P.Z., Trettin, R., Rudert, V. and Spaniol, T.P. (2004). Influence of Al2O3 content on hydraulic reactivity of granulated blast-furnace slag, and the interaction between Al2O3 and CaO. *Advances in Cement Research*, 16(1), pp.1–7. doi:https://doi.org/10.1680/adcr.2004.16.1.1.

Wedding, P., Hogan, F. and Meusel, J. (1981). Evaluation for Durability and Strength Development of a Ground Granulated Blast Furnace Slag. *Cement, Concrete and Aggregates*, 3(1), p.40. doi:https://doi.org/10.1520/cca10201j.

Yang, Z., Xiong, X., Chen, S., Briseghella, B., Marano, G.C. and Zhang, Y. (2023). Effect of fineness on the hydration and microstructure of cementitious materials with high-volume steel slag and blast furnace slag. *Journal of Building Engineering*, 72, pp.106682–106682. doi:https://doi.org/10.1016/j.jobe.2023.106682.

Zhang, Y., Zhang, S., Chen, Y. and Çopuroğlu, O. (2022). The effect of slag chemistry on the reactivity of synthetic and commercial slags. *Construction and Building Materials*, 335, p.127493. doi:https://doi.org/10.1016/j.conbuildmat.2022.127493.

CHAPTER 5: PERFORMANCE EVALUATION OF SLAG-CEMENT MORTAR MIXES

5.1. Introduction

This chapter incorporates results from the different mortar tests that were conducted in this study, as described in phase 3 of chapter 3. The mortar tests which were conducted for both the novel OBF slag and conventional BF slag, for comparison, are:

- Workability,
- Compressive strength, and
- Drying shrinkage.

The results are discussed critically and compared with observations from literature in order to draw conclusions. Furthermore, the interpretation of the results is done in conjunction with the preliminary characterization results discussed in chapter 4. The chemical composition, the glass content, the fineness, and the mixing ratio are the main parameters that determine the cementitious performance of slag when blended with cement as highlighted in chapter 4. Moreover, the chemical compositions of the ground granulated slag samples in this study (TKSE, AMSA, GGOBFS1, GGOBFS2) are similar, leaving the glass content, the fineness, and the mixing ratio as the properties that can influence differences in cementitious performance. Hence, the synergy of these three parameters will dictate the similarities and differences in cementitious performance. It should be noted that the reference Portland cement (PC) which was used is the AfriSam 52.5R Rapid Hardening Cement.

5.2. Workability

5.2.1. Importance

Workability tests are conducted to evaluate the flowability, or fluidity of the slag-cement mix. The test provides an indication of the mobility of the mortar mix (cement, slag, sand, water) immediately after mixing, before placement and compaction (Hewlett and Liska, 2019). The extent of workability is determined by the rate of complex reactions in the mixture of slag, cement, and water to form binding phases before compaction and placement. Therefore, the workability test can also be seen as an indirect measurement of the slag's reactivity. Slag samples of the same chemical composition, fineness and glass count are expected to behave similarly upon mixing. Moreover, any changes in these properties are expected to contribute to differences in workability. In flow table tests, mortar mixes with higher workability will demonstrate comparatively lower reactivity by spreading more at an equivalent water to binder ratio. Bediako and Kevern (2016) noted that the usage of SCM's has an influence on the water demand of paste, mortar, and concrete in order to achieve the desired workability. The addition of the slag has the potential to decrease the water demand of pure Portland cement because the slag is relatively less reactive compared to Portland cement (Gupta, 2016). Therefore, the water reduction potential and improved workability of the slag-cement mortar depend upon the reactivity of the slag, which is directly linked to the performance-defining parameters (chemical composition, glass content, fineness, and substitution ratio).

5.2.2. Workability results

The results obtained in this study from flow table tests are summarised in Figure 77.

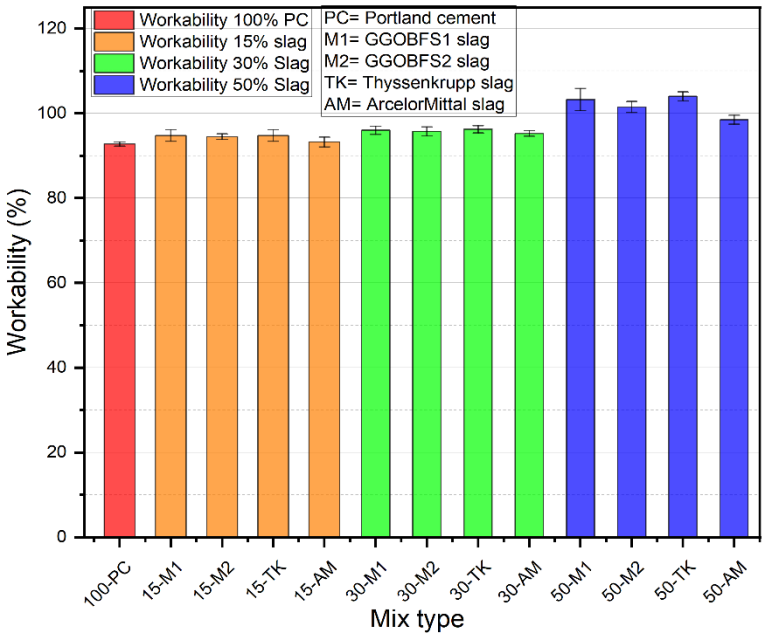


Figure 77: Workability results

5.2.3. Effect of substitution ratio

As described in chapter 3, the mixing ratios used were 1-part cementitious material (reference cement or cement/slag), 3-parts standard sand, and 0.5-part water. The general observation from the results in Figure 77, is that an increase in slag substitution increases the workability of the mortar mix and the impact of the novel OBF slag is similar to the conventional BF slag. However, the influence of substitution ratio is only noticeably at 50% slag as the 15% and 30% slag substitution are roughly similar as shown in Figure 77. This is illustrated by the workability value of 92.7% for the 100% pure Portland cement mix compared to values of 94.7%, 96%, and 103.2% when the reference cement was substituted by 15%, 30%, and 50% respectively of GGOBFS1. The same trends were observed for the conventional BF slag samples (TkSE, AMSA), and this observation is further in agreement with results discussed in the study (Meusel and Rose, 1983). Islam et al., (2011) investigated the behaviour of mortar mixes at 10%, 20%, 30%, 40%, 50%, 60% and 70% partial replacement of Portland cement with conventional BF slag and found out that the optimal substitution is 40% for high compressive and tensile strength. It can be seen that additional increments in slag substitution (>50%) may improve the workability further, but other desired mechanical properties such as the compressive and tensile strength of the mortar mix may be adversely affected.

5.2.4. Effect of fineness and glass content

The highest obtained workability is 104% for 50% substitution of the TkSE slag compared to the 98.4% workability observed for the AMSA slag at equivalent substitution. The TKSE slag has the lowest fineness – compared to the AMSA, GGOBFS1, and GGOBFS2 slags. This demonstrates that slags with higher fineness do not achieve a greater improvement in

workability, even at higher substitution. Moreover, this effect can be attributed to the greater surface area at higher fineness, which results in a higher level of reactivity. Similarly, the effect of fineness on workability was observed for the novel OBF slags, with GGOBFS2 having a higher fineness than GGOBFS1, and the corresponding workability values are 101.5% and 103.2%, respectively.

Table 12: Summary of workability, particle size and glass count

Properties	**PC**	**GGOBFS1**	**GGOBFS2**	**TKSE**	**AMSA**
Glass count (%)		90	95	95	95
% passing (-30µm)		73	87	70	77
Workability (%)					
PC 100	92.7	-	-	-	-
PC/15 Slag	-	94.7	94.5	94.7	93.2
PC/30 Slag	-	96.0	95.7	96.4	95.3
PC/50 Slag	-	103.2	101.5	104.0	98.4

Any potential effect of glass count on workability was not observed in these results because all the slag samples had relatively the same glass content, with TKSE, AMSA, GGOBFS2 having 95% glass and with GGOBFS1 having 90% glass. Comparing the workability of the TKSE slag to the GGOBFS1, since they both have relatively lower fineness, it can be seen that the difference in workability at lower slag substitutions (15%, 30%) is smaller compared to the difference at higher slag substitution (50%). Moreover, the workability of GGOBFS1 at 50% substitution is lower than that of TKSE even though TkSE has a higher glass content of 95% and a lower fineness. This could be due to the fact that the difference in glass content between the two slags being very small, leaving the fineness to dictate the trend in workability. Overall, the glass content does not have any impact on workability in this study. The fact that workability tests are taken right after mixing (< 4 minutes duration), minimizes the impact of chemical interactions on the workability results and indirectly makes the effect of glass content negligeable.

The workability with all the slag samples at 30% substitution ranges between 95.3% and 96.4%. This highlights the similarities between the novel OBF slag and the conventional BF slag in terms of workability. The AMSA slag has the lowest workability value at 95.3% possibly due to its relatively higher fineness. This demonstrate that higher fineness of the slag is beneficial to accelerate the hydration reaction, but also comes at a cost in term of high-water demand, or reduced workability if the slag's particle size is very fine (Hewlett and Liska, 2019; Brough and Atkinson, 2002; Wang et al., 1994).

It can be seen that the workability of the novel OBF slag is similar to that of the conventional BF slags. However, differences in workability may arise when performance-defining properties of the slag are not the same, especially the fineness as per this study. Chemical composition and glass content have minimal effect on workability due to small duration of workability test (<4 minutes). Overall, accounting for some manual experimental errors, the differences in workability are very minimal between the slags, especially for the lower slag substitution mixes

(15%, and 30%). This is because workability measurements are taken right after mixing, inhibiting the individual influence of the slag, particularly when its proportion in the mix is very low.

5.2.5. Workability and water demand enhancements

The workability values obtained in this study are lower than the standard specified workability ranging from 105% to 115% (ASTM/C1437−20). Increasing the water to binder ratio (w/b) will increase the workability of the mortar mix; however, an increment in w/b has repercussions on the mechanical properties of the mix, such as increased porosity of the mix matrix, reduced strength, and decreased durability (Sutan et al., 2011; Durekovic, 1995).

The usage of chemical admixtures, known as superplasticizers, is generally explored in order to achieve the target workability at a low w/b ratio, while still maintaining improved mechanical properties of the mix whether it is concrete, or mortar (Erdogdu, 2005; Durekovic, 1995; Bediako and Kevern, 2016; Gołaszewski and Szwabowski, 2004). Therefore, the results from this study show that both the novel OBF slag and the conventional BF slag can increase the workability of the mortar mix, with higher levels of slag substitution resulting in higher workability. Moreover, superplasticizers can be used in order to further enhance the workability in relation to water demand, and any deterioration in the mechanical properties of the mortar mix.

5.3. Compressive strength

5.3.1. Importance

Compressive strength tests are among the methods used to evaluate the reactivity of cement blended with SCM's, including ground granulated blast furnace slag. A higher reactivity of the slag contributes to a faster rate of compressive strength development and higher strengths. Furthermore, strength tests help to evaluate the activity index of the slag and classify different slags in terms of grades (grade 80, grade 100, grade 120) using the relative strength of blended slag-cement mortar to compare to pure cement mortar as per ASTM C989.

5.3.2. Strength tests results

Mortar cubes in this study were cast in 50 x 50 x 50mm moulds according to ASTM C109-23. The compressive strength test results, with 15%, 30%, and 50% slag were compared with the reference cement, at curing ages in a range from 2 to 168 days, are shown in Figure 78.

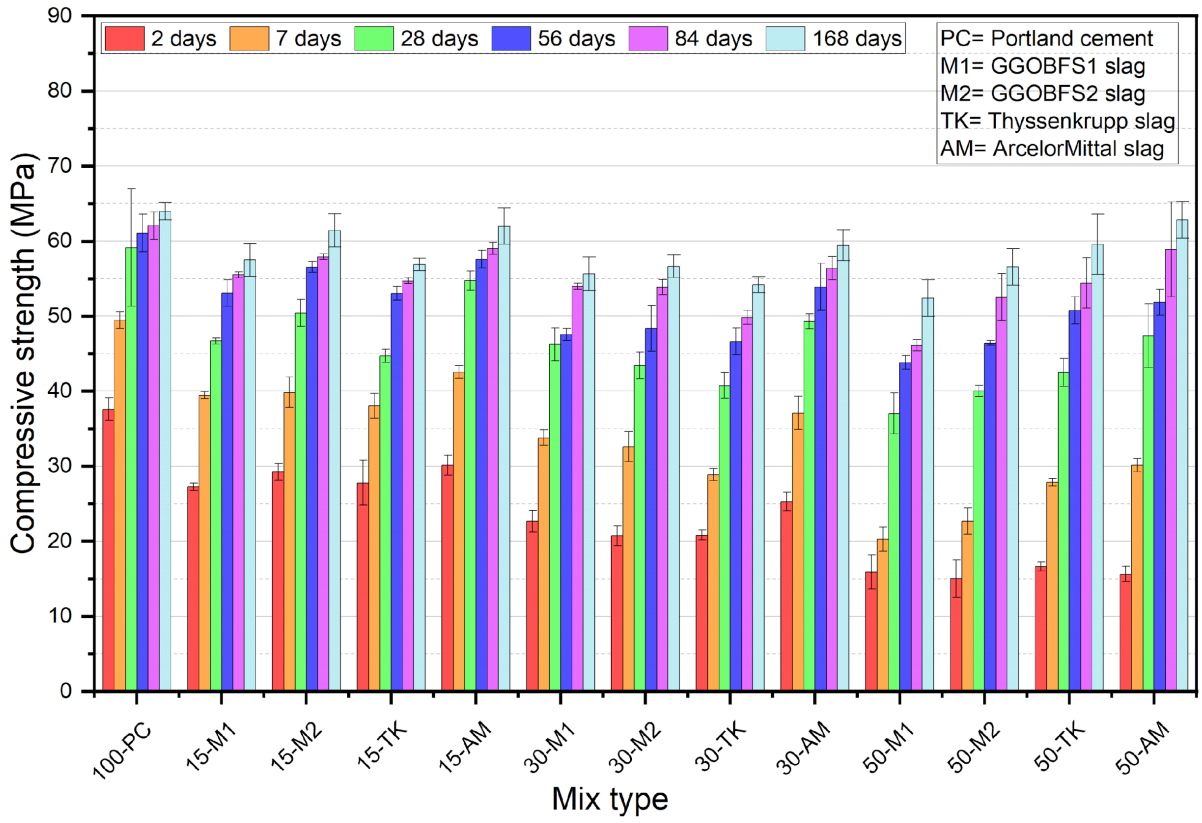


Figure 78: Compressive strength results

From the results in Figure 78, using the 2 days' curing age, it can be seen that the 100% Portland cement (PC) mortar mix displays the highest strength at 37 MPa, with a gradual decrease in strength as PC is substituted by the slag. For instance, the substitution with GGOBFS1 decreased the strength by 10 MPa, 15 MPa, and 21 MPa at 15%, 30%, and 50% replacement respectively for the 2 days curing age. The same trends were observed for the rest of the slag samples, and the level of reduction in strength is expected to depend upon the reactivity of the individual slag sample. Comparing individual slag performance, the AMSA slag showed marginally the lowest reduction in strength from the reference mortar mix, followed by the GGOBFS2 slag. Norrarat et al. (2019) noted that during slag cement hydration, the three processes that contribute to strength development are the hydration of PC, the reactivity of the slag and the packing effect of small particles. This contributes to the comparatively higher reactivity of the GGOBFS2 and AMSA slag samples since they are finer than the TkSE and GGOBFS1 slag samples. However, the differences in chemical composition between the slags should also be considered.

As the curing age increases, all the blended slag cement mixes start catching up with the reference cement mix, even for the higher substitution mixes (50%). At 28 days of curing, the compressive strength of the reference PC is 59 MPa and the strength differential reduces for the rest of the curing ages. On the other hand, the slag samples display slower early strength development, with significant improvement only after 7 days of curing. It can be seen that more than 90% of the strength for the reference cement is gained within the first 28 days of curing. This observation is in agreement with the value denoted in (SANS 50197-1:2013) that the

strength of a 52.2R cement mortar specimen should be ≥52.2 MPa after 28 days. Moreover, the slower rate of strength development of the blended slag-cements is also dependent on the amount of PC replaced by the slag: the higher the amount of PC replaced, the slower the strength development. However, this is only applicable to early ages since the difference in strength development is smaller after 28 days for the same slag sample. To further emphasize on the rate of strength development, the strength results were re-plotted in terms of strength gain as shown in Figure 79.

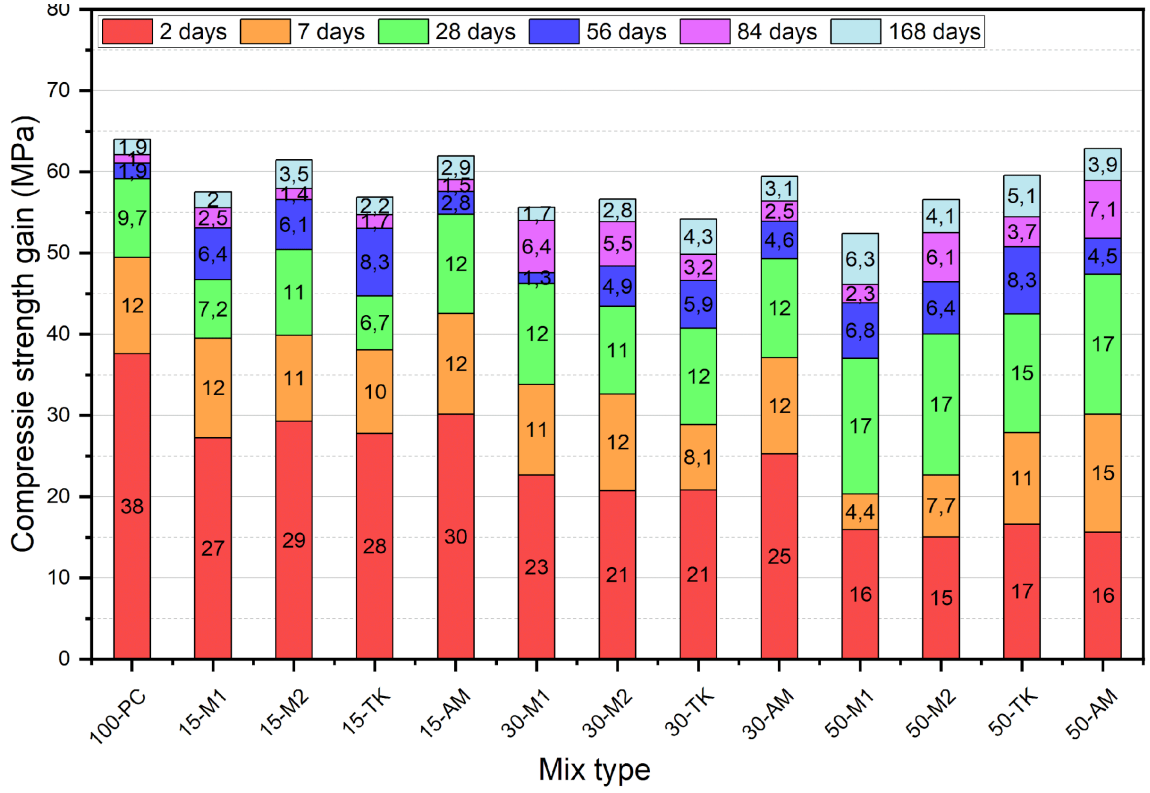


Figure 79: Strength gain results

A comparison of the 4 slag samples on a compressive strength basis, as per Figure 79, shows that the AMSA slag is the best performing slag overall. This is clearly illustrated by its consistent higher strength at each curing age and for all the replacement levels (15%, 30%, 50%), compared to the GGOBFS1, GGOBFS2 and TkSE slag results. Using the 15% substitution at 28 days curing interval, the GGBFS2 slag has the highest at 54 MPa, followed by GGOBFS2 at 52 MPa, then GGOBFS1 at 47 MPa, and TkSE at 44 Mpa. This highlights that increased fineness leads to increased compressive strength, which is also as reported in the studies by Sakai et al., 1992 and Binici et al. 2007. The second-best performing slag is GGOBFS2; however, its strength development performance shows some inconsistency. This can be explained with reference to the 30% slag substitution, where the strength of GGOBFS2 was lower, at 21 MPa, than that of GGOBFS1, at 23 MPa, for 2 days' curing, and further, the GGOBFS2 strength is equal only after 84 days of curing. Moreover, at 50% slag substitution, the GGOBFS2 strength was lower up to 7 days, compared to the TkSE strength, with matching strength reached after 28 days of curing.

The strength gain results in Figure 79 show that the rate of strength gain seems to be dependent on firstly the hydration of PC. It is through the hydration of alite and belite in cement that calcium hydroxide (CH), is formed. This, in turn, activates the slag and reacts with amorphous SiO_2 and Al_2O_3 from the slag through what is known as the pozzolanic reaction to produce calcium silicate hydrate (C-S-H) gel and calcium aluminosilicate hydrate (C-A-S-H) gel (Ahmad et al., 2023; Kolani et al., 2012; Islam et al., 2011). The CaO from the slag also contributes to the production of C-A-S-H and C-S-H by increasing the CaO/SiO_2 (C/S) ratio, and it can also form C-A-H gels. It is also possible for Mg^{2+} in the slag to be accommodated in the C-S-H gel by partially replacing Ca^{2+}, or it can also form M-A-H (Stephant et al., 2015; Chen, 2006; Dunne, 2019). The hydration mechanisms of the slag-cement blend will be further discussed in chapter 6. It can be seen that the hydration of the slag-cement blend is dependent on the amount of CH generated, which is in turn reliant on the amount of Portland cement in the blended slag-cement. Hence, this explains how increments in slag substitution do not always yield higher strength, even in the longer term, as it also affects the C/S ratio of the main binding phase, C-S-H.

The other two factors that affect the rate of strength development are the overall reactivity of the slag, which is linked to its core properties, and the amount of slag used as replacement. With reference to the results in Figure 79, it is mainly the hydraulic reaction of PC and micro-filling effect of slag that controls the strength development between 2 and 7 days. This can be explained by the constant strength gain of 10 to 12 MPa at 15% substitution for all the slag samples. Similarly, the same phenomenon happens for the 30% substitution, except the strength gain of TkSE that was lower at 8 MPa. Interestingly, as the proportion of the slag increased to 50%, the differences between the strength gains amongst the slags became more noticeable, explained by the lower strength gain of 4 MPa for GGOBFS1 compared to the significantly larger gain of 15 MPa for the AMSA slag. This might be an indication of the fact that as the slag substitution increases, the impact of the micro-filling effect on the strength gain becomes more significant between 2 and 7 days. Unsurprisingly, since the micro-filling effect comes from the slag, higher slag substitution should clearly intensify that effect.

Between 7 and 28 days, it is a synergy of slag activity, micro-filling, and PC hydration that controls the rate of strength development, with the slag reactivity the dominant factor since sufficient CH is already released. However, the hydration of PC continues to have an effect on the strength development. Moreover, after 28 days, it is most likely the slag reactivity that has the major impact on the strength development. This is indicated by the low strength gain of 1.9 MPa, 1 MPa, and 1.9 MPa by the reference cement mix compared to the significant strength gains observed in blended slag-cement mixes after 56, 84, and 168 days, respectively. This shows that the blended slag-cement mixes continue to gain strength significantly, especially the 30% and 50% slag mixes. It has been highlighted that the hydraulic reaction of PC is faster than the pozzolanic reaction, which is linked to slag reactivity (Sun and Zhang, 2021; Chen and Brouwers, 2006). This explains the faster and higher strength gain from the specimens within the first 28 days, especially at lower slag substitution (15%), where above 80% of the strength was accumulated within the first 28 days. For slag samples that experienced delayed activation, such as GGOBFS1, and TkSE, the 28 days' cumulative strength is around 75%.

As per list of common cements in SANS 50197-1:2013 and BS-EN 197-1:2011, the 15%, 30% and 50% slag-cement mixing ratios fit the CEM II/A (6-20% slag), CEM II/B (21-35% slag), CEM III/A (36-65% slag) cements, respectively. Moreover, the strength classes are summarized in Table 13. It should be noted that the strengths in SANS 50197-1:2013 are tested using EN 196-1:2016 (or SANS 50196-1), which employs a 40x40x160 mm prism, first tested in flexure, then the two halves in compression. They therefore differ from the standard the 50x50x50 cube test conducted in this study, and the comparison of strength values in the subsequent paragraph is just used as a rough indication of strength performance.

Table 13: Summary of strength classes (BS-EN 197-1:2011)

Strength class	Early strength (MPa)		Standard strength (MPa)	
	2 days	7 days	28 days	
32.5 N	-	≥16	≥32.5	≤52.5
32.5 R	≥10	-		
42.5 N	≥10	-	≥42.5	≤62.5
42.5 R	≥20	-		
52.5 N	≥20	-	≥52.5	-
52.5 R	≥30	-		

Using the compressive strength results in Figure 79, It can be seen that only all 15% slag samples (CEM II/A-S) fit the 42.5 R strength class. The AMSA slag sample even reached the 52.5 R class due to its comparatively higher reactivity, followed by the GGOBFS2 sample that almost reached the requirement of the 52.5 N class at 15% slag substitution. Using the 30% slag substitutions, all the slag passed the 42.5 R strength class requirement with the exception of the TkSE slag sample that did not manage to reach 42.5 MPa at 28 days of curing due to its lower reactivity linked to lower fineness. Lastly, only the AMSA and surprisingly the TkSE samples met the 42.5 N strength class at 50% slag substitution. GGOBFS2 achieved a strength of 40 MPa at 50% slag substitution, hence could fit the 42.5 N strength class. However, all the 50% slag substitutions meet the 32.5 R strength class requirement. It is clear that the novel OBF slag and conventional BF slag demonstrate similar performance in terms of strength class for the different types of slag cement. Therefore, if ground accordingly as per ASTM C989 standard specifications, the novel OBF slag can also be used to manufacture different strength classes of cement as the conventional BF slag.

In summary, both the novel OBF slag and the conventional BF slag display similar strength development patterns because of their similarities in core properties such as the chemical composition, and the glass content. However, it can be seen that rate of strength development in blended slag-cement is a complex process to explain, and it is mainly governed by the synergy of the hydration of PC, the micro-filling effect of both PC and Slag, the amount of PC replaced by the slag, and the overall reactivity of the slag (linked to chemical composition, glass content, and fineness). Generally, the compressive strength increases with increasing fineness and glass content. Moreover, the addition of the slag to cement in mortar mixes

decreases the early strength development (< 28 days) while the late strength development is complex to predict and mainly depends upon the reactivity of the slag.

5.3.3. Slag activity index

The activity index is another key performance indicator of the slag reactivity. It is calculated from the ratio (expressed as %) of compressive strength for the 50% slag mortar mix to 100% PC mortar mix, as expressed in Equation 5.

$$Slag\ activity\ index = \frac{50\%\ Slag\ strength}{100\%\ PC\ strength} * 100 \quad (5)$$

The activity indices of the strength measurement results for the 50 % slag mortar mixes in this study were calculated and the results are summarized in Figure 80.

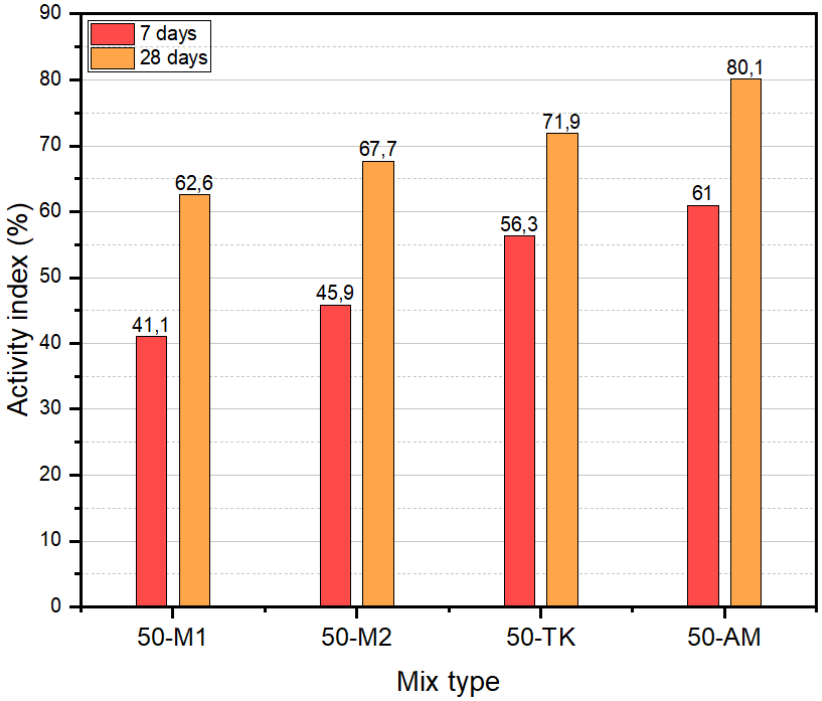


Figure 80: Activity index results

The results in Figure 80 show that the activity index increases as the curing age increases for the slag samples. For instance, the GGOBFS2 (50-M2), the activity index is 45.9% at 7 days, then increased to 67.7 % at 28 days of curing. This demonstrates how close the strength of blended 50% slag-cement mix gets to the strength of the 100% PC mortar mix as the curing age increases, and this further highlights the dominance of the PC hydration on the strength development at early curing ages. The activity indices of slags and the SANS 55167-1:2011 specifications are further summarized in Table 14.

Table 14: SANS specifications of activity index and fineness

Activity Index (%)	SANS 55167	GGOBFS1	GGOBFS2	TKSE	AMSA
7 days	≥ 45	41,1	45,9	56,3	61,0
28 days	≥ 70	62,6	67,7	71,9	80,1
Slag characteristics					
Surface area (m^2/kg)	≥ 275	255	267	258	296
Glass count (%)		90	95	95	95

As per SANS 55167-1:2011, the activity index at 7 days and at 28 days shall be not less than 45% and 70%, respectively. At 7 days, the GGOBFS2, TkSE, and AMSA slags conform to the minimum Activity Index requirement, with the AMSA slag having the highest activity index of 61% at 7 days of curing. In addition, the highest index value of 80.1% at 28 days of curing, was also achieved by the AMSA slag. It was further noted in SANS 55167-1:2011 that the activity index gives no direct information on the strength contribution of ground granulated BF slag in concrete, and the use of the ground granulated BF slag is not limited to the mixing ratio used in the activity index test. Therefore, the performance of the slag in cement is not only limited to the 50% mixing ratio.

The lower comparative performance of the GGOBFS2 slag might firstly be related to its wide particle size distribution (PSD) in case the samples taken for casting the different specimens were not closely homogeneous. Celik (2009) stated that the uniformity of the distribution is very important for cement strength development and if the fine and coarse tails are minimized to achieve a narrow PSD, improvement on the strength can be made. This is because the hydration rate of coarser particle is slower compared to the hydration of finer particles (Wang et al., 2005), while GGOBFS2 had a mixed amount of finer and coarser particles, with 37% of particles less than 10 µm, and with 60% of particles between 10 and 100 µm as noted in chapter 4 of this study. Secondly, all the slags milled at laboratory scale (GGOBFS1, GGOBFS2, TkSE) were ground to a lower fineness level than the AMSA slag (in terms of Blaine surface area) and did not meet the minimum standard fineness of 80% passing 45 µm and a corresponding Blaine fineness of 275 m^2/kg as per ASTM C989. This influences their relatively lower activity indices compared to the industrially milled AMSA slag sample.

5.3.4. Effect of water/binder ratio

The water to binder ratio (w/b) plays a crucial role during the hydration of either pure PC cement, or blended slag-cement since water acts as the reactant to the formation of the main binding phase C-S-H and ultimately, the production of CH. The w/b ratio was kept constant in this study at 0.5 but was changed to 0.4 for one mix (15% GGOBFS1) in order to investigate the impact of this change at two early curing intervals, and the results are shown in Figure 81.

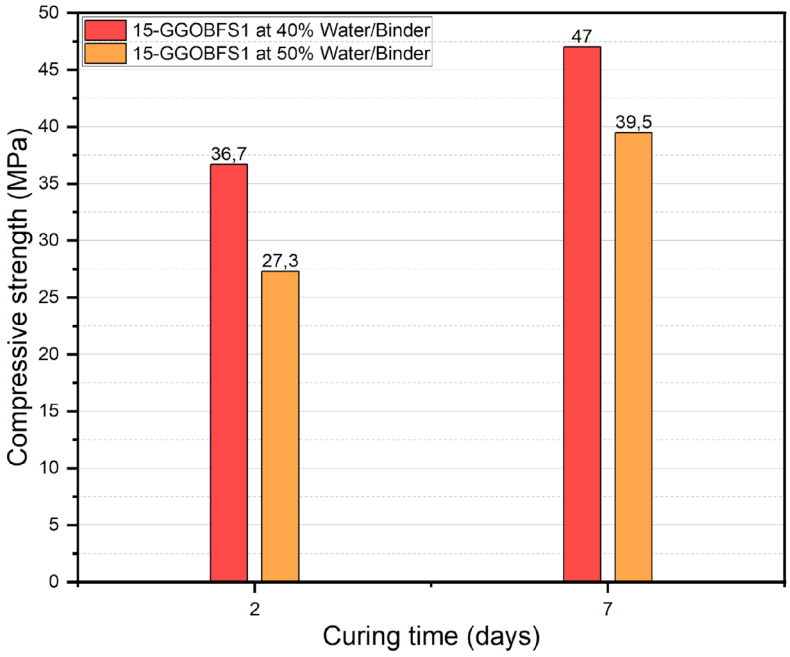


Figure 81: Impact of water to binder ratio

As per Figure 81, it can be seen that the 15% GGOBFS1 mortar mix responded to a reduction in the w/b ratio as the compressive strength increased from 27.3 MPa to 36.7 MPa at 2 days of curing with the w/b ratio decreased from 50% to 40%. The same phenomenon was observed at the 7 days' curing interval as the strength increased from 39.5 MPa to 47 MPa. This illustrates the effect of excess water on mortar strength. The excess moisture will eventually evaporate partly from the hydration reaction which releases heat due to normal from drying of the specimen, but the corresponding compressive strength will be lower. The increment in strength due to a reduction in w/b ratio was also observed by Sun and Zhang (2021) where the long-term compressive strength was lower at 50 MPa for 0.45 w/b compared to 75 MPa at 0.34 w/b with curing for 360 days.

As shown in the previous section on workability, decreasing the w/b ratio will decrease the workability and can lead to the specimen having unreacted slag and cement, which will in turn reduce the strength. It can be seen that the selection of both high and low values for the w/b ratio has consequences since the extra moisture will eventually evaporate from the cured mortar, possibly leading to high porosity (Sutan et al., 2011), while less water will lead to incomplete hydration processes as shown by the water dependence of hydration reactions. The 0.5 w/b ratio was used in this study since it was defined by the standard testing procedure. The main key point is to identify the stoichiometrically required amount of water for the mix through experiments. However, the hydration reactions of cement are very complex to isolate, and even more complex for the hydration of blended slag-cement.

5.4. Drying shrinkage

5.4.1. Importance

Drying shrinkage is another important performance indication of either concrete, or mortar performance. Drying shrinkage is due to moisture loss after setting as opposed to plastic

shrinkage, which generally occurs before setting. Moreover, it can either be at an early age during the first day of batching, or at later ages, after 24 hours (Taylor and Wang, 2014; Tia et al., 2005). Yuan et al. (2015) stated that drying shrinkage of concrete is a principal cause for bridge deck cracking and subsequent deterioration. Several factors have been found to influence the shrinkage of concrete, including the mix design, environmental conditions, and construction procedures. There is conflicting information in the literature whether the addition of slag increases, or decreases the drying shrinkage of concrete, or mortar specimens.

5.4.2. Drying shrinkage results

In this study, the drying shrinkage was evaluated for mortar mixes made from 100% PC and blended slag cement with the novel OBF and the conventional BF slag at 3 replacement levels (15%, 30%, and 50%). The tests were conducted as per ASTM/C596 – 23, and the results are summarized in Figure 82.

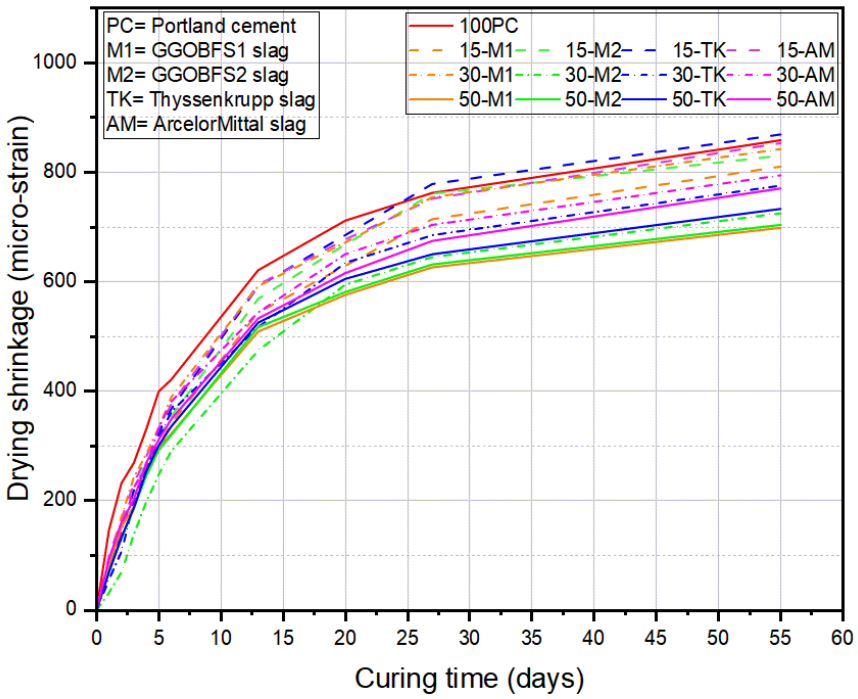


Figure 82: Drying shrinkage results for all replacement levels

The results in Figure 82 show that the control mix with 100% PC has a higher cumulative strain, especially for early ages (< 20 days). Thereafter the 15% slag-cement blended mixes displayed higher cumulative shrinkage. However, the difference is very marginal compared to the reference mix. The results in Figure 82 were replotted for each slag substitution level in order to better understand the impact of each slag substitution as shown in Figures 83, 84, and 85.

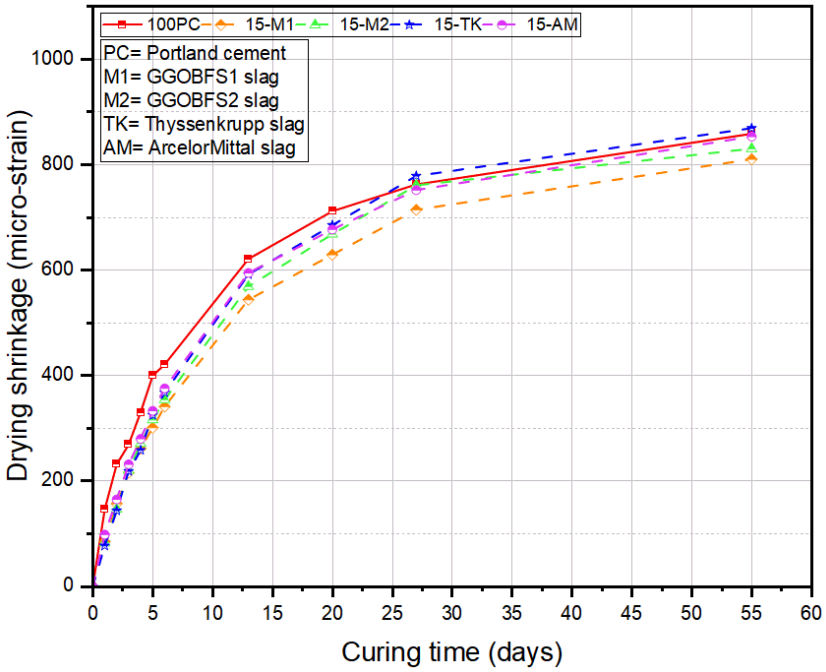


Figure 83: Drying shrinkage results for 15% slag substitution

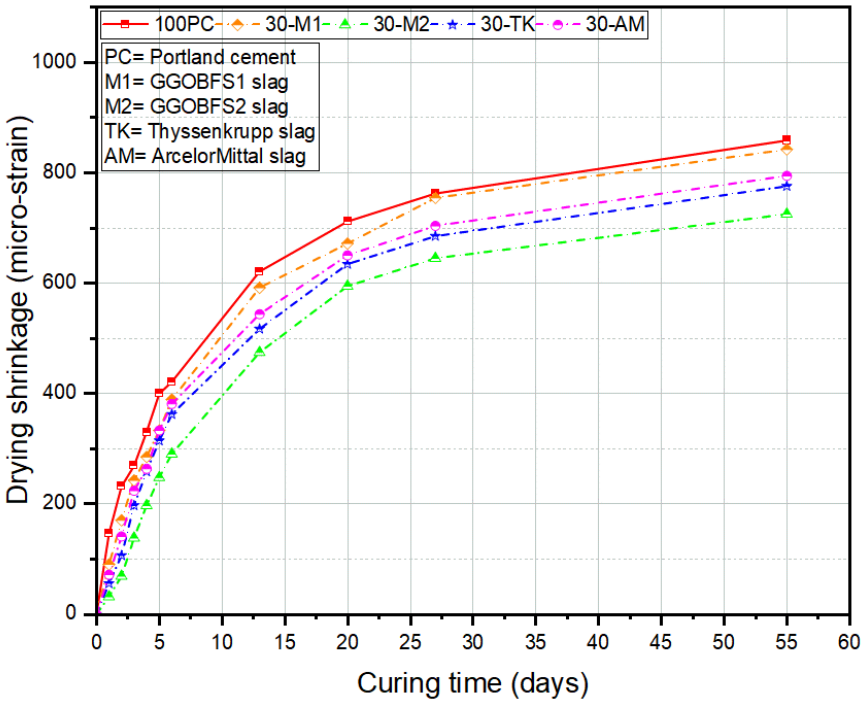


Figure 84: Drying shrinkage results for 30% slag substitution

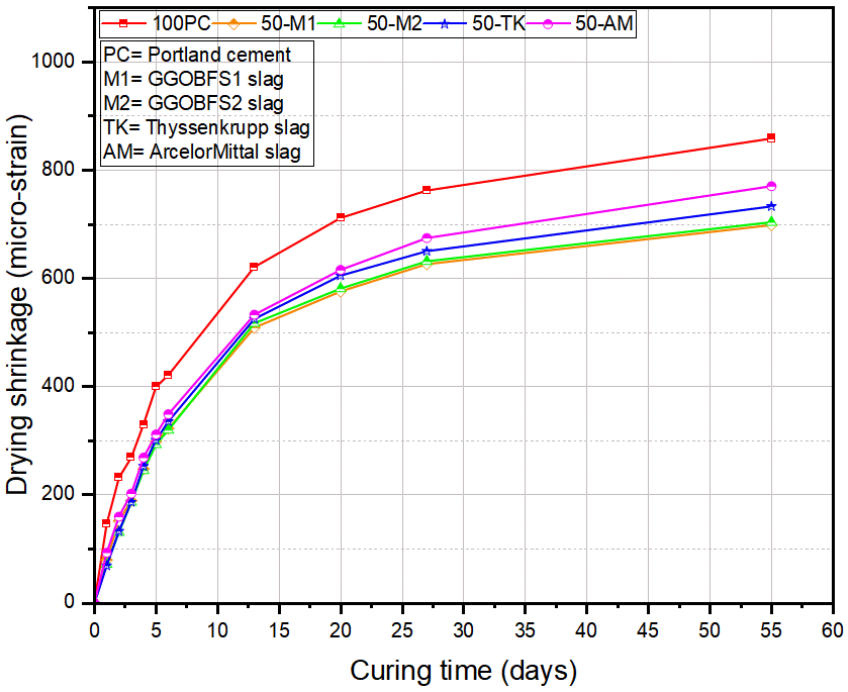


Figure 85: Drying shrinkage results for 50% slag substitution

From the trends observed in Figures 83, 84, and 85 for the 3 slag substitution levels, it can be seen that as the proportion of the slag increases, the strain in the specimen decreases accordingly. For instance, GGOBFS1 was the slag sample that decreased the strain the most at the 15% substitution level, as per Figure 83, and the decrement is approximately 50 micro-strains. Similarly, for GGOBFS2, at the 30% substitution level, as per Figure 84, the decrement is around 120 micro-strains. Lastly, for the 50% substitution level, the decrement is around 150 micro-strains as shown in Figure 85. The 15% TkSE sample displayed a higher shrinkage than that of the 100% PC as per Figure 83, while the same phenomenon also happens to GGOBFS1 at 30% substitution. It is clear that while comparing the different slag samples in this study, there is no consistent trend for all the substitution levels and for both the conventional BF slag and the novel OBF slag.

In summary, the replacement of PC by the slag in mortar specimens does decrease the drying shrinkage, as indicated by measurements taken up to 55 days, with increasing slag content resulting in lower shrinkage levels. The observed change is small, (< 150 micro-strains) for replacement levels up to 50%. The Slag Cement Association (SCA) conducted a critical review based on published shrinkage research data and concluded that slag cement seems to have a marginal effect on increasing the drying shrinkage. The practical meaning of the slight increase and decrease in drying shrinkage of the mortar specimens remains to be explored. Overall, the change in drying shrinkage with the addition of either the novel OBF, or the conventional BF slag is small. Therefore, based on the results observed in this study, it can be concluded that the replacement of PC by either the novel OBF, or the conventional BF slag decreases the drying shrinkage of the mortar mixes, and the decrement level is proportional to the amount of PC replaced by the slag.

5.5. Qualitative observations: greening effect

During the strength measurement tests, as the cubic specimens break, a temporary blue to greenish coloration was observed on the freshly exposed surfaces of broken specimens containing blended slag-cement. This temporary coloration of the specimen surface is known as the greening effect as per (Couvidat et al., 2021; Le Cornec et al., 2017; Sioulas and Sanjayan, 2001). An image illustrating this coloration for the 50% slag cement mixes is shown in Figure 86.

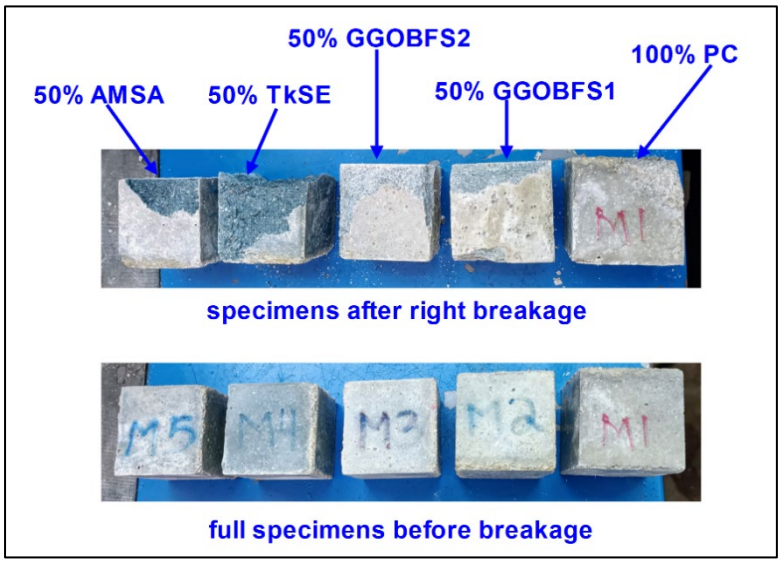


Figure 86: greening effect of novel OBF slag compared to conventional BF slag at 84 days

Several studies have linked this temporary coloration to the sulphur content of the slag and iron compounds (Vernet, C., 1982; Sioulas and Sanjayan, 2001). Other authors have pointed out that the greening effect is linked to the progressive oxidation of polysulphide complexes that are initially present in GGBFS during curing (Le Cornec et al., 2017). The greening effect does disappear in a few days or weeks after exposure to air and the specimen's surface takes on a light grey colour; however, the inside remains green for years since it is not exposed to air. Le Cornec et al. (2017) stated that no indications of the effect on mechanical properties of concrete specimens have been reported, nor evidence of impacts on occupational health, or environmental consequences during demoulding of the concrete. Couvidat et al. (2020) conducted leaching experiments to evaluate the environmental impact and found that the sulphur is present mainly as sulphides, and oxidation leads to the formation of thiosulphates and sulphates as the main products. However, the sulphate levels were lower than threshold limit values for both inert waste and alternate materials reused in road construction. Furthermore, no chromium, or other hazardous metals, were detected in the leachates. This highlights the non-hazardous and negligible environmental impact associated with the greening effect.

There are different theories in the literature regarding the origin of this discoloration, but the common factor is the sulphur content of GGBFS. Piatak et al., (2015) reported that GGBFS usually contains noticeable amounts of sulphur between 1.0 and 1.9 wt.%, mostly under reduced form. The novel OBF slag has a relatively low sulphur content (< 0.30%) compared to the commonly observed sulphur content of 1 – 2% in conventional BF slags (Roy, 2009).

From the image in Figure 86, it can be seen that the greening effect in the novel OBF slag samples (GGOBFS1, GGOBFS2) is relatively minor, almost unnoticeable compared to the greening effect observed for the conventional BF slag samples (AMSA, TkSE). This supports the conclusion that the degree of the greening effect is also dependent on the amount of sulphur present in the slag. Moreover, during the experiments, it has been noted that the intensity of coloration increases as the slag starts to react with PC, and the reaction becomes significant after 7 days of curing as per the trends observed in the strength development results.

The degree greening effect was moderate for the 30% mixes and almost unnoticeable for the 15% mortar mixes. This reaffirms the statement by Sioulas and Sanjayan (2001) that the degree or intensity of the coloration increases with increasing slag content since the coloration originates from compounds in the slag. For the novel OBF slag, however, the intensity of the coloration was still very low even at 50% replacement, indicating the low level of these colour-inducing compounds in the novel OBF slag. Schrama et al. (2017) stated that coke is the main source of sulphur in BF-BOF steelmaking, even though approximately 40% of sulphur is removed through the coking process, leaving around 0.5% of sulphur in the final coke. In comparison, the OBF process uses less coke than the BF process since 90% of the iron is already in the metallic state after the DRI process. This results in the low sulphur content of the novel OBF slag and ultimately, less intensity of greening effect.

5.6. CO_2 emissions reduction with addition of the novel OBF slag

The CO_2 emissions reduction with slag addition has been approximated in previous studies, and the observations in Figure 87 was adapted from (Bolte et al, 2023; Szpotowicz and Toth, 2024) using the 28-days compressive strength data from this study.

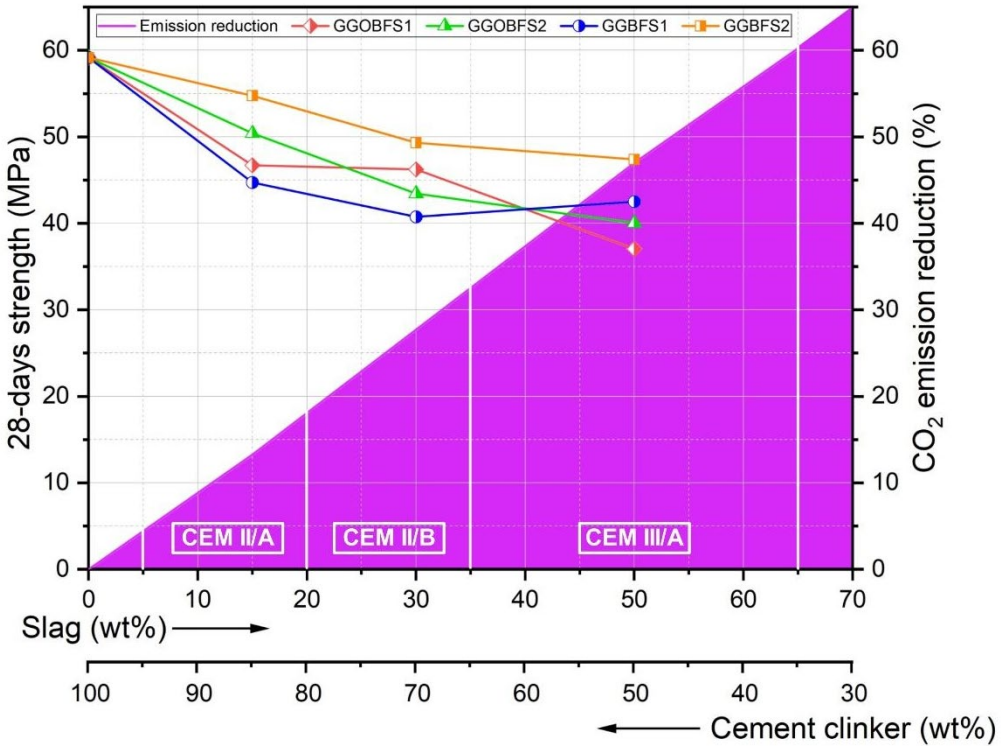


Figure 87: CO_2 emissions reduction with slag addition

The 28-days strength was selected in order to account for the individual reactivity of the slag, which only start to significantly contribute to the strength gain of specimens after 7 days. Figure 87 show that the slag substitution level is inversely proportional to the 28-days strength, the more reactive the slag, the lower the strength drop compared to the 0% slag, even at high slag substitution like for GGBFS2, previously labelled as AMSA. The trends for GGBFS1 GGOBFS1, and GGOBFS2 are mixed up beyond 15% slag substitution due to associated experimental errors and reactivity related factors. Overall, it can be seen that the CO_2 emissions in the cement industry can be reduced by increasing the proportion slag in slag-cement blends. Similar to the conventional BF slag, the novel OBF slag can also reduce up to 60% of CO_2 emissions associated with clinker production depending on the type of cement produced (CEM II, or CEM III). Moreover, if the reactivity of the slag is enhanced by further modifying the chemical composition, the CO_2 reduction potential can even go beyond 60%.

5.7. Conclusions

Based on the Workability, Compressive strength, and Drying shrinkage tests, the novel OBF slag has displayed similar and comparable results to the conventional BF slag. The two slag types have similar core properties (chemical composition and glass count) that define the cementitious performance for ground granulated slags. Slight differences in workability, compressive strength, and drying shrinkage arise when performance-defining properties of the slag such as, the fineness and the glass content are not the same. Higher fineness of the slag is beneficial to accelerate the hydration reaction in terms of strength development, but also comes at a cost in terms of high water-demand, or reduced workability if the slag's particle size is very fine.

From visual examination of cured mortar specimens, before and after crushing (to expose the internal appearance), the intensity of the greening effect is lower in the novel OBF slag compared to the conventional BF slag due to the relatively lower sulphur content of the novel OBF slag. Moreover, similar to the conventional BF slag, the usage novel OBF slag can also reduce up to 60% of CO_2 emissions associated with clinker production along with the energy requirement. Unlike the BF slag, the novel OBF slag possesses relatively lower embodied CO_2 associated with its production. Generally, the addition of slag to the cement mortar mixes has the following effects:

- The workability of the mortar mix increases, and higher slag substitution is equivalent to higher workability.
- The early strength development decreases (< 28 days) while the late strength development is complex to predict and mainly depends upon the reactivity of the slag and its proportion in the mix.
- The rate of strength development in blended slag-cement is mainly governed by the synergy of the hydration of PC, the micro-filling effect of slag, the amount of PC replaced by the slag, and the overall reactivity of the slag (linked to chemical composition, glass content, and fineness).
- The compressive strength increases with increasing slag fineness and glass content; however, more tests should be conducted to confirm these trends since the slag samples in this study have roughly similar but not identical chemical compositions.

- The drying shrinkage decreases, and the decrement level is very minimal and proportional to the amount of PC replaced by the slag.

References

Ahmad, M.A., Ranaivomanana, H., Bonnet, S., L'Hostis, V. and Buttin, P. (2023). Study of Hydration Properties for Blast Furnace Slag-Blended Cement: Prediction of Slag Hydration Kinetics. *Rilem bookseries*, pp.165–176. doi:https://doi.org/10.1007/978-3-031-33187-9_16.

ASTM C109/C109M – 23. Standard Test Method for Compressive Strength of Hydraulic Cement Mortars (Using 50 mm [2 in.] Cube Specimens). DOI: 10.1520/C0109_C0109M-23.

ASTM C989/C989M − 22 Standard Specification for Slag Cement for Use in Concrete and Mortars. DOI: 10.1520/C0989_C0989M-22.

ASTM/C1437 − 20. Standard Test Method for Flow of Hydraulic Cement Mortar. DOI:10.1520/C1437-20.

ASTM/C596 – 23. Standard Test Method for Drying Shrinkage of Mortar Containing Hydraulic Cement, ASTM International, West Conshohocken, PA, USA. DOI:10.1520/C0596-23.

Bediako, M. and Kevern, J. (2016). Effects of Chemical Admixture on Flow and Strength Properties of Calcined Clay Used as a Supplementary Cementitious Material. *British Journal of Applied Science & Technology*, 13(5), pp.1–6. doi:https://doi.org/10.9734/bjast/2016/22905.

Binici, H., Temiz, H. and Köse, M.M. (2007). The effect of fineness on the properties of the blended cements incorporating ground granulated blast furnace slag and ground basaltic pumice. *Construction and Building Materials*, 21(5), pp.1122–1128. doi:https://doi.org/10.1016/j.conbuildmat.2005.11.005.

Bolte, G., Schade, T. and Bullerjahn, F. (2023). Synergies of steel and cement industry: how to replace declining GBFS quantities by scrap based, engineered EAF-slag. In: *Proceedings of the 8th International Slag Valorisation Symposium*. Mechelen, Belgium: KU Leuven Institute for Sustainable Metals and Minerals.

Brough, A.R. and Atkinson, A. (2002). Sodium silicate-based, alkali-activated slag mortars. *Cement and Concrete Research*, 32(6), pp.865–879. doi:https://doi.org/10.1016/s0008-8846(02)00717-2.

BS EN 197-1: 2011. Cement. Composition, Specifications and Conformity Criteria for Common Cements. European Committee for Standardization. British Standards Institution, London.

Celik, I.B. (2009). The effects of particle size distribution and surface area upon cement strength development. *Powder Technology*, 188(3), pp.272–276. doi:https://doi.org/10.1016/j.powtec.2008.05.007.

Chen, W. 2007. *Hydration of slag cement - Theory, Modelling and Application*. Doctor of Philosophy, University of Twente, Enschede.

Chen, W. and Brouwers, J. (2006). The hydration of slag, part 2: reaction models for blended cement. *Journal of Materials Science*, 42(2), pp.444–464. doi:https://doi.org/10.1007/s10853-006-0874-1.

Couvidat, J., Diliberto, C., Meux, E., Cotelle, S., Bojic, C., Izoret, L. and Lecomte, A. (2021). Greening effect of slag cement-based concrete: Environmental and ecotoxicological impact. *Environmental Technology & Innovation*, 22, p.101467. doi:https://doi.org/10.1016/j.eti.2021.101467.

Couvidat, J., Diliberto, C., Meux, E., Izoret, L. and Lecomte, A. (2020). Greening effect of concrete containing granulated blast-furnace slag composite cement: Is there an environmental impact? *Cement and Concrete Composites*, 113, p.103711. doi:https://doi.org/10.1016/j.cemconcomp.2020.103711.

Dunne, C. ed., (2019). *SME mineral processing & extractive metallurgy handbook volume 1*. Englewood, Colorado Society For Mining, Metallurgy & Exploration.

Durekovic, A. (1995). Cement pastes of low water to solid ratio: An investigation of the porosity characteristics under the influence of a superplasticizer and silica fume. *Cement and Concrete Research*, 25(2), pp.365–375. doi:https://doi.org/10.1016/0008-8846(95)00022-4.

Erdogdu, S. (2005). Effect of retempering with superplasticizer admixtures on slump loss and compressive strength of concrete subjected to prolonged mixing. *Cement and Concrete Research*, 35(5), pp.907–912. doi:https://doi.org/10.1016/j.cemconres.2004.08.020.

Gołaszewski, J. and Szwabowski, J. (2004). Influence of superplasticizers on rheological behaviour of fresh cement mortars. *Cement and Concrete Research*, 34(2), pp.235–248. doi:https://doi.org/10.1016/j.cemconres.2003.07.002.

Gupta, S. (2016). Effect of content and fineness of slag as high-volume cement replacement on strength and durability of ultra-high-performance mortar. *Journal of Building Materials and Structures*, 3(2), pp.43–54. doi:https://doi.org/10.34118/jbms.v3i2.23.

Hewlett, P.C. and Liska, M. (Eds) (2019). *Lea's Chemistry of Cement and Concrete*, 5th Edition, Elsevier Science & Technology, Butterworth-Heinemann, Oxford, UK.

Islam, M.M., Islam, M.S., Rahman, M.A. and Das, A. (2011). Strength Behavior of Mortar Using Slag as Partial Replacement of Cement. *MIST Journal: GALAXY (DHAKA)*, 3. doi:https://doi.org/10.3329/mist.v3i0.8053.

Kolani, B., Buffo-Lacarrière, L., Sellier, A., Escadeillas, G., Boutillon, L. and Linger, L. (2012). Hydration of slag-blended cements. *Cement and Concrete Composites*, 34(9), pp.1009–1018. doi:https://doi.org/10.1016/j.cemconcomp.2012.05.007.

Le Cornec, D., Wang, Q., Galoisy, L., Renaudin, G., Izoret, L. and Calas, G. (2017). Greening effect in slag cement materials. *Cement and Concrete Composites*, 84, pp.93–98. doi:https://doi.org/10.1016/j.cemconcomp.2017.08.017.

Meusel, J.W. and Rose, J.H. (1983). Production of Granulated Blast Furnace Slag at Sparrows Point, and the Workability and Strength Potential of Concrete Incorporating the Slag. *Special publication - Royal Society of Chemistry/Special publication*, 79, pp.867–890. doi:https://doi.org/10.14359/6730.

Norrarat, P., Tangchirapat, W., Songpiriyakij, S. and Jaturapitakkul, C. (2019). Evaluation of Strengths from Cement Hydration and Slag Reaction of Mortars Containing High Volume of Ground River Sand and GGBF Slag. *Advances in civil engineering*, 2019, pp.1–12. doi:https://doi.org/10.1155/2019/4892015.

Piatak, N.M., Parsons, M.B. and Seal, R.R. (2015). Characteristics and environmental aspects of slag: A review. *Applied Geochemistry*, 57, pp.236–266. doi:https://doi.org/10.1016/j.apgeochem.2014.04.009.

Roy, A. (2009). Sulfur speciation in granulated blast furnace slag: An X-ray absorption spectroscopic investigation. *Cement and Concrete Research*, 39(8), pp.659–663. doi:https://doi.org/10.1016/j.cemconres.2009.05.007.

Sakai, K., Watanabe, H., Suzuki, M. and K Hamazaki (1992). Properties of Granulated Blast-Furnace Slag Cement Concrete. *American concrete association*, 132, pp.1367–1384. doi:https://doi.org/10.14359/1232.

SANS 50197-1:2013. South African National Standard for Cement Part 1: Composition, Specifications and Conformity Criteria for Common Cements, South African Bureau of Standards, Pretoria, South Africa

SANS 55167-1:2011. Ground granulated blast furnace slag for use in concrete, mortar and grout Part 1: Definitions, specifications and conformity criteria.

Schrama, F.N.H., Beunder, E.M., Van den Berg, B., Yang, Y. and Boom, R. (2017). Sulphur removal in ironmaking and oxygen steelmaking. *Ironmaking & Steelmaking*, 44(5), pp.333–343. doi:https://doi.org/10.1080/03019233.2017.1303914.

Sioulas, B. and Sanjayan, J.G. (2001). The coloration phenomenon associated with slag blended cements. *Cement and Concrete Research*, 31(2), pp.313–320. doi:https://doi.org/10.1016/s0008-8846(00)00371-9.

Slag Cement Association. 2005. Effect of slag cement on shrinkage in concrete. Slag Cement in Construction, No. 27.

Stephant, S., Chomat, L., Nonat, A. and Charpentier, T. (2015). Influence of the slag content on the hydration of blended cement. *Hal.science*. [online] doi:https://cea.hal.science/cea-02509185.

Sun, J. and Zhang, P. (2021). Effects of different composite mineral admixtures on the early hydration and long-term properties of cement-based materials: A comparative study. *Construction and Building Materials*, 294, p.123547. doi:https://doi.org/10.1016/j.conbuildmat.2021.123547.

Sutan, N.M., Hamdan S., Sobuz, H.R., Laja, V.L., Islam, M.S. (2011). Porosity and strength of pozzolan modified cement systems. *Concrete Research Letters*, 2(4), pp.326-33.

Szpotowicz, R. and Toth, C. (2024). Reducing Energy Demand in Concrete Pavements by the Use of Blended Cements. *Acta Technica Jaurinensis*, 17(3), pp.118–129. doi:https://doi.org/10.14513/actatechjaur.00749.

Taylor, P. and Wang, X. (2014). *Concrete Pavement Mixture Design and Analysis (MDA): Factors Influencing Drying Shrinkage*. [online] National Concrete Pavement Technology Center, Iowa State University. Available at: https://api.semanticscholar.org/CorpusID:10136772 [Accessed 12 Dec. 2024].

Tia, M., Y. Liu, and D. Brown. 2005. Modulus of elasticity, creep and shrinkage of concrete. Department of Civil & Coastal Engineering, University of Florida.

Vernet, C., 1982. Comportement de l'ion S^{2-}au cours de l'hydratation des ciments riches en laitier (CLK). Formation de solutions solides de S^{2-}dans les aluminates hydrates hexagonaux.

Wang, P.Z., Trettin, R. and Rudert, V. (2005). Effect of fineness and particle size distribution of granulated blast-furnace slag on the hydraulic reactivity in cement systems. *Advances in Cement Research*, 17(4), pp.161–167. doi:https://doi.org/10.1680/adcr.2005.17.4.161.

Wang, S.-D., Scrivener, K.L. and Pratt, P.L. (1994). Factors affecting the strength of alkali-activated slag. *Cement and Concrete Research*, 24(6), pp.1033–1043. doi:https://doi.org/10.1016/0008-8846(94)90026-4.

Yuan, J., Lindquist, W., Darwin, D. and Browning, J. (2015). Effect of slag cement on drying shrinkage of concrete. *ACI Materials Journal*, [online] 112(2). doi:https://doi.org/10.14359/51687129.

CHAPTER 6: PERFORMANCE EVALUATION OF SLAG-CEMENT PASTES

6.1. Introduction

This chapter includes discussions about the results obtained from the slag-cement paste mixes. The main test conducted on paste mixes is the R^3 reactivity (Rapid, Reliable and Relevant) test as well as the phase evolution of binders in slag-cement paste mixes at varied curing ages. The investigation of phase evolution was done using X-Ray diffractometry (XRD), and Scanning electron microscopy (SEM) as described in chapter 3 of this study. The heat and phase evolutions of the novel OBF slag and the conventional BF slag are linked to the reactivity of the slag. As highlighted in chapter 4, the chemical compositions of the main slag samples in this study (TKSE, AMSA, GGOBFS1, GGOBFS2) are roughly similar, leaving the glass content, the fineness, and the mixing ratio as the properties that can influence differences in cementitious performance among the slags in this study. The results are critically discussed and compared with observations from the literature in order to draw conclusions. It should be noted that the Portland cement (PC) used in this study is the CEM I 52.5R, Rapid Hard Cement, and the following cement notations will be used along this chapter:

- C= CaO
- S = SiO_2
- A = Al_2O_3
- M= MgO
- H= H_2O
- $\bar{S}$= SO_3
- $\bar{C}$= CO_3

6.2. Difference between pozzolanic and hydraulic reaction

It is important to emphasize the difference between hydraulic and pozzolanic reactions. A hydraulic reaction is regarded as the reaction of calcium silicate (CS) compounds in cement such as alite (C_3S), and belite (C_2S) with water (H) to generate the main binding phase, calcium silicate hydrate (C-S-H) and portlandite (CH) as a by-product as per Equation 1. On the other hand, a pozzolanic reaction is the reaction of silica (S) and aluminium oxide (A) from a pozzolanic material, including slag, to form secondary C-S-H or C-A-S-H as per Equations 2 and 3 (Sun and Zhang, 2021; Chen and Brouwers, 2006; Dunne, 2019).

- (C_3S and C_2S) from Portland cement + H = Primary C-S-H + CH (1)
- SiO_2 from pozzolanic materials + CH = Secondary C-S-H (2)
- Amorphous SiO_2 and Al_2O_3 + CH = C-A-S-H (3)

Other reactions, Equations 6-8, are also reported to occur during the hydration of blended slag cement since the slag, being latent hydraulic, displays some hydraulic properties once activated by CH (Chen and Brouwers, 2006; Stephant et al., 2015; Chen, 2007):

- Amorphous CaO and SiO_2 + H = Secondary C-S-H (6)
- Amorphous CaO and Al_2O_3 + H = C-A-H (7)
- Amorphous MgO and Al_2O_3 + H = M-A-H (8)

It should be noted that the above reactions are just simplified versions of the actual hydraulic and pozzolanic reactions in cement blended with slag. These reactions are generally complex in nature as it will be discussed later in section 4 of this chapter.

6.3. Reactivity results

6.3.1. Importance

The reactivity of the slags in this study was evaluated using the R^3 reactivity test. It should be noted that this test does not differentiate between hydraulic and pozzolanic reactivity; however, it provides information on the combined chemical reactivity (Avet et al., 2016; Londono-Zuluaga et al., 2022). In addition, the reactivity tests were conducted as per ASTM/C1897 – 20 to assess the chemical reactivity (hydraulic and pozzolanic) of the novel OBF slag in comparison to the conventional BF slags by measuring the heat released over a hydration period of 7 days. Further details of the experimental procedure can be found in chapter 3 of this study. Generally, a slag with higher reactivity will release a comparatively higher amount of heat during hydration. As noted in the previous chapters, the reactivity of the slag is linked to the combined effect of its core properties: the chemical composition, the glass content, and the fineness.

6.3.2. Cumulative heat results

The reactivity tests were performed using a Calmetrix I-Cal 4000H 4-chamber isothermal Calorimeter. The cumulative heat results obtained after the slag cement pastes, at 40°C , as per the mix design and test procedure set out in chapter 3, are shown in Figure 88. It should be noted that the tests were conducted for 7 days but the results are shown for the first 72 hours in order to clearly highlight the differences and similarities between the mixes.

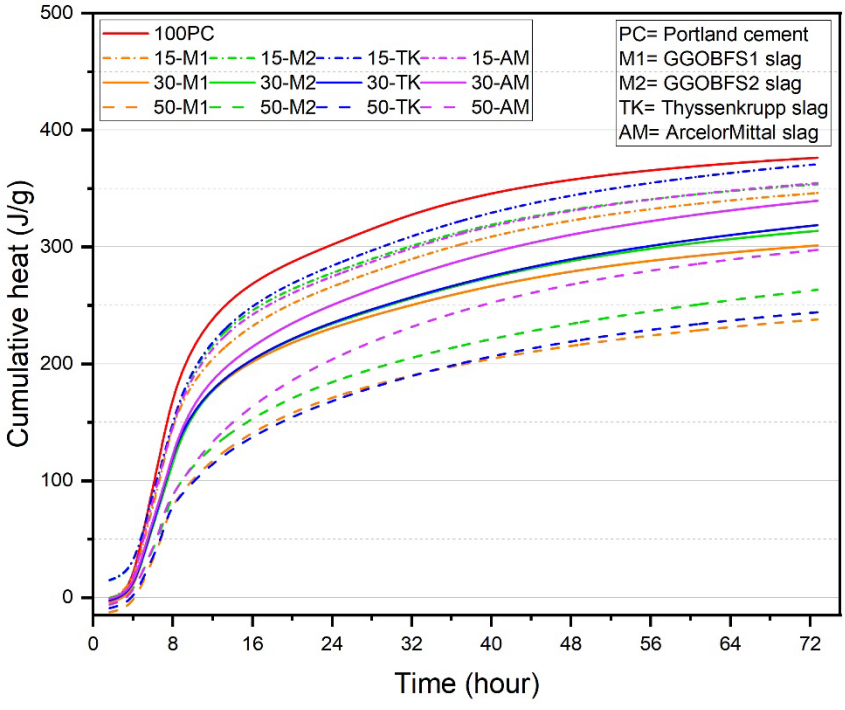


Figure 88: Cumulative heat release over 72 hours

From a broad point of view, the results in Figure 88 show that the 100% PC mix released the highest amount of heat, with a 72-hours cumulative total of approximately 375 J/g. This is expected since the hydraulic reactions in pure PC are more exothermic compared to the pozzolanic and hydraulic reactions in blended slag cements (Dunne, 2019; Hewlett and Liska, 2019). As the slag was substituted, the cumulative heat release decreases in relation to the amount of PC replaced. This is in agreement with the report by Kolani et al. (2012) that the reduction of heat of hydration is among the main reasons for the use of GGBFS in blended slag cements, which ultimately lowers the thermal stresses in concrete.

The 15% slag mixes reduce the 72-hours' cumulative heat of hydration of PC from 375 kJ to a range of 345 – 370 J/g for the 4 slag blends. The slag sample showing the highest heat reduction is GGOBFS1 at 345 J/g, whereas the slag sample with lowest heat reduction is TkSE at 370 kJ. This demonstrates the relatively higher reactivity of the TkSE slag at the 15% substitution level. This is unexpected since the TkSE slag sample had the lowest fineness as determined by the Blaine test. A possible explanation might either be due to experimental errors since the TkSE curve started at a comparatively higher level as shown in Figure 88, or the lower slag substitution of 15% might have led to the individual effect of slag being minimally accounted for in the overall heat released of the mix.

For the 30% slag mixes, the cumulative heat of hydration of PC after 72 hours was reduced to a range of 300 – 337.5 J/g. The AMSA slag sample showed higher cementitious capabilities by reducing the cumulative heat of hydration to only 337.5 kJ. The same trends can be observed for the 50% slag/cement mixes, where the AMSA slag reduces the cumulative heat of hydration to 297.5 J/g. In comparison, the mixes with the GGOBFS1 and TKSE slags showed reduced cumulative heat of hydration of 237.5 and 245.5 J/g, respectively. GGOBFS2 is the second-best performing slag for the 30% and 50% slag substitutions in terms of cumulative heat released, and this is unsurprising since it had a fineness that was second to the AMSA slag. However, as per the project objectives, the novel OBF slag displays similar cementitious performance to the conventional BF slag in terms of cumulative heat release as summarized in Table 15.

Table 15: cumulative heat released over 72 hours by the main slag samples

	72 hours Cumulative heat released (J/g)		
Slag addition (%)	**15%**	**30%**	**50%**
GGOBFS1	345	300	237,5
GGOBFS2	352,5	312,5	262,5
TkSE	370	317,5	242,5
AMSA	352,5	337,5	297,5

With similar chemical compositions and equivalent glass count levels of the four slag samples, the fineness can be considered in comparing the heat of hydration values. A higher fineness of

the slag is equivalent to lower cumulative heat reduction of PC in blended cement at a given substitution, highlighting the higher reactivity of the slag. The sensitivity of the R^3 reactivity test to fineness was also noted by Blotevogel et al., (2020) and Wang, et al., (2005).The cumulative heat of hydration can be further reduced by either increasing the proportion of slag, or by decreasing the fineness of the slag. In both instances, other properties of the mortar or concrete mix, such as workability, compressive strength, and drying shrinkage, will also be affected. Therefore, a balance between fineness and slag substitution ratio needs to be achieved depending on the desired mechanical properties of the final concrete or mortar mix.

The results in Figure 88, further demonstrate that both the novel OBF slag and the conventional BF slag reduce the cumulative heat of hydration at the different substitution levels, as an indication of similarities between the two slag types (2 OBF slags and 2 BF slags). Nonetheless, similar to other mechanical properties discussed in chapter 5, differences in cementitious performance between the two slag types can be noticed when the core properties of the slag are not the same. In this case, the effect of fineness is considered significant, since other properties such as the chemical composition and the glass content are relatively similar as shown in chapter 4. It should be noted that GGOBFS1 was the slag sample with the lowest Blaine fineness and a lower glass content, of 90%. Escalante et al. (2001) noted that a lower glass content is associated with lower reactivity: hence the lowest reactivity, as displayed by GGOBFS1 at all the substitution levels in Figure 88, can be linked to the glass count.

6.3.3. Power (rate of heat evolution)

From Figure 88, it can also be observed that the cumulative heat release increased rapidly for the first 8 hours and was then followed by a relatively lower rate between 8 and 24 hours, before the gradual decline in the rate of increase in cumulative heat release. To better understand this phenomenon, Figure 89 shows the results of the heat released per unit time for the first 24 hours, where major changes in power, or rate of heat released were observed.

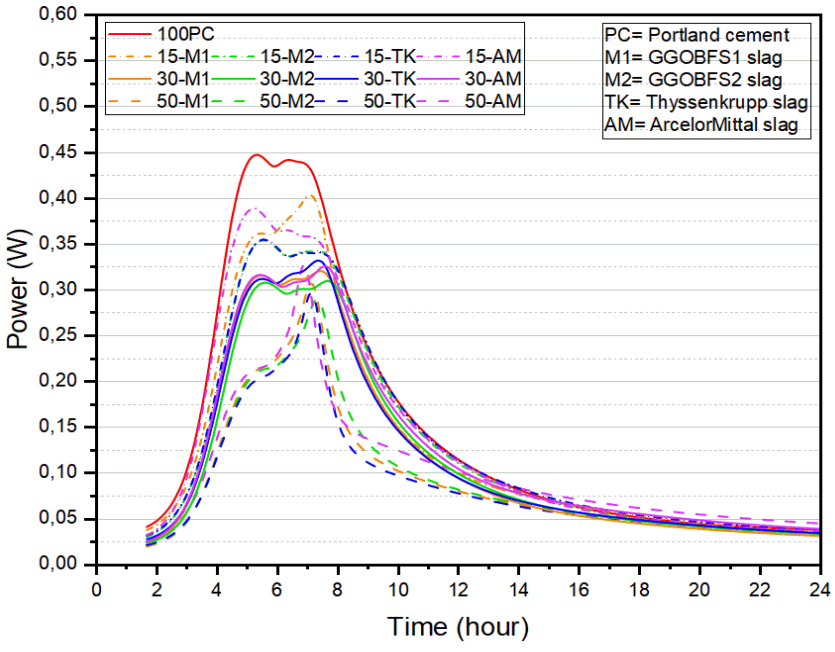


Figure 89: Rate of heat evolution results

The results in Figure 89, showing the change in the rate of heat evolution over the initial 24-hour period, indicate good agreement with the cumulative heat release results. The 100% PC mix achieved the highest rate of heat evolution, of approximately 0.45 W, demonstrating its relatively higher reactivity and this occurred after 5.5 hours.

The 15% slag substitution results in a decrease of the maximum rate of heat released down to 0.33 W, which decreased further to 0.30 W for the 30% slag substitution and to 0.27 W for the 50% slag substitution for the lowest performing slag in each substitution level. Moreover, the rate of heat evolution results further indicates that most of the exothermic reactions occur intensively between 1.5 and 10 hours. This intensive heat-evolution period is also dependent on the proportion of slag in the mix, with higher slag proportions corresponding to a lower intensive heat evolution period. Using 0.15 W, as the lower limit in order to quantify this intensive heat-evolution period, it can be seen that 15% slag proportion mixes start from 3.3 to 10.5 hours, whereas the 50% slag proportion mixes start from 4.3 hours to 8.6 hours. This is an illustration of the slag substitution ratio being inversely proportional to the rate of heat evolution.

Jansen et al. (2012) noted that the main contribution to the heat of hydration within the first 12 hours of the reaction of PC is the hydration of alite (C_3S) to form C-S-H and CH. Scholer et al. (2017) further added that changes in the heat evolution in the early ages of hydration are influenced by the reaction kinetics of alite and its products (C-S-H and CH). Based on the results in Figure 89, it can be seen that the reaction kinetics of alite are affected by the slag substitution in blended mixes, explaining the gradual changes in the rate of heat evolution observed as PC was replaced with slag at 15%, 30% and 50%. This same theory may also be the cause of the gradual change in early strength development that was observed in chapter 5 as the slag substitution was increased.

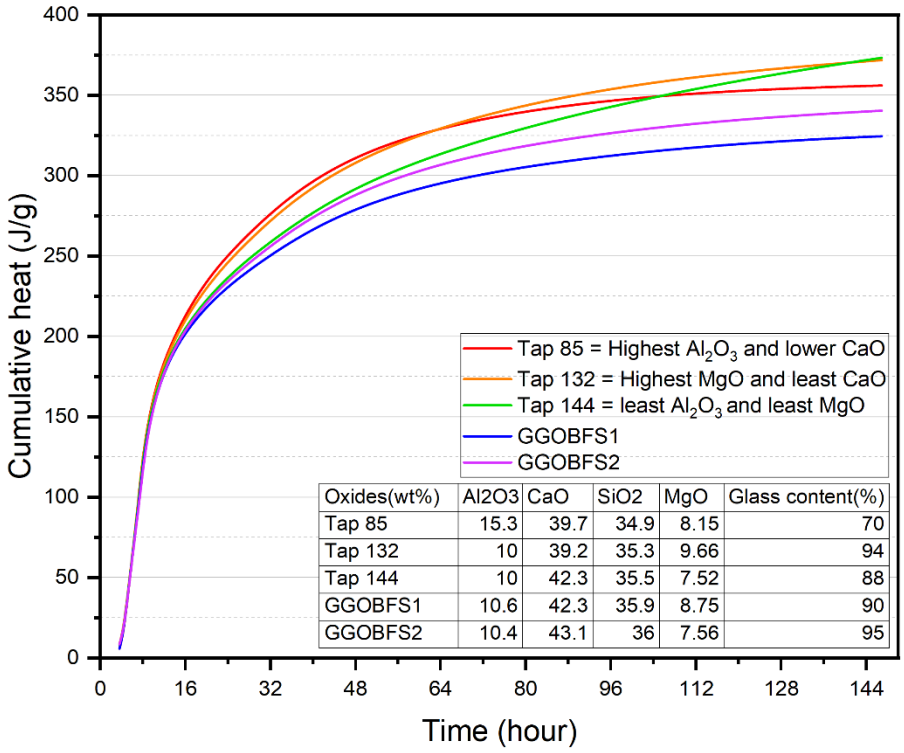
It should be noted that these rates of heat evolution are not the same as the observed rates at standard conditions (25°C): the R^3 test in this study was run at 40°C, in order to accelerate the reaction of the slag in the shorter analysis period. The curing temperature has been found to strongly influence the reactivity of slag in blended slag-cement mixes (Wang et al., 2019; Escalante et al., 2001). Moreover, the individual reactivity of the slag barely contributes to the early heat evolution (< 12 hours) at standard conditions, and the rate of heat evolution seems to also be dependent on the filling effect of the slag as a mineral addition to PC (Gutteridge and Dalziel, 1990; Scholer et al., 2017). This explains the slight, yet noticeable, differences observed in the rate of heat evolution for the slag samples at the same slag substitution ratio for the first 12 hours since the R3 test was run at non-standard conditions (40°C).

In this study, it can be stated that the difference brought by each slag to the early hydration of blended slag-cement is linked to the filler effect, the fineness, and the individual reactivity of the slag. In addition, Scholer et al. (2017) also included the chemistry of the pore solution, and surface characteristics of the mineral additions as contributing factors that affect the early age hydration of PC. Overall, both the novel OBF slag and the conventional BF slag displayed similar patterns in terms of rate of heat evolution at the different substitution levels as shown in Figure 89. However, the trends in the rate of heat evolution vary for the different slag samples (GGOBFS1, GGOBFS2, AMSA, TkSE) within the first 12 hours, demonstrating the

minimal impact of the individual slag reactivity on the early age hydration of blended slag-cement at the test temperature of 40°C.

6.3.4. Comparison of variations of OBF slags

To assess the effect of chemical composition, 5 variations of the OBF slag including GGOBFS1 and GGOBFS2 were tested using the R^3 reactivity test. The cumulative heat results along with the chemical composition of major oxides (SiO_2, Al_2O_3, MgO, CaO) are shown in Figure 90.



Oxides(wt%)	Al2O3	CaO	SiO2	MgO	Glass content(%)
Tap 85	15.3	39.7	34.9	8.15	70
Tap 132	10	39.2	35.3	9.66	94
Tap 144	10	42.3	35.5	7.52	88
GGOBFS1	10.6	42.3	35.9	8.75	90
GGOBFS2	10.4	43.1	36	7.56	95

Figure 90: Effect of chemical composition on the cumulative heat release of slag-cement at 30%

With reference to the results in Figure 90, it can be seen that within the first 12 hours, the cumulative heat release values for the different variations of OBF slag are similar at a common value of around 175 J/g. This further highlights the insignificant contribution of the individual slag reactivity to heat evolved during the early hydration age (<12 hours), with significant contributions only arising from the hydration of PC. The Tap 85 slag sample, with an Al_2O_3 content of 15.3%, demonstrates a relatively higher gain in cumulative heat release within the first 62 hours, after which the gain in cumulative heat decreased significantly compared to all the other variations of OBF slag. This is aligned with the observation in the studies of Blotevogel et al., (2020) and Wang et al., (2004) that the relative performance of GGBFS with the highest Al_2O_3 content and the lowest CaO content decreased over time. An increase in Al_2O_3 content of GGBFS was associated with the enhancement of early age heat of reaction and strength (Wang et al., 2004; Whittaker et al., 2014).

It was further noted that Al_2O_3 also reacts with the liberated MgO from GGBFS during the hydration of slag cement to form hydrotalcite phases (M-A-$\bar{C}$-H). This leads to reduced incorporation of aluminium (Al) in the Al-substituted calcium silicate hydrate (C-A-S-H), such

as gehlenite, or stratlingite phases (Haha et al., 2011; Wassing, 2003). Blotevogel et al. (2020) stated that hydrotalcite-like phases seem to be more prominent in the most reactive slag samples. It can be clear that the formation of hydrotalcite phases from the MgO in slag seems to be a desirable feature in blended slag cement since it purifies the C-S-H gel by limiting the aluminium incorporation. The importance of hydrotalcite was also highlighted in alkali-activated cement where its formation led to higher long-term strength due to reduced pore volume and formation of a C-S-H gel structure more similar to the C-S-H gel formed during hydration of pure PC (Haha et al., 2011; Bernal et al., 2014). Moreover, the formation of Al-bearing phases, such as ettringite (C-A-$\bar{S}$-H), has been found to be very exothermic with a corresponding enthalpy of formation of -17,535 kJ/mol under standard conditions, compared to the -1916 kJ/mol observed for C-S-H under standard conditions (Lothenbach et al., 2019). This maybe the reason for observation of higher cumulative heat release in the early ages for the Tap 85 slag sample. However, the actual effect of Al_2O_3 still to be measured and confirmed through more experiments.

The Tap 132 slag sample also demonstrated higher gains in cumulative heat release after 144 hours compared to GGOBFS1, and GGOBFS2. This might be due to its high MgO content of 9.66% while its CaO content was lower and very similar to that of Tap 85 at around 39%. On the other hand, the Tap 144 slag sample showed a slower, but sustained gain in cumulative heat release and exceeded the Tap 132 value at around 140 hours. Tap 144 has a higher CaO content of 42.3% compared with the 39.2% CaO content in Tap 132. Moreover, the MgO content of Tap 144 is the lowest at 7.52%. However, the sum of basic oxides (CaO + MgO) in Tap 144 is slightly higher than that of Tap 132, also Tap 144 has a comparatively lower glass content than Tap 132.The overall higher basic oxide content of Tap 144 might be the reason of for the slightly higher cumulative heat release compared to Tap 132 since they have the same Al_2O_3 content of 10%.

It can be seen that at a constant basic oxides level, a higher MgO slag (> 7.5%) is likely to display higher early strength development while a higher CaO slag (> 40%) is likely to display comparatively lower early strength development with sustained growth in the later ages. The significance of the difference between Tap 144 and Tap 132 in later ages of hydration still needs to be proven through further tests. This information is crucial, especially for the slag designing process, since the chemical composition will be modified in ways that favour improved cementitious performance. It should be noted that the comparison in this section is based mainly on chemical composition, while other parameters such as the glass content and the fineness would have had some effect on these results. For instance, the glass content of Tap 85, Tap 132, and Tap 144 were 70%, 94%, and 88% respectively as shown in Figure 90. Therefore, the glass content also influenced the trends in cumulative heat results. Moreover, GGOBFS1 and GGOBFS2 showed comparatively lower cumulative heat release at the end of the 146 hours' period. This might be linked to the relative differences in fineness and glass contents among the OBF slag samples.

6.3.5. Correlation of R^3 reactivity and compressive strength results

Several authors have found a strong linear correlation between the heat evolution and the early age compressive strength (Bentz et al., 2012; Pronina et al., 2018; Blotevogel et al., 2020). The

R^3 test can therefore be utilised to quickly predict the reactivity of the slag. Pronina et al. (2018) noted that the heat evolved seems to be proportional to the strength development and may be used as an important indicator of the reactivity of slag. On the other hand, Blotevogel et al. (2020) found a coefficient of determination (R^2) of 0.87 between the heat evolved and the compressive strength at 2 days and highlighted that the correlation of R3-test results is better than usage of traditional reactivity indices calculated from chemical composition, especially for the early age (2 days), since R^2 for later ages was very low. The cumulative heat results at 24 hours were normalized using the total 40 g of solid cementitious binder as per the mix design. The normalized data were correlated to the 2 days' compressive strength results discussed in chapter 5 of this study, and the results are shown in Figure 91. This was done for all the substitution levels and for both the novel OBF slag and the conventional BF slag.

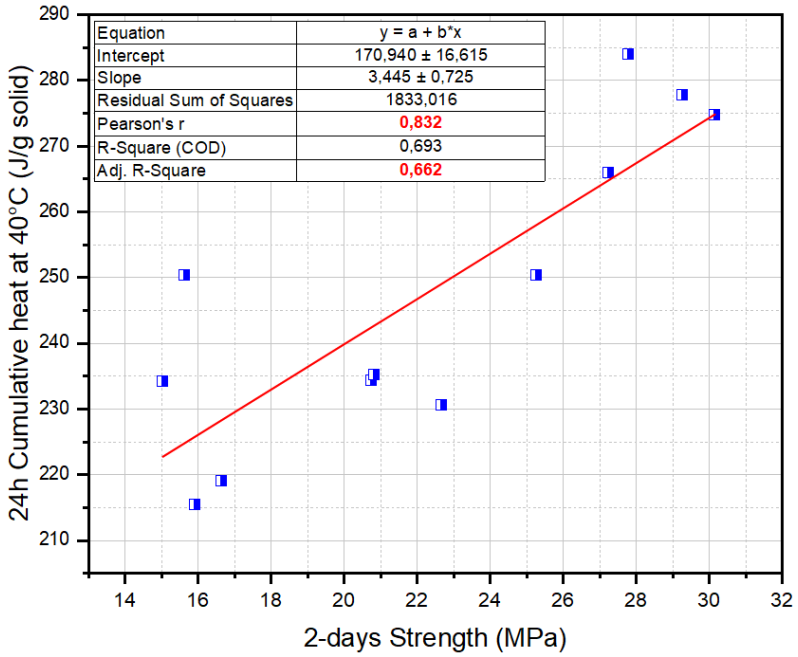


Figure 91: Correlation of R3 test results with the 2 days compressive strength results

The results in Figure 91 show quite good correlation between the cumulative heat release and the 2 days' compressive strength of the mortar mixes. The R2 value is 0.664, demonstrating how the regression line will predict the strength from cumulative heat release data. The Pearson correlation coefficient of 0.832 indicates a strong positive correlation between the two variables. The highest cumulative heat release per gram of solid at 24 hours in the 50% mixes was achieved for the AMSA slag sample with a corresponding value of 250 J/g, followed by GGOBFS2 at 234 J/g. Moreover, the 50% slag substitutions have the lowest variation in compressive strength ranging from 15 to 16.7 MPa, and the highest variation in cumulative heat release per gram of solid from 215 to 250 J/g. On the other hand, the 30% slag substitutions have the highest variation in compressive strength from 22.7 to 25.3 MPa. The lowest variation in cumulative heat per gram of solid ranging from 266 to 284 J/g can be seen from the 15% mixes. The obtained values of heat released per unit weight of cement are within the ranges reported by Blotevogel et al. (2020).

The effect of working temperature was not assessed in this study, but in the study the 1-day cumulative heat release for tests run at 40°C was very similar to the 6-days' cumulative value for 20°C, where the heat evolution slows down (Avet et al., 2016). It was noted that the high-working temperature accelerates the rate of pozzolanic reactions. Pozzolanic reactions in PC blends depend on the hydration reaction of PC that releases the CH which then reacts with the pozzolanic material. If increasing the temperature accelerates the pozzolanic reaction, then the hydration reaction of PC is also accelerated by the increased temperature.

Overall, all the slag substitutions gave results with significant variation from the regression line in this study. These variations result from the specific characteristics of each slag since the overall hydration process was accelerated by working at non-standard temperature (40°C), allowing the individual reactivity of the slag to influence the results. Therefore, the variation between the slag samples needs to be reduced by having similar physical and chemical properties (fineness, composition and glass content) in order to generate models that can easily predict the early strength from heat of hydration data. When reducing the variability between the slags by using only the two novel OBF slag samples (GGOBFS1, GGOBFS2), the adjusted R^2 becomes slightly higher at 0.723 as shown in Figure 92.

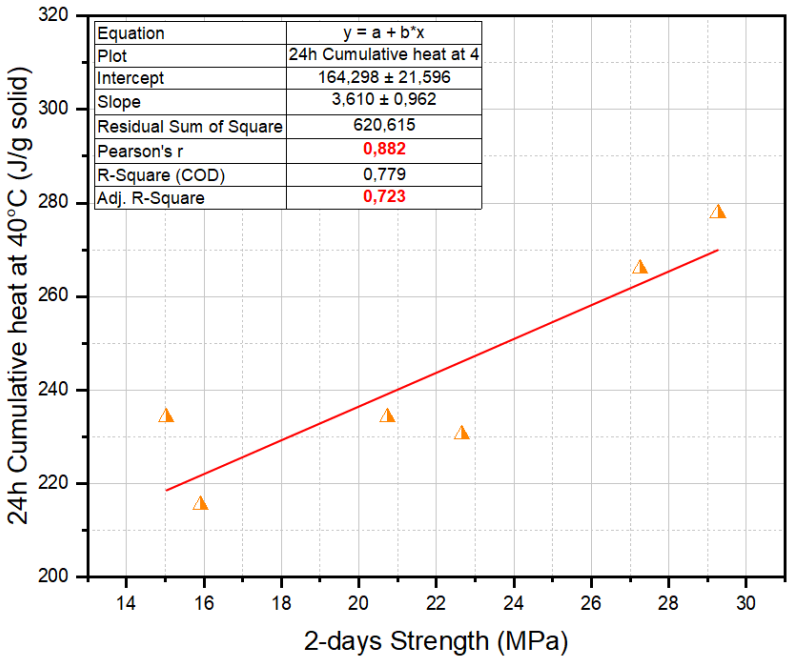


Figure 92: Correlation of R3 test with the 2 days compressive strength results for OBF slags

This shows the potential for reliable prediction of actual strength data when slag samples with less variation are used to generate the regression line. In all the cases, the results in Figure 91, and Figure 92 highlight a strong, positive, and linear relationship between the cumulative heat release and the 2 days strength of slag cement mixes. Moreover, unlike the investigations by Blotevogel et al. (2020), the coefficient of determination (R^2) did not change as the curing age increased to 7 days. However, the variability among the slags in this study, especially in terms of Blaine fineness, is very significant and might have affected the trends in the results.

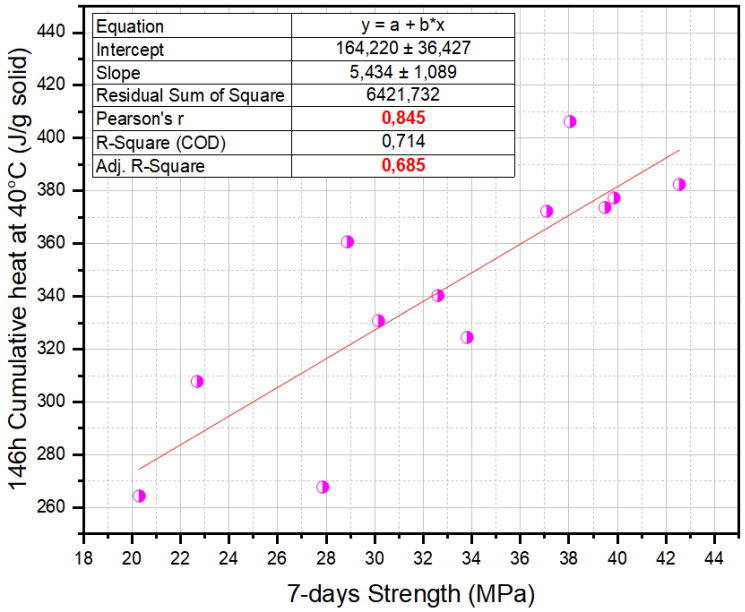


Figure 93: Correlation of R3 test results with 7 days compressive strength results

Figure 93 shows an example using the 7-days' compressive strength data and the longest curing hours in the cumulative heat results (146 hours). It can be seen that the coefficient of adjusted R^2 for 7 days is 0.685, but the variation in terms of strength increased significantly with each substitution level. For instance, the variation in strength in the 50% slag substitution group was the least at 2 days, but it is now widened from 21 to 31 MPa at 7 days, highlighting the deterioration of the linear correlation between the two variables as the curing age increases.

6.3.6. Correlation of R^3 reactivity and Blaine fineness

The Blaine fineness test results were correlated to the 24h cumulative heat release per gram of solid at 30% slag substitution and the results are summarized in Figure 94.

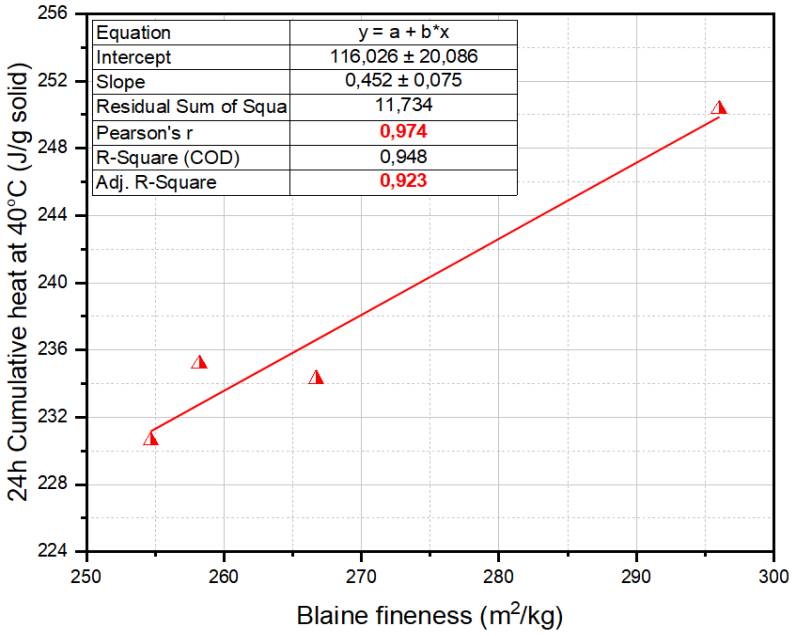


Figure 94: Correlation of R3 test results with Blaine fineness results

The effect of fineness on the heat of hydration is shown in Figure 94, where the results indicate a significant linear correlation between the Blaine fineness of the slag and the cumulative heat release per gram of cementitious binder. However, further experiments need to be conducted to confirm this correlation. The corresponding adjusted R^2 is 0.923 with a Pearson correlation coefficient of 0.974, highlighting the strength and positivity of the correlation. As noted earlier in this chapter, the reactivity of the slag is very low and a higher temperature is required for R^3 reactivity tests in order to effectively account for the contribution of the slag reactivity to the heat evolution. Therefore, if the test procedures for cumulative heat measurement and compressive strength are unchanged, as per this study, the generated regression lines can be used to predict the 2-days' compressive strength. However, data alignment with the regression decreases with increasing curing age. The adjusted R^2 is lower – in the range of 0.6 to 0.7 – indicating that the uncertainty of the predictions will be high.

In summary, the novel OBF slag behaves similarly to the conventional BF slag in terms of heat evolution, highlighting that the reactions occurring during the hydration of these two slags are similar. The rate of heat evolution strongly depends on the reactivity of the slag, which is linked to the chemical composition, fineness and glass content. In this study, changes in heat released by each slag sample seem to have followed the trends in fineness of the slags since other slag properties were generally similar. Slag with high fineness demonstrates high cumulative heat release and rate of hydration. Moreover, the early strength development of slag-cement blends can easily be predicted from the heat of hydration data provided that the regression line was generated using slag samples of the same properties (similar chemical composition, glass content, and fineness).

6.4. Hydrated phases evolution in slag-cement pastes

Before characterizing the different phases in the paste of the novel OBF slag, it is crucial to highlight the common phases that are generally found in hydrated slag-cement pastes. The slag, being latent hydraulic, makes the prediction and identification of phases a complex process since many reactions are occurring interactively from the slag and from the cement.

6.4.1. Common phases in slag-cement pastes

Hewlett and Liska (2019) stated that the GGBFS will hydrate in water even without the presence of an alkali source to form aluminium-substituted calcium silicate hydrate (C-A-S-H) binder along with secondary Mg-Al phases known as hydrotalcite, fitting the M-A-H and M-A-$\bar{C}$-S structures depending on the availability of Magnesium in the slag and carbonate. More specifically in cement nomenclature, the hydrotalcite-like phases can include quintinite, $Mg_4Al_2(OH)_{12}CO_3 \cdot 3H_2O$ and/or meixnerite $Mg_6Al_2(OH)_{18} \cdot 4H_2O$ as well as true hydrotalcite, $Mg_6Al_2(OH)_{16}CO_3 \cdot 4H_2O$ (Mills et al., 2012).

The nomenclature of these phases is very complex since they can easily change based on the chemistry of the slag and cement. Table 16 summarizes the names and estimated chemical compositions of the common phases that can be expected in hydrated slag-cement pastes as well as their main structures, as per the findings in the following studies (Matschei et al., 2007; Hewlett and Liska, 2019; Feng et al., 2015).

Table 16: Common phases in hydrated slag-cement pastes

Phases and composition	Structure	Chemical name
Mono-sulphate ($C_4A\hat{S}H_{12}$, Afm) Ettringite ($C_4A\hat{S}_3H_{32}$, Aft)	C-A-Ŝ-H	Hydrous calcium aluminium sulphate
Hydrotalcite (M_4AH_{10}), Meixnerite, Quintinite	M-A-H M-A-Ĉ-S	Magnesium-aluminium hydroxy carbonate Magnesium-aluminium hydrotalcite
Hydrogarnet (C_3AH_6) Siliceous hydrogarnet ($C_3AS_{0.8}H_{6.4}$) Mono-carboaluminate ($C_4A\hat{C}H_{11}$)	C-A-H	Calcium aluminate hydrate
Stratlingite Gehlenite (C_2ASH_8)	C-A-S-H	Calcium silico-aluminate hydrate
Jennite Tobermorite	C-S-H	Calcium silicate hydrate
Portlandite	CH	Calcium hydroxide

These phases coexist along with un-hydrated cement and slag in hydrated paste mixes depending on the curing age and degree of hydration since it is very unlikely for complete hydration of either the slag, or the reference cement to occur (Hewlett and Liska, 2019). Monosulphate ($C_4A\bar{S}H_{12}$) is less stable and over time is converted to the more stable variant, Ettringite ($C_4A\bar{S}_3H_{32}$), as reported in Hewlett and Liska (2019). The AFm and AFt phases may, at times, also contain Fe to form Fe-mono-sulphate and Fe-ettringite (Feng et al., 2015). The Jennite-type C–S–H has a higher Ca/Si ratio of around 1.67 compared to the tobermorite-type C–S–H with a Ca/Si ratio as low as 0.83 as reported by Lothenbach et al., (2008) and Matschei et al., (2007). The Ca/Si ratio is lowered when slag is added to the mix due to the SiO_2 content in slag. Hence, the C-S-H gel found in hydrated slag-cement paste is most likely the tobermorite-type, especially at later ages, once the slag has reacted.

6.4.2. Hydration products characterization

The characterization of hydration products was done using scanning electron microscopy equipped with energy dispersive X-ray spectroscopy (SEM-EDS) to obtain the composition and the morphology of the product's surface, whereas the phases were confirmed using X -Ray diffractometry (XRD). The identification of phases from the micrographs was done with the help of the EDS composition results by following the atomic ratios summarized in Table 17, as consolidated by Taylor and Newbury (1984). In conjunction with this technique, the identification of phases in backscatter electron (BSE) imaging was also used. This technique stipulates that the brightness of visualized areas decreases in the following order: non-hydrated cement grain > portlandite (CH) > other hydration products, typically the C-S-H phase > pores (Hewlett and Liska, 2019).

Table 17: Atomic ratios of hydrated phases in cement pastes

	C-S-H	CH	AFm	Hydrogarnet
Mg/Ca	0.03	0.01	0.00	0.11
Al/Ca	0.08	0.03	0.55	0.36
Si/Ca	0.60	0.04	0.04	0.32
S/Ca	0.03	0.004	0.24	0.04
Fe/Ca	0.02	0.01	0.00	0.26
(Al + Fe)/Ca	0.11	0.04	0.55	0.63
Ca/Si	1.67			

Hewlett and Liska (2019) further noted that the C-S-H and CH phases exhibit high compositional variations depending on whether they form around the boundaries of unhydrated cement grains or within the pore space originally filled by water. Most spots (regions) usually contain both phases including other hydrated phases, but dominated by one major phase as follows:

- Composition high in Ca + Si, low in Al + Fe : denotes spot high in C-S-H
- Composition very high in Ca, low in Si and Al + Fe : denotes spot high in CH
- Composition high in Ca and Al + Fe, low in Si : denotes spot high in AFm (alumina, ferric oxide monosubstituted phase)
- Magnesium tends to associate with compositions containing Al and Fe

6.4.2.1. Comparison of pure cement and blended slag-cement

The image of the 100% cement paste was compared with the image of the 50% blended slag-cement mix at 1000x magnification, for 2 days' curing, as shown in Figure 95. It is clear that the microstructure of the two pastes is generally similar except that in the blended slag-cement paste, coarse size slag particles can be seen in Figure 95b compared to the finer cement particles in Figure 95a. This is attributed to the fact that the Portland cement sample in this study (with a Blaine fineness of 389 m^2/kg) was finer than the slag samples (with Blaine fineness below 300 m^2/kg), as shown in Chapter 4.

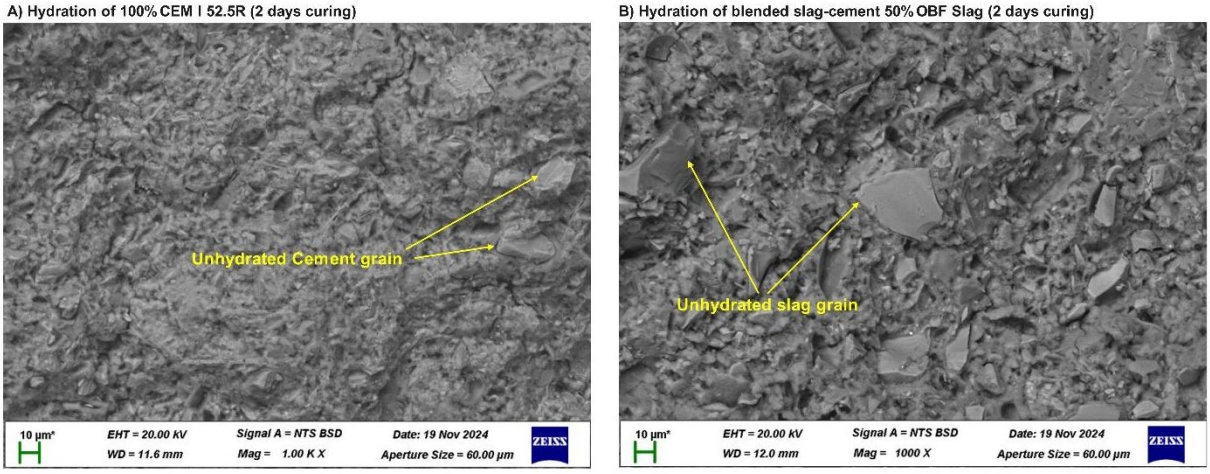


Figure 95: pure cement and blended slag-cement microstructure

6.4.2.2.Hydration of cement with curing time

The effect of curing time on morphological and phase-chemical composition change was assessed for the 100% cement paste and the SEM results from 2 to 56 days are presented in Figure 96 while the XRD results are shown in Figure 97.

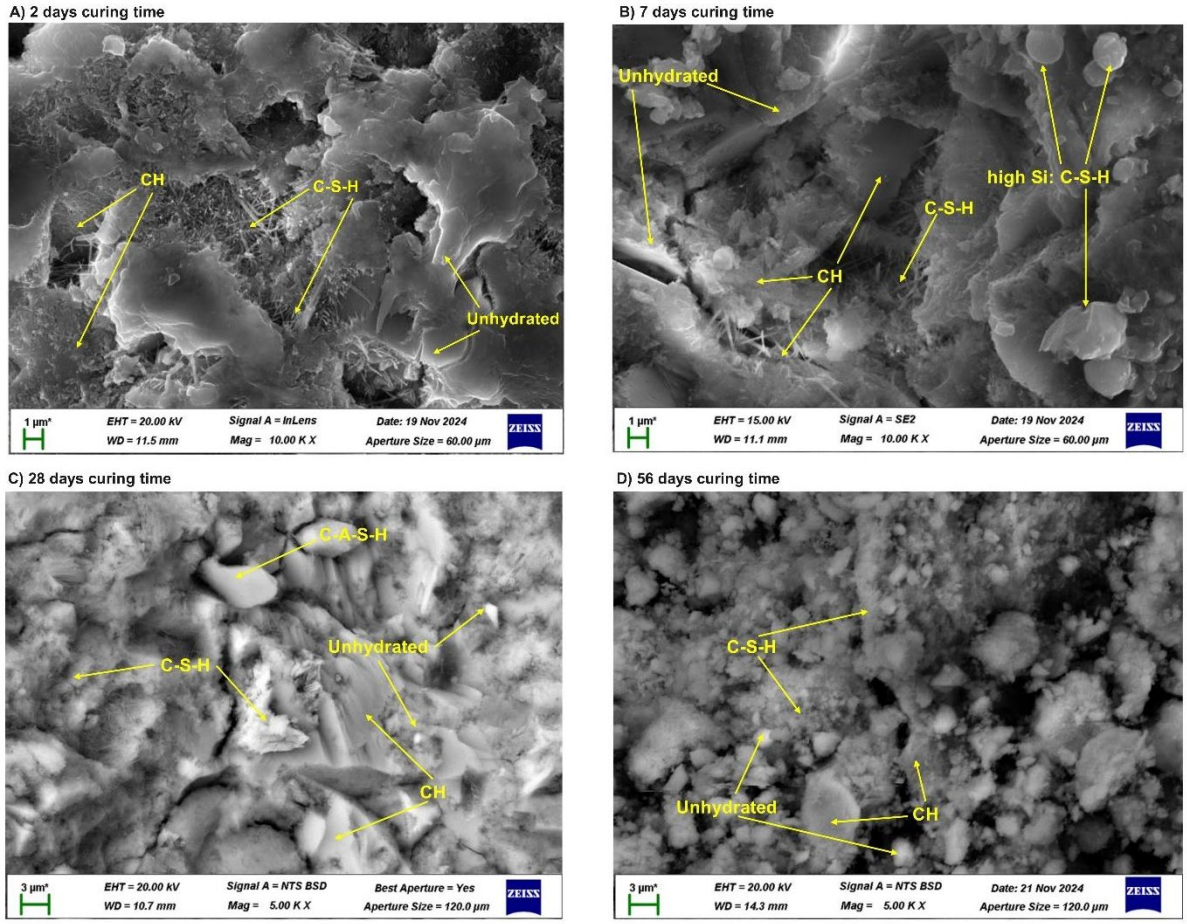


Figure 96: Hydration of 100% cement with curing time (a. 2-days, b. 7-days, c. 28-days, and d. 56-days) – secondary electron images

As per Figure 96, the main identified phases are C-S-H, CH, and some unhydrated cement grains from 2 days of curing, up to 56 days of curing. The results indicate that even at 56 days, the hydration process can be expected to continue and not all the cement has reacted throughout the process. A certain degree of hydration is expected, which should be affected by the components in the main hydration reactions of cement as well as the feasibility and the kinetics of these reactions. It is interesting to note the transformation of the C-S-H phase, which started with fibrous, vein-like phases with visible pores in Figure 96a, and the microstructure changes throughout the hydration process into densely packed particles with less fibrous-like phases as shown in Figure 96d. This morphological transformation of C-S-H is also described by Richardson (2004). The composition of the C-S-H was also varying at different spots, denoted by the region of high Si and low Ca in Figure 96b. On the other hand, the CH formed as plate, or gel-like phases, at 2 days of curing in Figure 96a , and then becomes denser and blockier as the hydration process progresses and the CH crystals grow as shown in Figure 96c. Generally,

as the curing age increases, it becomes more difficult to visually differentiate the hydrated phases, and it is in this instance where the BSE identification technique becomes very useful.

A particle fitting the structure of C-A-S-H was also identified in Figure 96c: this spot had higher alumina compared to silica, indicating the presence of either mono-sulphate or ettringite. However, the sulphur content was very low for it to be ettringite (AFt), and it also contains a quite substantial amount of Si to be considered as stratlingite. It is therefore concluded that this particle is likely to be either mono-sulphate (AFm), or stratlingite (C-A-S-H).

The X-ray diffractograms for the hydration phase evolution of the 100% cement paste are presented in Figure 97.

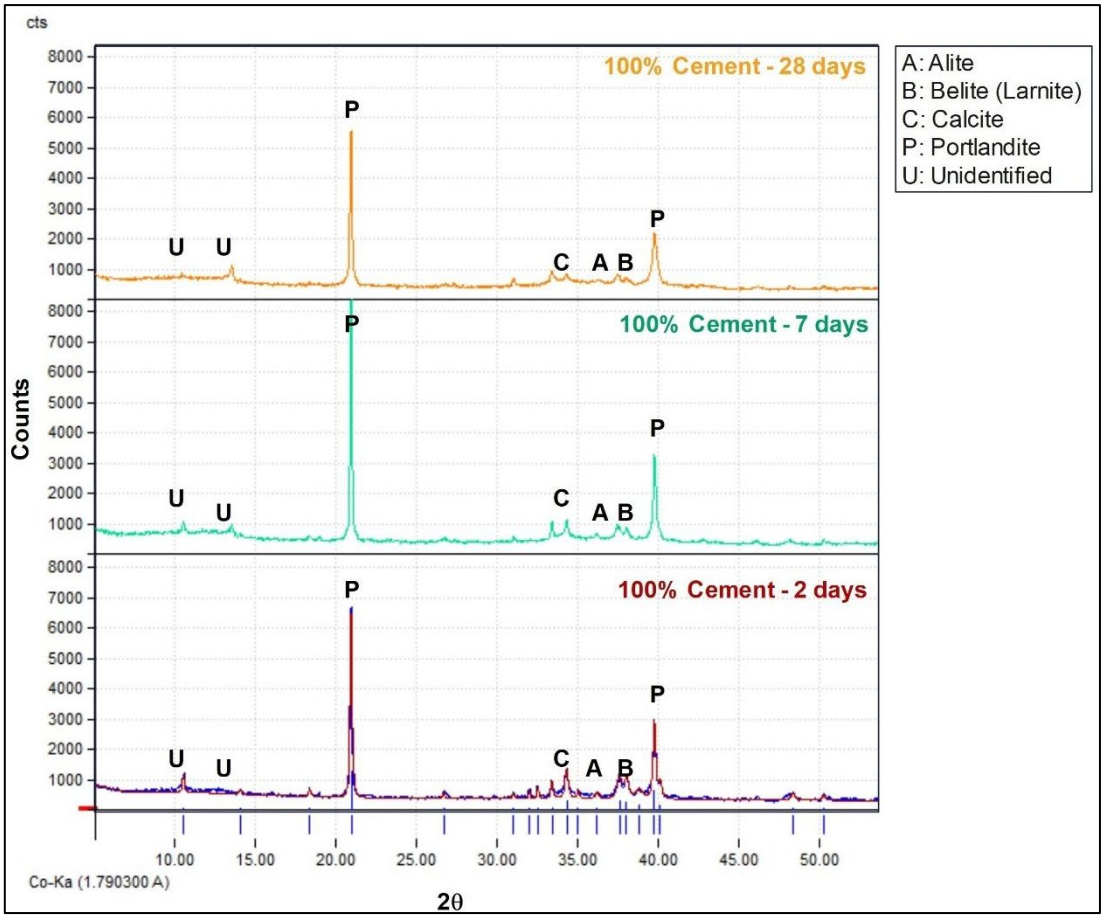


Figure 97: Hydration of 100% cement with curing time (2,7, and 28 days) - XRD

As can be seen in Figure 97, the X-ray diffractometry could not detect the primary binding phase (C-S-H) responsible for strength development in cement. However, portlandite (CH), a by-product of C_3S and C_2S hydration was detected. Alizadeh (2009) highlighted that it is difficult for C-S-H to be identified by X-ray diffractometry due to its poorly crystalline and nano-structure phase, while a similar theory was also elaborated half a century ago by Bernal et al. (1952). Hence, the crystals of C-S-H are not well-defined and lack sharp diffraction peaks. This amorphous nature of C-S-H makes it very difficult to quantify the change in phase formation using XRD results. Portlandite, on the other hand, formed well-defined crystalline phases, enabling identification via X-ray diffractometry.

The results in Figure 97 show a decrease in the intensity of alite (C_3S) and belite (C_2S), indicating that the hydration reaction continues over time from 2 to 28 days, just as shown in the SEM results, since the reactants of cement hydration appear to be consumed over the course of this period. Moreover, the lower detected intensities of alite and belite at 2 days of curing compared to the original intensities in pure cement, shown in Figure 98, demonstrate that the majority of these two compounds, particularly alite, is consumed before the end of 2 days of curing.

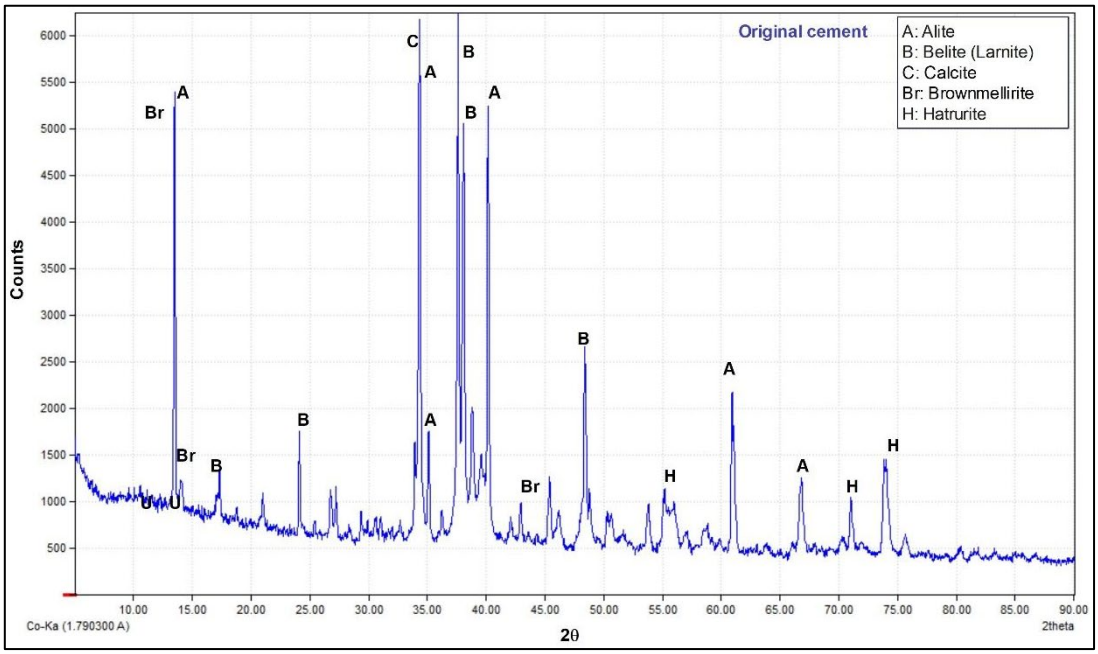


Figure 98: Original cement-XRD

This further indicates that most of the main hydration reactions occur within the first 48 hours, thereby raising the question of the cause of the strength development at later ages (more than 2 days). Similar observations about the duration of main hydration reactions were made by Taylor (1997) using the change in rate of heat evolution as shown in Figure 99.

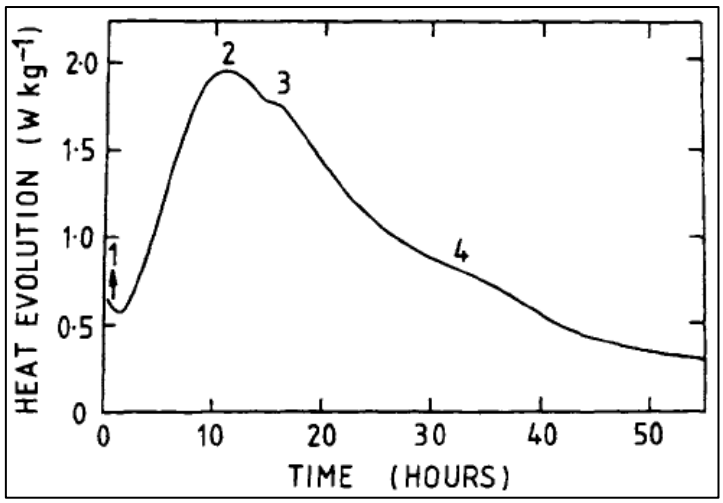


Figure 99: Rate of heat evolution at 20°C for a typical Portland cement

The initial peak (1) corresponds to exothermic wetting and early-stage reactions of cement producing rods of AFt phases, peak (2) corresponding the generation of C-S-H and CH from the hydration of C_3S, and the rate of heat evolution continue to gradually decreases through peak (3) and (4) while still generating C-S-H and CH. Taylor (1997) further highlighted that the hydration process of C_3S may be divided into five stages: the initial reaction, the induction period , the acceleratory period, the deceleration period, and the final slow-reaction stage. All of these stages occur within the first 48 hours as shown in Figure 99. It is clear that the compositional change of the binder (C-S-H) is minimal beyond 2 days and the cause of late strength development may be linked to the morphological change of the binder (C-S-H) as well as the minimal compositional change. However, it should be noted that the compositions of C-S-H and CH vary widely at various spots within the specimen.

The morphological change may be due to the evaporation of water from the specimen, and the filling of pores by the binder and portlandite throughout the entire hydration process, thereby increasing the strength of the specimen. This theory agrees with the observations made on the strength development of the 100% cement mix discussed in chapter 5 of this study. The increment in strength was very significant within the first 2 days at about 38 MPa, compared to the 12 MPa strength gain that was observed after 7 days, while the strength-gain continues to decrease as shown in Figure 100.

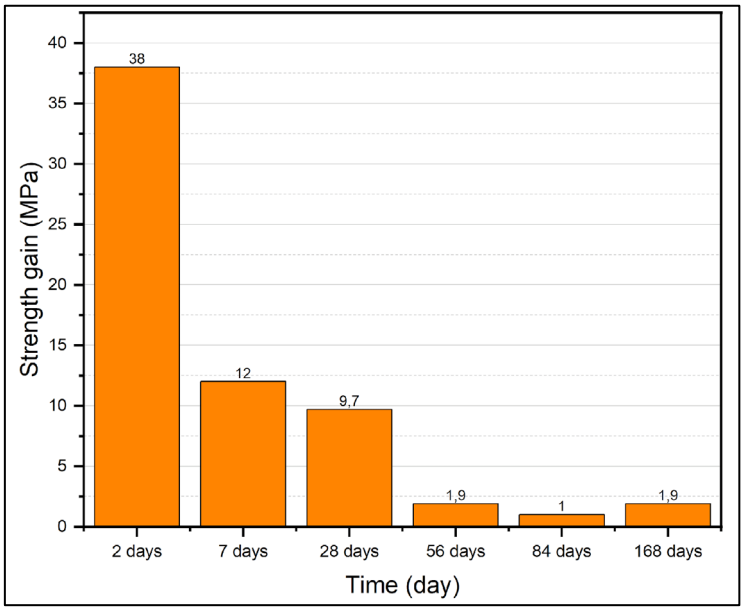


Figure 100: Strength gain of the 100% cement mix

It is difficult to make conclusions using the XRD results because of the undetected amorphous phase (C-S-H) along with other hydrated phases that could not be identified for similar reasons. The detected amount of alite and belite at 2 days seems to be very low, based on the intensity of peaks shown in Figure 97, to link the significant strength gains at 7 and 28 days of curing to the change in composition of the binder. The results in Figure 100 indicate that the extent of hydration of the 100% cement mix is significant up to 28 days, after which the strength gain is substantially lower. In conclusion, the combination of the SEM, XRD, and strength development results demonstrates that the hydration of the 100% cement mix within the first

2-days is strongly influenced by the formation and compositional change of the binder, after which it is the synergy of morphological and compositional changes of the binding phases that contribute to the strength development of the specimen.

6.4.2.3. Hydration of blended slag-cement with curing time and varied slag/cement ratio

In order to compare the hydration of pure cement to that of blended slag-cement, the SEM images of the hydration of the 50% slag-cement paste from 7 to 56 days are set out in Figure 101. It should be noted that the slag used in this section is GGOBFS2.

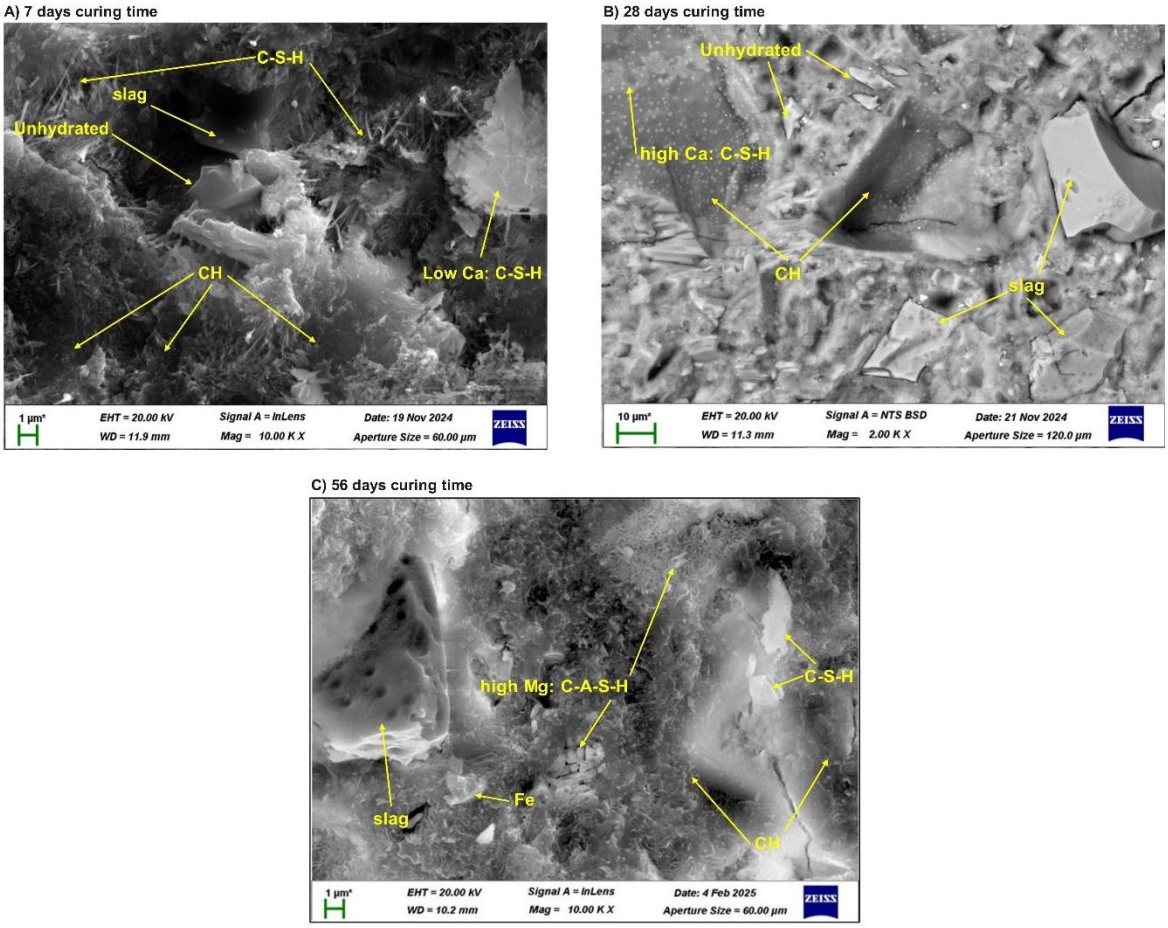


Figure 101: Hydration of blended slag-cement with curing time-SEM

As per the results in Figure 101, the C-S-H appears fibrous or vein-like at 7 days and the morphology changes as the hydration process progresses, similar to the observations for the pure cement paste. However, the presence of unhydrated slag grains can be noted in the blended slag-cement mix, and this makes the microstructure of the C-S-H and CH more disordered. This effect, coupled with the reduced amount of cement in the blended mix leads to slower early strength development, as discussed in chapter 5.

The EDS results show that the C-S-H in the blended slag-cement has a very low level of Ca compared to the pure cement paste, although there is a variation in composition of C-S-H at different spots. Richardson (2004) also indicated that the C-S-H in blended cements contains a reduced mean Ca/Si ratio, changing the morphology from fibrillar to a foil-like morphology. This is associated with a tobermorite-type structure of C-S-H ($Ca_5Si_6O_{16}(OH)_2.4H_2O$) rather

than the jennite-type structure ($Ca_9Si_6O_{18}(OH)_6.8H_2O$) which has a higher mean Ca/Si ratio. Similar to the 100% cement paste, as the curing time increases, the microstructure of the blended slag-cement paste becomes denser and the phases become difficult to isolate and identify.

The presence of C-A-S-H is also noted in Figure 101c. However, the composition of the C-A-S-H in the blended slag-cement paste seems to have high magnesia and alumina, and this can also possibly be linked to a hydrotalcite structure (M-A-H) similar to the phases made by Mills et al. (2012) although the carbon was not accounted for in the EDS results. Moreover, the substantial presence of lime and alumina may also provide a link to a hydrogarnet structure (C-A-H). The inclusion of Fe was also identified in Figure 101c, highlighting the presence of entrained Fe droplets contributed by the slag to the blended slag-cement paste. This arises typically from the Fe that could not drop down to the metal zone during smelting.

The XRD results of the blended slag-cement pastes are presented in Figure 102.

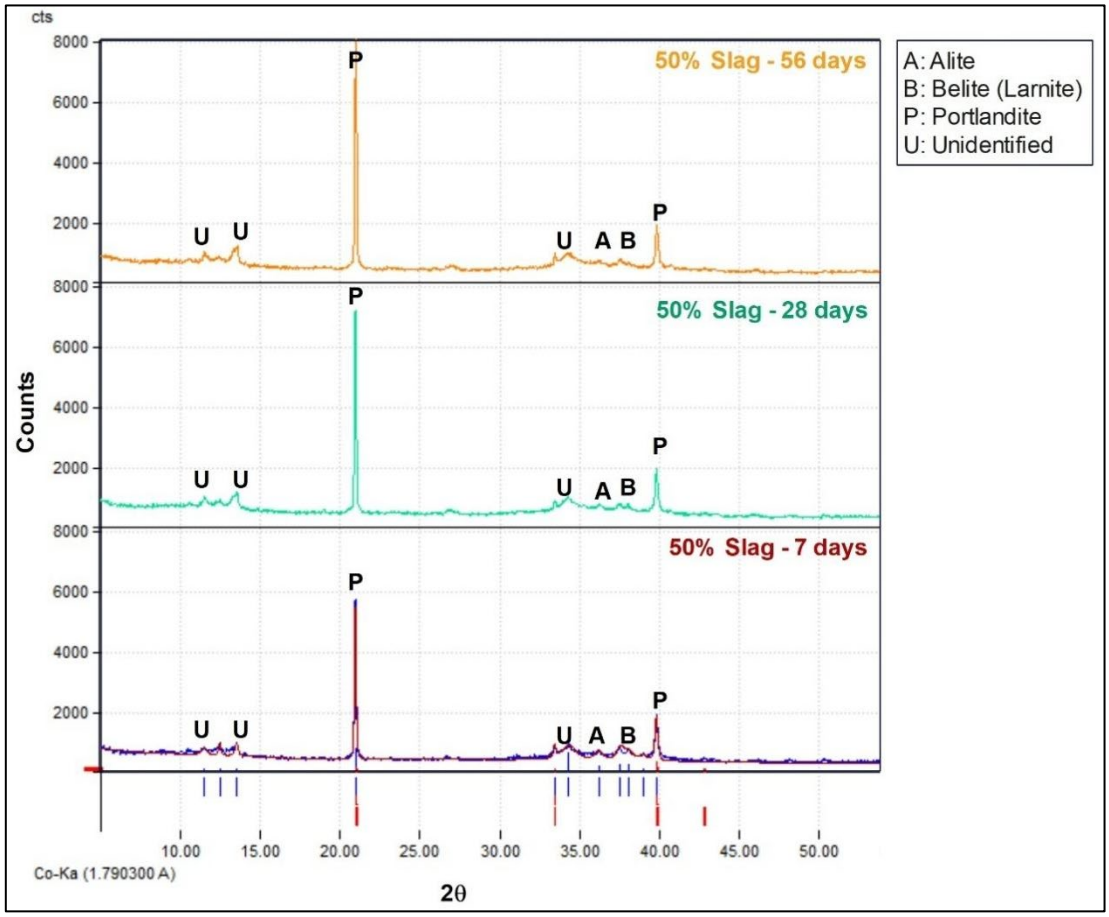


Figure 102: Hydration of blended slag-cement with curing time (7 – 56 days) - XRD

The hydration phases formed in the blended-slag cement paste are very similar to those observed in the pure cement paste. The C-S-H was also not identified, while portlandite, alite and belite were identified. However, the intensity of peaks for alite and belite appears very low in the blended slag-cement compared to the observations for the 100% cement paste. This may be due to the comparatively lower amount of cement used in the blended slag-cement paste.

There are two unidentified phases at 18º and 33º that grow as the curing time increases. These phases could be either of the hydrated products since they are forming as the curing time increases. Moreover, the broader-hump nature of their peaks suggests that their structures are not well-defined and may be very fine-grained materials. Therefore, these can be either the C-S-H or C-A-S-H binding phase.

In order to better understand the influence of slag substitution, XRD analyses were performed on blended slag-cement mixes containing 15%, 30%, and 50% slag at 56 days of curing. The results are illustrated in Figure 103.

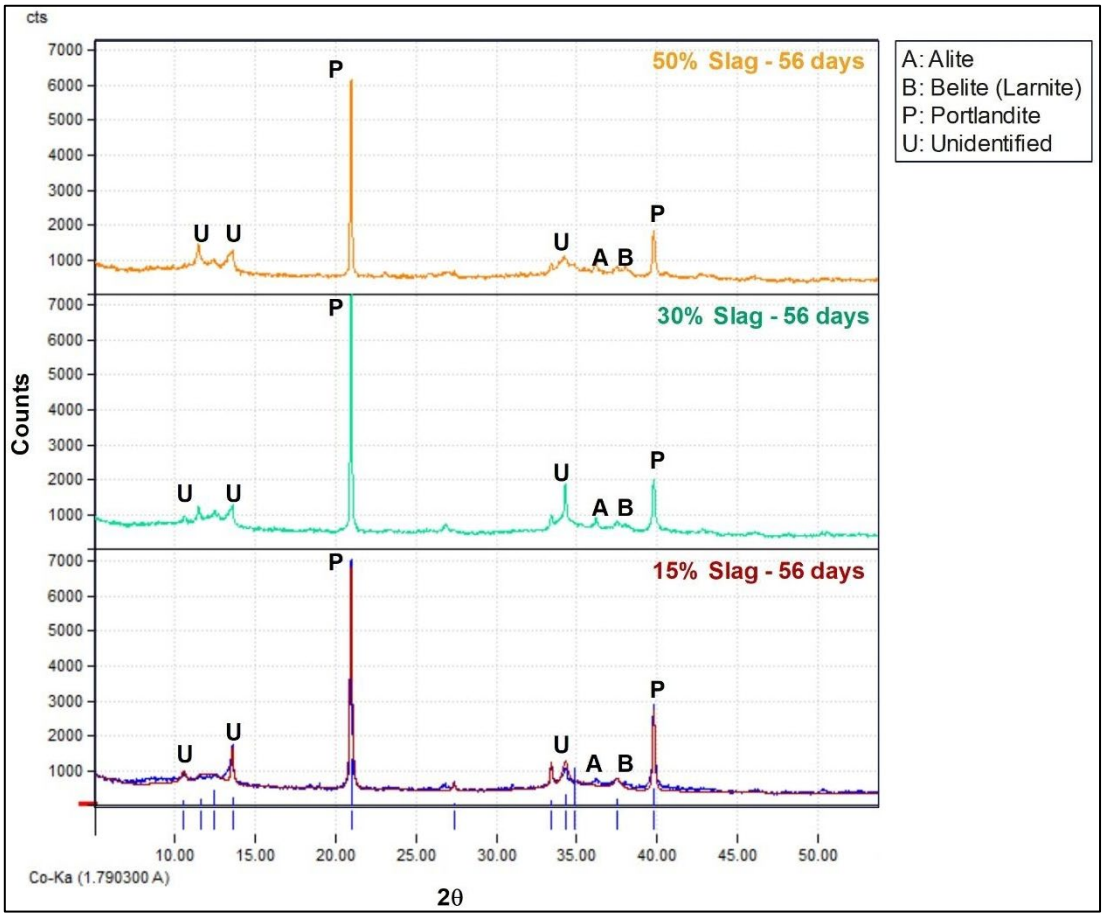


Figure 103: Effect of slag substitution ratio on phase formation at 56 days

The results in Figure 103 show that the ratio of the slag in blended slag-cement does not have much impact on the nature of the phases that form after hydration, it does, however, slightly affect the quantity of the phase. This can be explained by the fact that as the slag substitution ratio increases from 15% to 50%, the peak-intensity of the unidentified phase at 14º along with that of portlandite seems to decrease. The decrease in the level of portlandite formed is expected since the generated portlandite reacts with the silica and alumina from the slag, through the pozzolanic reaction, in order to produce the C-A-S-H binder. Hence, the amount of portlandite should decrease as the proportion of the slag in the blended slag-cement mix increases. However, this was not the case for the 30% slag substitution as it appears to have the highest intensity counts of portlandite compared to the rest of the blended slag-cement mixes.

The peaks of alite and belite seem to be more prominent in the lower slag substitution (15%) than in the higher slag substitution (50%). This can also be linked to the reduced amount of cement in the higher slag substitution mix. Overall, the hydration of blended slag-cement pastes has similar phase evolution to the pure cement pastes. However, the blended slag-cements have C-S-H with lower mean Ca/Si ratios and higher levels of incorporation of other hydration products, like C-A-S-H and C-A-H, as well as some incorporation of magnesia in the hydration products.

6.4.2.4. Comparison of GGOBFS and GGBFS blended slag-cement hydration

The SEM images of GGOBFS and GGBFS blended slag-cement at 56 days of curing, containing 50% slag are shown in Figure 104.

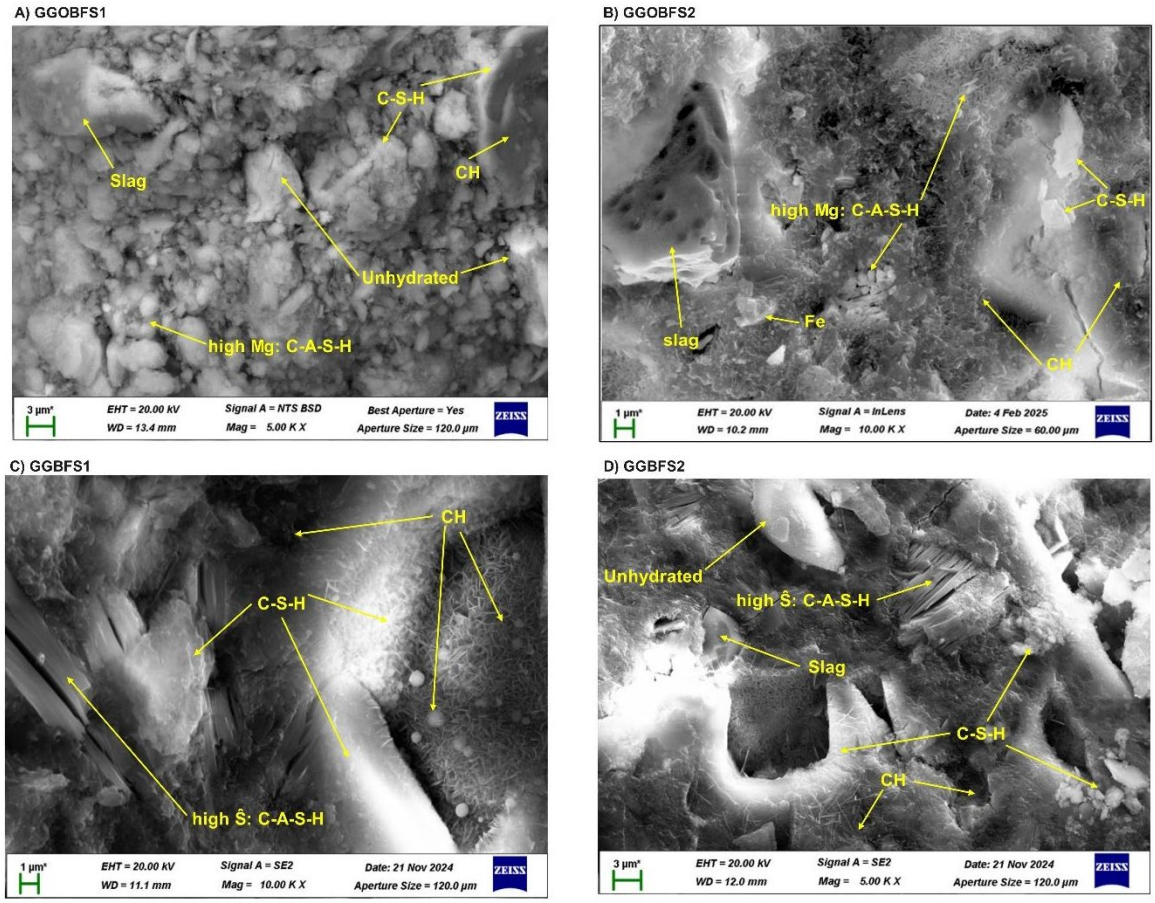


Figure 104: GGOBFS and GGBFS blended slag-cement hydration-SEM

The results in Figure 104 show the same phases observed in the preceding section, with CH, C-A-S-H, and C-S-H as major phases. C-A-S-H appears to have a slabby and larger vein-like morphology compared to C-S-H. The main difference between the hydration of blended slag-cement with GGOBFS and GGBFS appears to be in the composition of the C-A-S-H phase. The C-A-S-H in GGBFS has a high sulphur-intake, thereby making the phase resemble either ettringite or mono-sulphate, whereas the C-A-S-H in GGOBFS has little sulphur intake, making the composition similar to either hydrotalcite for high MgO spots, or hydrogarnet for low MgO and high Al_2O_3 spots in SEM micrographs. This observation is aligned with the observed chemical composition in chapter 4, which indicated that GGOBFS has less sulphur

due to the lower coke-requirement for the OBF process compared to the conventional BF process.

The XRD results of the different slag cements in 50% slag-cement mixes are shown in Figure 105.

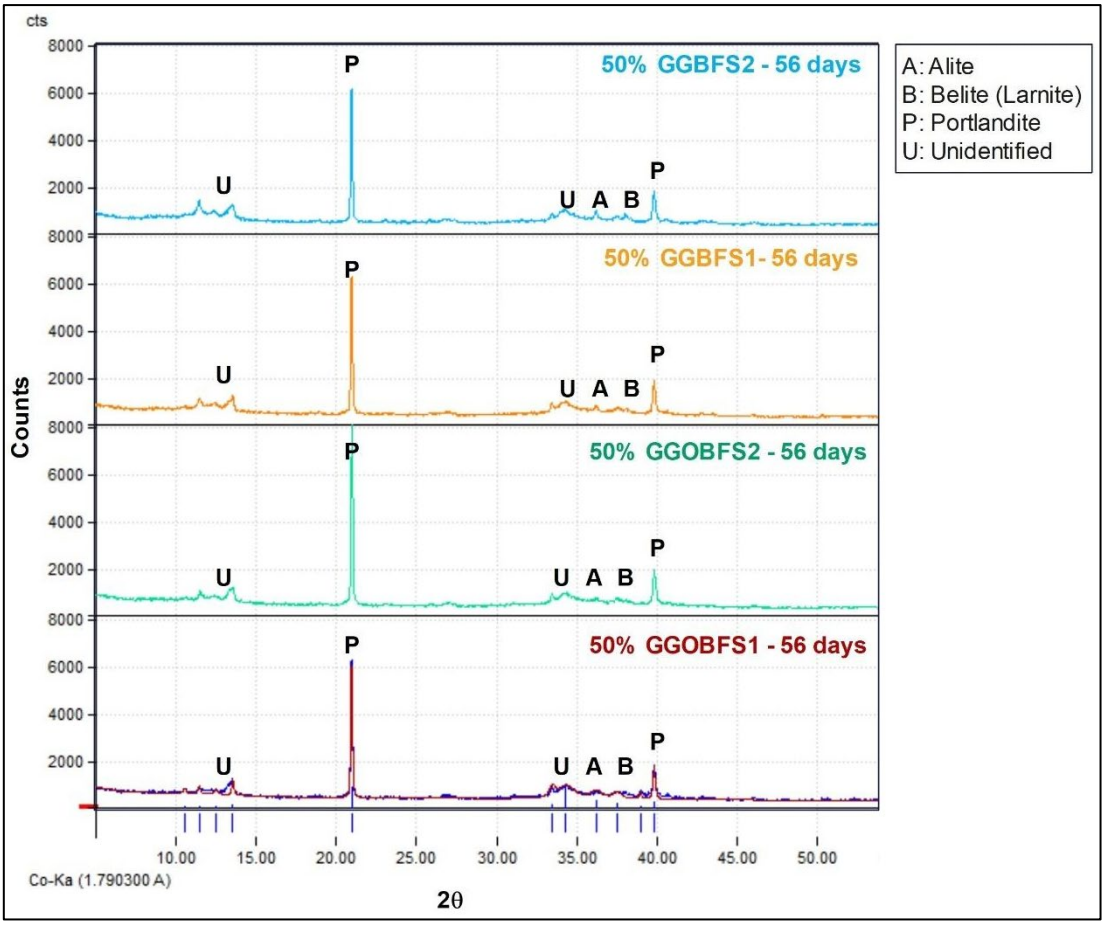


Figure 105: GGOBFS and GGBFS blended slag-cement hydration-XRD

As can be seen in Figure 105, the diffractograms of GGOBFS and GGBFS are very similar , thereby further highlighting the similarities of phases that form during the hydration of blended slag-cement paste with GGOBFS and GGBFS. However, the differences in the nature of C-A-S-H are not shown since this phase, along with C-S-H, is amorphous and undetectable by XRD analysis.

6.5. Conclusion

In summary, the novel OBF slag behaves in a similar manner to the conventional BF slag in terms of heat evolution, highlighting that the reactions occurring during the hydration of these two slags are similar. The rate of heat evolution depends strongly on the reactivity of the slag, which is linked to the chemical composition, fineness and glass content. In this study, changes in heat released by each slag sample seem to have followed the trends in fineness of the slags since the other slag properties assessed, covering chemical composition, were generally similar. Slag with high fineness demonstrates high cumulative heat release and rate of hydration. Furthermore, the results indicate a significant linear correlation between the fineness

of the slag and cumulative heat release per gram of solid cementitious binder. The corresponding coefficient of determination is 0.923 and a Pearson correlation coefficient of 0.974, highlighting the strength and positivity of the correlation.

The main phases that form during the hydration of blended slag-cement and pure cement are C-S-H, CH, and C-A-S-H. The C-S-H phase has a fibrous morphology with a poorly crystalline structure, making it undetectable via XRD analysis. The CH phase has gel-like, or blocky morphology with a well-defined crystal structure and is detectable by XRD analysis. The C-A-S-H phase has a similar morphology to C-S-H but is thicker, and also has an amorphous structure undetectable by XRD analysis. The overall microstructure of the paste gets densely packed with increasing curing time as the hydration reactions continue and the excess water evaporates. The hydration of the paste within the first 2-days is strongly influenced by the formation and compositional change of the binders (C-S-H, C-A-S-H, CH), after which it is the synergy of morphological and compositional changes of the binding phases that contributes to the strength development of the specimen. The compositional change has more effect on the late strength development in blended slag-cement mixes since the reactivity of the slag only becomes prominent at later ages.

The phases that evolve during the hydration of blended slag-cements with GGOBFS and GGBFS are very similar. The main difference lies in the composition of the C-A-S-H phase. The C-A-S-H in GGBFS has a high sulphur-intake, thereby making the phase resemble either ettringite or mono-sulphate, whereas the C-A-S-H in GGOBFS has little sulphur intake, making the composition similar to either hydrotalcite for high MgO spots, or hydrogarnet for low MgO and high Al_2O_3 spots in SEM micrographs. This dissimilarity arises from the fact that GGOBFS has less sulphur compared to GGBFS, owing to the lower coke requirement for the OBF process compared to the conventional BF process.

References

Alizadeh, R. (2009). Nanostructure and engineering properties of basic and modified calcium-silicate-hydrate systems. University of Ottawa (Canada). *Dissertation Abstracts International*, 71(06), p.3815. doi:https://doi.org/10.20381/ruor-13206.

ASTM/C1897 – 20. Standard Test Methods for Measuring the Reactivity of Supplementary Cementitious Materials by Isothermal Calorimetry and Bound Water Measurements. DOI:10.1520/C1897-20.

Avet, F., Snellings, R., Alujas Diaz, A., Ben Haha, M. and Scrivener, K. (2016). Development of a new rapid, relevant and reliable (R3) test method to evaluate the pozzolanic reactivity of calcined kaolinitic clays. *Cement and Concrete Research*, 85, pp.1–11. doi:https://doi.org/10.1016/j.cemconres.2016.02.015.

Bentz, D.P., Barrett, T., De la Varga, I. and Weiss, W.J. (2012). Relating Compressive Strength to Heat Release in Mortars. *Advances in Civil Engineering Materials*, 1(1), p.20120002. doi:https://doi.org/10.1520/acem20120002.

Bernal, J.D., Jeffery, J.W. and Taylor (1952). Crystallographic research on the hydration of Portland cement. A first report on investigations in progress. *Magazine of Concrete Research,* 4(11), pp.49–54. doi:https://doi.org/10.1680/macr.1952.4.11.49.

Bernal, S.A., San Nicolas, R., Myers, R.J., Mejía de Gutiérrez, R., Puertas, F., van Deventer, J.S.J. and Provis, J.L. (2014). MgO content of slag controls phase evolution and structural changes induced by accelerated carbonation in alkali-activated binders. *Cement and Concrete Research*, 57, pp.33–43. doi:https://doi.org/10.1016/j.cemconres.2013.12.003.

Binici, H., Temiz, H. and Köse, M.M. (2007). The effect of fineness on the properties of the blended cements incorporating ground granulated blast furnace slag and ground basaltic pumice. *Construction and Building Materials*, 21(5), pp.1122–1128. doi:https://doi.org/10.1016/j.conbuildmat.2005.11.005.

Blotevogel, S., Ehrenberg, A., Steger, L., Doussang, L., Kaknics, J., Patapy, C. and Cyr, M. (2020). Ability of the R3 test to evaluate differences in early age reactivity of 16 industrial ground granulated blast furnace slags (GGBS). *Cement and Concrete Research*, 130, pp.105998–105998. doi:https://doi.org/10.1016/j.cemconres.2020.105998.

Chen, W. 2007. Hydration of slag cement - Theory, Modelling and Application. Doctor of Philosophy, University of Twente, Enschede.

Chen, W. and Brouwers, J. (2006). The hydration of slag, part 2: reaction models for blended cement. *Journal of Materials Science*, 42(2), pp.444–464. doi:https://doi.org/10.1007/s10853-006-0874-1.

Dunne, C. ed., (2019). *SME mineral processing & extractive metallurgy handbook volume 1.* Englewood, Colorado Society For Mining, Metallurgy & Exploration.

Escalante, J.I., Gómez, L.Y., Johal, K.K., Mendoza, G., Mancha, H. and Méndez, J. (2001). Reactivity of blast-furnace slag in Portland cement blends hydrated under different conditions. *Cement and Concrete Research*, 31(10), pp.1403–1409. doi:https://doi.org/10.1016/s0008-8846(01)00587-7.

Feng, P., Miao, C. and Bullard, J.W. (2015). Factors Influencing the Stability of AFm and AFt in the Ca–Al–S–O–H System at 25°C. *Journal of the American Ceramic Society*, 99(3), pp.1031–1041. doi:https://doi.org/10.1111/jace.13971.

Gutteridge, W.A. and Dalziel, J.A. (1990). Filler cement: The effect of the secondary component on the hydration of Portland cement. *Cement and Concrete Research*, 20(6), pp.853–861. doi:https://doi.org/10.1016/0008-8846(90)90046-z.

Haha, M.B., Lothenbach, B., Le Saout, G. and Winnefeld, F. (2011). Influence of slag chemistry on the hydration of alkali-activated blast-furnace slag — Part I: Effect of MgO. *Cement and Concrete Research*, 41(9), pp.955–963. doi:https://doi.org/10.1016/j.cemconres.2011.05.002.

Hewlett, P.C. and Liska, M. (Eds) (2019). *Lea's Chemistry of Cement and Concrete*, 5th Edition, Elsevier Science & Technology, Butterworth-Heinemann, Oxford, UK.

Jansen, D., Goetz-Neunhoeffer, F., Lothenbach, B. and Neubauer, J. (2012). The early hydration of Ordinary Portland Cement (OPC): An approach comparing measured heat flow with calculated heat flow from QXRD. *Cement and Concrete Research*, 42(1), pp.134–138. doi:https://doi.org/10.1016/j.cemconres.2011.09.001.

Kolani, B., Buffo-Lacarrière, L., Sellier, A., Escadeillas, G., Boutillon, L. and Linger, L. (2012). Hydration of slag-blended cements. *Cement and Concrete Composites*, 34(9), pp.1009–1018. doi:https://doi.org/10.1016/j.cemconcomp.2012.05.007.

Londono-Zuluaga, D., Gholizadeh-Vayghan, A., Winnefeld, F., Avet, F., Haha, M.B., Bernal, S.A., Çizer, Ö., Cyr, M., Dolenec, M., Durdzinski, P., Haufe, J., Hooton, D., Kamali-Bernard, S., Li, X., Marsh, A., Marroccoli, M., Mrak, M., Muy, Y., Patapy, C. and Pedersen, M.K. (2022). Report of RILEM TC 267-TRM phase 3: vaIidation of the R3 reactivity test across a wide range of materials. *Materials and Structures*, 55(5). doi:https://doi.org/10.1617/s11527-022-01947-3.

Lothenbach, B., Kulik, D.A., Matschei, T., Balonis, M., Baquerizo, L., Dilnesa, B., Miron, G.D. and Myers, R.J. (2019). Cemdata18: A chemical thermodynamic database for hydrated Portland cements and alkali-activated materials. *Cement and Concrete Research*, 115, pp.472–506. doi:https://doi.org/10.1016/j.cemconres.2018.04.018.

Lothenbach, B., Matschei, T., Möschner, G. and Glasser, F.P. (2008). Thermodynamic modelling of the effect of temperature on the hydration and porosity of Portland cement. *Cement and Concrete Research*, 38(1), pp.1–18. doi:https://doi.org/10.1016/j.cemconres.2007.08.017.

Matschei, T., Lothenbach, B. and Glasser, F.P. (2007). Thermodynamic properties of Portland cement hydrates in the system CaO–Al2O3–SiO2–CaSO4–CaCO3–H2O. *Cement and Concrete Research*, 37(10), pp.1379–1410. doi:https://doi.org/10.1016/j.cemconres.2007.06.002.

Mills, S., Christy, A.G., Génin, J.-M.R., Kameda, T. and Colombo, F. (2012). Nomenclature of the hydrotalcite supergroup: natural layered double hydroxides. *Mineralogical Magazine*, 76(5), pp.1289–1336. doi:https://doi.org/10.1180/minmag.2012.076.5.10.

Pronina, N., Krüger, S., Bornhöft, H., Deubener, J. and Ehrenberg, A. (2018). Cooling history of a wet-granulated blast furnace slag (GBS). *Journal of Non-Crystalline Solids*, [online] 499, pp.344–349. doi:https://doi.org/10.1016/j.jnoncrysol.2018.07.054.

Richardson, I.G. (2004). Tobermorite/jennite- and tobermorite/calcium hydroxide-based models for the structure of C-S-H: applicability to hardened pastes of tricalcium silicate, β-dicalcium silicate, Portland cement, and blends of Portland cement with blast-furnace slag,

metakaolin, or silica fume. *Cement and Concrete Research*, 34(9), pp.1733–1777. doi:https://doi.org/10.1016/j.cemconres.2004.05.034.

Scholer, A., Lothenbach, B., Winnefeld, F., Haha, M.B., Zajac, M. and Ludwig, H.-M. (2017). Early hydration of SCM-blended Portland cements: A pore solution and isothermal calorimetry study. *Cement and Concrete Research*, 93, pp.71–82. doi:https://doi.org/10.1016/j.cemconres.2016.11.013.

Stephant, S., Chomat, L., Nonat, A. and Charpentier, T. (2015). Influence of the slag content on the hydration of blended cement. *Hal.science*. [online] doi:https://cea.hal.science/cea-02509185.

Sun, J. and Zhang, P. (2021). Effects of different composite mineral admixtures on the early hydration and long-term properties of cement-based materials: A comparative study. *Construction and Building Materials*, 294, p.123547. doi:https://doi.org/10.1016/j.conbuildmat.2021.123547.

Taylor, H.F.W. (1997). *Cement chemistry. 2nd ed*. London: Thomas Telford Publishing, p.212. doi:https://doi.org/10.1680/cc.25929.

Taylor and Newbury, D.E. (1984). An electron microprobe study of a mature cement paste. *Cement and Concrete Research*, 14(4), pp.565–573. doi:https://doi.org/10.1016/0008-8846(84)90134-0.

Wang, L., Quan, H. and Li, Q. (2019). Evaluation of Slag Reaction Efficiency in Slag-Cement Mortars under Different Curing Temperature. *Materials*, 12(18), p.2875. doi:https://doi.org/10.3390/ma12182875.

Wang, P.Z., Trettin, R., Rudert, V. and Spaniol, T.P. (2004). Influence of Al_2O_3 content on hydraulic reactivity of granulated blast-furnace slag, and the interaction between Al_2O_3 and CaO. *Advances in Cement Research*, 16(1), pp.1–7. doi:https://doi.org/10.1680/adcr.2004.16.1.1.

Wassing, W. (2003). Relationship between the chemical reactivity of granulated blast furnace slags and the mortar standard compressive strength of the blast furnace cements produced from them. *Cem. Int*, *1*(5), pp.95-109.

Part II: DRI-OBF-SVF

Extension of the Direct Reduced Iron (DRI) and Open Bath Furnace (OBF) circuit with a Slag Valorisation Furnace (SVF) stage

The second part of this project covers the feasibility of integrating an extra slag valorisation furnace (SVF) into the DRI-OBF circuit in order to extend the life span of the OBF refractory materials and increase the total volume output of the slag. Unlike the first part of this project, which aimed to fulfil the dual objectives of meeting both metallurgical and cementitious requirements in one furnace (OBF), the second part incorporates a different approach with meeting each objective in two separate furnaces. The first furnace (OBF) prioritizes the metallurgical conditions by producing an intermediate slag (OBF Gen2) that is less corrosive to the refractory lining materials in the OBF, whereas the second furnace (SVF) prioritizes the valorisation of the intermediate slag (OBF Gen2) into a cementitious product such as, a BF equivalent, or higher CaO slag close to the composition of cement clinker.

Cement specifications commonly have a maximum MgO level of 5 – 6%, and this MgO level is way below the saturation limit for a furnace operating at 1500°C thereby leading to corrosion of the refractory. Hence, the requirement to increase the MgO level of the slag in the OBF for refractory protection and then reduce it to cement specification in the SVF slag. In this respect, the design approach is covered in chapter 7 while the evaluation of the slag properties along with the mass and energy balances are conducted in chapter 8. A schematic representation of the process extension with the Slag Valorisation Furnace is shown in Figure 106.

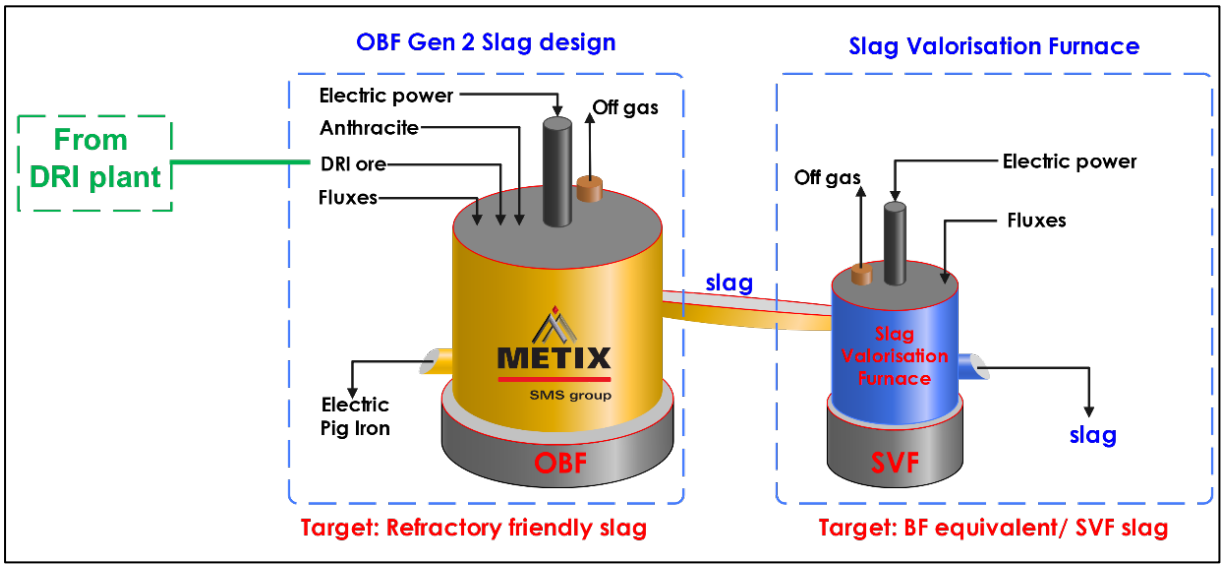


Figure 106: DRI-OBF-SVF configuration

CHAPTER 7: OBF-SVF SLAG REFRACTORY DESIGN

7.1. Introduction

This chapter is mainly dedicated to the study of the slag-refractory interactions in the OBF. This includes a design procedure for an intermediate slag composition that is more compatible with the OBF by prioritizing the metallurgical conditions, followed by a subsequent modification of the intermediate slag into a BF slag equivalent in the SVF. Moreover, this chapter briefly covers the fundamentals of refractory materials selection as well as the refractories that are commonly employed in iron and steel production.

The slag-refractory design procedure includes the study of the gangue distribution in the DRI, the selection of suitable refractory materials, and the selection of the proposed slag compositions by investigating the possible new slag zone in the Al_2O_3-CaO-SiO_2-MgO system that could be less corrosive to the selected refractories in the OBF Gen2 and in the SVF. The work of this chapter is done using FactSage, an effective software package that can be used to generate thermodynamics data of various materials.

7.2. Phases nomenclature

It is important to note the different names of common chemical phases that will be used throughout this chapter. In that respect, Figure 107 summarizes the names of these phases, their chemical formulas as well as a typical quaternary diagram, generated at 15% MgO.

Phase name	Chemical composition
Slag-liq	Molten oxides
Corundum(alpha)	Al_2O_3(s4)
Mullite	$Al_6Si_2O_{13}$(s)
Akermanite(me	$Ca_2MgSi_2O_7$(s)
Merwinite	$Ca_3MgSi_2O_8$(s)
Anorthite	$CaAl_2Si_2O_8$(s2)
Solid	$CaMg_2Al_{16}O_{27}$(s)
Diopside(cl-py)	$CaMgSi_2O_6$(s)
Lime	CaO(s)
Cordierite	$Mg_2Al_4Si_5O_{18}$(s)
Forsterite	Mg_2SiO_4(s)
Sapphirine	$Mg_4Al_{10}Si_2O_{23}$(s)
Spinel	$MgAl_2O_4$(s)
Periclase	MgO(s)
Merwinite	$MgOCa_3O_3Si_2O_4$(s)
Proto-enstatite	$MgSiO_3$(s3)
Tridymite(h)	SiO_2(s4)
Cristobalite(h)	SiO_2(s6)
Alite	Ca_3SiO_5(s)
Belite	Ca_2SiO_4(s)
Hatrurite	Ca_3SiO_5(s)
Gehlenite	$Ca_2Al_2SiO_7$(s)

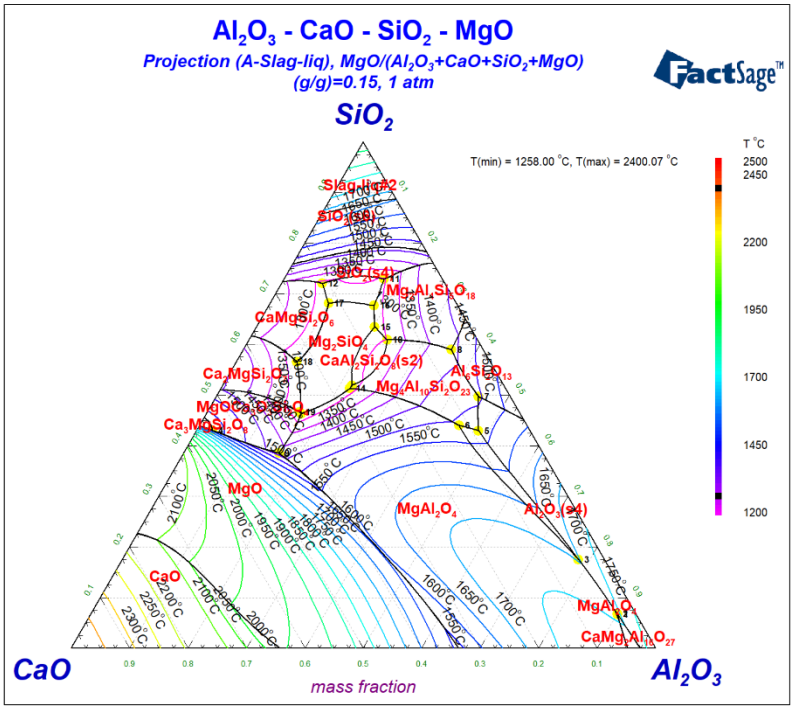


Figure 107: Names of common phases and typical quaternary diagram, generated at 15% MgO

7.3. DRI gangue distribution

7.3.1. Short literature survey

Gangue materials are impurities found in the DRI alongside iron minerals. The gangue composition of the DRI plays a very important role during the slag designing process since the gangue composition will dictate the type and mass of fluxing materials that need to be added in order to reach a targeted slag composition. While DRI pellets are predominantly made up of Fe, the proportion of gangue materials helps to distinguish between DR-grade (>66% Fe total), and BF-grade DRI (>57% Fe total) as per recent studies (Nicholas and Basirat, 2022b; Kim and Sohn, 2022). A literature survey covering major DRI gangue compositions around the world has shown variations in chemical composition as illustrated in Table 18.

Table 18: Typical DRI compositions

Reference	MgO	CaO	Al_2O_3	SiO_2	Gangue	Fe mineral	Total Fe	Total	From	Grade
(Li et al., 2022a)	0,4	0,27	0,2	4,64	5,51	94,82	68,38	100,33	Magnetite	DR
(Mao et al., 2022)	2,55	1,45	3,76	5,67	13,43	86,00	62,02	99,43	Hematite	BF
(Li et al., 2022b)	0,68	1,34	0,63	2,7	5,35	93,20	67,21	98,55	Magnetite	DR
(Scharm et al., 2022)	0,04	2,4	0,56	3,36	6,36	92,46	66,68	98,82	Hematite	DR
(Shahabuddin et al., 2024)	0,07	0,04	3,01	6,71	9,83	80,65	56,50	90,48	Goethite	BF
(Cavaliere et al., 2022)	1,03	0,51	0,57	11,8	13,86	86,14	62,12	100,00	Hematite	BF
TkSE	1,58	0,72	0,45	6,25	9,00	90	64,90	99,00	Hematite	BF

From the data in the above table, BF-grade DRI contains between 9 and 15% of gangue materials while DR-grade DRI contains less than 8% of gangue materials, without accounting for the carbon added during the DRI process. Most BF-grade DRI ores contain between 60 and 65% Fe. However, when dealing with an ore that contains goethite/limonite ($Fe_2O_3.nH_2O$) as the main Fe mineral, the Fe content will then be below 60% because of the bound water and the LOI being more than 5% similar to DRI composition by Shahabuddin et al. (2024). The gangue compositions in Table 18, were normalized to 100 and plotted on a quaternary diagram Al_2O_3-CaO-SiO_2-MgO shown in Figure 108, considering an operating temperature of 1500°C, an atmospheric pressure of 1 atm, and at constant MgO of 8%. The original MgO content of each gangue composition was not considered.

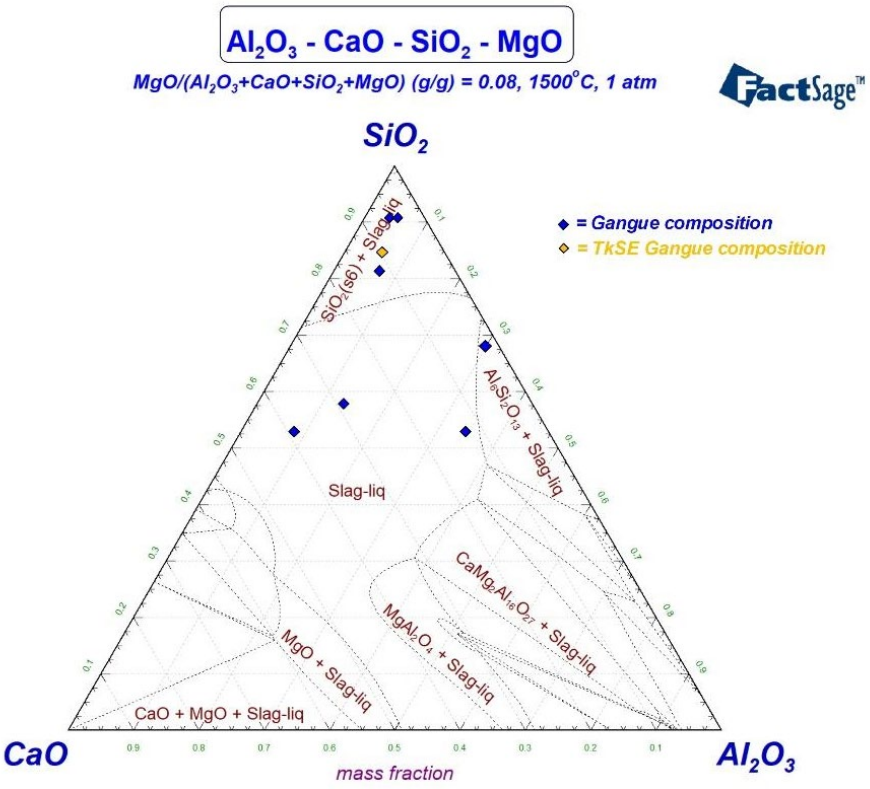


Figure 108: DRI gangue distribution in Al_2O_3-CaO-SiO_2-MgO system

This survey indicates that most DRI gangues are acidic as shown in blue in the quaternary diagram, with roughly >50% silica (SiO_2) content, including the TkSE gangue, shown in yellow, which has a normalized SiO_2 content of 84% in the CaO-SiO_2-Al_2O_3 system, and goes down to 70% when accounting for MgO. The proportion of gangue materials based on the DRI grade might be different, but the gangue distribution is roughly the same in the acidic region. It can be seen that SiO_2 is the predominant component in the DRI gangue composition, and the remaining major components (Al_2O_3, CaO, MgO) are randomly distributed in varied proportions depending on the geological origin of the DRI.

7.3.2. Selected gangue distribution for slag design

As indicated earlier in chapter 1, DR-grade Fe ores are scarce and only comprise 4% of the global Fe ores in the market (Nicholas and Basirat, 2022a). Furthermore, the usage of DR-grade Fe pellets along with Fe scrap is limited to the electric arc furnace (EAF), which can only process Fe feedstock with little impurities. On the other hand, the novel open bath furnace (OBF) is capable of processing both the DR-grade and BF-grade DRI pellets, with the latter generating more slag due to their relatively higher gangue proportions. Moreover, very acidic gangues (high SiO_2) will require more fluxing materials to get to a target slag composition since the slag is basic (low SiO_2). The selection of a gangue composition that is very acidic for the designing process is ideal because the results in terms of furnace size will be overestimated, thereby making the furnace versatile to handle different levels of acidity in terms of gangue composition. Taking these factors into account, the slag designing process will be based on the TkSE BF-grade DRI, which has 70% SiO_2, and the mass balance will be computed using two gangue proportions, 10% and 15% as summarized in Table 19.

Table 19: Selected gangue distribution and proportion for slag design

Normalized gangue distribution (%)				Gangue proportion in the DRI (%)
SiO_2	MgO	Al_2O_3	CaO	
70	17	5	8	10
70	17	5	8	15

7.3.3. Fluxing materials

Most DRI gangue can easily form a slag with no addition of fluxing materials as shown in Figure 107. However, the majority of DRI gangue compositions are far away from the liquidus line for either MgO-rich, or $MgAl_2O_4$ refractories, indicating that the corrosion will be very high. Fluxing materials play a very important role in modifying the behaviour of the slag by changing its chemical composition. Moreover, the amount and the types of fluxes used depend upon the gangue composition of the DRI, the required final slag composition, as well as the key performance indicators of the furnace operations. The fluxes used in the slag designing process and their functions are as follows:

- Bauxite to supplement the Al_2O_3 content
- Burnt lime to control the CaO content
- Burnt dolomite to adjust the MgO and CaO content of the slag
- Quartzite to control the SiO_2 content of the slag

7.4. Refractories in iron and steel production

7.4.1. Importance

Refractories are specialized materials that help to contain the molten iron, steel, or slags in order to keep the integrity of the furnace during these high temperature processes. According to Biswas and Sarkar (2020), refractories are solid materials, capable of withstanding very high temperatures (1400 - 2500 °C). They can prevent corrosion to liquid metal and slag and are resistant to hot abrasion and erosion. Moreover, refractories are composed of oxides, nitrides and carbides, used in combination to overcome temperature fluctuations, high temperature deformation, and with adequate load-bearing capacity.

Refractories can be classified in many ways, based on the installation mode (shaped or unshaped), the type of bonding (fired, tempered), and lastly, the chemical composition (acid, basic, or neutral) (Fang et al., 1999; Horckmans et al., 2019). Every pyrometallurgy process requires specific types of refractory materials that can make the production process more efficient and decrease the risk of refractory failure. This indicates that wrong selection of refractory materials makes the production process vulnerable, unsafe, and with a shorter campaign life. Therefore, the selection of suitable refractory materials for a process is paramount to the success of the process. Moreover, the current technological development of iron and steelmaking processes also necessitates an exploration of advanced refractory materials capable of efficiently sustaining these newly developed technologies, which applies in this case to the DRI-OBF technology.

7.4.2. Types of refractory wear

The three different types of refractory wear that occur at the hot face (surface of contact between slag and refractory) are abrasion, erosion, and corrosion. Abrasion occurs when the refractory surface wears off due to the scrubbing action of moving solids. Corrosion occurs from chemical reaction between the liquid slag and solid phases at the hot face of the refractory, and lastly, erosion is the wearing away of the disintegrated refractory surface due to the washing action of the moving slag (Biswas and Sarkar, 2020). Generally, the refractory surface is firstly weakened by corrosion, and then erosion occurs (Den Hoed, 1999). Sometimes, poor physical properties of the refractory can lead to slag penetration into the refractory, which will lower its solidus temperature, and eventually lead to erosion.

7.4.3. Properties of refractories

The properties of refractories can be broadly grouped into three categories: chemical, physical, and thermal. The main and common properties of the refractory include, low and high temperature strength, thermal shock resistance, porosity, and thermal conductivity (Akiyoshi et al., 2017; Banerjee, 2004). This study focuses on the chemical interaction between the molten slag and the selected refractories. In this respect, the information derived in this chapter only considers the corrosion of the refractory surface by the molten slag at the selected temperature. The equilibrium is dictated by the saturation levels of solid phases from the refractory in the molten slag, and these can ultimately assist with predicting the degree of corrosion.

Jansson et al. (2005) highlighted that the resistance of refractories toward the slag is determined first of all by equilibrium relations, demonstrating that a slag that is already saturated with a solid phase, cannot further attack a refractory consisting of that solid phase. According to Biswas and Sarkar (2020), other slag properties such as the viscosity, temperature and the surface tension also affect the refractory wear. However, these properties depend on the selected slag composition. Hence, the slag designing process in this study will also take those properties into consideration before selecting the optimal slag composition for the OBF Gen2.

7.4.4. Common refractories in the steel industry

Conventionally, blast furnaces are lined with carbon bricks, silicon carbide (SiC), and in addition, high alumina bricks are used (Thethwayo and Steenkamp, 2020; Almeida et al., 2017). In contrast, modern electric arc furnaces are lined with MgO-rich, and high alumina/magnesite bricks (Qin and Qi, 2012; Li et al., 2000) for the different areas in the furnace. The main areas are the free board, the side wall, the hearth and the roof which is equipped with water-cooled jackets to regulate the temperature and improve the performance of the refractory. The slag is mostly in contact with the lower region of the side wall, whereas the metal is in contact with both the lower side wall and the hearth.

Refractories in the BOF process should resist high temperature and the generated basic slag while in the EAF, the refractories should also resist the mechanical impingement of the scrap iron, as well as the localized hot spots caused by the arcing (Banerjee, 2004). Therefore, the refractories in the EAF must have good mechanical strength, high refractoriness (high temperature resistance), and resistance to basic slag. Moreover, for slags that are undersaturated

in the basic oxide (MgO), the incorporation of cooling systems in the refractory reduces the solidification temperature at the hot face, causing the creation of freeze linings composed of slag constituents (Naudé and Shapiro, 2010). It can be seen that the freeze lining layer helps protect the refractory from further corrosion since its composition is similar to the slag. Therefore, the corrosion of refractory can be minimized by producing a slag that is saturated in the main constituent of the refractory, or by installing cooling systems in the refractory that can facilitate the formation of freeze linings. The installation of cooling systems might also increase the overall energy loss of the process.

7.4.5. Refractory performance tests

The making of refractory materials is an art reserved to refractory manufacturers because two refractories might have the same name based on chemical composition, but different performances based upon how they were crafted. The testing of refractory properties is usually indicative of the refractory performance in real applications (Banerjee, 2004). There are several performance tests that are conducted to assess the different properties of the refractory, but in this study the interest is on tests that evaluate the resistance of refractories to corrosion as described by Brosnan (2004). Moreover, corrosion tests can either be static, or dynamic including both finger testing and crucible testing (Reynaert et al., 2020). An illustration of the crucible test is shown in Figure 109, in which the thickness of the dissolved brick (Dd), the depth of infiltration (Di) and the height of the remaining slag level (Hrs) are indicated after a corrosion test

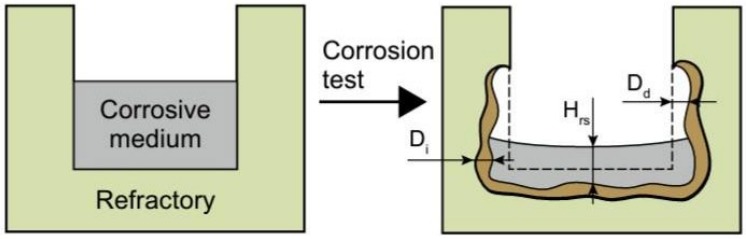


Figure 109: Crucible corrosion test (Reynaert et al., 2020)

Reynaert et al. (2020) further noted that dynamic tests provide data closer to the industrial working conditions. The most commonly employed dynamic test is the rotating finger test. Moreover, several refractory materials can also be tested in the same crucible using a semi-static, induction furnace test, or a fully dynamic, rotary slag test. It should be noted that in the induction furnace test, the induction heating helps with the heating and stirring of steel, and the slag is only heated through the heat transfer from the steel. An illustration of the rotating finger test, and the induction furnace test are shown in Figure 110.

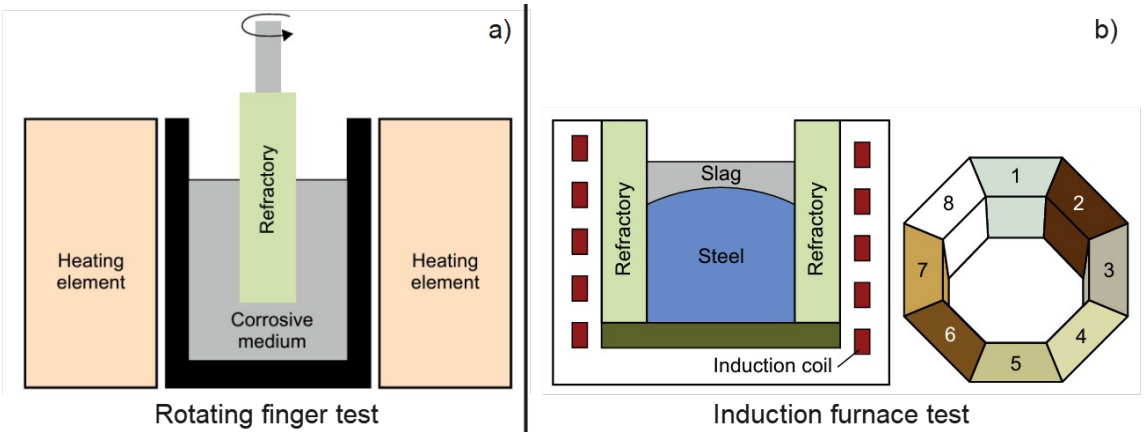


Figure 110: (a) Rotating finger test, and (b) Induction furnace heating test (Reynaert et al. 2020)

A comparison of corrosion test parameters for the different types of corrosion tests is also summarized in Table 20, which highlights the advantages and disadvantages of each corrosion test (Reynaert et al., 2020).

Table 20: Advantages and disadvantages of corrosion tests (Reynaert et al. 2020)

	Sessile drop test	Crucible test	Finger test	Rotating finger test	Induction furnace	Rotary slag test
Thermal gradient	No	No	No	No	Yes	Yes
Slag volume	Small	Small	Big	Big	Medium	Medium
Slag renewal	No	No	Possible	Possible	Possible	Yes
Interaction between brick	No	No	Possible	Possible	Possible	Possible
Temperature control	Good	Good	Good	Good	Good	Difficult
Atmosphere control	Possible	Possible	Possible	Possible	Possible	Impossible
Slag agitation	No	No	No	Strong	Medium	Strong
Possibility to test the thermal shock resistance	No	No	Yes	Yes	No	Yes
Easy to realize	Very easy	Very easy	Easy	Easy	Difficult	Difficult
Cost	Very cheap	Cheap	Average to expensive	Average to expensive	Average to expensive	Expensive
Scale	Low	Low	Medium	Medium	High	High

Generally, the extent of dissolution or infiltration of the refractory by the slag is calculated by comparing the thickness of the refractory before and after the corrosion test (Ko, 2002).

7.4.6. Refractory selection for OBF and SVF

Electric arc furnaces are usually operated in submerged arc mode depending on the commodity, whereas the novel OBF technology is operated in open arc mode, where the heat dissipation towards the refractory is relatively high due to the electrode not being immersed in the slag. Therefore, basic refractories that are able to handle high operating temperatures such as the MgO-rich refractories are ideal for this novel OBF technology.

Carbon refractories are suitable for the slag but are prone to corrosion by the metal due to the relatively low carbon saturation of the electric pig iron compared to the conventional pig iron from the BF. The slag, however, is almost inert to carbon refractory since most of the iron

oxide has already been reduced in the DRI process, thereby minimizing the reaction of FeO in the slag with C from the refractory, commonly observed in conventional BF. Li et al. (2000) pointed out that the local corrosion of MgO-C in steelmaking is due to cyclic dissolutions of MgO and graphite from the refractory into slag and metal phases, respectively. Therefore, MgO-rich refractory can still be used in the OBF Gen2 with a molten slag that is saturated in MgO, thereby reducing the corrosion of the refractory and extending the lifespan of the OBF's refractories.

In the SVF, a carbon refractory can be used because there is no production of hot metal, only valorisation of the liquid slag from the OBF Gen2. However, this should be done at low oxygen partial pressure to avoid the oxidation of carbon: either a reducing, or an inert atmosphere would be ideal. On the other hand, an MgO-rich refractory cannot be considered because the intended SVF products (BF equivalent slag, high CaO slag) are undersaturated in MgO, demonstrating that the refractory wear will still be significant. Magnesium Aluminium Spinel ($MgAl_2O_4$) refractories were not tested during the smelting campaign but can also serve as good refractory options for the OBF Gen2, especially for slag compositions that are saturated in Al_2O_3. Therefore, the two refractories that will be considered in this study are MgO-rich and $MgAl_2O_4$ for the OBF Gen2, whereas the SVF will be lined with a carbon refractory on the side wall and the hearth, which will be inert to the slag. The performance of MgO-rich refractories can also be enhanced with the addition of other minor elements such as chromium and carbon to produce MgO-Cr_2O_3 and MgO-C, respectively.

7.5. OBF Gen2 Slag design

7.5.1. Criteria for selection of slag compositions

From the preceding sections, it has been suggested that the TkSE gangue composition will be used along with MgO-rich and $MgAl_2O_4$ refractories in the OBF Gen2. Ideally, a slag should have the same tendency (basic or acidic) as the refractory. For these novel high MgO slags, the basicity value of CaO/SiO_2 is misleading; however, the saturation levels of CaO and MgO will dictate the degree of corrosion. Hence, the basicity ratio that will be considered is $(CaO+MgO)/SiO_2$. Furthermore, most DRI gangue compositions are acidic with varied acidity levels (amount of SiO_2). The fluxing requirement will therefore vary with the gangue composition of the DRI. The initial OBF slag was not directly exposed to the MgO periclase phase, however, it was closely exposed to Merwinite as shown in green in Figure 111.

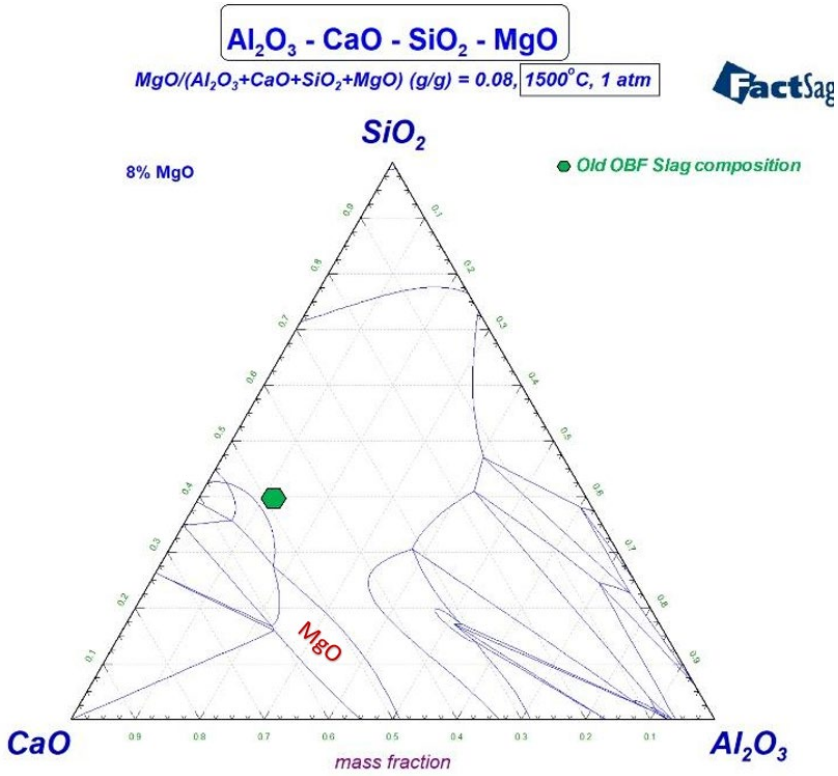


Figure 111: Position of old OBF slag with respect to periclase

The following design criteria were considered in order to obtain the suggested high MgO slag compositions:

- The selected slag should be fully liquid at the selected compositions.
- The amount of CaO will always be higher than the amount of MgO in the slag because of the dolomite ratio (CaO/MgO = 1,4). In the slag, this ratio should be between 1,1 and 1,7 for minimum fluxing requirement.
- The MgO content should not increase to a level that will push the liquidus temperature of the basic slag beyond 1500°C (26% is found to be the maximum limit for this condition at a minimum CaO/MgO of 1,1).
- CaO content should be exchanged with MgO in order to control their saturations and ultimately the refractory wear.
- MgO should be at most 26% and CaO at least 30%. However, with $MgAl_2O_4$ refractory, the CaO and MgO contents can go down to at least 25% and 15%, respectively.
- The SiO_2 content can be kept between 30% and 42%, considering the liquidus of 1500°C and the high SiO_2 content (> 50%) of DRI gangue compositions.
- The OBF Gen2 slag should have a composition that can easily be reverted back to a BF equivalent slag in the SVF without consuming excessive fluxing materials.

The position of a collection of acidic gangue compositions (which includes the TkSE gangue composition) is shown in the blue hexagon. In comparison, the position of the new slag compositions is shown in red in Figure 112.

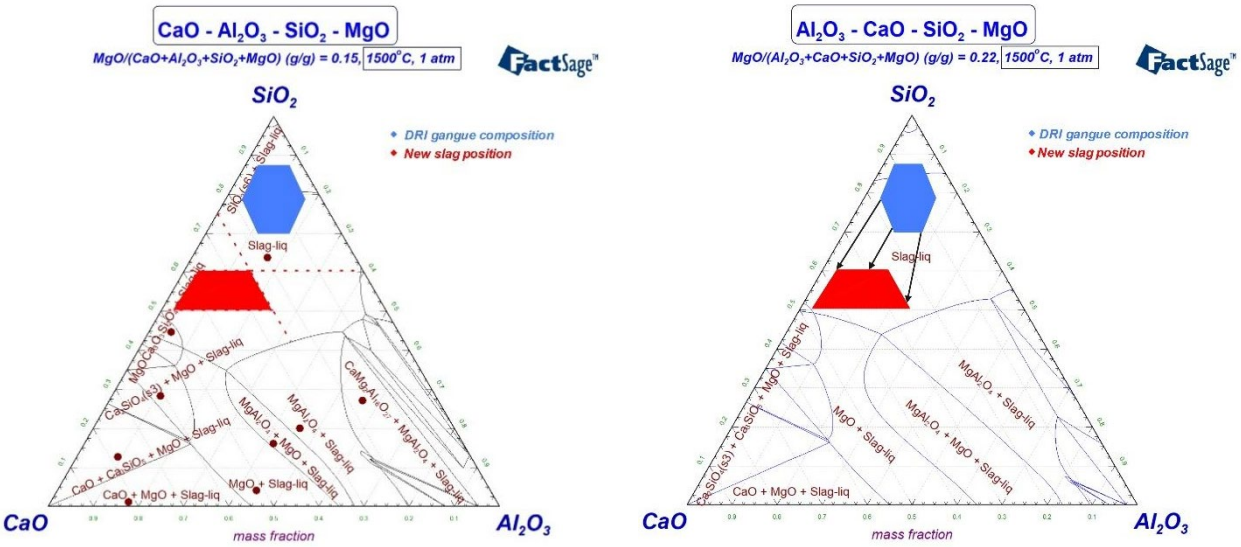


Figure 112: Position of new slag compositions (left: at 15% MgO, right: at 22% MgO)

Comparing the two diagrams in Figure 112, it can be seen that as the MgO content of the slag increases, while keeping the proportion of the other components (Al_2O_3, SiO_2, CaO) the same, the liquidus lines of both MgO (periclase) and $MgAl_2O_4$ (spinel) get closer to the position of the selected slags. This shows that the liquidus temperature might be slightly higher compared to the scenario on the left, however, the saturation levels of MgO are favourable, and there will be less corrosion of the pure MgO refractory (periclase). Fang et al. (1999) noted that MgO refractories have high refractoriness (capable of handling high operating temperatures) and are commonly used in basic environments. They are, however, susceptible to hydration and must be stored and handled appropriately prior to installation. Moreover, this hydration susceptibility can be reduced by combining MgO with other elements such as carbon, and chromium.

In the studies (Bavand-Vandchali et al., 2009; Zhu et al., 2014; Zhang et al., 2001), it has been reported that Al_2O_3 reacts with MgO from a MgO-C refractory, leading to the formation of $MgAl_2O_4$ spinel, which enhances the ceramic bonding of the matrix and improves the overall corrosion resistance of the MgO-C refractory. This scenario might occur when working with high Al_2O_3 slag on a MgO-rich refractory. In these instances, there might be some sacrifice in terms of superheat, however, the corrosion of the refractory will be minimal. Das et al. (2021) noted that high Al_2O_3 in the BF slag has an adverse impact on the liquidus temperature and the slag viscosity, whereas high MgO decreases both the liquidus temperature and the slag viscosity. It was further noted that the adverse impact of high Al_2O_3 (18 to 24%) slag can be minimized by increasing the MgO content in the slag (9 to 14%).

7.5.2. Selected slag compositions for each refractory

For simplicity of the slag designing process in this study, three slag compositions were taken for each refractory at different levels of MgO. The compositions were selected in such a way that the slag should be directly above the liquidus line of the solid phases in the refractory. Hence, the far bottom corners of the red trapezoid in Figure 112 were used to select the 6 possible slag compositions.

Moreover, the left corner was used for MgO-rich refractory, and the right corner was used for $MgAl_2O_4$ refractory. The different levels of MgO are shown in the 3D quaternary systems in Figure 113.

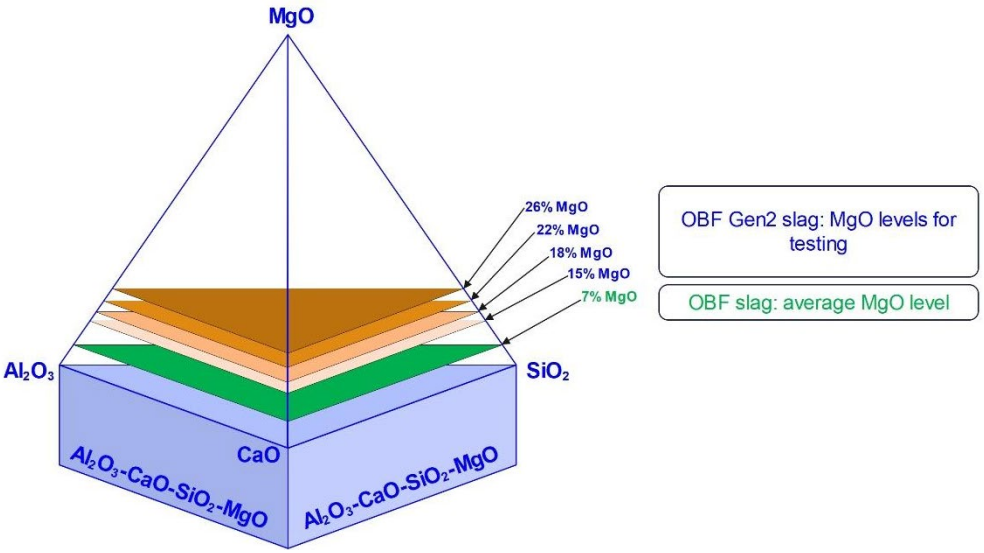


Figure 113:3D quaternary diagram of the new slags

Figure 113 shows that the average MgO level of the original OBF slags is approximately 7%, while the new slags will have MgO levels between 15% and 26% for the different points. Moreover, the lower limit of the MgO level (15%) will be for slags that also contain high Al_2O_3 (> 11%), whereas the higher limit (26%) will be for slags with minimum Al_2O_3 (< 7%). The selected OBF Gen2 slag compositions are summarized in Table 21.

Table 21: Summary of the selected slag composition for the OBF

	Slag No	Total	%SiO_2	%MgO	%Al_2O_3	%CaO	CaO+MgO/ SiO_2	CaO/MgO	Al_2O_3 +SiO_2
For MgO-rich refractories	1	100	41	22	3	34	1,36	1,56	44
	2	100	38	26	7	29	1,42	1,13	45
	3	100	42	22	3	32	1,29	1,43	46
For $MgAl_2O_4$ refractories									
	4	100	36	18	18	28	1,28	1,56	54
	5	100	41	15	19	25	0,97	1,67	60
	6	100	38	15	23	25	1,07	1,67	60

7.5.3. Evaluation of liquidus temperatures

7.5.3.1. MgO-rich refractory

The three slags that were designed for MgO-rich refractory are slags 1, 2 and 3. They have a very low Al_2O_3 content, in the range of 3 to 7%. FactSage was used to generate the liquidus of these systems at constant MgO content of 22% for slags 1 and 3, and 26% for slag 2 as shown in Figure 114.

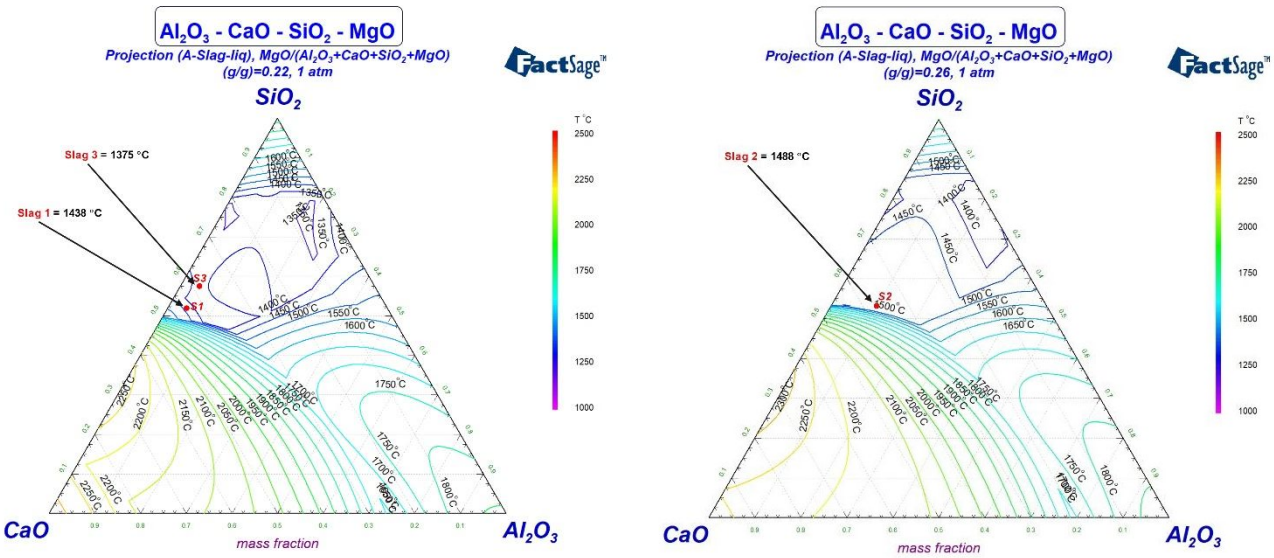


Figure 114: Liquidus temperatures of slag 1 to 3 for MgO-rich refractory

Based on the results in Figure 114, it can be seen that the approximated liquidus temperatures of slags 1, 2, and 3 are 1438 °C, 1488 °C, and 1375 °C, respectively. Moreover, as the MgO content increased from 22% to 26%, the liquidus temperature increased. The slag with higher CaO also has a slightly higher liquidus temperature for constant MgO, as is the case for Slags 1 and 3.

7.5.3.2. $MgAl_2O_4$ refractory

The three slags for $MgAl_2O_4$ refractory are slags 4, 5, and 6, which contain very high Al_2O_3, in the range of 18% and 23% as per Table 21.

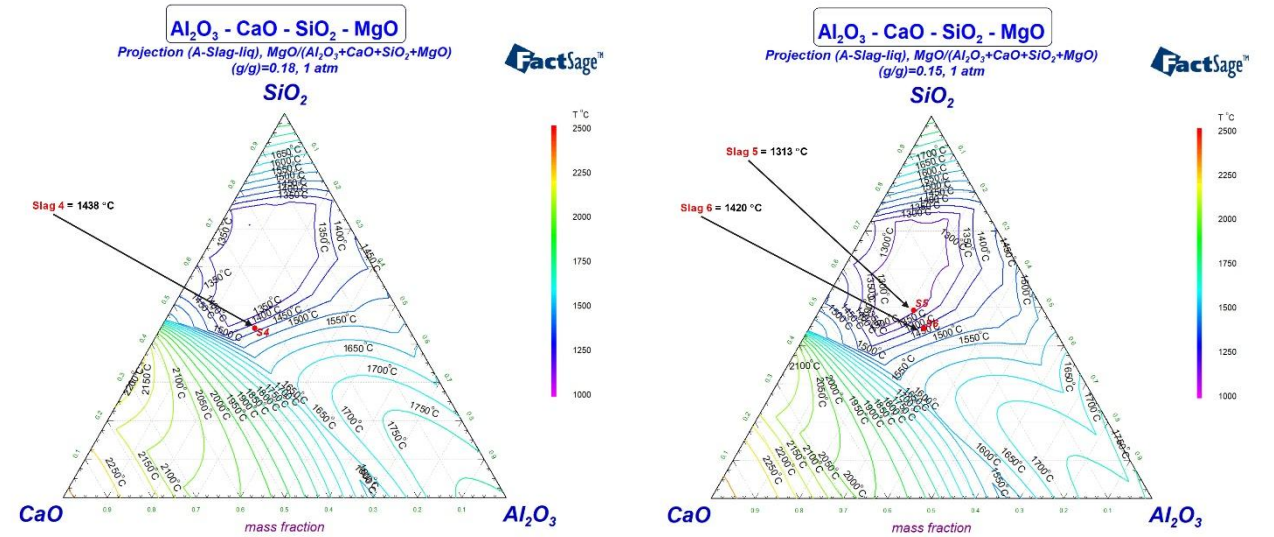


Figure 115: Liquidus temperatures of slag 4 to 6 for $MgAl_2O_4$

The results in Figure 115, show that the liquidus temperatures of slags 4, 5, and 6 are 1438 °C, 1313 °C, and 1420 °C, respectively. The slag that has more SiO_2 and Al_2O_3 seems to have a low liquidus temperature. However, the high Al_2O_3 content also indicates that the fluidity of the slag will be very low necessitating to work at a higher temperature than the liquidus (Das

et al., 2021). The viscosity and thermal conductivity, along with other properties of the selected slags, will be discussed in chapter 8.

The approximated liquidus temperatures were also generated using FactSage, and the results are summarized in Table 22.

Table 22: Liquidus temperatures of the selected slags

Refractory	Slag type	T1	T2	Liquidus(°C)
MgO-rich	Slag 1	1425	1450	**1438**
	Slag 2	1475	1500	**1488**
	Slag 3	1350	1400	**1375**
$MgAl_2O_4$	Slag 4	1425	1450	**1438**
	Slag 5	1300	1325	**1313**
	Slag 6	1400	1440	**1420**

7.5.4. Process flexibility and slag corrosion assessment

7.5.4.1. Effect of MgO content and operating temperature for MgO-rich refractory

The MgO content will play a crucial role in the properties of these new high MgO slags, hence investigating the behaviour of the system upon change of MgO content is of paramount importance. The MgO content was changed from 22% to 26% at a constant temperature of 1500 °C and the resulting superimposed quaternary system is shown in Figure 116.

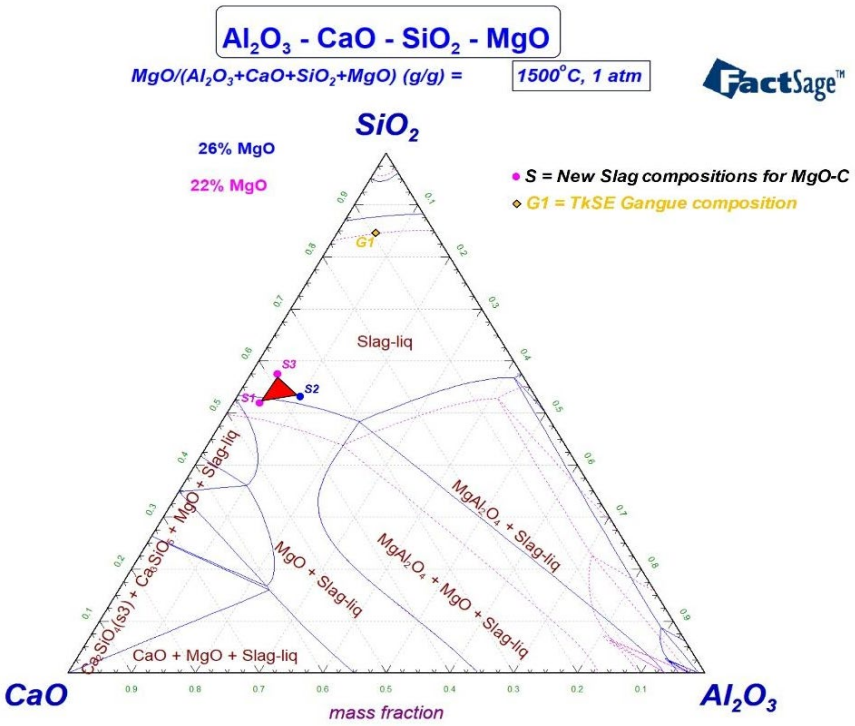


Figure 116: Effect of MgO content at constant temperature for MgO-rich refractory

The results in Figure 116, show the first scenario of modifying the gangue composition of the DRI by increasing the MgO content. As the MgO content increases, the slag becomes closer to the saturation levels (liquidus line), and thus the liquidus temperature increases. This can be seen by comparing slag 1 (liquidus temperature of 1438 °C) and slag 2 (liquidus temperature of 1488 °C). These temperatures are close to the selected operating temperature of 1500 °C depending upon their distances to the liquidus lines of their MgO contents. Generally, the further the position of the slag to the periclase phase, the lower the liquidus temperature and the saturation level of MgO, which ultimately implies higher driving force of corrosion. Slag 3 will likely corrode the refractory more than slag 1 and 2. Moreover, increasing the MgO content of the slag beyond 26% will push the liquidus temperature beyond 1500°C and the superheat will be significantly higher.

The temperature was also changed from 1450 °C to 1550 °C while considering that all three points were on the 22% MgO plane, and the results are summarized in Figure 117.

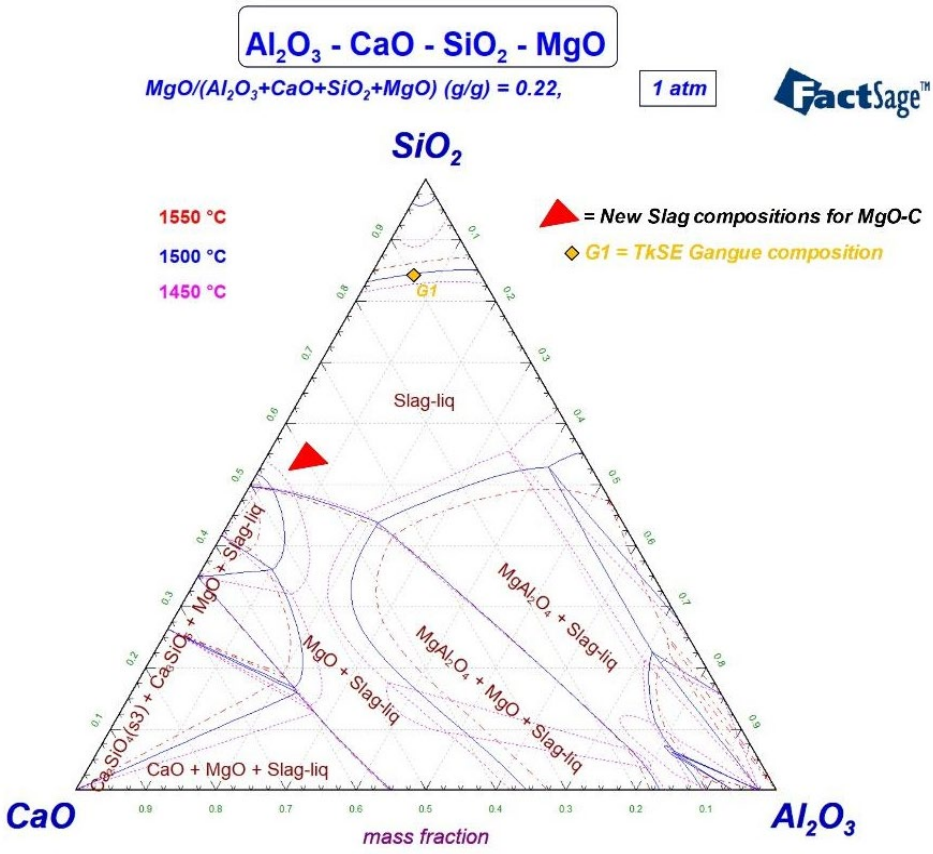


Figure 117: Effect of temperature at constant MgO content for MgO-rich refractory

The slight change in temperature at constant MgO does not change the saturation level of MgO in the slag with respect to the periclase phase. This is shown in Figure 117 where the liquidus line of MgO barely moved as the temperature was changed from 1450°C to 1550°C. However, the position of the $MgAl_2O_4$ spinel decreased considerably compared to the periclase as the temperature was increased by 100°C from 1450°C. This shows that the MgO-C refractory is more likely to be flexible to the change in operating temperature during smelting operations without affecting corrosion. Furthermore, the triangle formed by slags 1, 2, and 3 is a good

region to operate in, even the version of slag 2 but on the 22% MgO plane promises also good behaviour. However, the operating temperature should be > 1500°C to avoid forming a solid Akermanite ($Ca_2MgSi_2O_7$) phase, shown at 1450°C. Overall, slag 3 has a relatively low liquidus temperature and might be the best option among the three, but the mass and energy balance in chapter 8 will ultimately dictate the best slag composition.

7.5.4.2. Effect of CaO content and temperature for $MgAl_2O_4$ refractory

The effect of CaO content was also investigated at lower levels between 25% and 28%.

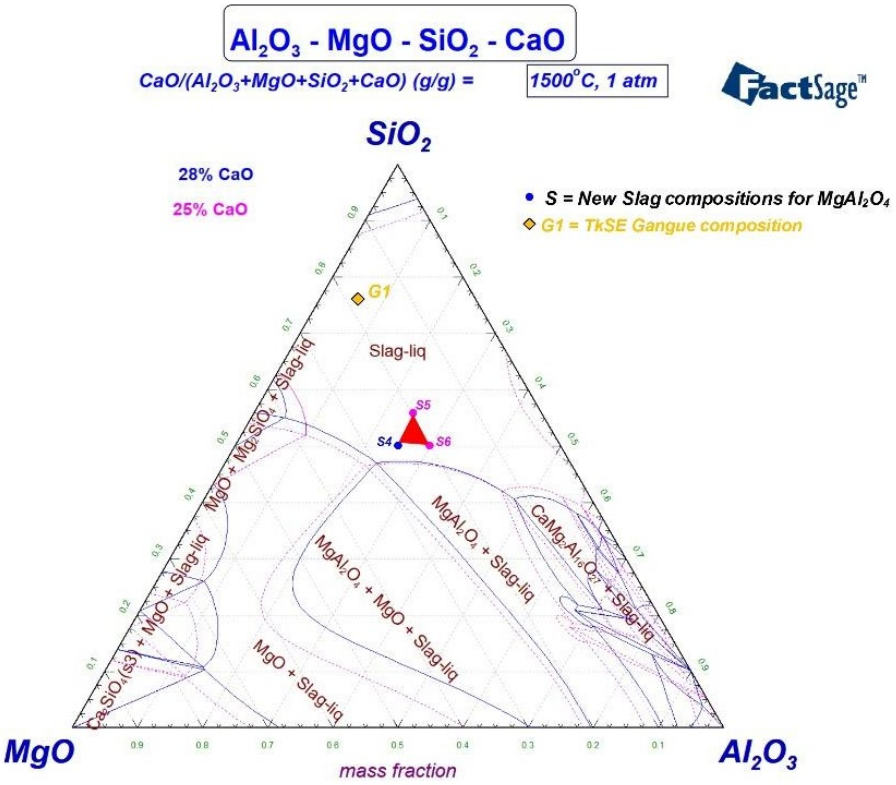


Figure 118: Effect of CaO content at constant temperature for the $MgAl_2O_4$ refractory

The change in CaO content from 25% to 28% didn't really have an impact on slags 4, 5, and 6 as per Figure 118. While the liquidus lines barely moved, slags 4 and 6 are closer to $MgAl_2O_4$ compared to slag 5. This explains their relatively high liquidus temperatures of 1438°C and 1420°C, respectively. Slags 4 and 5 have roughly the same Al_2O_3 content, and the liquidus temperature of slag 5 is 1313°C because it has a CaO content of 25% compared to the 28% in slag 4. This shows that an increment in CaO at constant high Al_2O_3 levels leads to an increment in liquidus temperature. Similar to the high MgO slags, the temperature was also changed for the high Al_2O_3 slags, and the results are shown in Figure 119.

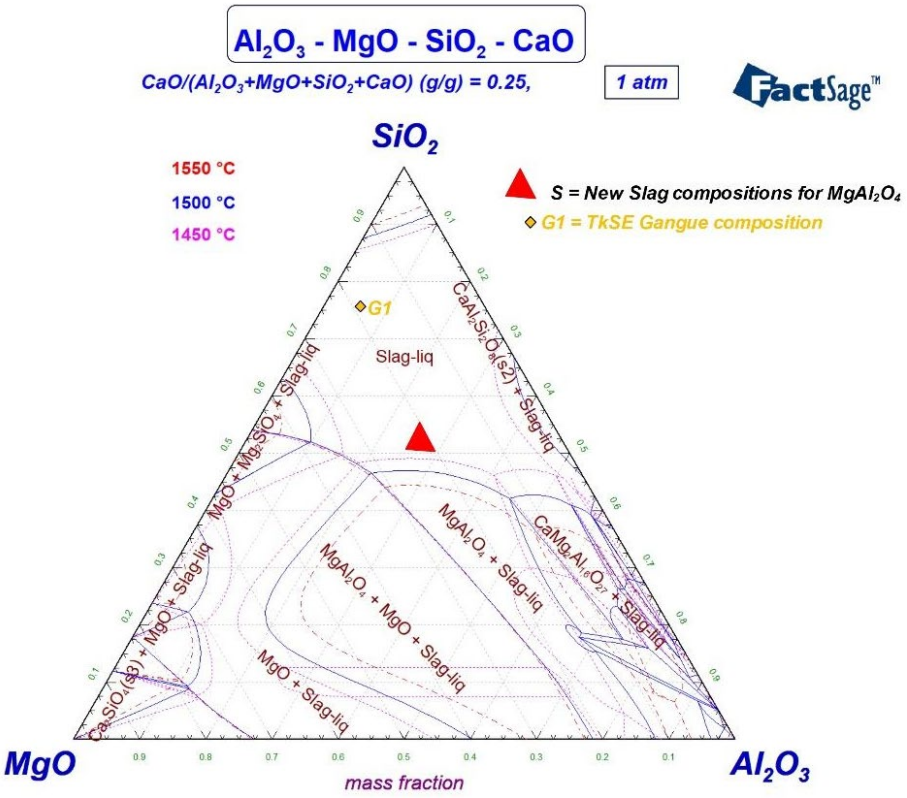


Figure 119: Effect of temperature at constant CaO for the $MgAl_2O_4$ refractory

For low CaO (25%), high MgO and high Al_2O_3 slags, the change in temperature also has a drastic impact on the shift of the liquidus line in terms of $MgAl_2O_4$ as shown in Figure 119. From the high Al_2O_3 slags, slag 5 has a lower liquidus temperature than slags 4 and 6, however, its corrosiveness towards the refractory is higher since its position is relatively far from the liquidus line.

$MgAl_2O_4$ seems to be the most sensitive to temperature change and also to the change in MgO content of the slag. On the other hand, MgO (periclase) only demonstrates sensitivity to the change in MgO content of the slag. In summary, the MgO rich refractories such as MgO-C will likely display high stability in terms of operational temperature change and also flexibility in terms of slag composition variations for the selected slags in this study. Slags 3 and 5 will likely be more corrosive to their respective refractories. Nonetheless, the practical significance of the corrosion needs to be confirmed through experimental tests.

7.6. SVF Slag design

As discussed earlier in this chapter, the SVF serves the purpose of valorising the OBF Gen2 slag into two possible products, namely, a high CaO slag, or a BF slag equivalent with composition similar to the OBF slag generated in part 1 of this study.

7.6.1. BF equivalent slag

The valorisation into a blast furnace equivalent slag has already been done and demonstrated in part 1 of this study. The OBF slag is very similar to the conventional BF slag in terms of cementitious properties as discussed in chapters 4, 5, and 6. However, the OBF slag's

corrosiveness towards the MgO-C refractory has led to the development of the OBF gen 2 slag. The OBF Gen2 slag is developed with the intention of reducing the corrosion towards the MgO-C refractory, thereby extending the life span of the refractory, and providing the possibility of increasing the total volume output of the slag without affecting the operational conditions of the furnace.

Carbon refractories could not be used in the OBF because of the low carbon-saturation of the metal, which leads to corrosion. The BF slag is inert to carbon refractories but it is undersaturated in MgO, demonstrating that it will corrode the refractory if a MgO-C refractory is used in the SVF. Unlike the OBF which produces the metal and the slag, the SVF only produces the slag. Moreover, the furnace will be built with two tapholes to accommodate the tapping of metal droplets that settle from the slag during the SVF process. Therefore, a carbon refractory serves as a good option for the SVF to produce a BF equivalent slag, or even a high CaO slag.

7.6.2. Feasibility of clinker production in the SVF

Clinker is the main component of cement: it is made up of crystalline phases such as alite ($3CaO.SiO_2$), belite ($2CaO.SiO_2$), and others as discussed in chapter 2. However, what is important in this section is the chemical composition of clinker. Guetteche et al. (2012) noted a clinker chemical composition of 65% CaO, 22% SiO_2, 5% Al_2O_3, and 1% MgO. The results in Figure 120 were generated using FactSage at 65% CaO for the Al_2O_3-CaO-SiO_2-MgO system.

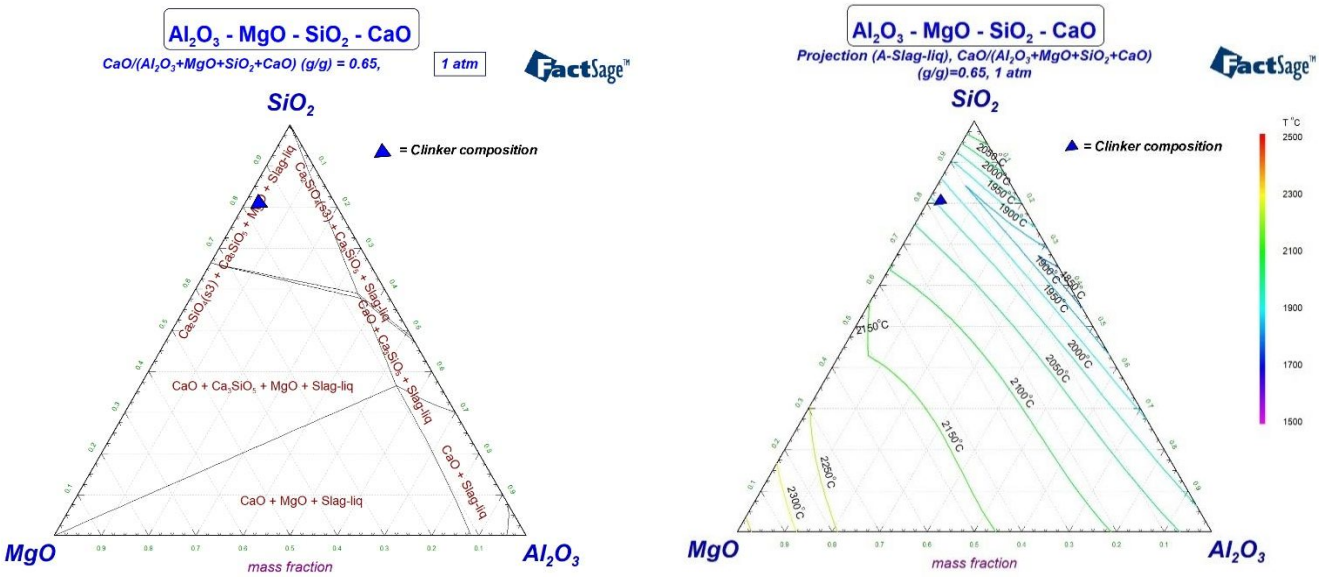


Figure 120: Quaternary system of clinker at 65% CaO (left: isothermal at 1500°C, right: projections)

The results in Figure 120 shows that liquid clinker cannot be produced at 1500°C as per the isothermal diagram on the left. This is because the slag will be a solid solution of alite ($3CaO.SiO_2$), belite ($2CaO.SiO_2$), and some MgO. The diagram on the right shows that the liquidus temperature of clinker is close to 2000°C, which is exceedingly high for a normal operating furnace. Moreover, the slag region is shown in Figure 121, for 2000°C at 65% CaO.

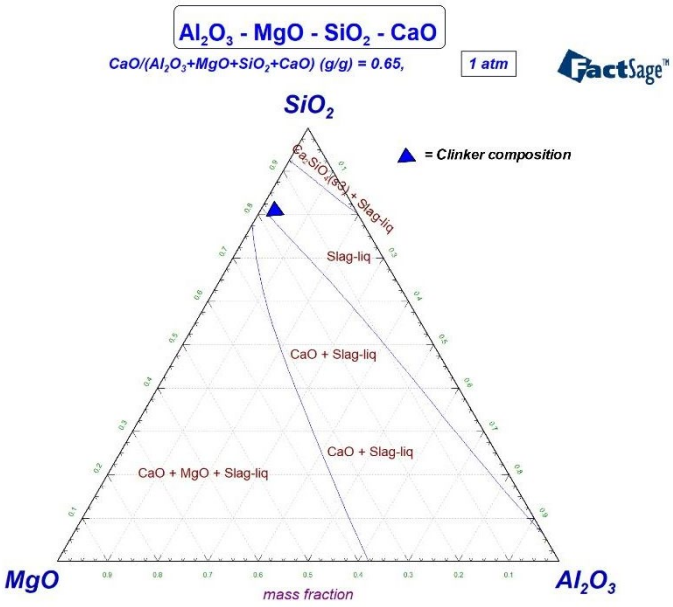


Figure 121: Isothermal diagram of clinker at 2000°C and 65% CaO

Figure 121 confirms that clinker is indeed liquid at 2000°C. However, the operating temperature should be around 2200°C to allow the superheat since the composition is very close to the liquidus line. Working at such excessive temperatures is prone to high energy consumption and high refractory wear, making the overall process non-viable from both an economic and even process point of view.

Clinker is usually produced in a rotary kiln using a blended charge of limestone and clay. The major components such as alite and belite form at solid state at lower temperatures between 1000°C and 1450°C and air cooled to prevent the recrystallization of belite from alite (Li et al., 2014). The rotary kiln produces clinker in nodule form: typically cooled in a grate cooler where air is blown through the clinker bed. FactSage was used in this study to confirm the temperature of formation of alite and belite.

Table 23: Activities of calcium silicate system between 1000°C and 1600°C

Activities of C-S 1000 to 1600 °C					
2CaO + SiO2 =	**CaSiO3**	**Ca2SiO4**	**Ca3Si2O7**	**Ca3SiO5**	**CaO**
1000 °C	0,09	1	0,27	0,13	0,18
1100 °C	0,08	1	0,17	0,19	0,22
1200 °C	0,07	1	0,12	0,24	0,26
1300 °C	0,06	1	0,08	0,3	0,3
1400 °C	0,05	1	0,06	0,35	0,34
1500 °C	0,05	1	0,05	0,39	0,38
1600 °C	0,04	1	0,04	0,43	0,42
3CaO + SiO2 =					
1000 °C	0,02	1	0,05	0,75	1
1100 °C	0,02	1	0,04	0,86	1
1200 °C	0,02	1	0,03	0,95	1
1300 °C	0,02	1	0,02	1	0,99
1400 °C	0,02	1	0,02	1	0,97
1500 °C	0,02	1	0,02	1	0,97
1600 °C	0,02	1	0,01	1	0,98

Table 23 shows that belite can form even below 1000°C provided CaO/SiO_2 is ≥ 2 in the composition of the materials, whereas alite can only start forming at 1300°C provided that the CaO/SiO_2 of the system is ≥ 3 because of the temperature range in which alite becomes stable. The higher slag formation temperature is due to the high melting point of these compounds. In summary, clinker cannot be produced directly in the furnace at liquid state. Two possible alternative process methods to liquid clinker production would be:

- **First alternative method:** producing a high CaO slag at 1500°C near a kiln. Then, mix it with fine and solid extra burnt lime and ultimately form alite at solid state. However, quick temperature drops will be the problem and alite might end up recrystallizing to belite, which is less hydraulic. This route will need a slag valorisation furnace, a kiln, a cooler, and also intensive process optimization. All these factors increase both the capital and operational cost of the process compared to the cost of the valorised product (clinker). Therefore, this route is also not viable.
- **Second alternative method:** producing a high CaO slag, more reactive than the BF slag, and then water granulate it similar to the OBF slag in part 1 of this study.

7.6.3. High CaO slag (SVF slag)

The possible liquid high-CaO slag that can be produced in the furnace at around 1500°C, has between 48 to 50% CaO as shown in Figure 122. Any further increase in CaO content, will require an increment in temperature. Moreover, it will require more burnt lime addition in the SVF compared to a BF equivalent slag, which typically has less than 43% CaO.

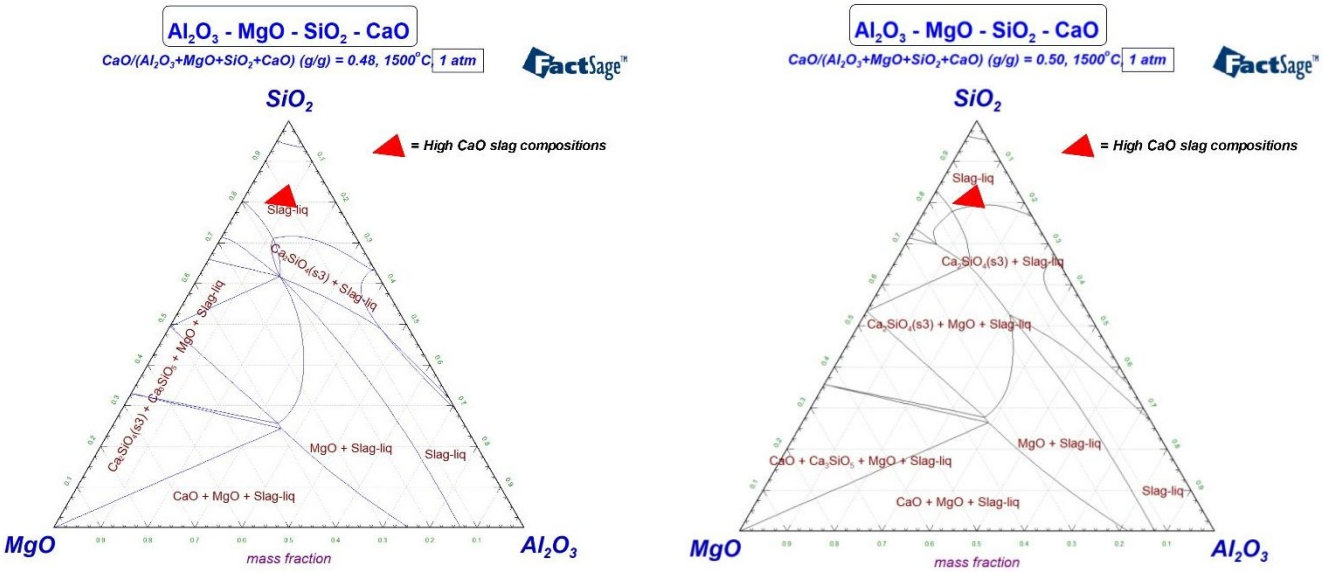


Figure 122: Quaternary diagram for 48% CaO at 1500°C

From Figure 122, it can be seen that the increment in CaO from 48% to 50% has resulted in the upwards shift of the liquidus line, demonstrating the increase in temperature. Moreover, to have a high CaO slag, the SiO_2 content should also be high for a low temperature slag.

7.6.3.1. Effect of temperature

The temperature was increased from 1500°C to 1600°C as shown in Figure 123.

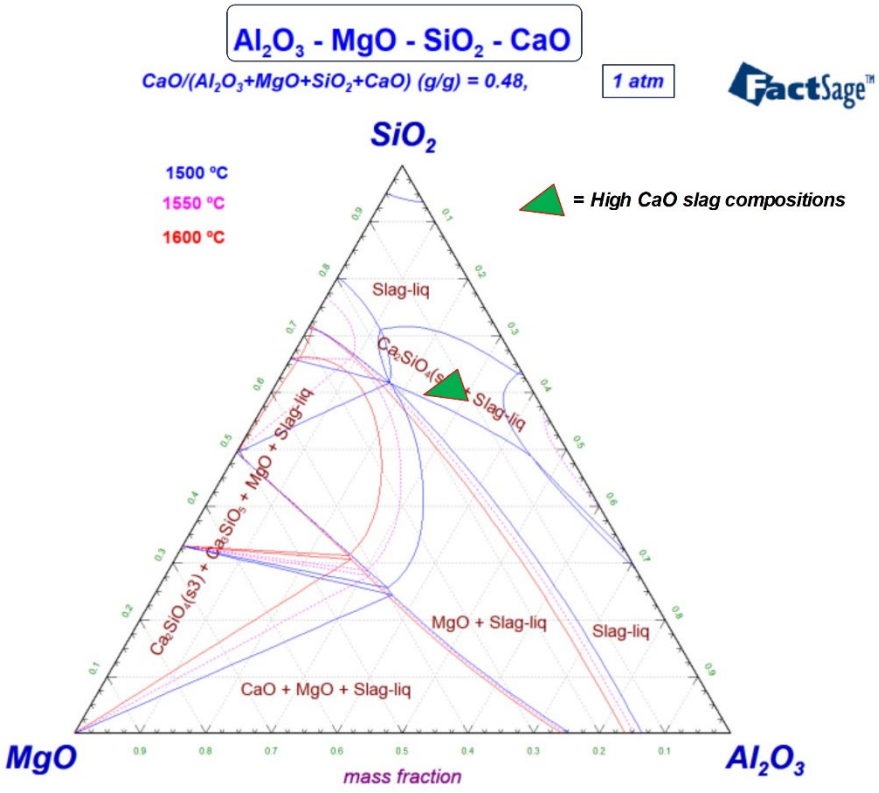


Figure 123: Effect of temperature for high CaO slag

Working at a slightly high temperature, for example at 1600°C, opens up the slag region as per Figure 123. This presents the possibility of lowering the SiO_2 content of the slag and increasing the Al_2O_3 content while having a CaO content of 50%. This will reduce the need of extra quartzite in the SVF and improve the latent hydraulic properties of the slag due to high CaO, and pozzolanic reaction due to SiO_2 and Al_2O_3.

7.6.3.2. Effect of CaO content

In the case of high CaO slags, the CaO must be controlled carefully since any further increment will drastically increase the liquidus temperature as shown in Figure 124.

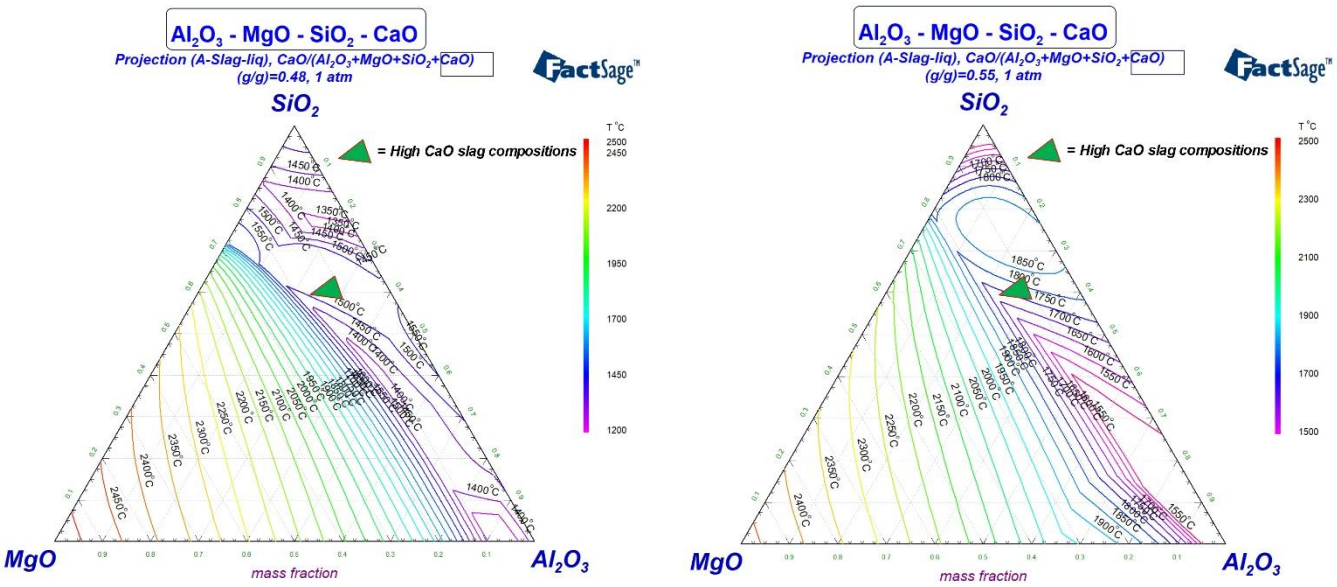


Figure 124: Effect of increment in CaO content for high CaO slag (SVF slag)

With the CaO content increased from 48% to 55%, the liquidus temperature has increased to between 1750°C and 1800°C. Moreover, in such scenarios, the slag can only be fully liquid when the Al_2O_3 content is further increased as shown on the right in Figure 124. This might complicate the process since the fluidity of the slag will be affected. Hence, the maximum recommended CaO content for high CaO slags in this study is 50%.

7.6.4. Selected slag compositions for the SVF

From the overall discussion in this section, the following slag compositions can be considered as the possible SVF products as summarized in Table 24.

Table 24: Selected SVF products

Refractory	SVF Product type	Total	%SiO_2	%MgO	%Al_2O_3	%CaO	Working temp (°C)
Carbon	OBF slag	100	37	7	12	44	1500
	SVF slag 1	100	32	5	15	48	1500
	SVF slag 2	100	42	4	4	50	1600

The SVF slags will most likely perform better than the OBF slag due to their slightly improved cementitious properties. This is because the proportion of network modifiers (CaO, MgO) will be slightly higher in the SVF slags compared to the OBF slag, particularly CaO (Zhang et al., 2022; Blotevogel et al., 2020). The selection of any favourable slag composition from the three SVF products will depend upon the overall added value of the improvement. Moreover, the added value should be determined through cementitious and refractory tests.

7.7. Conclusions

This chapter has used equilibrium relations between the solid phases in the refractory and the liquid slag to generate slag compositions that can minimize the corrosion of the refractory. The distance between the position of the slag composition and the liquidus line (point of saturation) was considered as the driving force to predict the degree of corrosion. Longer distances indicate

that the slag composition is undersaturated in the solid MgO phase from the refractory, ultimately resulting in high degree of corrosion. The aim was to increase the MgO content of the slag so as to reduce the degree of corrosion without excessively increasing the liquidus temperature of the slag beyond 1500°C.

The selected refractories are MgO-rich and $MgAl_2O_4$ for the OBF Gen 2, and a carbon refractory for the SVF. To simplify the mass and energy balance calculations in the following chapter (chapter 8), the TkSE's gangue distribution is considered at 10% and 15% gangue proportion in the DRI. The selected slag compositions for the OBF Gen2 and the SVF are summarized in Figure 125.

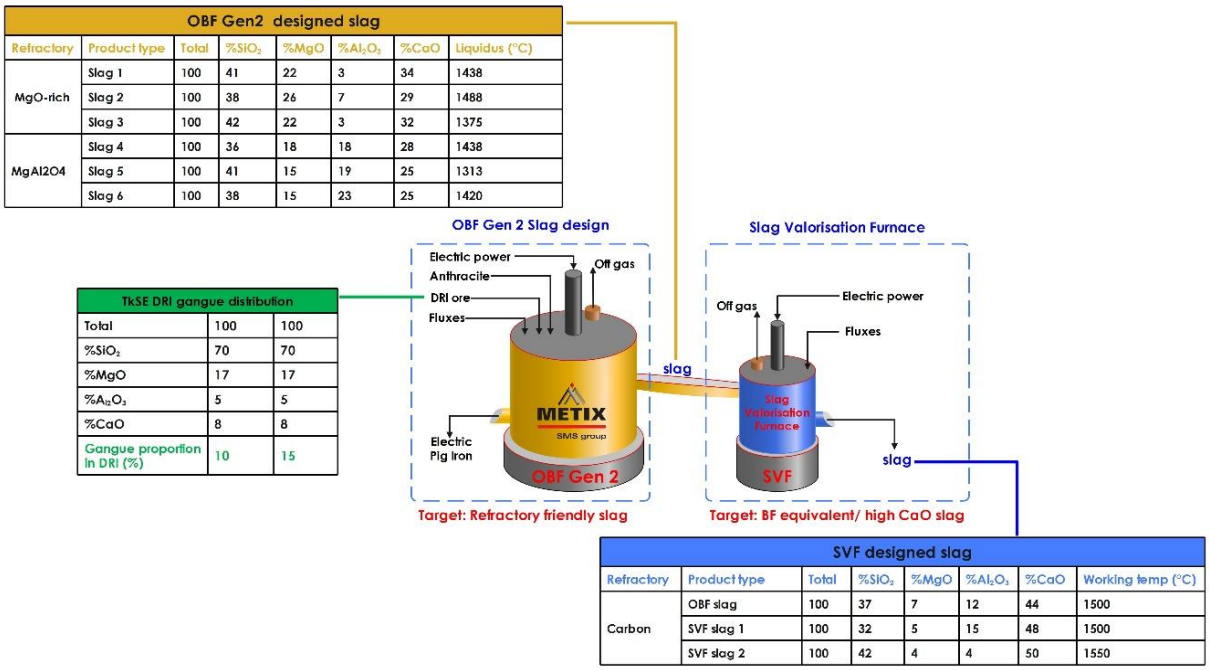


Figure 125: OBF and SVF slag design summary

The suggested slag compositions will be compared in chapter 8 in terms of other slag properties such as viscosity, thermal conductivity, slag production rate, fluxes and energy requirements. Overall, a slag composition with minimal flux addition and energy consumption will be prioritized during mass and energy balances. Minimum slag production rate in the OBF Gen2 will also be prioritized in correlation with the slag composition that promises a higher thermal conductivity.

References

Akiyoshi, M.M., Christoforo, A.L., Luz, A.P. and V.C. Pandolfelli (2017). Thermal conductivity modelling based on physical and chemical properties of refractories. *Ceramics International*, 43(6), pp.4731–4745. doi:https://doi.org/10.1016/j.ceramint.2016.11.091.

Almeida, B.V., Neves, E.S., Silva, S.N. and Junior, F.V. (2017). Blast Furnace Hearth Lining: Post Mortem Analysis. *Materials Research*, 20(3), pp.814–818. doi:https://doi.org/10.1590/1980-5373-mr-2016-0875.

Banerjee, S. (2004). *Properties of refractories. In Schacht C.A (eds) Refractories Handbook.* New York: Marcel Dekker, pp.3–11. doi:https://doi.org/10.1201/9780203026328.

Bavand-Vandchali, M., Sarpoolaky, H., Golestani-Fard, F. and Rezaie, H.R. (2009). Atmosphere and carbon effects on microstructure and phase analysis of in situ spinel formation in MgO–C refractories matrix. *Ceramics International*, 35(2), pp.861–868. doi:https://doi.org/10.1016/j.ceramint.2008.03.001.

Blotevogel, S., Ehrenberg, A., Steger, L., Doussang, L., Kaknics, J., Patapy, C. and Cyr, M. (2020). Ability of the R3 test to evaluate differences in early age reactivity of 16 industrial ground granulated blast furnace slags (GGBS). *Cement and Concrete Research*, 130, pp.105998–105998. doi:https://doi.org/10.1016/j.cemconres.2020.105998.

Brosnan, D.A. (2004). *Corrosion of refractories. In Schacht C.A (eds) Refractories Handbook.* New York: CRC press, pp.39–79. doi:https://doi.org/10.1201/9780203026328.

Cavaliere, P., Perrone, A., Silvello, A., Stagnoli, P. and Duarte, P. (2022). Integration of Open Slag Bath Furnace with Direct Reduction Reactors for New-Generation Steelmaking. *Metals*, 12(2), p.203. doi:https://doi.org/10.3390/met12020203.

Das, K., Agrawal, A., Reddy, A.S. and Ramna, R.V. (2021). FactSage Studies to Identify the Optimum Slag Regime for Blast Furnace Operation. *Transactions of the Indian Institute of Metals*, 74(2), pp.419–428. doi:https://doi.org/10.1007/s12666-020-02144-y.

den Hoed, P. (1999). An application of phase diagrams in the characterization of refractory corrosion. SAIMM School Refractory Materials: Basic Principles and Applications. *Southern African Institute of Mining and Metallurgy*, Johannesburg.

Fang, H., Smith, J.D. and Peaslee, K.D. (1999). Study of spent refractory waste recycling from metal manufacturers in Missouri. *Resources, Conservation and Recycling*, 25(2), pp.111–124. doi:https://doi.org/10.1016/s0921-3449(98)00059-7.

Guetteche, M.N., Zergua, A. and Hannachi, S. (2012). Investigating the Local Granulated Blast Furnace Slag. *Open Journal of Civil Engineering*, 02(01), pp.10–15. doi:https://doi.org/10.4236/ojce.2012.21002.

Horckmans , L., Nielsen , P., Dierckx, P. and Ducastel , A. (2019). Recycling of refractory bricks used in basic steelmaking: A review. *Resources, Conservation and Recycling*, 140, pp.297–304. doi:https://doi.org/10.1016/j.resconrec.2018.09.025.

Jansson, S., Brabie, V. and Jonsson, P. (2005). Corrosion mechanism and kinetic behaviour of MgO-C refractory material in contact with CaO-Al2O3-SiO2-MgO slag. *Scandinavian Journal of Metallurgy*, 34(5), pp.283–292. doi:https://doi.org/10.1111/j.1600-0692.2005.00748.x.

Kim, W. & Sohn, I. 2022. Critical challenges facing low carbon steelmaking technology using hydrogen direct reduced iron. *Joule* 6(10): 2228–2232.

Ko, Y.C. (2002). Role of spinel composition in the slag resistance of Al_2O_3–spinel and Al_2O_3–MgO castables. *Ceramics International*, 28(7), pp.805–810. doi:https://doi.org/10.1016/s0272-8842(02)00046-9.

Li, P., Li, Y., Yu, J., Gao, P. and Han, Y. (2022a). Kinetics and microstructural changes during fluidized reduction of magnetite with hydrogen at low temperatures. *International Journal of Hydrogen Energy*, 47(73), pp.31140–31151. doi:https://doi.org/10.1016/j.ijhydene.2022.07.032.

Li, S., Gu, H., Huang, A., Zou, Y., Yang, S. and Fu, L. (2022b). Thermodynamic analysis and experimental verification of the direct reduction of iron ores with hydrogen at elevated temperature. *Journal of Materials Science*, 57(43), pp.20419–20434. doi:https://doi.org/10.1007/s10853-022-07855-9.

Li, X., Xu, W., Wang, S., Tang, M. and Shen, X. (2014). Effect of SO3 and MgO on Portland cement clinker: Formation of clinker phases and alite polymorphism. *Construction and Building Materials*, 58, pp.182–192. doi:https://doi.org/10.1016/j.conbuildmat.2014.02.029.

Li, Z., Mukai, K. and Tao, Z. (2000). Reactions Between MgO-C Refractory, Molten Slag and Metal. *ISIJ International*, 40(Suppl), pp.S101–S105. doi:https://doi.org/10.2355/isijinternational.40.suppl_s101.

Mao, X., Garg, P., Hu, X., Li, Y., Nag, S., Kundu, S. and Zhang, J. (2022). Kinetic analysis of iron ore powder reaction with hydrogen—carbon monoxide. *International Journal of Minerals Metallurgy and Materials*, 29(10), pp.1882–1890. doi:https://doi.org/10.1007/s12613-022-2512-6.

Naudé, C.P. and Shapiro, M.D. (2010). Implementation of the first commercial scale dc smelter for ferronickel production from low grade laterite ores—technology building blocks and lessons learned. *Journal of the Southern African Institute of Mining and Metallurgy*, 110(12), pp.725–732.

Nicholas, S. & Basirat, S. 2022a. Iron ore quality a potential headwind to green steelmaking—Technology and mining options are available to hit net-zero steel-targets. https://ieefa.org/resources/iron-ore-quality-potential-headwind-green-steelmaking-technology-and-mining-options-are, viewed 2024-06-10.

Nicholas, S. & Basirat, S. 2022b. Solving iron ore quality issues for low-carbon steel. https://ieefa.org/resources/solving-iron-ore-quality-issues-low-carbon-steel, viewed 2024-06-10.

Qin, J. and Qi, J.L. (2012). Analysis on the Refractory Erosion of the Electric Arc Furnace and Study on the Measures of Protecting the Furnace Lining. *Advanced Materials Research*, 602-604, pp.2082–2086. doi:https://doi.org/10.4028/www.scientific.net/amr.602-604.2082.

Reynaert, C., Sniezek, E. and Szczerba, J. (2020). CORROSION TESTS FOR REFRACTORY MATERIALS INTENDED FOR THE STEEL INDUSTRY - A REVIEW. *Ceramics - Silikaty*, 64(3), pp.1–9. doi:https://doi.org/10.13168/cs.2020.0017.

Scharm, C., Küster, F., Laabs, M., Huang, Q., Volkova, O., Reinmöller, M., Guhl, S. and Meyer, B. (2022). Direct reduction of iron ore pellets by H2 and CO: In-situ investigation of the structural transformation and reduction progression caused by atmosphere and temperature. *Minerals Engineering*, 180, pp.107459–107459. doi:https://doi.org/10.1016/j.mineng.2022.107459.

Shahabuddin, M., Rahbari, A., Sabah, S., Brooks, G., Pye, J. and Rhamdhani, M.A. (2024). The performance and charge behaviour in melter/smelter for the production of hot metal in hydrogen DRI-based steelmaking. *Ironmaking & Steelmaking Processes Products and Applications*. doi:https://doi.org/10.1177/03019233241265179.

Thethwayo, B.M. and Steenkamp, J.D. (2020). A review of carbon-based refractory materials and their applications. *Journal of the Southern African Institute of Mining and Metallurgy*, 120(11). doi:https://doi.org/10.17159/2411-9717/1011/2020.

Zhang, S.-N., Marriott, N.J. and Lee, W.H. (2001). Thermochemistry and microstructures of MgO–C refractories containing various antioxidants. *Journal of The European Ceramic Society*, 21(8), pp.1037–1047. doi:https://doi.org/10.1016/s0955-2219(00)00308-3.

Zhang, Y., Zhang, S., Chen, Y. and Çopuroğlu, O. (2022). The effect of slag chemistry on the reactivity of synthetic and commercial slags. *Construction and Building Materials*, 335, p.127493. doi:https://doi.org/10.1016/j.conbuildmat.2022.127493.

Zhu, T., Li, Y., Sang, S., Jin, S. and Wang, H. (2014). Formation of hollow MgO-rich spinel whiskers in low carbon MgO–C refractories with Al additives. *Journal of the European Ceramic Society*, 34(16), pp.4425–4432. doi:https://doi.org/10.1016/j.jeurceramsoc.2014.07.028.

CHAPTER 8: SLAG-REFRACTORY DESIGN EVALUATIONS

8.1. Introduction

The previous chapter incorporated a designing process and selection of the possible slag compositions in the OBF that are less corrosive towards MgO-rich and $MgAl_2O_4$ refractories. Likewise, three possible slag products were suggested for the SVF and a carbon lining was recommended since carbon is non-wettable by the slag. This chapter analyses the physical properties of the selected slag compositions in the OBF such as the viscosity, the thermal conductivity, and electrical conductivity. These are very important properties since the novel OBF is an electrical furnace. The physical properties of the slag are determined using FactSage software, models from the literature as well as an automated spreadsheet developed in the study (Mills et al., 2011). Moreover, a detailed mass and energy balance is performed on the different slag compositions for both the OBF and SVF using Excel solver and HSC chemistry 10 software. This will lead to a comparative assessment of all the slag compositions in terms of the highlighted properties. At the end of this chapter, the slag composition that performs best overall in the OBF and SVF, will be selected and recommended for experimental trials.

8.2. Slag viscosity

Viscosity is a very important parameter in furnace operations because it provides a measure of the fluidity of the slag (Zhang et al., 2014; Sohn and Min, 2012). The slag needs to be fluid enough so that it can easily be tapped from the furnace and separated from the metal. Xing et al., (2019) highlighted that the temperature and the chemical composition of the slag are the two most important factors that influence the slag viscosity. The temperature is usually stable during smelting operations, hence, to control the viscosity, the chemical composition of the slag must be monitored. It should be noted that the liquidus temperature of the slag is not an indication of viscosity because the slag can be liquid, and yet its fluidity does not permit efficient furnace operations.

8.2.1. Measurement

The main components of the BF slag and the novel OBF slag are CaO, MgO, SiO_2, and Al_2O_3. Viscosity data that have been generated for synthetic slags in the Al_2O_3-CaO-SiO_2-MgO system has been reported by several researchers (Machin and Yee, 1954; Forsbacka et al., 2003; Shankar et al., 2007; Park et al., 2008). However, the accuracy of these measurements is questionable in view of the difficulty of measuring high temperature viscosities and also, the industrial slags also incorporate minor inclusions that may or may not have an effect on the viscosity of the slag. Moreover, the accuracy of the equipment and how the measurements were taken for these data are all contributing to the uncertainty to correlated values. Hence, the correlated data from these viscosity measurements are not a true representation of the actual viscosity of the industrial slags, but can be taken as referential indications of the viscosity.

8.2.2. Predictive models

Chen et al., (2014) stated that high-temperature viscosity measurements are costly, and can take a tremendous amount of time to generate. Hence, quite a significant number of models

have been developed to predict the viscosity of the slag based upon its chemical composition, which is directly linked to the structure of the silicate melts (Iida et al., 2000; Mills and Sridhar, 1999; Hu et al., 2012). These models might provide close representation of the viscosity of the slag, but there are still a lot of discrepancies in the generated viscosity data depending on the factors taken into consideration during the model development process. A list of a few most widely used models for BF slags are shortly described.

8.2.2.1. Urbain model

The Urbain model is based on the Weymann-Frenkel liquid viscosity model, and it is among the most commonly used models to predict the slag viscosity of silicate melts (Urbain et al., 1987; Urbain, 1987). The Urbain model was later optimized in 1987 and does generate quite reliable results.

8.2.2.2. Riboud model

Riboud further optimized the Urbain model, simplifying the model equations and optimizing parameters using viscosity data of blast furnace slag (Riboud et al., 1981). The main components should be in the following ranges: SiO_2 (28-48%), CaO (13-52%), and Al_2O_3 (0-17%).

8.2.2.3. Iida model

The Iida model was developed based on the slag basicity index, and optimized parameters obtained from experimental data. Later, Al_2O_3 was accounted for as amphoteric as well as considering the change in basicity with respect to temperature in the CaO-MgO-Al_2O_3-SiO_2 system. This led to the optimized model coefficients changing with temperature (Iida et al., 2000). The predicted viscosity values when applying the Iida model closely fit with the viscosity data obtained experimentally for many blast furnace type slags. The model can predict slag viscosities even for exceedingly high MgO content and it was applied to the following composition ranges: MgO (17.8-38.4), CaO (1.8-19.6%), Al_2O_3 (24.6–31.5%) and SiO_2 (25.6-41.2%) (Forsbacka et al., 2003). Mills et al. (2011) stated that the claimed accuracy with this model comes from its calibration with experimental data for each family of slags.

8.2.2.4. FactSage model

FactSage, as described in chapter 7, is a sophisticated software package that generates thermodynamic data. The incorporated model for viscosity is not described; however, it requires the composition as well as the liquidus temperature of the slag in order to generate the viscosity.

8.2.3. Viscosity models: sensitivity and uncertainty

All these models generate viscosity data using the internal structure of the silicate melts, which is primarily determined by the chemical composition of the slag. SiO_2 is considered as a network former, MgO and CaO are considered as network modifiers. Al_2O_3 on the other hand, is considered in some models as network former, and other models take into account the amphoteric nature of Al_2O_3 depending on the concentrations of basic oxides (MgO, CaO).

Furthermore, every model incorporates a certain degree of uncertainty; however, models that self-adapt based on the amphoteric nature of Al_2O_3 seem to generate results that closely fit experimental data. Lastly, each model should be applied appropriately based on the composition ranges specified by the author.

Chen et al. (2014) argued that the viscosity of industrial slags is generally lower than the viscosity of synthetic slags that are mostly used in the development of the above models. The lower viscosity of industrial slags has been attributed to the combined effect of minor inclusions as well as other components such as FeO, MnO, and TiO_2 (Kucharski et al., 1989; Urbain et al., 1982; Shiraishi et al., 1978; Shankar et al., 2007). However, the individual effect of these inclusions is still debatable, with various authors having controversial views. This demonstrates that further studies are required in order to investigate and develop understanding of the individual effect of these inclusions on the viscosity of BF slags.

8.2.4. Viscosities of the selected slag compositions for the OBF and SVF

Using the Urbain, Riboud, and Iida models from the slag properties spreadsheet in the study (Mills et al., 2011), the viscosity data for the selected slag composition in this study are summarized in Table 25 along with the viscosity data generated using FactSage.

Table 25: Calculated viscosities of the selected slags in the OBF and SVF

OBF Slags					Viscosity at 1500°C (dPa.s)				
Slag No	**SiO_2**	**MgO**	**Al_2O_3**	**CaO**	**Chen**	**FactSage**	**Riboud**	**Iida**	**Urbain**
1	**41**	**22**	**3**	**34**	0,22	1,90	1,43	1,91	3,00
2	**38**	**26**	**7**	**29**	0,18	1,93	1,49	2,11	4,00
3	**42**	**22**	**3**	**32**	0,74	2,06	1,66	2,22	3,14
4	**36**	**18**	**18**	**28**	3,59	3,11	4,96	4,55	8,50
5	**41**	**15**	**19**	**25**	6,35	5,19	11,02	6,60	12,20
6	**38**	**15**	**23**	**25**	6,06	5,12	11,31	6,92	12,97
SVF products									
Product type	**SiO_2**	**MgO**	**Al_2O_3**	**CaO**					
SVF slag 1	**32**	**5**	**15**	**48**	1,72		2,86	2,60	4,65
SVF slag 2	**42**	**4**	**4**	**50**	2,21		2,51	1,84	3,00
OBF slag	**37**	**7**	**12**	**44**	2,68	2,38	1,71	1,69	3,38

The Chen model, which uses Equation 9 was also added to the viscosity data of the selected slags (Chen et al., 2014).

$$[V] = 0.005 + 0.0262[SiO_2] + 0.0184[Al_2O_3] - 0.0172[CaO] - 0.0244[MgO] \quad (9)$$

Where $[SiO_2]$, $[CaO]$, $[Al_2O_3]$ and $[MgO]$ are in weight percentage and $[V]$, the viscosity, is in Pa.s.

The Chen model can predict the viscosity of slags having a wide range of compositions with an estimated coefficient of error of 10%, especially for high Al_2O_3 slags. The slag compositions are, however, restricted to SiO_2 (30–45%), Al_2O_3 (5-25%, CaO (25-50%), and MgO (0-15%). Moreover, the model fits the selected slag compositions in this study well, except for exceedingly high MgO (>15%) slags where the values should be out of range based on the

limits provided by the model author. This is the case for slags with viscosity below 1 dPa.s. This shows further that this model is not applicable for such levels of MgO.

8.2.5. OBF slag viscosities comparison

From the general trends in the results in Table 25, the slags with exceedingly high MgO (>15%) display lower viscosity overall for all the models, namely for slags 1, 2, and 3. Moreover, slag 1 has the lowest viscosity for all the OBF slag compositions for all the models. This can be attributed to its high MgO, high CaO, and low Al_2O_3 content. Slag 1 is followed by slag 2 for the FactSage, Iida and Riboud models. An exception is the Urbain model which generated a value that is greater for slag 2 compared to slag 3. Xing et al., (2019) stated that the increment of MgO content decreases the viscosity and breaks the complex structures of slag.

All the high Al_2O_3 slags (Slag 3, Slag 4, and Slag 5) generated viscosity values that are greater than 3 dPa.s, with slag 5 and 6 having viscosity values greater than 10 dPa.s. Chen et al. (2014) compared the viscosities of industrial BF slags to synthetic slags and found that at 1500°C, the viscosities of the industrial BF slags are in the range of 3 to 5 dPa.s. This demonstrates that for the high Al_2O_3 slags in this study, slag 4 seems to generate a viscosity value that is within the range of industrial BF slag. Moreover, slags 5 and 6 have viscosity values around 5 and 6 dPa.s as per the FactSage and Iida models. These two slags might require a slight increment in temperature beyond 1500°C in order to decrease their viscosities and make the smelting operations smoother. However, these measurements are not a true representation of the industrial value of viscosity.

Zhang et al. (2014) stated that TiO_2 and MgO have a more prominent effect on depolymerizing the network than CaO in slags containing high Al_2O_3. Slags 4, 5, and 6 contain between 15 and 18% MgO, which is higher than the 7% MgO commonly observed in BF slags. This underlines the fact that the viscosity value should be lower because of their relatively high MgO contents. Hence, it is only through experimental tests that accurate viscosity values for each slag composition can be evaluated.

8.2.6. SVF product viscosities comparison

All the 3 SVF products have relatively similar viscosity values based on all the models used in this study as per Table 25. The OBF slag has the lowest viscosity among the SVF products for the Iida and Riboud models, except for the Chen model where SVF slag 1 is the lowest, and the Urbain model where SVF slag 2 is the lowest. Overall, all three SVF products indicate good viscosities on an industrial scale since their viscosity values are all less than 5 dPa.s at 1500°C. This can be attributed to the high CaO content (>48%), which counteracts even the high Al_2O_3 (15%) content of SVF slag 1.

In real industrial practice, the viscosity of the slag can be decreased more by replacing the same weight of CaO by MgO as per the conclusions made in the studies (Machin et al., 1952; Chen et al., 2014). This is because MgO has a relatively lower molar mass than CaO, and replacing the same mass of CaO by MgO results in an increased mole ratio of $(CaO+MgO)/SiO_2$ and further modification of the silicate network.

8.2.7. Comparison of viscosity model results

Based on the viscosity values generated by the different models in Table 25., the FactSage and Iida models seem to generate closely fitted results for all the slags in this study. The Riboud and Urbain models seem to generate similar results for high Al_2O_3 (>19%) slags. On the other hand, the Riboud model generates close viscosity values to the Iida and FactSage models for high MgO slags (slag 1, 2, and 3). Lastly, the Chen model also generated viscosity values that are in agreement with the values from the Riboud and Iida models for slags 4, 5, 6 and all the SVF products. Overall, the Urbain model generated higher viscosity values, followed by the Riboud model in comparison with the rest of the models that generated viscosity values less than 7 dPa.s. A comparison of the Iida and FactSage models for slags 1 to 6 is shown in Figure 126.

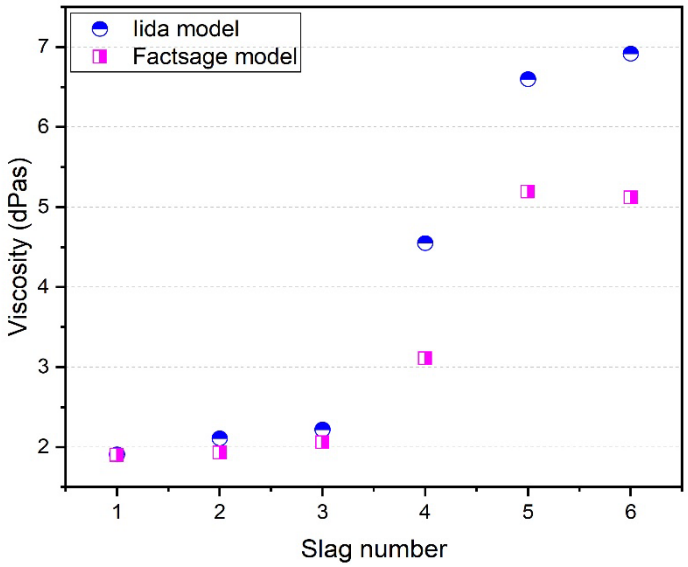


Figure 126: Comparison of the Iida and FactSage viscosity models

It can be seen that for the high MgO slag (slags 1, 2, and 3), both models generated almost similar viscosity values, whereas for high Al_2O_3 slags (slags 4, 5, and 6), the deviations between the two models become very significant. Moreover, the FactSage model generates lower viscosity values between the two. In summary, the classification of the different slag based on viscosity at 1500°C in the OBF and SVF is as follows:

- **OBF Slags**: Slag 1 < Slag 2 = Slag 3 < Slag 4 < Slag 5 = Slag 6
- **SVF products**: OBF slag < SVF slag 2 < SVF slag 1

8.3. Thermal conductivity of the slag

8.3.1. Importance

The thermal conductivity is another crucial physical property of the slag in addition to the viscosity (Ozawa et al., 2006; Kang et al., 2014), especially for emerging electrical furnaces such as the novel OBF. With the operation of the OBF being in open arc mode, the process relies on the thermal conductivity of the slag to transmit heat to the metal once most of the melted Fe has settled at the bottom of the furnace. Therefore, it is the slag thermal conductivity that will define the temperature difference between the slag and the metal. The heat distribution between the coke bed zone and the slag in the conventional BF operations is different compared

to the heat distribution between the slag and the electrode in the novel OBF operations. A slag with very low thermal conductivity implies that the temperature difference between the slag and the metal will be very large, and the metal might end up being tapped cold. This will require a high operating temperature in order to increase the temperature of the metal, which is both energy-consuming and detrimental to the lifespan of the refractory materials. Hence, the thermal conductivity of the slag must be controlled to avoid such occurrences.

8.3.2. Measurement

Several authors have highlighted a strong link between the thermal conductivity and the viscosity of the slag since both the temperature dependence of viscosity and thermal conductivity have been developed using the Arrhenius equation (Kang and Morita, 2006; Hayashi et al., 2001; Zhang et al., 2023). In the study (Mills,1993), it has been highlighted that the thermal conductivity of the slag at the liquidus temperature decreases almost linearly as the silicate network becomes more depolymerized, or as the ratio of non-bridging oxygen per tetrahedron (NBO/T) decreases, demonstrating how thermal conduction is greater through covalent bonds than ionic bonds. The temperature dependence of thermal conductivity and viscosity was also further noted: an increment in temperature has a tendency to loosen the structure of the slag network, thus decreasing both the thermal conductivity and the viscosity. This correlation between the viscosity and thermal conductivity was used in a study (Mills et al., 2011) to develop a model that estimates the value of thermal conductivity of various slag compositions based on viscosity data. In real industrial processes, there are always contributions from radiation and convection, but the contributions are smaller in the transient hot wire (THW) method compared to the laser pulse (LP) method (Mills et al., 2011). Therefore, similar to viscosity, the estimated thermal conductivity values carry a certain degree of uncertainties from experiments to modelling and calculations.

The Mills spreadsheet form the research (Mills et al., 2011), which incorporates the thermal conductivity model, was used to estimate the thermal conductivity of the selected slag compositions in this study and the values are summarized in Table 26.

Table 26: Estimated thermal conductivities of selected slags in the OBF and SVF

OBF Slags					**Thermal conductivity at 1500°C (W/m.K)**
Slag No	**SiO_2**	**MgO**	**Al_2O_3**	**CaO**	
1	**41**	**22**	**3**	**34**	0,125
2	**38**	**26**	**7**	**29**	0,127
3	**42**	**22**	**3**	**32**	0,131
4	**36**	**18**	**18**	**28**	0,178
5	**41**	**15**	**19**	**25**	0,223
6	**38**	**15**	**23**	**25**	0,225
SVF products					
Product type	**SiO_2**	**MgO**	**Al_2O_3**	**CaO**	
SVF slag 1	**32**	**5**	**15**	**48**	0,152
SVF slag 2	**42**	**4**	**4**	**50**	0,147
OBF slag	**37**	**7**	**12**	**44**	0,132

8.3.3. Comparison of thermal conductivities of slags

The results in Tables 26 show that slags that displayed high viscosity in the preceding section such as slags 5 and 6, also have higher corresponding thermal conductivities. This indicates the direct proportional relationship of viscosity and thermal conductivity as highlighted in the studies (Kang and Morita, 2006; Mills, 1993). The observed trends in thermal conductivity are similar to the viscosity trends. The thermal conductivities are within the 0.125 and 0.225 W/m.K range, with slag 1 being the least thermal conductive since it was the least viscous for most viscosity models. Therefore, the more viscous the slag, the higher the thermal conductivity and a balance between these two physical properties of the slag needs to be achieved during furnace operations.

8.4. Electrical conductivity of the slag

8.4.1. Importance

The metal is an electronic conductor, whereas the slag is an ionic conductor as shown in the previous section. Wang et al., 2015 stated that the electrical conductivity of molten slags is an important parameter in a number of metallurgical processes, like submerged-arc processes or even plasma-refining processes. In this respect, electrical conduction is most likely a very important parameter in the novel OBF process since it also uses electricity as the energy source.

8.4.2. Measurement

Mills et al. (2011) showed that the electrical conductivity is linked to the motion of cations in the slag under the influence of an applied field. The degree of polymerization of the silicate network, the concentration, size, and charge of cations are the main factors that affect the electrical conductivity of the slag. Smaller cations such as Na, Li, and K are more mobile whereas, divalent cations such as, Ca, Mg, Sr, and Ba have a relatively higher charge, resulting in higher polarization, which ultimately affects the electrical conductivity (Zhang and Chou, 2010; Seetharaman and Sichen, 1994). Generally, slags containing more Li^+, Na^+, and K^+, have higher electrical conductivity than slags containing divalent cations such as Ca^{2+}, and Mg^{2+} (Mills et al., 2011). A higher degree of polymerization of the network structure leads to lower electrical conductivity as opposed to thermal conductivity. An increment in temperature loosens the network structure, thus increasing the mobility of cations, thereby increasing the electrical conductivity while lowering the thermal conductivity and viscosity (Zhang et al., 2011).

The thermal conductivity of the selected slags in this study was determined using the Mills model spreadsheet (Mills et al., 2011), developed using the data of correlation between viscosity and electrical conductivity covered in (Zhang et al., 2011). The correlation was done using the viscosity values from the Riboud, Iida and Urbain models. Table 27 summarizes the thermal conductivities of the selected slags for the OBF and SVF.

Table 27: Electrical conductivity values of selected slags for OBF and SVF

OBF Slags					Electrical conductivity at 1500°C ($\Omega^{-1}m^{-1}$)		
Slag No	**SiO_2**	**MgO**	**Al_2O_3**	**CaO**	**Riboud**	**Iida**	**Urbain**
1	**41**	**22**	**3**	**34**	0,691	0,540	0,368
2	**38**	**26**	**7**	**29**	0,668	0,496	0,289
3	**42**	**22**	**3**	**32**	0,607	0,475	0,354
4	**36**	**18**	**18**	**28**	0,240	0,259	0,152
5	**41**	**15**	**19**	**25**	0,122	0,189	0,112
6	**38**	**15**	**23**	**25**	0,120	0,181	0,106
SVF products							
Product type	**SiO_2**	**MgO**	**Al_2O_3**	**CaO**			
SVF slag 1	**32**	**5**	**15**	**48**	0,384	0,416	0,254
SVF slag 2	**42**	**4**	**4**	**50**	0,428	0,557	0,369
OBF slag	**37**	**7**	**12**	**44**	0,593	0,598	0,333

8.4.3. Comparison of electrical conductivity of slags

The results in Table 27 show that slag 1 has a relatively higher electrical conductivity for all the models, which is the opposite for the viscosity since it was the least viscous for all the models. Overall, the Urbain model generated the lowest electrical conductivity values, followed by the Iida, and lasty the Riboud model for the high MgO slags (Slag1, 2, and 3). This is exactly the opposite trend of the observations for the viscosity values in which the Urbain model had the highest viscosity values. However, for high Al_2O_3 slags (slags 4, 5, and 6), the trends are mixed. Similar to viscosity, this is most likely due to how Al_2O_3 was considered during the model development. Moreover, similar to thermal conductivity, the electrical conductivity values also contain a certain degree of uncertainties linked to modelling and correlations. Therefore, the viscosity and electrical conductivity in the slag are inversely proportional, justifying the direct proportional relationship between viscosity and electrical resistivity of the slag.

8.5. Trends in physical properties of the CaO-MgO-Al_2O_3-SiO_2 slag

It can be seen that all three above-mentioned physical properties of the slag depend on the structure of the silicate melts. The general trends can be summarized as follows: a higher degree of depolymerization of the silicate (SiO_2) structure by basic oxides (CaO, MgO) and in some cases by amphoteric oxide (Al_2O_3), leads to lower viscosity, lower thermal conductivity, and higher electrical conductivity, or lower electrical resistivity. A summary of the structure of molten slag along with the behaviour of physical properties is illustrated in Figure 127.

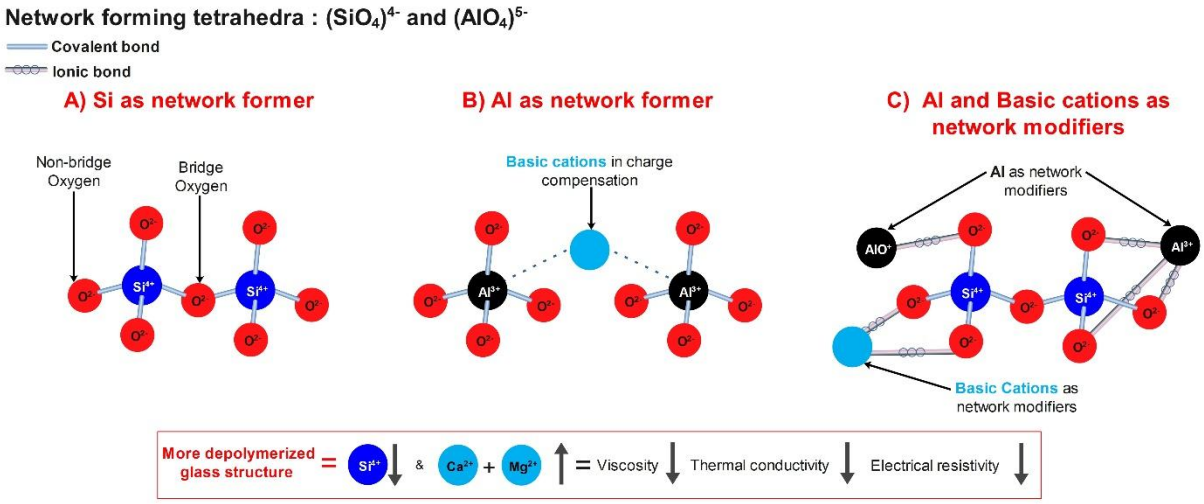


Figure 127: Structure of molten slag glass and physical properties

8.6. Mass balance

The mass balance from each slag composition in the OBF to each product in the SVF was performed using the solver function in excel. This was done in order to get the minimum mass of fluxing materials needed in order to convert the gangue distribution of the DRI into a targeted slag composition.

8.6.1. Feed materials

The composition and the proportion of the gangue in the DRI were kept as described in chapter 7 at 10% and 15% proportion of the DRI. This was within the expected gangue proportion for BF-grade DRI as discussed in chapter 7. Moreover, all the calculations were done for 1 ton of DRI, implying that the mass of the gangue materials in the DRI were 100 kg and 150 kg for the two gangue proportion levels, respectively. The compositions of the different fluxing materials are kept the same as in Part I of this study and are also summarized in Table 28 for the original and the normalized version to 4 components.

Table 28: DRI gangue and Fluxing materials compositions

Fluxes				
4 Components				
Burnt dolomite				
SiO_2	**MgO**	**Al_2O_3**	**CaO**	**Total**
1,04	39,06	1,04	58,85	100
Burnt lime				
SiO_2	**MgO**	**Al_2O_3**	**CaO**	**Total**
1,04	1,04	1,04	96,88	100
Bauxite				
SiO_2	**MgO**	**Al_2O_3**	**CaO**	**Total**
6,67	1,11	91,11	1,11	100
Quartzite				
SiO_2	**MgO**	**Al_2O_3**	**CaO**	**Total**
96,88	1,04	1,04	1,04	100
Original				
Burnt dolomite				
SiO_2	**MgO**	**Al_2O_3**	**CaO**	**Total**
1	37,5	1	56,5	96
Burnt lime				
SiO_2	**MgO**	**Al_2O_3**	**CaO**	**Total**
1	1	1	93	96
Bauxite				
SiO_2	**MgO**	**Al_2O_3**	**CaO**	**Total**
6	1	82	1	90
Quartzite				
SiO_2	**MgO**	**Al_2O_3**	**CaO**	**Total**
93	1	1	1	96
Gangue distribution				
SiO_2	**MgO**	**Al_2O_3**	**CaO**	**Total**
70,00	17,00	5,00	8,00	100

8.6.2. Calculation guide

The calculations of mass balance in this section are done only for the four major components of the slag, namely, CaO, MgO, Al_2O_3, and SiO_2. At this stage, no assumption of losses either to the metal, or the off-gas dusts is taken into consideration. These 4 components from the DRI gangue are mixed with the fluxing materials and the total goes into the slag to give a targeted slag composition. The Solver function in excel was used to calculate the minimum amount of each fluxing material needed to achieve the selected slag composition in the OBF Gen2, and subsequently the fluxes needed to change the OBF Gen2 slag composition into a valorised product in the SVF. Therefore, the calculations happen in two sequences as follows:

- DRI gangue + Fluxes = OBF Gen2 slags
- OBF Gen2 slags + Fluxes = SVF products

The mass balance calculations will be subdivided into 3 sections as per the 3 SVF products. A schematic illustration of the mass balance is further shown in Figure 128.



Figure 128: summary of mass balance calculations

8.6.3. Mass balance for OBF slag type in the SVF

The OBF slag type has 37% SiO_2, 7% MgO, 12% Al_2O_3, and 44% CaO. The fluxing materials requirement to an OBF slag type in the SVF from a TkSE gangue composition is summarized in Table 29.

Table 29: Fluxing requirement for OBF slag

Gangue proportion	Fluxes	Types of fluxes	Slag 1	Slag 2	Slag 3	Slag 4	Slag 5	Slag 6
10%	Fluxes in the OBF (kg)	Dolomite	53,6	78,0	52,5	48,4	22,5	29,8
		Bauxite	0,0	8,1	0,0	33,8	30,2	42,2
		Lime	20,7	0,0	15,3	20,6	23,1	23,7
		Quartz	1,0	0,0	0,1	0,0	0,0	0,0
		Total	75,3	86,1	67,8	102,7	75,7	95,7
	Fluxes in the SVF (kg)	Dolomite	0,0	1,0	2,2	0,0	0,0	0,0
		Bauxite	69,9	81,5	70,7	32,1	15,6	9,2
		Lime	213,5	291,4	221,1	201,8	140,7	156,6
		Quartz	152,2	212,7	155,5	140,9	79,9	97,0
		Total	435,6	586,5	449,5	374,8	236,1	262,8
	Overall total fluxes (kg)		510,8	672,6	517,3	477,5	311,8	358,5
	Overall OBF slag (kg)		175,3	186,1	167,8	202,7	175,7	195,7
	Overall SVF slag (kg)		610,8	772,6	617,3	577,5	411,8	458,5
15%	Overall total fluxes (kg)		766,4	999,6	768,1	715,9	467,7	537,6
	Overall OBF slag (kg)		262,9	279,1	251,6	304,0	263,6	293,5
	Overall SVF slag (kg)		916,4	1149,6	918,1	865,9	617,7	687,6

The results in Table 29 show that the slag composition that will require the least total of fluxing materials in the OBF Gen2 is Slag 3 with 67.8 kg of fluxes per ton of DRI. This is followed by

Slag 1 and Slag 5, which require a total of around 75 kg of fluxes each. On the other hand, Slag 4 will require the most fluxes at 102.7 kg in total. Moreover, the results further highlight that burnt dolomite is the most consumed flux for the high MgO slags (slags 1, 2, and 3), whereas for the high Al_2O_3 slags (slags 4, 5, and 6), a mix of burnt dolomite, burnt lime, and sintered bauxite will be required.

In the SVF, the most consumed flux is burnt lime, followed by quartzite, and this can be attributed to the high CaO and SiO_2 in the SVF products. The high MgO slags require more fluxing materials (>430 kg/ton DRI) in order to revert the slag composition back to OBF type slag in the SVF, whereas the high Al_2O_3 required less than 375 kg/ton DRI. Slag 5 requires the least fluxes in the SVF with a total of 236.1 kg to revert the composition to an OBF type slag, followed by Slag 6 at 262.8 kg. Furthermore, the highest flux quantity in the SVF will be needed for Slag 2 at a total of about 586.5 kg/ton of DRI.

Combining the totals of fluxing materials needed in the OBF Gen2 and SVF, Slag 5 has the least overall fluxing requirement of 311.8 kg/ton DRI, followed by Slag 6, Slag 5, Slag 1 and Slag 3. Slag 2 has the highest overall total in fluxing materials requirement of 672.6 kg/ton DRI. This can be explained by the fact that it has a MgO content of 26%, which is the highest among all the slags in the OBF Gen2, and reducing this MgO level to around 7% in the SVF, will require more fluxing materials. Moreover, the same scenario happened to Slags 1 and 2, which have around 22% MgO and a fluxing materials requirement of around 520 kg/ton of DRI in total. Therefore, higher MgO levels in OBF Gen2 translate to more fluxing requirement in the SVF to revert back to the targeted product.

The total output of the OBF Gen2 slag is lower for the higher MgO slags due to their low fluxing requirement in the OBF Gen2 compared to the high Al_2O_3 slags, but the difference is minimal. For instance, Slag 3 has a mass of 167.8 kg, whereas slag 6 has a mass of 195.7 kg. This trend is largely reversed, when adding the fluxes needed in the SVF to form the overall SVF slag. Slag 3 has a total SVF slag of 617.3 kg while Slag 6 has a total SVF slag of 458.5 kg, which is lower by around 159 kg. This demonstrates that it is easier to change the composition in the OBF Gen2, where the starting mass is the DRI gangue, and it is lower compared to the OBF slag, which is the starting mass in the SVF.

The gangue proportion does not change the trends in the overall fluxing requirement of the different slags, but it increases the amount proportionally for the fluxes and the total slag output. The values discussed above, have been calculated using 10% gangue proportion, which translates to 100 kg of gangue in the DRI. As per Table 29, when the gangue proportion was increased to 15%, the overall SVF slag output for Slag 5 moved from 411.8 kg to 617.7 kg/ton DRI, and the fluxing materials requirement increased from 311.8 kg to 467.7 kg/ton DRI. It can be seen that the 50% increase in gangue proportion resulted in an increase of around 50% in total slag output and fluxing materials requirement. This shows the direct proportional relationship between the gangue proportion, the fluxing materials requirement, and the total slag output.

In summary, it can be seen that the fluxing materials requirement, the gangue distribution and the gangue proportion dictate the total slag output in the OBF Gen2 and SVF. With reference

to the results in Table 29, the ranking of the OBF Gen2 in terms of overall slag requirement to produce OBF slag type in the SVF is as follows: Slag 5 < Slag 6 < Slag 4 < Slag 1 < Slag 3 < Slag 2. Furthermore, the reported volume of conventional BF slag is between 250 to 300 kg of slag per metric ton pig iron produced for typical iron ore grades of 60% to 66% (Ore and Curry, 2021; Horii et al., 2013). Using slag 5 in this study, the volume in the OBF is 175.7 kg/ton DRI, the gangue being 10% of the DRI means that the metal is 90% assuming 100% iron metallization. Hence, the slag production in the OBF Gen2 is around 195 kg/ton pig iron, which increased to around 457.6 kg/ton pig iron in the SVF. This demonstrates that the ranking of ironmaking configurations in terms of total slag output is DRI-OBF < BF < DRI-OBF-SVF.

8.6.4. Mass balance for SVF slag 1 type

The SVF slag 1 type contains 32% SiO_2, 5% MgO, 15% Al_2O_3, and 48% CaO. The fluxing materials requirement for an SVF slag 1 type is summarized in Table 30.

Table 30: Fluxing requirement for SVF slag 1

Gangue proportion	Fluxes	Types of fluxes	Slag 1	Slag 2	Slag 3	Slag 4	Slag 5	Slag 6
10%	Fluxes in the OBF (kg)	Dolomite	53,6	78,0	52,5	48,4	22,5	29,8
		Bauxite	0,0	8,1	0,0	33,8	30,2	42,2
		Lime	20,7	0,0	15,3	20,6	23,1	23,7
		Quartz	1,0	0,0	0,1	0,0	0,0	0,0
		Total	75,3	86,1	67,8	102,7	75,7	95,7
	Fluxes in the SVF (kg)	Dolomite	0,0	0,4	0,0	0,0	0,0	0,0
		Bauxite	138,3	166,7	136,5	96,7	61,6	60,4
		Lime	390,7	512,1	391,1	369,5	260,2	289,3
		Quartz	216,4	291,5	213,7	201,6	123,2	145,0
		Total	745,4	970,6	741,3	667,8	445,0	494,7
	Overall total fluxes (kg)		820,7	1056,7	809,1	770,5	520,7	590,4
	Overall OBF slag (kg)		175,3	186,1	167,8	202,7	175,7	195,7
	Overall SVF slag (kg)		920,7	1156,7	909,1	870,5	620,7	690,4
15%	Overall total fluxes (kg)		1232,1	1582,8	1213,4	1155,0	781,0	903,0
	Overall OBF slag (kg)		262,9	279,1	251,6	304,0	263,6	293,5
	Overall SVF slag (kg)		1382,1	1732,8	1363,4	1305,0	931,0	1053,0

From the results in Table 30, the trends in fluxing materials consumption for the OBF Gen2 is the same as in the previous section: the changes occurred based on the consumption of fluxes to get the targeted slag composition in the SVF. Overall, the trends are the same as Slag 5 < Slag 6 < Slag 4 < Slag 1 < Slag 3 < Slag 2. However, the mass has increased considerably and this can be attributed to the relative lower MgO content from 7 to 5%, higher Al_2O_3 from 12 to 15%, and most importantly higher CaO from 44 to 48% when comparing the SVF slag 1 type to the OBF slag type in the previous section. This has led to extra usage of bauxite in the SVF along with burnt lime and quartzite.

The total fluxing requirement for slag 5 increased from 311.8 kg to 520.7 kg/ton DRI in order to produce a SVF slag 1 composition in the SVF. Similarly, the overall slag production moved from 411.8 kg to 620.7 kg/ton DRI. On the other hand, for the slag 2, the total SVF slag production is even beyond a ton at 1156.7 kg/ton DRI. The gangue proportion also performed in the same manner as in the previous section. Increasing the gangue proportion to 15% resulted in a 50% increment in fluxing materials of Slag 2, at 781 kg/ton DRI. It is clear that more than 60% additional fluxing materials are required to produce a SVF slag 1 type compared to an OBF slag type in the SVF. Therefore, the production of an OBF slag type in the SVF is favourable in terms of fluxing materials consumption compared to the production of a SVF slag type.

8.6.5. Mass balance for SVF slag 2 type

The SVF slag 2 type contains 42% SiO_2, 4% MgO, 4% Al_2O_3, and 50% CaO. The fluxing materials requirement to an SVF slag 2 type is summarized in Table 31.

Table 31: Fluxing requirement for SVF slag 2

Gangue proportion	Fluxes	Types of fluxes	Slag 1	Slag 2	Slag 3	Slag 4	Slag 5	Slag 6
10%	Fluxes in the OBF (kg)	Dolomite	53,6	78,0	52,5	48,4	22,5	29,8
		Bauxite	0,0	8,1	0,0	33,8	30,2	42,2
		lime	20,7	0,0	15,3	20,6	23,1	23,7
		Quartz	1,0	0,0	0,1	0,0	0,0	0,0
		Total	75,3	86,1	67,8	102,7	75,7	95,7
	Fluxes in the SVF (kg)	Dolomite	0,0	0,0	0,2	0,0	17,3	40,5
		Bauxite	36,0	38,1	35,5	0,0	0,0	0,8
		lime	567,8	733,6	566,7	536,5	482,9	664,0
		Quartz	450,4	584,5	445,5	422,6	375,8	542,4
		Total	1054,2	1356,3	1047,8	959,2	876,0	1247,6
	Overall total fluxes (kg)		1129,4	1442,4	1115,6	1061,9	951,7	1343,3
	Overall OBF slag (kg)		175,3	186,1	167,8	202,7	175,7	195,7
	Overall SVF slag (kg)		1229,4	1542,4	1215,6	1161,9	1051,7	1443,3
15%	Overall total fluxes (kg)		1699,5	2185,4	1669,5	1592,9	1427,8	1978,5
	Overall OBF slag (kg)		262,9	279,1	251,6	304,0	263,6	293,5
	Overall SVF slag (kg)		1849,5	2335,4	1819,5	1742,9	1577,8	2128,5

The results in Table 31, show that the further increase of CaO and SiO_2, together with the decrease in Al_2O_3 of the SVF slag 2, have led to an overall increase in fluxing materials requirement and total SVF slag output. The trends in flux consumptions are the same, but the mass of fluxes needed is higher compared to either the OBF slag type, or the SVF slag 1 type.

Slag 5 still needs the least fluxing materials with an overall SVF slag output of 1051.7 kg/ ton DRI, whereas Slag 6 is no longer in second position. This is most likely due to its higher Al_2O_3 of 23%, which needs to be reduced to 4% so as to have a SVF slag 2 compared to SVF slag 1 which has 15% Al_2O_3. Therefore, the ranking in terms of fluxing materials requirement to produce a SVF slag 2 type is as follows: Slag 5 < Slag 6 < Slag 4 < Slag 1 < Slag 3 < Slag 2.

In summary, the most flexible slag based on the mass balance in this study is Slag 5 overall, and Slag 3 from the high MgO slags (Slag 1, 2, 3). The SVF product that requires the least fluxing materials to obtain is the OBF slag type. SVF slag 1 and SVF slag 2 can still be produced in the SVF, but require significantly more fluxing materials for this to be achieved. This means that the size of the furnace will be comparatively bigger when producing these two SVF slags as opposed to producing an OBF slag type. This ultimately translates into higher energy consumption. SVF slag 1 has a comparatively lower fluxing materials requirement. Moreover, post-tap modifications of the SVF slag 1 to a cement clinker composition is possible due to similarity in chemical composition. However, this will require extra kiln units and cooling technologies to achieve. Therefore, a comparative assessment of the economic and technological benefits for the production of these 3 products is necessary in order to select the most viable products in this route. This information will be covered in chapter 9 of this study.

8.6.6. Alternative high MgO and low Al_2O_3 slag for the OBF

The mass balance results have shown that slags that contain MgO (>22%) in the OBF, require more fluxing materials in the SVF because of the low MgO content of SVF products. Another alternative slag composition on the 15% MgO layer with low Al_2O_3 contents can be considered in order to minimize the fluxing materials requirement while still having high MgO. However, the difference in degree of corrosion between 15% MgO and 22% MgO slags towards MgO-rich refractories still needs to be investigated through experimental tests. This new slag composition is labelled Slag 7, and has a liquidus temperature close to 1450°C. The composition and physical properties of slag 7 compared to the best performing slag in terms of the mass balance (slag 5) are summarized in Table 32.

Table 32: Compositions and Physical properties of Slag 7 compared Slag 5

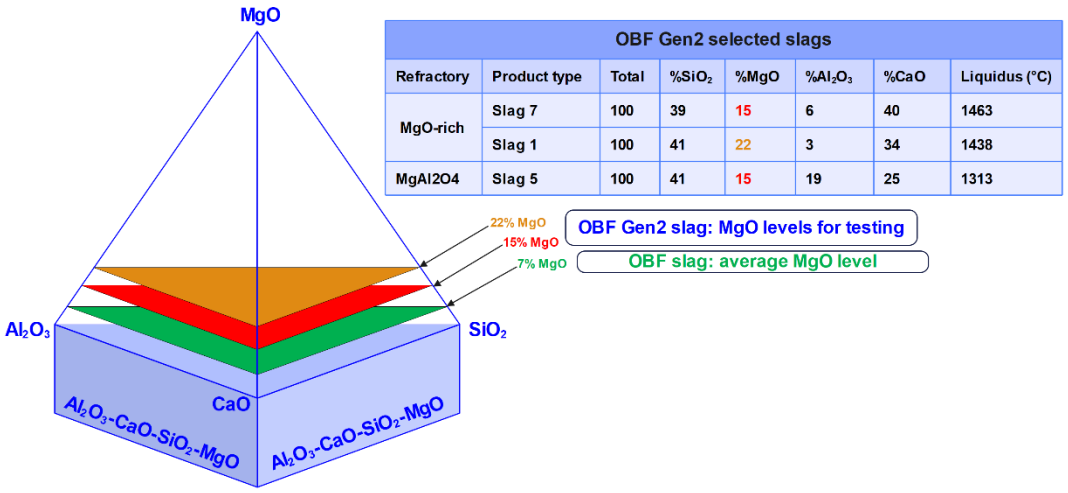
Composition (wt%)				
	SiO_2	**MgO**	**Al_2O_3**	**CaO**
Slag 7	39	15	6	40
Slag 5	41	15	19	25
Viscosity at 1500°C (dPa.s)				
	FactSage	**Riboud**	**Iida**	**Urbain**
Slag 7		1,428	1,911	3,003
Slag 5	5,185	11,019	6,601	12,196
Electrical conductivity 1500°C (W/m.K)				
Slag 7		0,691	0,540	0,368
Slag 5		0,122	0,189	0,112
Thermal conductivity 1500°C ($\Omega^{-1}m^{-1}$)				
Slag 7	0,125			
Slag 5	0,223			

Overall, the results in Table 32 show that the new Slag 7 is less viscous with lower thermal and electrical conductivities. This is because the new Slag 7 has a higher proportion of network modifiers (MgO, CaO) compared to Slag 5, which translates to a higher degree of depolymerization of the silicate network. Moreover, the comparison between the two slags in terms of the mass balance for the 3 products in the SVF is summarized in Table 33.

Table 33: Mass balance summary of Slag 7 compared Slag 5

			For OBF slag		**For SVF Slag 1**		**For SVF Slag 2**	
Gangue proportion	**Fluxes**	**Types of fluxes**	**Slag 7**	**Slag 5**	**Slag 7**	**Slag 5**	**Slag 7**	**Slag 5**
10%	**Fluxes in the OBF (kg)**	**Dolomite**	30,8	22,5	30,8	22,5	30,8	22,5
		Bauxite	6,5	30,2	6,5	30,2	6,5	30,2
		Lime	54,7	23,1	54,7	23,1	54,7	23,1
		Quartz	6,2	0,0	6,2	0,0	6,2	0,0
		Total	98,2	75,7	98,2	75,7	98,2	75,7
	Fluxes in the SVF (kg)	**Dolomite**	0,0	0,0	0,0	0,0	0,0	17,3
		Bauxite	45,6	15,6	97,7	61,6	19,8	0,0
		Lime	127,7	140,7	262,6	260,2	397,3	482,9
		Quartz	93,2	79,9	142,1	123,2	320,1	375,8
		Total	266,6	236,1	502,3	445,0	737,2	876,0
	Overall fluxes (kg)		364,8	311,8	600,5	520,7	835,4	951,7
	Overall OBF slag (kg)		198,2	175,7	198,2	175,7	198,2	175,7
	Overall SVF slag (kg)		514,8	411,8	750,5	620,7	985,4	1051,7
15%	**Overall fluxes (kg)**		545,2	467,7	897,5	781,0	1261,7	1427,8
	Overall OBF slag (kg)		296,3	263,6	296,3	263,6	296,3	263,6
	Overall SVF slag (kg)		695,2	617,7	1047,5	931,0	1411,7	1577,8

Slag 7 generates a slightly higher volume of OBF and SVF slag compared to Slag 5 as shown by the results in Table 33. However, compared to the other slags (slags 1, 2, 3, 4, and 6), Slag 7 requires the least fluxing requirement. In summary, the most flexible slags based on mass balance results in this study is Slag 5 overall, followed by Slag 7, and lastly, Slag 3 from the high MgO slags (Slags 1, 2, 3). Slags 1 and 3 have similar mass balances, which are like slags 5 and 6. Therefore, the slags that can be selected for experimental trials in this study are Slag 5, Slag 7 and Slag 3 as summarized in Figure 129. Moreover, the energy balances for the three selected slags are covered in the upcoming section. Generally, if the operating temperature is kept constant at 1500°C, a high fluxing materials requirement will translate to high energy consumption. These three slags can be recommended for experimental tests, and the difference amongst them might arise from their physical properties as well as their degree of corrosion towards the selected refractories. The slag composition with properties that are favourable for smelting operations in the OBF can be selected as the most viable slag composition.



OBF Gen2 selected slags							
Refractory	Product type	Total	%SiO_2	%MgO	%Al_2O_3	%CaO	Liquidus (°C)
MgO-rich	Slag 7	100	39	15	6	40	1463
	Slag 1	100	41	22	3	34	1438
MgAl2O4	Slag 5	100	41	15	19	25	1313

Figure 129: Selected OBF Gen2 slag compositions for energy balance calculations

It should be noted that Slag 7 has the potential to be directly granulated and tested for cementitious applications without valorisation if the intended product is a BF equivalent slag in terms of cementitious properties as reported in (Bernal et al., 2014). However, the main concern linked to high MgO slags is the volume expansion of concrete specimens made from these slags. Stutterheim (1960) conducted soundness tests to evaluate the volume expansion of concrete incorporating up to 50% of slag containing at most 20% MgO and found out that the cements were as sound as Portland cement. Further recommendations of performing soundness tests of high MgO slags before usage were suggested (Stutterheim, 1960). Hence, Slag 7 theoretically represents the best slag for the OBF Gen2 with, or without valorisation since it fits the composition of other BF slag around the world as shown in Table 34.

Table 34: Chemical compositions (%) of Blast furnace slags (Regourd and Bernard, 2019)

Source	CaO	SiO_2	Al_2O_3	MgO	Fe_2O_3	MnO	S
UK	40	35	16	6	0.8	0.6	1.7
Canada	40	37	8	10	1.2	0.7	2.0
France	43	35	12	8	2.0	0.5	0.9
Germany	42	35	12	7	0.3	0.8	1.6
Japan	43	34	16	5	0.5	0.6	0.9
Russia	39	34	14	9	1.3	1.1	1.1
South Africa	34	33	16	14	1.7	0.5	1.0
USA	41	34	10	11	0.8	0.5	1.3

The SVF product that requires the least fluxing materials to achieve is the OBF slag type. SVF slag 1 and SVF slag 2 can still be produced in the SVF, but require significantly more fluxing materials to be achieved. This means that the size of the furnace will be comparatively bigger when producing these two SVF slags as opposed to producing an OBF slag type. This ultimately translates to higher energy consumption. SVF slag 1 has a comparatively lower fluxing materials requirement. Moreover, post-tap modifications of the SVF slag 1 to a clinker composition is possible due to similarity in chemical composition. However, this will require extra kiln units and cooling technologies to achieve. Therefore, a comparative assessment of the economic and technological benefits for the production of these 3 products is necessary in order to select the most viable products in this route. The new flowsheet with the chosen OBF Gen2 slags and SVF slags for energy balance is shown in Figure 130.

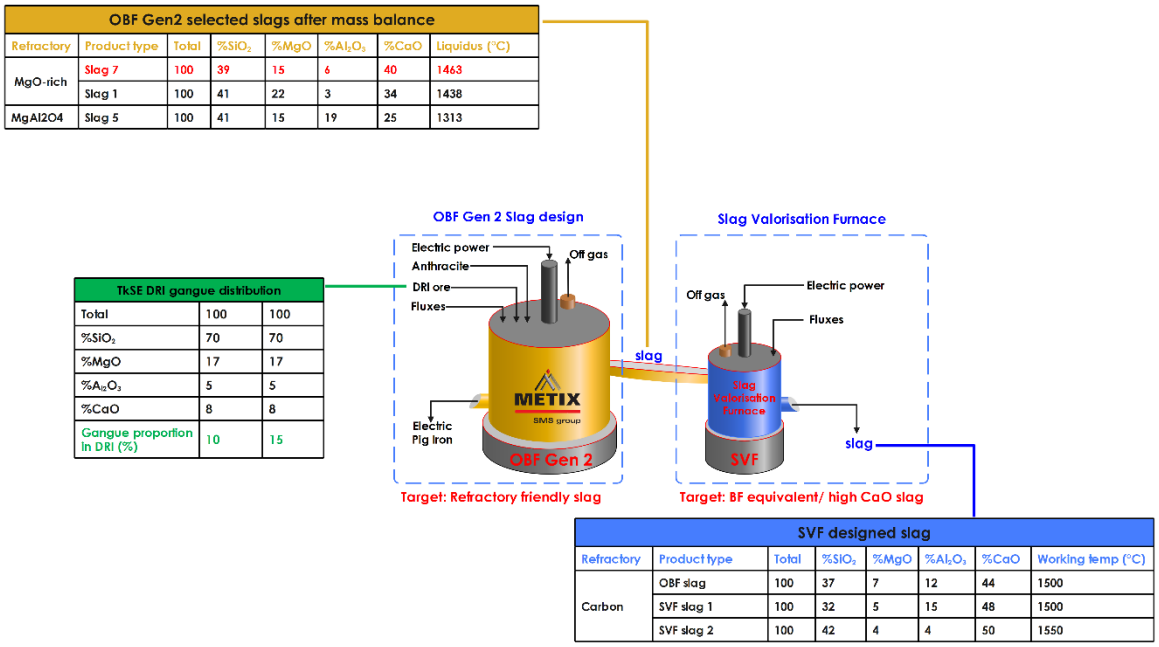


Figure 130: OBF Gen2 and SVF configuration for energy balance

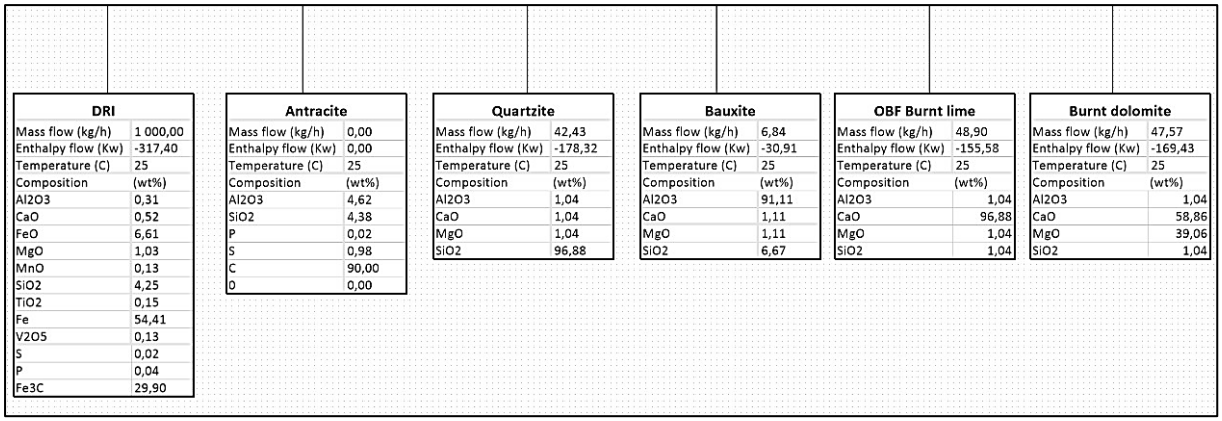
8.7. Energy balance

The energy balance is performed using the static model in HSC software. The total enthalpy flows (EF) of the feeds and products are calculated for the different slag types in the OBF and SVF. The specific energy required (SER) and consumption (SEC) are also calculated along

with slag/metal and fluxes/metal ratios. It should be noted that the calculations are done for 1 ton of DRI. Moreover, the OBF is setup to operate at 1500°C while the SVF is set up to operate at 1600°C. The raw materials are fed to the OBF while cold at 25°C while the produced OBF slag enters the SVF at 1500°C for valorisation.

8.7.1. Raw materials compositions and assumptions

The compositions of fluxing materials were kept as per the mass balance section, Figure 131 summarizes the compositions of the DRI, anthracite and fluxes used during energy balance calculations. It should be noted that anthracite is added to further allow the reduction of the remaining FeO to metallic Fe and balance the carbon content of the final hot metal.



DRI	
Mass flow (kg/h)	1 000,00
Enthalpy flow (Kw)	-317,40
Temperature (C)	25
Composition	(wt%)
Al2O3	0,31
CaO	0,52
FeO	6,61
MgO	1,03
MnO	0,13
SiO2	4,25
TiO2	0,15
Fe	54,41
V2O5	0,13
S	0,02
P	0,04
Fe3C	29,90

Antracite	
Mass flow (kg/h)	0,00
Enthalpy flow (Kw)	0,00
Temperature (C)	25
Composition	(wt%)
Al2O3	4,62
SiO2	4,38
P	0,02
S	0,98
C	90,00
0	0,00

Quartzite	
Mass flow (kg/h)	42,43
Enthalpy flow (Kw)	-178,32
Temperature (C)	25
Composition	(wt%)
Al2O3	1,04
CaO	1,04
MgO	1,04
SiO2	96,88

Bauxite	
Mass flow (kg/h)	6,84
Enthalpy flow (Kw)	-30,91
Temperature (C)	25
Composition	(wt%)
Al2O3	91,11
CaO	1,11
MgO	1,11
SiO2	6,67

OBF Burnt lime	
Mass flow (kg/h)	48,90
Enthalpy flow (Kw)	-155,58
Temperature (C)	25
Composition	(wt%)
Al2O3	1,04
CaO	96,88
MgO	1,04
SiO2	1,04

Burnt dolomite	
Mass flow (kg/h)	47,57
Enthalpy flow (Kw)	-169,43
Temperature (C)	25
Composition	(wt%)
Al2O3	1,04
CaO	58,86
MgO	39,06
SiO2	1,04

Figure 131: Raw materials compositions for energy balance calculations

The partition of major elements during simulation was done as per the assumptions in Table 35. Regarding other minor elements, the general assumption for the OBF was that 97% report to the slag and 3 % report to the off-gas dust as losses. On the other hand, there is no metal production the SVF, the proportion of elements reporting to the slag is increased to 99% and 1% is assumed lost to the off-gas dust. The slag is assumed metal-free, even though in reality some droplets of metal can be found in the slag.

Table 35: Elements distribution in OBF and SVF products

OBF Element Partition Factors									
Element	**Al**	**C**	**Ca**	**Fe**	**Mg**	**O**	**S**	**Si**	**V**
OBF Slag	97,00	39,00	97,00	1,00	97,00	62,26	67,00	87,00	17,00
OBF Metal	0,00	60,00	0,00	98,00	0,00	0,00	30,00	10,00	80,00
OBF Off gas	0,00	0,00	0,00	0,00	0,00	33,84	0,00	0,00	0,00
OBF Off gas dust	3,00	1,00	3,00	1,00	3,00	3,90	3,00	3,00	3,00
SVF Element Partition Factors									
Element	**Al**	**C**	**Ca**	**Fe**	**Mg**	**O**	**S**	**Si**	**V**
SVF Slag	99,00	0,00	99,00	99,00	99,00	99,00	30,00	99,00	99,00
SVF Off gas	0,00	99,00	0,00	0,00	0,00	0,00	0,00	0,00	0,00
SVF Off gas dust	1,00	1,00	1,00	1,00	1,00	1,00	70,00	1,00	1,00

The required metallurgical power (MP) is defined as per Equation 10:

$$MP = Total\ EF\ in\ products - Total\ EF\ in\ feeds \quad (10)$$

The total HL is assumed to be 15% of the required metallurgical power as per Equation 11 for both the SVF and OBF:

$$Total\ HL = 0.15 * (Slag + Metal + off\ gas + dusts + MP) \quad (11)$$

The total furnace power consumption (FPC) is the sum of the required metallurgical power and the total heat loss. The SER is the required metallurgical power per unit mass flow rate of hot metal produced. Similarly, the SEC is the total furnace power consumption per unit mass flow rate of hot metal produced. However, in the SVF, the SER and SEC are calculated per unit mass flow rate of slag produced.

8.7.2. Energy balance of selected production cases

The following production cases are considered for energy balance calculations, and this is in line with the different proposed slag compositions for the OBF and the SVF in Figure 130:

- Case 1: Production of Slag 7 in the OBF with valorisation to SVF slag 1
- Case 2: Production of Slag 7 in the OBF with valorisation to SVF slag 2
- Case 3: Production of Slag 1 in the OBF with valorisation to SVF slag 1
- Case 4: Production of Slag 1 in the OBF with valorisation to SVF slag 2
- Case 5: Production of Slag 5 in the OBF with valorisation to SVF slag 1
- Case 6: Production of Slag 5 in the OBF with valorisation to SVF slag 2

The first production case considers the generation of Slag 7 in the OBF followed by subsequent valorisation to SVF slag 1. The enthalpies as well as the important energy-related parameters of production case 1 are summarised in Figure 132.

Production case 1

Slag 7: OBF Energy Balance			
In		Out	
Stream Name	Enthalpy Flow [kW]	Stream Name	Enthalpy Flow [kW]
Antracite	0,0	Dust	-27,5
Quartzite	-178,3	Metal	376,5
DRI	-317,4	Slag	-622,8
Burnt lime	-155,6	Off gas	7,8
Burnt dolomite	-169,4		
Bauxite	-30,9		
Metallurgical power	747,4	Heat loss	72,2
Total Energy:	-104,2	Total energy:	-193,7
Parameters			
Furnace power consumption (kW):			698,5
Total Fluxes (kg/h)	145,7	Total Metal (kg/h)	889,7
SER (kWh/kg)	0,722	Total slag (kg/h)	205,6
SEC (kWh/kg)	0,785		

SVF Slag 1: Energy Balance			
In		Out	
Stream Name	Enthalpy Flow [kW]	Stream Name	Enthalpy Flow [kW]
OBF Slag	-622,8	Slag	-1 442,7
Burnt dolomite	-18,6	Dust	-15,4
Burnt lime	-469,8	Off gas	0,0
Quartzite	-280,4		
Bauxite	-253,2		
Metallurgical power	217,3	Heat loss	30,6
Total Energy:	-104,2	Total energy:	-193,7
Parameters			
Furnace power consumption (kW):			248,0
Total Fluxes (kg/h)	275,6	Total slag (kg/h)	476,3
SER (kWh/kg)	0,456		
SEC (kWh/kg)	0,521		

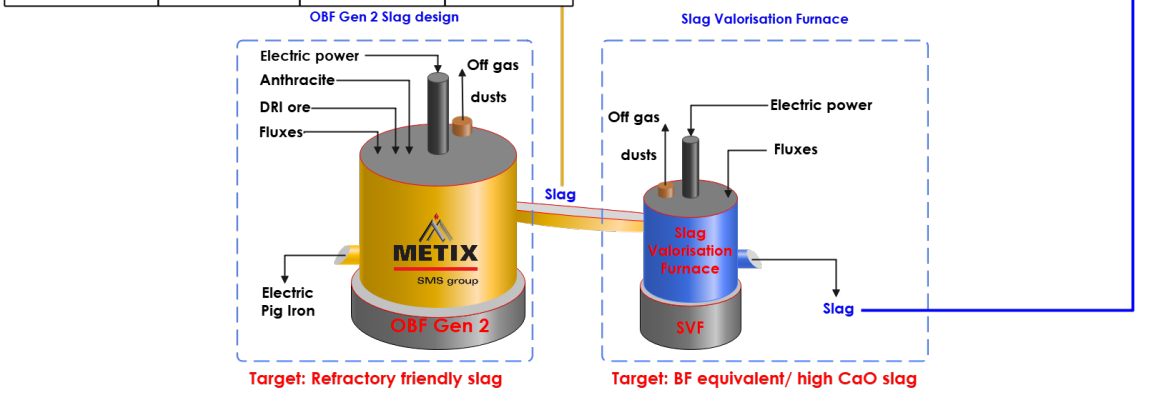


Figure 132: Production of Slag 7 in the OBF with valorisation to SVF slag 1

The required metallurgical power for this production scenario is 747.4 kW, the estimated heat loss is around 72.3 kW, and this brings the overall furnace power consumption to 889.7 kW. Moreover, 1 ton of DRI as per the provided composition yields around 889.7 kg of hot metal and 205.6 kg of corresponding slag in the OBF. The valorisation to SVF slag 1 requires about 275.6 kg of fluxes, most of which being burnt lime due to the high CaO content of the valorised slag, and this brings the final SVF slag 1 output to 476.3 kg .

The specific energy requirement for this production case is 0.72 kWh/kg of hot metal in the OBF while in the SVF, it is 0.45 kWh/kg of valorised slag. It can be seen that the SVF process does not require much metallurgical power and this is owing to the fact that the slag is fed hot to the SVF, thereby minimising the energy requirement. However, as previously shown in the mass balance section and in Figure 132, the SVF process requires a lot of fluxing materials to reach a targeted slag composition.

Similar energy-balance calculations were performed on the remaining production cases, and the results are summarized in the following figures from production case 2 to production case 6.

Production case 2

Slag 7: OBF Energy Balance			
In		Out	
Stream Name	Enthalpy Flow [kW]	Stream Name	Enthalpy Flow [kW]
Antracite	0,0	Dust	-27,5
Quartzite	-178,3	Metal	376,5
DRI	-317,4	Slag	-622,8
Burnt lime	-155,6	Off gas	7,8
Burnt dolomite	-169,4		
Bauxite	-30,9		
Metallurgical power	747,4	Heat loss	72,2
Total Energy:	-104,2	Total energy:	-193,7
Parameters			
Furnace power consumption (kW):			698,5
Total Fluxes (kg/h)	145,7	Total Metal (kg/h)	889,7
SER (kWh/kg)	0,722	Total slag (kg/h)	205,6
SEC (kWh/kg)	0,785		

SVF Slag 2: Energy Balance			
In		Out	
Stream Name	Enthalpy Flow [kW]	Stream Name	Enthalpy Flow [kW]
OBF Slag	-622,8	Slag	-1 827,0
Burnt dolomite	0,0	Dust	-19,4
Burnt lime	-719,2	Off gas	0,0
Quartzite	-735,8		
Bauxite	-21,3		
Metallurgical power	291,7	Heat loss	39,1
Total Energy:	-1 807,4	Total energy:	-1 807,4
Parameters			
Furnace power consumption (kW):			330,6
Total Fluxes (kg/h)	405,8	Total slag (kg/h)	605,2
SER (kWh/kg)	0,482		
SEC (kWh/kg)	0,546		

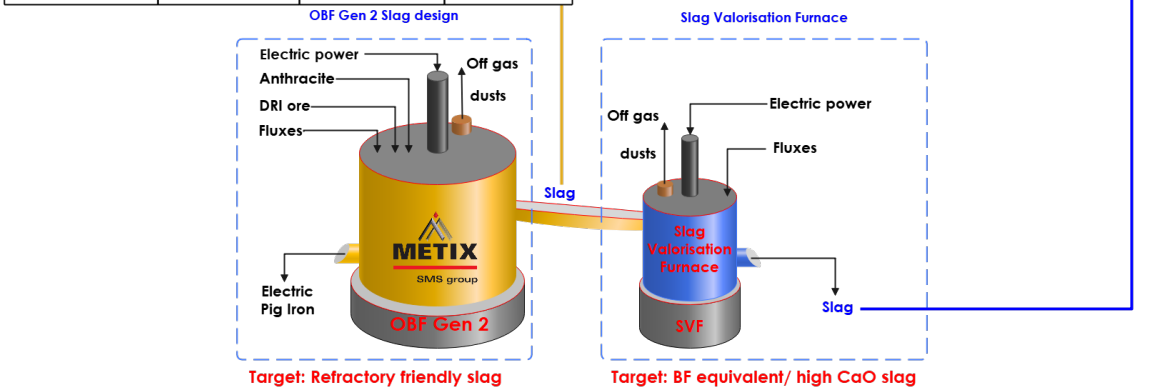


Figure 133: Production of Slag 7 in the OBF with valorisation to SVF slag 2

Production case 3

Slag 1: OBF Energy Balance			
In		Out	
Stream Name	Enthalpy Flow [kW]	Stream Name	Enthalpy Flow [kW]
Antracite	0,0	Dust	-38,5
Quartzite	-396,8	Metal	378,5
DRI	-317,4	Slag	-946,1
Burnt lime	-52,9	Off gas	9,0
Burnt dolomite	-487,3		
Bauxite	-15,6		
Metallurgical power	686,3	Heat loss	13,4
Total Energy:	-583,7	Total energy:	-583,7
Parameters			
Furnace power consumption (kW):			699,7
Total Fluxes (kg/h)	251,3	Total Metal (kg/h)	892,1
SER (kWh/kg)	0,769	Total slag (kg/h)	302,9
SEC (kWh/kg)	0,784		

SVF Slag 1: Energy Balance			
In		Out	
Stream Name	Enthalpy Flow [kW]	Stream Name	Enthalpy Flow [kW]
OBF Slag	-946,1	Slag	-2 650,1
Burnt dolomite	0,0	Dust	-28,3
Burnt lime	-1 012,8	Off gas	0,0
Quartzite	-567,6		
Bauxite	-534,1		
Metallurgical power	440,1	Heat loss	58,0
Total in:	-2 620,5	Total out:	-2 620,4
Parameters			
Furnace power consumption (kW):			498,1
Total Fluxes (kg/h)	571,5	Total slag (kg/h)	865,6
SER (kWh/kg)	0,508		
SEC (kWh/kg)	0,575		

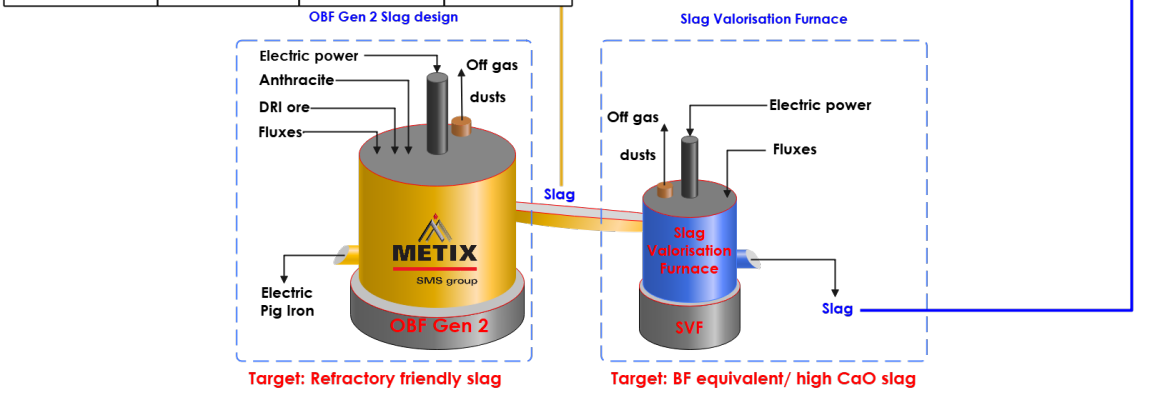


Figure 134: Production of Slag 1 in the OBF with valorisation to SVF slag 1

Production case 4

Slag 1: OBF Energy Balance			
In		Out	
Stream Name	Enthalpy Flow [kW]	Stream Name	Enthalpy Flow [kW]
Antracite	0,0	Dust	-38,5
Quartzite	-396,8	Metal	378,5
DRI	-317,4	Slag	-946,1
Burnt lime	-52,9	Off gas	9,0
Burnt dolomite	-487,3		
Bauxite	-15,6		
Metallurgical power	686,3	Heat loss	13,4
Total Energy:	-583,7	Total energy:	-583,7
Parameters			
Furnace power consumption (kW):			699,7
Total Fluxes (kg/h)	251,3	Total Metal (kg/h)	892,1
SER (kWh/kg)	0,769	Total slag (kg/h)	302,9
SEC (kWh/kg)	0,784		

SVF Slag 2: Energy Balance			
In		Out	
Stream Name	Enthalpy Flow [kW]	Stream Name	Enthalpy Flow [kW]
OBF Slag	-946,1	Slag	-2 664,6
Burnt dolomite	0,0	Dust	-28,3
Burnt lime	-1 093,9	Off gas	0,0
Quartzite	-961,9		
Bauxite	-59,2		
Metallurgical power	425,4	Heat loss	57,2
Total in:	-2 635,7	Total out:	-2 635,7
Parameters			
Furnace power consumption (kW):			482,6
Total Fluxes (kg/h)	588,8	Total slag (kg/h)	879,8
SER (kWh/kg)	0,484		
SEC (kWh/kg)	0,549		

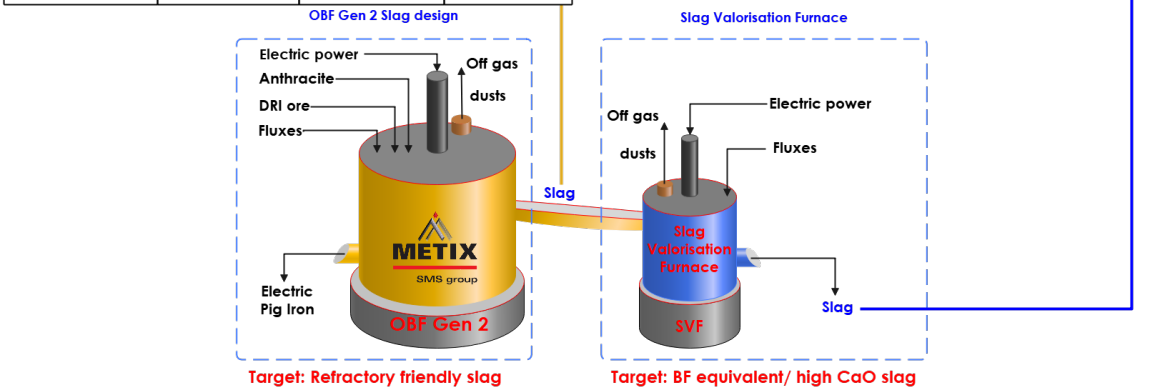


Figure 135: Production of Slag 1 in the OBF with valorisation to SVF slag 2

Production case 5

Slag 5: OBF Energy Balance			
In		Out	
Stream Name	Enthalpy Flow [kW]	Stream Name	Enthalpy Flow [kW]
Antracite	0,0	Dust	-28,9
Quartzite	-201,1	Metal	376,7
DRI	-317,4	Slag	-664,9
Burnt lime	-50,8	Off gas	8,0
Burnt dolomite	-166,6		
Bauxite	-166,9		
Metallurgical power	643,9	Heat loss	50,2
Total Energy:	-258,9	Total energy:	-258,9
Parameters			
Furnace power consumption (kW):			694,1
Total Fluxes (kg/h)	147,5	Total Metal (kg/h)	890,1
SER (kWh/kg)	0,723	Total slag (kg/h)	206,6
SEC (kWh/kg)	0,784		

SVF Slag 1: Energy Balance			
In		Out	
Stream Name	Enthalpy Flow [kW]	Stream Name	Enthalpy Flow [kW]
OBF Slag	-664,9	Slag	-1 877,5
Burnt dolomite	0,0	Dust	-20,0
Burnt lime	-796,3	Off gas	0,0
Quartzite	-469,6		
Bauxite	-237,0		
Metallurgical power	311,0	Heat loss	40,7
Total in:	-1 856,8	Total out:	-1 856,8
Parameters			
Furnace power consumption (kW):			351,7
Total Fluxes (kg/h)	414,5	Total slag (kg/h)	614,8
SER (kWh/kg)	0,506		
SEC (kWh/kg)	0,572		

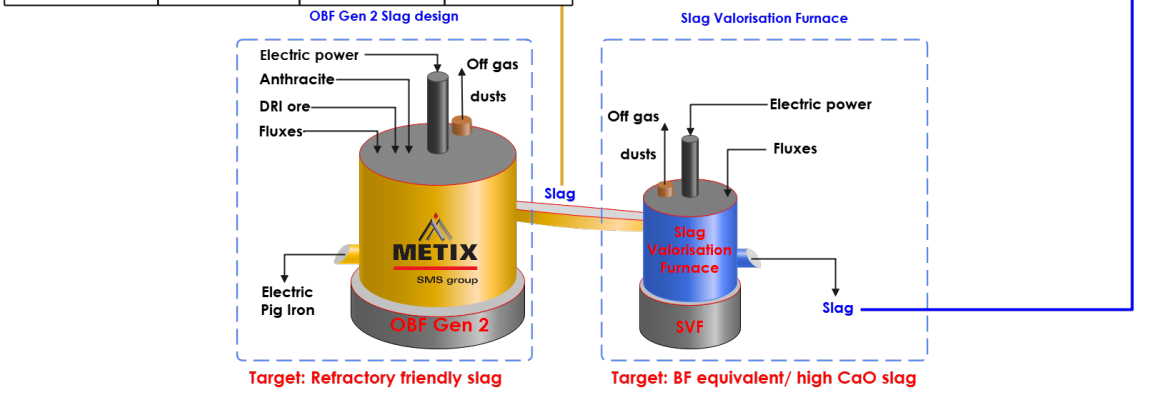


Figure 136: Production of Slag 5 in the OBF with valorisation to SVF slag 1

Production case 6

Slag 5: OBF Energy Balance			
In		Out	
Stream Name	Enthalpy Flow [kW]	Stream Name	Enthalpy Flow [kW]
Antracite	0,0	Dust	-28,9
Quartzite	-201,1	Metal	376,7
DRI	-317,4	Slag	-664,9
Burnt lime	-50,8	Off gas	8,0
Burnt dolomite	-166,6		
Bauxite	-166,9		
Metallurgical power	643,9	Heat loss	50,2
Total Energy:	-258,9	Total energy:	-258,9
Parameters			
Furnace power consumption (kW):			694,1
Total Fluxes (kg/h)	147,5	Total Metal (kg/h)	890,1
SER (kWh/kg)	0,723	Total slag (kg/h)	206,6
SEC (kWh/kg)	0,784		

SVF Slag 2: Energy Balance			
In		Out	
Stream Name	Enthalpy Flow [kW]	Stream Name	Enthalpy Flow [kW]
OBF Slag	-664,9	Slag	-2 760,9
Burnt dolomite	-89,7	Dust	-29,3
Burnt lime	-1 250,3	Off gas	0,0
Quartzite	-1 222,9		
Bauxite	0,0		
Metallurgical power	498,9	Heat loss	61,2
Total in:	-2 728,9	Total out:	-2 729,0
Parameters			
Furnace power consumption (kW):			560,1
Total Fluxes (kg/h)	709,2	Total slag (kg/h)	906,5
SER (kWh/kg)	0,550		
SEC (kWh/kg)	0,618		

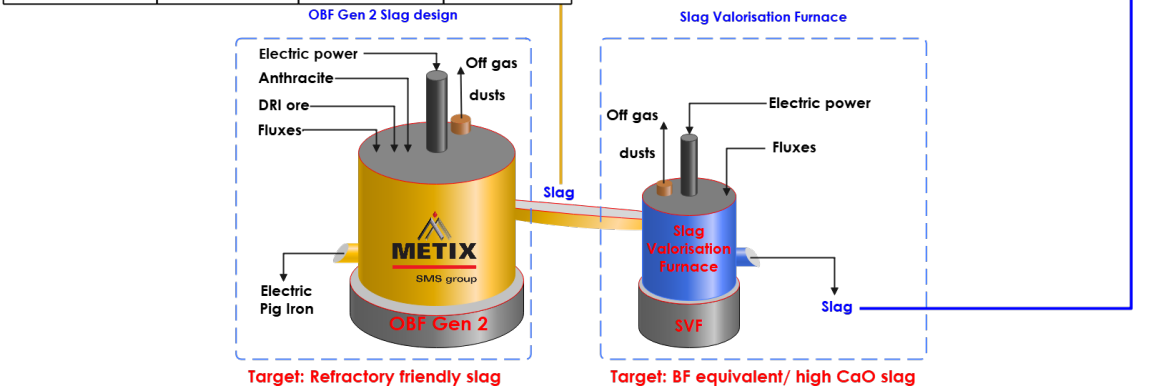


Figure 137: Production of Slag 5 in the OBF with valorisation to SVF slag 2

8.1.1. Summary of energy balance in selected production cases

This section compares the energy balance of all the production cases in the preceding section. More specifically in terms of metallurgical power (MP) and slag output in both the OBF and SVF. The SER from the OBF is roughly similar for the six production cases owing to the fact that the mass of the metal is the same and the variations among different MPs are lower. The only notable difference in terms of energy balance can be found in the SVF, and this is in agreement with the values in the preceding mass balance section. A comparison of the MPs and slag outputs for the different production cases in the SVF are summarized in Figure 138.

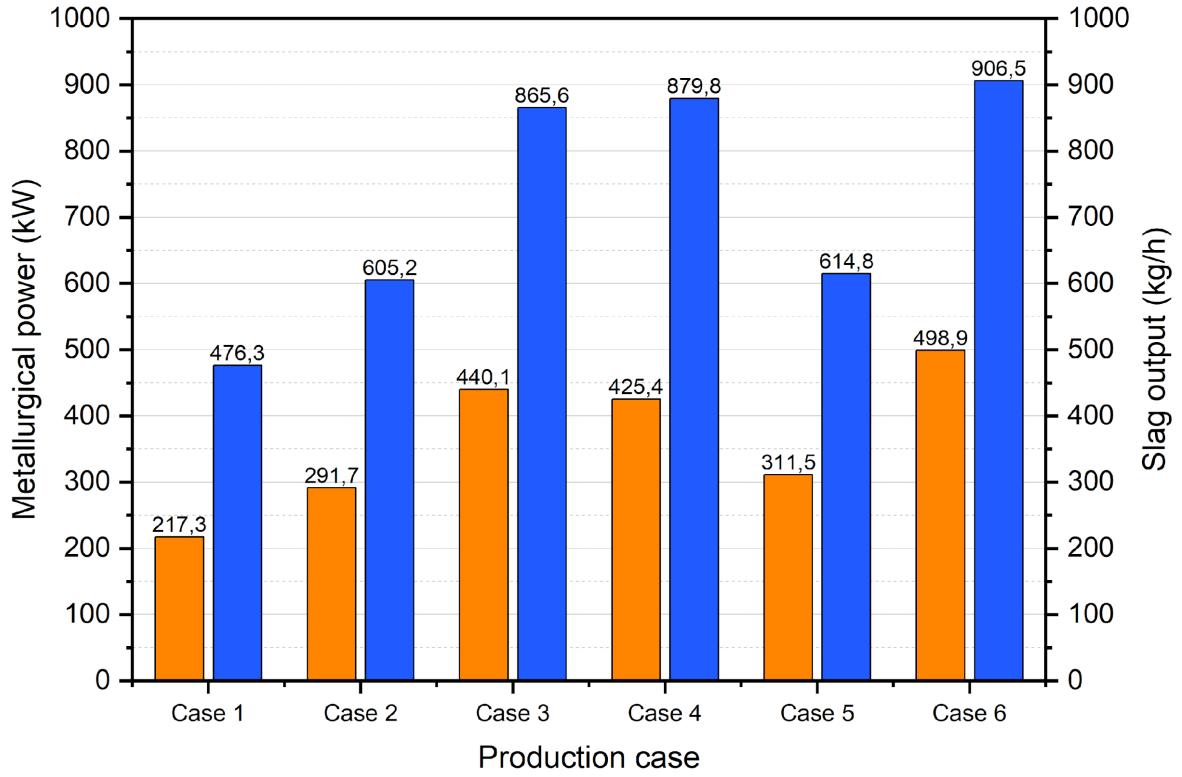


Figure 138: Comparison of energy requirement for different production cases in the SVF

From the proposed slag production cases, it can be seen that Case 1 is the least energy demanding in terms of metallurgical power at 217.3 kW and this is because it results in the lowest slag output of 476.3 kg/h as shown in Figure 138. Moreover, Case 2 and Case 5 are also roughly similar to Case 1 in terms of both slag output and metallurgical power requirements. On the other hand, Case 6, Case 3, and Case 4 require relatively high energy input due to the high volume of slag that will be produced in these cases. It should be noted that the volume of the slag is affected by the quantity of fluxing materials needed to achieve a target slag composition, which is firstly reliant on the original composition of gangue materials in the DRI. Therefore, the gangue composition of the DRI affects the mass balance for a given slag composition as well as the energy requirement to produce such slag.

The SVF slag output as well as the annual production capacity, will affect the size of the furnace, which can also have some repercussions on the capital cost of the process. Moreover, the total cost of the SVF process will also be dictated by the cost of the inputs, the CAPEX (capital expenditures), and the OPEX (operating expenses). From a mass and energy balance perspective, production case 1, 2, and 5 provide good results for the gangue composition selected in this study. Moreover, without knowledge of the gangue composition of the DRI that will be used to produce the target slags, it is difficult to definitively predict the optimal production case. In summary, the gangue proportion and distribution in the DRI, as well as the target slag composition are the major factors that will dictate both the mass and energy balances.

8.2. Conclusion and potential benefits of SVF slags

8.2.1. Reactivity enhancement and refractory life extension of the OBF

The main incentives of producing SVF slags are to further improve the cementitious reactivity of the OBF slag and to extend the campaign life of the OBF's refractory lining materials by producing a less corrosive slag (saturated in MgO) in the OBF. An illustration of cementitious reactivity enhancement is shown in Figure 139.

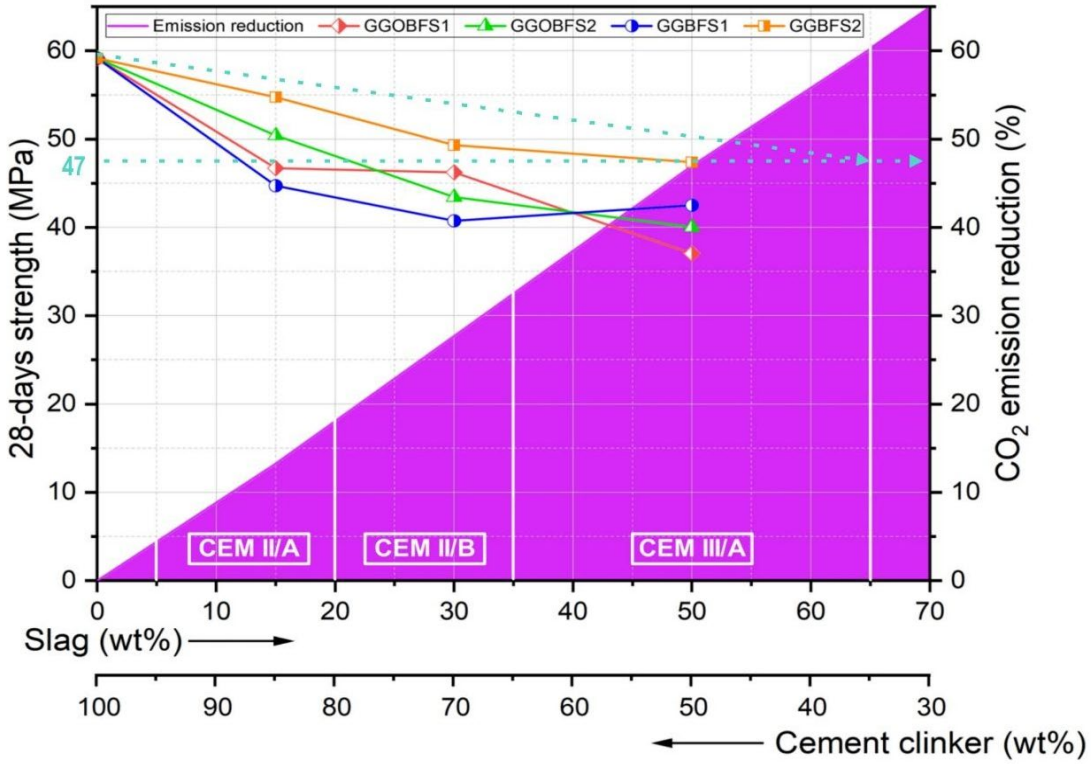


Figure 139: Reactivity enhancement of slag

Assuming that the required 28-days strength for a cementitious specimen in a given construction site is 47 MPa. Based on the results, GGBFS1 can reach that strength at 12% slag substitution, GGOBFS2 at 22% slag substitution, while GGBFS2 at 50% slag substitution saving up to 47% of CO_2 emissions. This highlights the contribution of the individual slag reactivity to the strength gain, the more reactive the slag, the higher the substitution for a given strength requirement. It has been noted in chapter 5 that the three parameters that contribute to strength development are the hydraulic reaction of cement, the micro-filling effect, and the slag reactivity (linked to its core properties: chemical composition, fineness, glass content). If SVF slag possesses higher cementitious reactivity, for instance like the arrow in light blue in Figure 139, the slag can replace up to 65% of clinker while reducing up to 60% of CO_2 emissions. It should be noted that the values are not reflective of the SVF slag, and were just used for illustration purposes. Therefore, the actual strength values of SVF slags will indicate the corresponding CO_2 emissions reduction and these values can only be obtained through experimental tests.

Generally, it is clear that the CO_2 emissions in the cement industry can be reduced by increasing the proportion slag in slag-cement blends as per Figure 139. However, the reactivity of the slag will dictate the amount of cement clinker that can be replaced without affecting the mechanical

strength required in a given application. Therefore, the enhancement of the slag reactivity has the potential to result in further CO_2 emission reduction in the cement industry.

8.2.2. Forecast of supplementary cementitious materials

Fly ash and GGBFS are presently the most widely consumed supplementary cementitious materials (SCMs) in the cement industry to lower CO_2 emissions associated with clinker production (Orozco et al., 2024). The current quest for green production processes and transition to carbon neutrality as per the 2015 Paris-agreement are causing declined interests in coal-fired power plants for renewable electricity, and phase-out of the BF technology from the steelmaking chain for low-CO_2 alternative ironmaking technologies. As such, there will be declined availability of fly ash and GGBFS. The materials that are most likely to emerge and take dominance as SCMs in the future are calcined clays and the novel granulated OBF slag due to their relatively lower CO_2 emissions as shown in Figure 140.

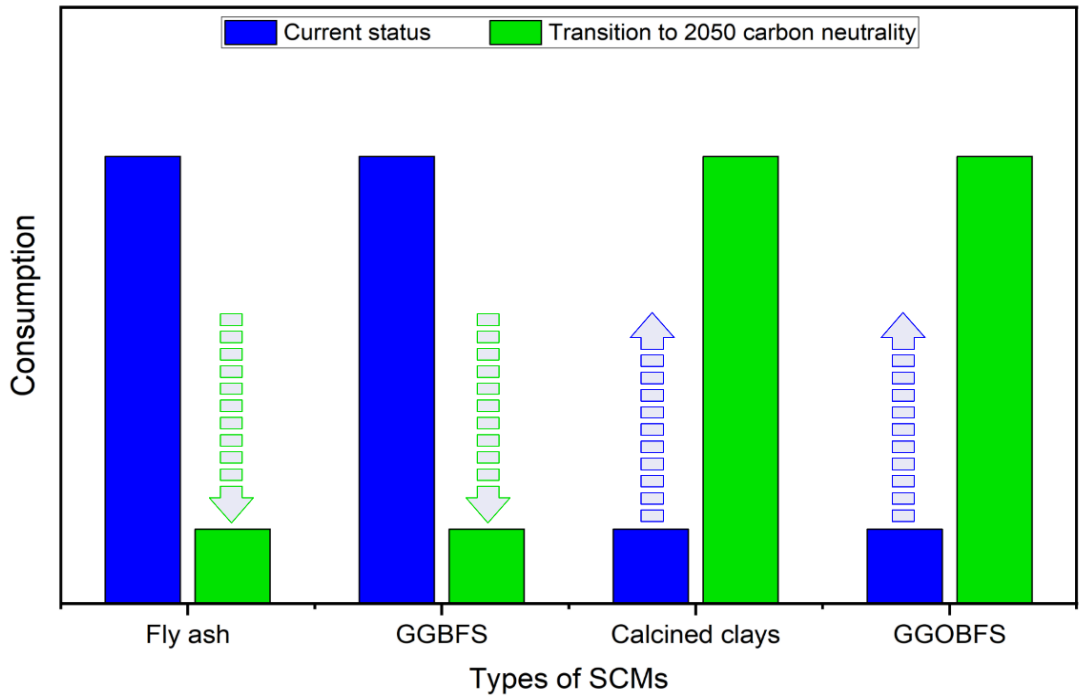


Figure 140: Forecast of SCMs consumption in the transition to 2050 carbon neutrality

If SVF slags are produced in the future, they will also be part of the green SCMs that can be used to save energy associated with clinker production and to reduce CO_2 emissions for environmental protection. Moreover, SVF slags are more likely to be pricier than OBF slags due to their expected higher cementitious performance as per the slag's glass structure theory and equilibrium relations elaborated throughout chapter 7 and 8. The OBF Gen2 slag is less corrosive than the normal OBF slag due to the MgO saturation, thereby protecting the OBF's refractory. Moreover, the cementitious valorisation of the OBF Gen2 slag results in the production of SVF slags, which theoretically should display higher cementitious performance than the normal OBF slag. However, the benefits of the OBF Gen2 and SVF slags need to be confirmed by conducting cementitious and refractory performance tests. Furthermore, a comparative assessment of the economic and technological benefits between the DRI-OBF and DRI-OBF-SVF is necessary in order to highlight the viability of the SVF slag.

References

Bernal, S.A., San Nicolas, R., Myers, R.J., Mejía de Gutiérrez, R., Puertas, F., van Deventer, J.S.J. and Provis, J.L. (2014). MgO content of slag controls phase evolution and structural changes induced by accelerated carbonation in alkali-activated binders. *Cement and Concrete Research*, 57, pp.33–43. doi:https://doi.org/10.1016/j.cemconres.2013.12.003.

Forsbacka, L., Holappa, L., Iida, T., Kita, Y. and Toda, Y. (2003). Experimental study of viscosities of selected CaO–MgO–Al_2O_3–SiO_2 slags and application of the Iida model. *Scandinavian Journal of Metallurgy*, 32(5), pp.273–280. doi:https://doi.org/10.1034/j.1600-0692.2003.00652.x.

G. Urbain, F. Cambier, M. Deletter and M. R. Anseau (1981). "Viscosity of Silicate Melts," Transactions and Journal of British Ceramics Society, 80(4), pp. 139-141.

Hayashi, M., Ishii, H., Susa, M., Fukuyama, H. and Nagata, K. (2001). Effect of ionicity of nonbridging oxygen ions on thermal conducti...: Ingenta Connect. *Physics and Chemistry of Glasses*, 42(1), pp.6–11.

Horii, K. & Tsutsumi, N. & Kitano, Y. & Kato, T. (2013). Processing and reusing technologies for steelmaking slag. *Nippon Steel Technical Report*. pp.123-129.

Hu, X., Ren, Z., Zhang, G., Wang, L. and Chou, K. (2012). A model for estimating the viscosity of blast furnace slags with optical basicity. *International Journal of Minerals Metallurgy and Materials*, 19(12), pp.1088–1092. doi:https://doi.org/10.1007/s12613-012-0675-2.

Iida, T., Sakai, H., Kita, Y. and Koichi Shigeno (2000). An Equation for Accurate Prediction of the Viscosities of Blast Furnace Type Slags from Chemical Composition. *ISIJ International*, 40(Suppl), pp.S110–S114. doi:https://doi.org/10.2355/isijinternational.40.suppl_s110.

Kang, Y. and Morita, K. (2006). Thermal Conductivity of the CaO–Al2O3–SiO2 System. *ISIJ International*, 46(3), pp.420–426. doi:https://doi.org/10.2355/isijinternational.46.420.

Kang, Y., Lee, J. and Morita, K. (2014). Thermal Conductivity of Molten Slags: A Review of Measurement Techniques and Discussion Based on Microstructural Analysis. *ISIJ International*, 54(9), pp.2008–2016. doi:https://doi.org/10.2355/isijinternational.54.2008.

Kucharski, M., Stubina, N.M. and Toguri, J.M. (1989). Viscosity Measurements of Molten FeO–SiO_2, FeO–CaO–SiO_2, and FeO–MgO–SiO_2 Slags. *Canadian Metallurgical Quarterly*, 28(1), pp.7–11. doi:https://doi.org/10.1179/cmq.1989.28.1.7.

Machin, J.S. and Yee, T.B. (1954). Viscosity Studies of System CaO–MgO–Al_2O_3–SiO_2: IV, 60 and 65% SiO_2. *Journal of the American Ceramic Society*, 37(4), pp.177–186. doi:https://doi.org/10.1111/j.1151-2916.1954.tb14019.x.

Machin, J.S., Yee, T.B. And Hanna, D.L. (1952). Viscosity Studies of System CaO–MgO–Al_2O_3–SiO_2: III, 35, 45, and 50% SiO_2. *Journal of the American Ceramic Society*, 35(12), pp.322–325. doi:https://doi.org/10.1111/j.1151-2916.1952.tb13057.x.

Mills, K.C. (1993). The Influence of Structure on the Physico-chemical Properties of Slags. *ISIJ International*, 33(1), pp.148–155. doi:https://doi.org/10.2355/isijinternational.33.148.

Mills, K.C. and Sridhar, S. (1999). Viscosities of ironmaking and steelmaking slags. *Ironmaking & Steelmaking*, 26(4), pp.262–268. doi:https://doi.org/10.1179/030192399677121.

Mills, K.C., Yuan, L. and Jones, R.T. (2011). Estimating the physical properties of slags. *Journal of the Southern African Institute of Mining and Metallurgy*, 111(10), pp.649–658. Available at: https://www.scielo.org.za/scielo.php?script=sci_arttext&pid=S2225-62532011001000002 [Accessed 1 Dec. 2024].

Ore, I. and Curry, K.C. (2021). *2018 Minerals Yearbook SLAG-IRON AND STEEL [ADVANCE RELEASE]*. [online] USGS science for a changing world. Available at: https://pubs.usgs.gov/myb/vol1/2018/myb1-2018-iron-steel-slag.pdf [Accessed 4 Dec. 2024].

Orozco, C., Babel, S., Tangtermsirikul, S. and Sugiyama, T. (2024). Comparison of environmental impacts of fly ash and slag as cement replacement materials for mass concrete and the impact of transportation. *Sustainable Materials and Technologies*, [online] 39, p.e00796. doi:https://doi.org/10.1016/j.susmat.2023.e00796.

Ozawa, S., Susa, M., Goto, T., Endo, R. and Mills, K.I. (2006). Lattice and Radiation Conductivities for Mould Fluxes from the Perspective of Degree of Crystallinity. *ISIJ International*, 46(3), pp.413–419. doi:https://doi.org/10.2355/isijinternational.46.413.

Park, J.H., Kim, H. and Min, D.J. (2008). Novel Approach to Link between Viscosity and Structure of Silicate Melts via Darken's Excess Stability Function: Focus on the Amphoteric Behavior of Alumina. *Metallurgical and Materials Transactions B-process Metallurgy and Materials Processing Science*, 39(1), pp.150–153. doi:https://doi.org/10.1007/s11663-007-9122-6.

Regourd, M.M. and Bernard, S.K. (2019). Cements Made From Blastfurnace Slag. In: *Hewlett and Liska (eds) Lea's Chemistry of Cement and Concrete 5th edition.* Butterworth-Heinemann, Oxford, UK: Elsevier Science & Technology, pp.469–507. doi:https://doi.org/10.1016/b978-0-08-100773-0.00010-1.

Riboud, P.V., Roux Y., Lucas, L.D., and Gaye, H. (1981). Improvement of continuous casting powders. *Fachber. Huettenprax. Metallweiterverarb*, [online] 19(10), pp.859–869. Available at:http://pascalfrancis.inist.fr/vibad/index.php?action=getRecordDetail&idt=PASCAL8300209860 [Accessed 1 Dec. 2024].

Seetharaman, S. and Sichen, D. (1994). Estimation of the viscosities of binary metallic melts using Gibbs energies of mixing. *Metallurgical and Materials Transactions B*, 25(4), pp.589–595. doi:https://doi.org/10.1007/bf02650079.

Shankar, A., Görnerup, M., Lahiri, A.K. and Seetharaman, S. (2007). Experimental Investigation of the Viscosities in $CaO\text{-}SiO_2\text{-}MgO\text{-}Al_2O_3$ and $CaO\text{-}SiO_2\text{-}MgO\text{-}Al_2O_3\text{-}TiO_2$ Slags. *Metallurgical and Materials Transactions B*, 38(6), pp.911–915. doi:https://doi.org/10.1007/s11663-007-9087-5.

Shiraishi, Y., Ikeda, K., Tamura, A. and T. Saitô (1978). On the Viscosity and Density of the Molten $FeO–SiO_2$ System. *Transactions of the Japan Institute of Metals*, 19(5), pp.264–274. doi:https://doi.org/10.2320/matertrans1960.19.264.

Sohn, I. and Min, D.J. (2012). A Review of the Relationship between Viscosity and the Structure of Calcium-Silicate-Based Slags in Ironmaking. *steel research international*, 83(7), pp.611–630. doi:https://doi.org/10.1002/srin.201200040.

Stutterheim, N. (1960). Properties and Uses of High-Magnesia Portland Slag Cement Concretes. *ACI Journal Proceedings*, 56(4), pp.1027–1046. doi:https://doi.org/10.14359/8128.

Urbain, G. (1987). Viscosity estimation of slags. *Steel Research*, 58(3), pp.111–116. doi:https://doi.org/10.1002/srin.198701513.

Urbain, G., Bottinga, Y. and Pascal Richet (1982). Viscosity of liquid silica, silicates and alumino-silicates. *Geochimica et Cosmochimica Acta*, 46(6), pp.1061–1072. doi:https://doi.org/10.1016/0016-7037(82)90059-x.

Wang, Y., Wang, L. and Chou, K. (2015). Estimating Electrical Conductivities of CaO-MgO-Al2O3-SiO2 Using Ion-Oxygen Parameter. *High Temperature Materials and Processes*, 35(3), pp.253–259. doi:https://doi.org/10.1515/htmp-2014-0195.

Xing, X., Pang, Z., Mo, C., Wang, S. and Ju, J. (2019). Effect of MgO and BaO on viscosity and structure of blast furnace slag. *Journal of Non-Crystalline Solids*, 530, pp.119801–119801. doi:https://doi.org/10.1016/j.jnoncrysol.2019.119801.

Zhang, G.-H. and Chou, K.-C. (2010). Simple Method for Estimating the Electrical Conductivity of Oxide Melts with Optical Basicity. *Metallurgical and Materials Transactions*, 41(1), pp.131–136. doi:https://doi.org/10.1007/s11663-009-9298-z.

Zhang, G.-H., Yan, B.-J., Chou, K.-C. and Li, F.-S. (2011). Relation Between Viscosity and Electrical Conductivity of Silicate Melts. *Metallurgical and Materials Transactions B*, 42(2), pp.261–264. doi:https://doi.org/10.1007/s11663-011-9484-7.

Zhang, L., Jiang, K., Xie, F. and Lu, D. (2023). Relation between Viscosity and Conductivity of CaO-MgO-FeO-Al2O3-SiO2 System for Copper Smelting Slags. *Metals*, 13(4), pp.786–786. doi:https://doi.org/10.3390/met13040786.

Zhang, S., Zhang, X., Liu, W., Lv, X., Bai, C. and Wang, L. (2014). Relationship between structure and viscosity of CaO–SiO2–Al2O3–MgO–TiO2 slag. *Journal of Non-Crystalline Solids*, 402, pp.214–222. doi:https://doi.org/10.1016/j.jnoncrysol.2014.06.006.

CHAPTER 9: CONCLUSIONS AND RECOMMENDATIONS

Global warming and the depletion of natural resources are among the most pressing challenges that the world is currently experiencing, and which can have a drastic impact on the future of human civilization on earth. The impact of climate change on society and the global economy has been intensified by the increase in global GHG emissions, with CO_2 emissions representing more than 80%, and the recent occurrences of extreme weather-related events. Several countries are seeking to achieve net-zero CO_2 emissions by 2050 through the implementation of the 2015 Paris agreement. As a result, emissions taxes are on the rise and environmental regulations have become stricter, putting every carbon-consuming industry under pressure to decarbonize its operations in order to stay relevant and competitive in the global market. This includes the steelmaking and cement industries.

The utilisation of slags to the cement industry as supplementary cementitious materials (SCMs) prevents massive landfilling of waste slags and allows conservation of natural resources. It reduces the proportion of CO_2-intensive clinker used in cement by replacing it with slag, thereby reducing the overall energy requirement of cement production. These are attributes that will promote sustainability, mitigate the impacts of global warming, and allow fulfilment of zero-waste steel production. The current transition towards decarbonized (green) steel production has led to the exploration of the Direct Reduced Iron – Open Bath Furnace (DRI-OBF) technology as a green ironmaking alternative to the conventional Blast Furnace (BF) ironmaking technology.

This dissertation has studied the cementitious properties and evaluated the cementitious performance of the novel OBF slag arising from this green ironmaking process so that it can be used as a low-CO_2 alternative to the conventional BF slag in the making of eco-friendly cement. In addition, the dissertation has proposed ways of extending the campaign life of the OBF refractory as well as enhancing the cementitious performance of the slag in order to mitigate the costs associated with furnace refractory replacement and to further reduce CO_2 emissions.

9.1. Summary of main findings

The cementitious performance has been predicted using the physical and chemical properties of both the novel OBF and the conventional BF slags. It has been shown that the chemical composition, the glass content, the fineness, and the slag substitution ratio are the main parameters that in combination determine the cementitious performance of slag. Fineness is the parameter that has been found to dictate the trends in the cementitious performance of the slags in relation to age of curing, since the other important parameters such as the chemical composition and the glass count, are roughly similar for the four main slag samples in this study (GGOBFS1, GGOBFS2, AMSA, TkSE). While the chemical compositions are roughly similar, there are some differences and more well-defined experimental tests need to be conducted to affirm the individual influence of each factor in isolation on the cementitious performance.

The novel OBF slag has a very similar chemical composition to conventional BF slags. With similar chemical composition, the degree of depolymerization of the OBF slag glass can be assumed to be the same as the degree of depolymerization of the conventional BF slag glass, since the proportions of network formers and network modifiers are the same in the glass structure. Furthermore, the glass count of the GGOBFS2, AMSA, and TkSE samples is 95% while GOBFS1 has a lower glass count of 90%, which may have contributed to its underperformance in comparison to the other slags. Lastly, the trends in fineness have ranked the AMSA and GGOBFS2 slags on the same scale as the best slags, with AMSA being the top-ranked since the GGOBFS2 slag has a wider PSD.

Cementitious application tests have been performed using mortar (slag + cement + water + sand) and paste (slag + cement + water) mixes to assess the predicted cementitious performance of the novel OBF and conventional BF slag.

In mortar tests covering workability, strength development, and drying shrinkage used in this study, the novel OBF slag has displayed similar and comparable results to the conventional BF slag. Slight differences in workability, compressive strength, and drying shrinkage arise when performance-defining properties of the slag such as the fineness and the glass content are not the same. Higher fineness of the slag is beneficial to accelerate the hydration reaction in terms of strength development, but also comes at a cost in terms of high water-demand, or reduced workability if the slag's particle size is very fine. Moreover, from visual examination of cured mortar specimens, the intensity of the greening effect is lower in the novel OBF slag compared to the conventional BF slag due to the relatively lower sulphur content of the novel OBF slag. The following effects occur in mortar mixes upon addition of the slag.

- The workability of the mortar mix increases, and higher slag substitution is equivalent to higher workability.
- The early strength development decreases (< 28 days) while the late strength development is complex to predict and mainly depends upon the reactivity of the slag.
- The rate of strength development in blended slag-cement is mainly governed by the synergy of the hydration of PC, the micro-filling effect of slag, the amount of PC replaced by the slag, and the overall reactivity of the slag (linked to chemical composition, glass content, and fineness).
- The compressive strength increases with increasing slag's fineness and glass content however, more tests should be conducted to confirm these trends since the slag samples in this study have roughly similar but not identical chemical compositions.
- The drying shrinkage decreases, and the decrement level is very minimal and proportional to the amount of PC replaced by the slag.

Chemical reactivity and the evolution of hydration phases are the main tests that were conducted on slag-cement paste mixes. It should be noted that the reported rates of heat evolution are not the same as those which would be observed at standard conditions (25°C) since the R^3 test in this study was conducted at 40°C in order to accelerate the reaction of the slag in the shorter analysis period. Moreover, the R^3 test does not distinguish between hydraulic and pozzolanic reactions, and instead provides an indication of the overall chemical reactivity of the slag-cement paste mix.

The novel OBF slag behaves in a similar manner to the conventional BF slag in terms of heat evolution, highlighting that the reactions occurring during the hydration of these two slags are similar. The rate of heat evolution strongly depends on the reactivity of the slag, which is linked to the chemical composition, fineness and glass content. In this study, changes in heat released by each slag sample seem to have followed the trends in fineness of the slags since the other slag properties assessed, covering chemical composition, were generally similar. Slag with high fineness demonstrates high cumulative heat release and rate of hydration. Furthermore, the results indicate a significant linear correlation between the fineness of the slag and cumulative heat release per gram of solid cementitious binder. The corresponding coefficient of determination is 0.923 and a Pearson correlation coefficient of 0.974, highlighting the strength and positivity of the correlation.

The main phases that form during the hydration of blended slag-cement and pure cement are C-S-H, CH, and C-A-S-H. C-S-H has a fibrous morphology with a poorly crystalline structure, making it undetectable via XRD analysis. CH has gel-like, or blocky morphology with a well-defined crystal structure and detectable by XRD analysis. C-S-A-H has a similar morphology to C-S-H but thicker, also with an amorphous structure undetectable by XRD analysis. The overall microstructure of the paste gets densely packed with increasing curing time as the hydration reactions continue and the excess water evaporates. The hydration of the paste within the first 2-days is strongly influenced by the formation and compositional change of the binders (C-S-H, C-A-S-H, CH), after then it is the synergy of morphological and compositional changes of the binding phases that contribute to the strength development of the specimen. The compositional change has more effect on the late strength development in blended slag-cement mix since the reactivity of the slag only becomes prominent at later ages.

The phases that evolve during the hydration of blended slag-cement with GGOBFS and GGBFS are very similar, the main difference lies in the composition of the C-A-S-H phase. The C-A-S-H in GGBFS has high sulphur-intake, thereby making the phase resemble either ettringite or mono-sulphate, whereas the C-A-S-H in GGOBFS has little sulphur intake, making the composition similar to either hydrotalcite for high MgO spots, or hydrogarnet for low MgO and high Al_2O_3 spots in SEM micrographs. This dissimilarity comes from the fact that GGOBFS has less sulphur compared to GGBFS owing to the lower coke-requirement for the OBF process compared to the conventional BF process.

A comparison of the physical, chemical, and cementitious properties between the novel OBF slag (GGOBFS) and the conventional BF slag (GGBFS) in this dissertation has shown that the two slags have similar characteristics in cementitious applications. The OBF slag could therefore be used as an alternative to BF slag in the cement industry to replace cement clinker in order to lower the industry CO_2 emissions. Considering the combined CO_2 emissions from the cement and steel industries, the OBF slag – through this low emission ironmaking route – has the potential to reduce these emissions to a lower level than is currently possible with conventional granulated blast furnace slag.

9.2. Future outlook of ironmaking and SCMs

The rate of adoption of this new ironmaking technology will influence the phase-out time of the existing BF technology. However, the DRI-OBF ironmaking process is currently not 100% carbon-free, and the path to carbon-neutral steel production hinges around the successful development of green hydrogen production for DRI processes, the usage of renewable electricity in the OBF process, and the incorporation of carbon capture, utilisation and storage (CCUS) technologies.

The application of the OBF technology will result in an increase in the overall production output of direct reduced iron (DRI), and lessen the iron ore quality restriction in DRI processes, thereby increasing the market share of low-grade iron ores which are readily available. From the perspective of carbon-neutrality, the ironmaking and steel technologies that are currently promising and future-proof are the DRI-OBF and the DRI/Scrap-EAF production routes, with the former expected to have a higher market share, similar to the current share of BF technology.

The implementation of the DRI-OBF ironmaking technology can potentially reduce up to 50% of CO_2 emissions per ton of steel in conjunction with the current natural-gas based DRI process, compared to the conventional BF ironmaking. Moreover, the CO_2 emission reduction could reach as high as 90%, depending on sufficient availability of green hydrogen at reasonable prices. Similar to the BF slag, the utilization of the OBF slag in cement can reduce up to 60% of CO_2 emissions per ton of cement and a significant amount of energy associated with clinker production can be saved. Therefore, it is the development of innovative technologies, and the synergy with the cement industry to utilize slags, that can bring the steel industry closer to its goal of zero-waste and carbon-neutral production.

Fly ash and GGBFS are presently the most widely consumed supplementary cementitious materials (SCMs) in the cement industry, to lower CO_2 emissions associated with clinker production. The current quest for green production processes and the transition to carbon neutrality, in accordance with the 2015 Paris agreement, are causing declining interest in coal-fired power plants in favour of renewable electricity, and phase-out of the BF technology from the steelmaking chain with conversion to low-CO_2 alternative ironmaking technologies. Consequently, there will be reduced availability of fly ash and GGBFS in future. The materials that are most likely to emerge and become dominant as SCMs in the future are calcined clays and the novel granulated OBF slag due to their relatively lower CO_2 emissions.

9.3. Recommendations

More well-defined experimental tests should be conducted to confirm the individual effect of chemical composition, glass content and fineness on the cementitious performance since the slag samples in this study have roughly similar but not identical chemical compositions. A narrow PSD with at least 80% passing 40 μm is recommended for ground granulated slag in order to obtain consistent results, as determined for the AMSA slag sample. In addition, the chemical composition must be within the specified range, preferably with a major proportion of network modifiers (CaO and MgO) in order to have a more depolymerized glass structure, which in turn will favour fast hydration of the slag. The slag should have at least 95% glass to counteract the effect of the inert crystalline phases, and the level of prominent impurities,

including TiO_2, should be controlled to less than 2%. The potential negative effect of TiO_2 was, however, not identified in this study.

The early strength development of slag-cement blends can be predicted from the heat of hydration data, provided that the regression line relating these two parameters is generated using slag samples with the same chemical and physical properties (similar chemical composition, glass content, and fineness). Therefore, for future comparisons of novel slags of different chemical compositions, the effects of glass content and fineness must be isolated for accurate determination of differences.

To ensure longer campaign life of the OBF refractory materials, the production of an OBF Gen2 slag composition with an additional furnace unit, known as a slag valorisation furnace (SVF) has been proposed in this dissertation. The OBF Gen2 slag is less corrosive than the normal OBF slag due to the MgO saturation, thereby protecting the MgO-rich OBF refractory. The cementitious valorisation of the OBF Gen2 slag results in the production of SVF slags, which theoretically should display higher cementitious performance than the normal OBF slag due to their highly depolymerized glass structure. However, the benefits of the OBF Gen2 and SVF slags need to be confirmed by conducting cementitious and refractory performance tests. Furthermore, a comparative assessment of the economic and technological benefits between the DRI-OBF and DRI-OBF-SVF process routes is necessary in order to assess the viability of the proposed SVF slags.

If SVF slags are produced in the future, they will also be part of the green SCMs that can be used to save energy associated with cement clinker production and to reduce CO_2 emissions for environmental protection. SVF slags are likely to have a higher cost than OBF slags due to their expected higher cementitious performance. However, the total cost of the SVF process will be dictated by the cost of the inputs, the CAPEX, and the OPEX. The production of a slag with higher CO_2 reduction potential than the BF slag, through the SVF process, will increase the demand for slag from the cement industry. This will enable the DRI-OBF-SVF process to achieve an unprecedented milestone by supplying a slag that can further lower the combined CO_2 emissions from the steel and cement industries compared to the existing positive environmental impact of conventional BF slag. The additional CO_2 emission reduction, compared to the current position with conventional BF slag, will arise mainly from the new ironmaking process.

Therefore, the evaluation of the untapped potential of the slags arising from these emerging technologies in the iron and steel industry is highly recommended. It will benefit both the steelmaking and cement industries, and the world at large, in terms of sustainable environmental protection and the conservation of natural resources through the re-utilisation of wastes as an alternative to large-scale landfilling. Moreover, future optimization test works of the cementitious performance of these novel slags are highly recommended with a focused approached of the detailed effect of fineness, glass content, and chemical composition.

APPENDICES

A. Publications

Three research outputs have been generated from this research project: one conference paper submitted for the 9th International Slag Valorisation Symposium in Belgium 2025 and two journal papers in preparation for submission to the *Journal of Sustainable Metallurgy* (*J. Sustain. Metall.)*. The conference paper has been accepted and an oral presentation will be given on the 11 April 2025 at KU Leuven, Belgium.

The titles of the two journal papers and the full conference manuscript are

Journal paper 1:

Novel open bath furnace (OBF) slag: a low-CO_2 alternative to conventional blast furnace (BF) slag for cementitious applications

Journal paper 2:

Cementitious performance evaluations of mortar made from the novel OBF slag compared with the conventional BF slag

Full conference manuscript:

Valorising a Novel Open Bath Furnace Slag as a Viable Supplementary Cementitious Material

Moise KALENGA[1,2], Ernst KLEYNHANS[1], Stephan LOUW[1], Jeremy GAYLARD[2], Paul DEN HOED[2], Janina KANJEE[3]

[1] Metix (Pty) Ltd (SMS group), Process Engineering, 2196 Johannesburg, South Africa
[2] University of the Witwatersrand, School of Chemical and Metallurgical Engineering, 2050 Johannesburg, South Africa
[3] University of the Witwatersrand, School of Civil and Environmental Engineering, 2050 Johannesburg, South Africa

2948897@students.wits.ac.za, ernst.kleynhans@sms-group.com, stephan.louw@sms-group.com, jeremy.gaylard@wits.ac.za, paul.denhoed@wits.ac.za, janina.kanjee@wits.ac.za

Introduction

Ground granulated blast furnace (GGBF) slag, a by-product of steelmaking, has been widely utilized as a clinker substitute in cement production due to its latent hydraulic properties.[1] The valorisation of blast furnace (BF) slag, along with other supplementary cementitious materials (SCMs) such as fly ash and calcined clay in blended cements, has significantly contributed to reducing the cement industry's carbon dioxide (CO_2) emissions, which currently account for approximately 7% of total global emissions.[2] However, as BF technology, a major source of CO_2 emissions in steelmaking, is being phased out in favour of more eco-friendly and

sustainable technologies, the availability of BF slag is diminishing.[3,4] This study investigates a novel BF-equivalent slag generated through the melting of directly reduced iron (DRI) in an open bath furnace (OBF) powered by renewable energy sources. A DRI process based on natural gas in combination with an OBF can save up to 50% of CO_2 emissions compared with the conventional BF ironmaking.[5] As BF technology is replaced, BF slag will be phased out, necessitating the new OBF slag to effectively serve as a clinker substitute. The cementitious properties of this new OBF slag, however, remain unknown at this stage. Therefore, the assessment of cementitious performance of the novel OBF slag is an essential stage prior to its acceptance as an approved supplementary cementitious material for use in the making of eco-friendly cement.

Materials and procedures

The slag samples for this study were produced in a 1 MW OBF prototype, designed and manufactured by Metix (Pty) Ltd, as part of the testing campaign to mitigate risks associated with the DRI OBF ironmaking technology. The OBF melted the DRI pellets and further reduced the remaining iron oxide with the addition of anthracite. Fluxes were added to modify the chemistry of the OBF slag to a BF slag equivalent. The molten slag leaving the open bath furnace was quenched in a jet of water to generate a granulated product with more than 95% glass content. The granulated OBF slag (GOBFS) was then compared with industrial granulated blast furnace slags from Germany (GBFS1) and South Africa (GGBFS2) in terms of composition, structure (glass content), and cementitious performance, which was evaluated through compressive strength development. In preparation for the cement application tests, GBFS1 and the OBF slag were milled in batches of 1kg in a laboratory ball mill to a similar fineness of the industrially-milled GGBFS2 for comparable assessment. The laboratory milling time for each batch was 5 hours, with particle size distribution measurement used for fineness control. The production set-up for the novel OBF slag is illustrated in **Figure1.**

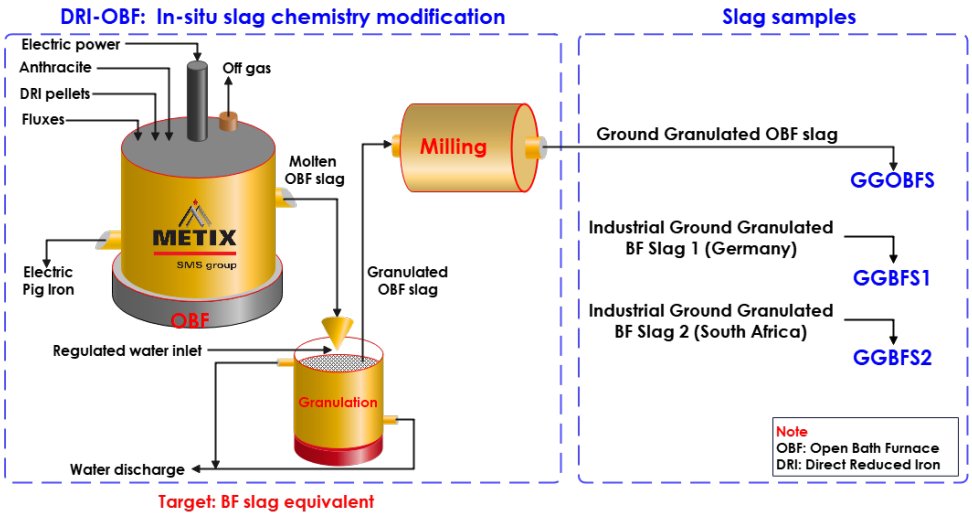


Figure 1: Production set-up for the novel OBF slag with slag sample nomenclature

The fineness of the ground slag was measured by Blaine air permeability which is the industry reference method as per standard specifications.[6,7] The reference cement used for the cementitious test was a CEM I 52.5R cement, with a Blaine fineness of 389m^2/kg.
The Blaine fineness values for the slag samples were as follows: GGOBFS (267 m^2/kg), GGBFS1(258 m^2/kg) and GGBFS2 (296 m^2/kg), respectively.

Mortar casting

The mortar-mix design followed standard specifications in SANS 55167-1:2011, which is similar to BS EN 196-1 standards,[87] with a ratio of cementitious material to standard sand to water of 1:3:0.5. The standardised sand is from Société Nouvelle du Littoral (SNL) in Paris France. Compressive strength tests were performed on mortar cubes of dimensions 50×50×50 mm. The blended slag-cement mixes contained 30% of each slag and were compared to the 100% Portland cement mix. The mortar cubes were cured in the steel casting moulds for 24 hours at 23 ± 2 °C, and then submerged in water after demoulding, until tested for compressive strength at intervals ranging from 2 to 84 days. The mortar cube specimens were subjected to an increasing compressive load until they broke, with the force (measured in kN) applied at a constant loading rate (40 kN/min). The compressive strength of 4 specimens was determined at each aging interval for every mix, and the average value was considered as the compressive strength for that age. The chemical composition of the slag samples was determined by ICP-OES while the total sulphur was determined using a LECO Infrared Combustion Analyzer, and the glass content was quantified using an optical microscopy technique. The results are summarized in Table 1.

Table 1: Chemical composition and glass content of slag samples

Components (wt%)	Al_2O_3	CaO	SiO_2	MgO	TiO_2	FeO	S	Total	Glass content
GGOBFS	10.43	43.10	36.00	7.56	1.40	0.32	0.19	99.00	95 %
GGBFS1	11.14	42.76	37.07	6.07	0.54	0.28	1.14	99.00	95 %
GGBFS2	16.60	35.65	35.13	9.07	0.81	0.50	1.31	99.06	95 %

Mortar strength development

The strength gain results for the 100% PC (CEM I 52.5R) mix and the 30% slag substitution mixes are shown in Figure 2.

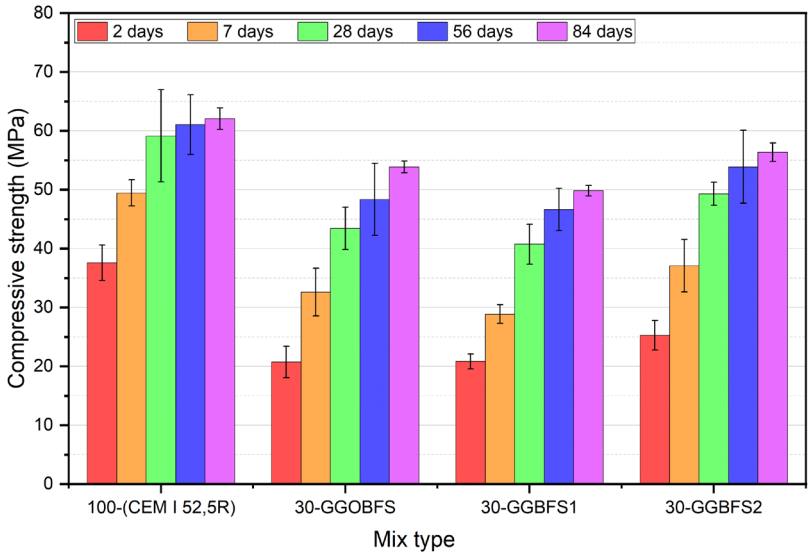


Figure 2: Compressive strength results up to 84 days (at 95% confidence level)

The hydration of the 100% PC mortar mix is rapid, achieving a strength of 50 MPa after 7 days of curing. For the slag cement mixes, the novel OBF slag, GGOBFS, exhibited similar strength development to the reference slags, GGBFS1 and GGBFS2. At 2 days, GGOBFS had the same strength, 21 MPa, as GGBFS1, and its strength gains at 7 and 28 days were almost identical to GGBFS2. However, GGBFS2 had the highest 2-day strength of 25 MPa compared to that of GGOBFS at 21 MPa. It has been previously noted[8] that during blast furnace slag-cement hydration, three processes contribute to strength development: the hydration of PC, the reactivity of the slag, and the packing effect of small particles. This supports the observed strength performance of GGBFS2 since it has the highest fineness, followed by GGOBFS, and GGBFS1. The early strength development (2-7 days) of the slag-cement mix is primarily influenced by the hydration of PC and the fineness of the slag, as other slag properties (e.g. chemical composition, glass content) are similar, as shown in Table 1. BF slag possesses inherent hydraulic properties that are activated by the generated portlandite, $Ca(OH)_2$ from the hydration of PC.[1] The reactivity of the slag starts significantly to influence the strength gain after 7 days, once enough portlandite has been generated. In addition, the intensity of the greening effect, which is a temporary greenish blue coloration commonly observed on the outer surface of blended slag-cement specimens owing to the progressive oxidation of polysulphide complexes, [9] was observed to be less in the novel OBF slag-cement mixes due to the lower sulphur content in the novel OBF slag compared to conventional BF slags.

Conclusions

This study has demonstrated the potential of the novel OBF slag as a viable SCM. In terms of cementitious performance assessed following curing at several ages, up to 84 days, the novel OBF slag (GGOBFS) displayed similar strength development trends to the conventional BF slags (GGBFS1, GGBFS2), highlighting their similarities in terms of strength development. While similar in chemical composition to conventional BF slag, the novel OBF slag contains less sulphur, leading to less intensity of the greening effect in cured OBF slag-cement

specimens. On the basis of the reported test results, the OBF slag can be used as a suitable lower-CO_2 alternative to the BF slag currently utilised in the cement industry. This will result in mitigation of CO_2 emissions from both the steelmaking and the cement industries in the current race towards meeting global climate targets.

References

P.C. Hewlett and M. Liska (eds), *Lea's Chemistry of Cement and Concrete*, 5th edition, Butterworth-Heinemann, Oxford, UK (2019).

M. Schneider, "The cement industry on the way to a low-carbon future", *Cem. Concr. Res.* **124**: 105792 (2019).

A. Ehrenberg, "Today's and future slags—Potentials and challenges". *ce/papers*, **6**(6): 241−256 (2023).

O. Olsson, V. Vogl and B. Nykvist, "Phasing out the blast furnace to meet global climate targets", *Joule* **5**(10): 2646−2662 (2021).

Midrex Technologies. *MIDREX® Process*. [online] Midrex Technologies, Inc. Available at https://www.midrex.com/technology/midrex-process/ [Accessed 26 Dec. 2024] (2024).

BS EN 196-6. Methods of testing cement Determination of fineness. European Committee for Standardization. British Standards Institution, London (2018).

SANS 55167-1. Ground granulated blast furnace slag for use in concrete, mortar and grout Part 1: Definitions, specifications and conformity criteria (2011).

P. Norrarat, W. Tangchirapat, S. Songpiriyakijand, C. Jaturapitakkul, "Evaluation of Strengths from Cement Hydration and Slag Reaction of Mortars Containing High Volume of Ground River Sand and GGBF Slag", *Advances in civil engineering*, **2019**: 1–12 (2019).

J. Couvidat, C. Diliberto, E. Meux, S. Cotelle, C. Bojic, L. Izoret and A. Lecomte, "Greening effect of slag cement-based concrete: Environmental and ecotoxicological impact", *Environmental Technology & Innovation*, **22**: 101467 (2021).

B. Experimental data

The experimental data are provided in the following tables for reference:

Table 36: PSD data of non-ground granulated slags

Sample ID	Screen size (µm)	6700	3350	2360	1700	422	212	106	75	-75	Total
GOBFS1	Mass (g)	0,00	81,00	109,00	214,00	847,00	45,00	7,00	1,00	3,00	1307,00
	Mass (%)	0,00	6,20	8,34	16,37	64,80	3,44	0,54	0,08	0,23	
	Cumulative retained (%)	0,00	6,20	14,54	30,91	95,72	99,16	99,69	99,77	100,00	
	Cumulative passing (%)	100,00	93,80	85,46	69,09	4,28	0,84	0,31	0,23	0,00	
GOBFS2	Mass (g)	0,00	37,00	143,00	324,00	1258,00	107,00	18,00	4,00	5,00	1896,00
	Mass (%)	0,00	1,95	7,54	17,09	66,35	5,64	0,95	0,21	0,26	
	Cumulative retained (%)	0,00	1,95	9,49	26,58	92,93	98,58	99,53	99,74	100,00	
	Cumulative passing (%)	100,00	98,05	90,51	73,42	7,07	1,42	0,47	0,26	0,00	
ArcelorMittal	Mass (g)	0,00	19,00	98,00	283,00	3187,00	554,00	175,00	57,00	86,00	4459,00
	Mass (%)	0,00	0,43	2,20	6,35	71,47	12,42	3,92	1,28	1,93	
	Cumulative retained (%)	0,00	0,43	2,62	8,97	80,44	92,87	96,79	98,07	100,00	
	Cumulative passing (%)	100,00	99,57	97,38	91,03	19,56	7,13	3,21	1,93	0,00	
ThyssenKrupp	Mass (g)	0,00	3,00	2,00	202,00	2534,00	340,00	143,00	21,00	43,00	3288,00
	Mass (%)	0,00	0,09	0,06	6,14	77,07	10,34	4,35	0,64	1,31	
	Cumulative retained (%)	0,00	0,09	0,15	6,30	83,36	93,70	98,05	98,69	100,00	
	Cumulative passing (%)	100,00	99,91	99,85	93,70	16,64	6,30	1,95	1,31	0,00	

Table 37: Effect of ball charge composition

Ball load seasoning (fine and coarse grind balance) & charge load variation													
Change	Speed	Run	Feed	Screen size (µm)	212	180	125	90	75	63	45	-45	Total
1	28 rpm	BM 2	Tap 122 wet	Mass (g)	38,00	3,17	11,08	16,09	4,01	14,22	7,38	4,16	98,11
				Mass (%)	38,73	3,23	11,29	16,40	4,09	14,49	7,52	4,24	
				Cumulative retained (%	38,73	41,96	53,26	69,66	73,74	88,24	95,76	100,00	
				Cumulative passing (%)	61,27	58,04	46,74	30,34	26,26	11,76	4,24	0,00	
2	28 rpm	BM 3	Tap 122 dried (1h)	Mass (g)	48,00	4,01	12,52	10,76	3,70	10,30	6,79	3,76	99,84
				Mass (%)	48,08	4,02	12,54	10,78	3,71	10,32	6,80	3,77	
				Cumulative retained (%	48,08	52,09	64,63	75,41	79,12	89,43	96,23	100,00	
				Cumulative passing (%)	51,92	47,91	35,37	24,59	20,88	10,57	3,77	0,00	
		BM 4	Tap 122 continue d 1 (2h)	Mass (g)	32,80	6,87	14,39	15,66	6,33	11,98	6,34	4,20	98,57
				Mass (%)	33,28	6,97	14,60	15,89	6,42	12,15	6,43	4,26	
				Cumulative retained (%	33,28	40,25	54,84	70,73	77,15	89,31	95,74	100,00	
				Cumulative passing (%)	66,72	59,75	45,16	29,27	22,85	10,69	4,26	0,00	
		BM 5	Tap 122 continue d 2 (3h)	Mass (g)	19,79	6,05	15,60	18,80	8,54	20,66	7,84	2,54	99,82
				Mass (%)	19,83	6,06	15,63	18,83	8,56	20,70	7,85	2,54	
				Cumulative retained (%	19,83	25,89	41,51	60,35	68,90	89,60	97,46	100,00	
				Cumulative passing (%)	80,17	74,11	58,49	39,65	31,10	10,40	2,54	0,00	
3	28 rpm	BM 6	Tap 123 (1h)	Mass (g)	19,46	8,15	18,47	18,95	5,32	17,12	13,92	5,48	106,87
				Mass (%)	18,21	7,63	17,28	17,73	4,98	16,02	13,03	5,13	
				Cumulative retained (%	18,21	25,84	43,12	60,85	65,83	81,85	94,87	100,00	
				Cumulative passing (%)	81,79	74,16	56,88	39,15	34,17	18,15	5,13	0,00	
		BM 7	Tap 123 continue d 1 (2h)	Mass (g)	0,59	0,29	3,28	22,96	12,56	24,45	24,50	18,34	106,97
				Mass (%)	0,55	0,27	3,07	21,46	11,74	22,86	22,90	17,14	
				Cumulative retained (%	0,55	0,82	3,89	25,35	37,09	59,95	82,86	100,00	
				Cumulative passing (%)	99,45	99,18	96,11	74,65	62,91	40,05	17,14	0,00	
		BM 8	Tap 123 continue d 2 (3h)	Mass (g)	0,18	0,54	1,04	16,28	11,32	24,88	42,65	25,39	122,28
				Mass (%)	0,15	0,44	0,85	13,31	9,26	20,35	34,88	20,76	
				Cumulative retained (%	0,15	0,59	1,44	14,75	24,01	44,36	79,24	100,00	
				Cumulative passing (%)	99,85	99,41	98,56	85,25	75,99	55,64	20,76	0,00	
		SM 1	Tap 123 (1h BM + 1h SM)	Mass (g)	1,29	0,49	3,19	10,32	9,99	25,27	31,39	33,76	115,70
				Mass (%)	1,11	0,42	2,76	8,92	8,63	21,84	27,13	29,18	
				Cumulative retained (%	1,11	1,54	4,30	13,22	21,85	43,69	70,82	100,00	
				Cumulative passing (%)	98,89	98,46	95,70	86,78	78,15	56,31	29,18	0,00	
		SM 2	Tap 123 (1h BM + 2h SM)	Mass (g)	1,07	0,87	9,69	12,26	30,46	19,43	32,06	26,65	132,49
				Mass (%)	0,81	0,66	7,31	9,25	22,99	14,67	24,20	20,11	
				Cumulative retained (%	0,81	1,46	8,78	18,03	41,02	55,69	79,89	100,00	
				Cumulative passing (%)	99,19	98,54	91,22	81,97	58,98	44,31	20,11	0,00	

Table 38: Effect of milling time

Milling time extension (3h to 4h to 5h)													
4	28 rpm	BM 9	Tap 121 (2h)	Mass (g)	6,95	6,12	17,90	21,52	8,68	20,98	18,08	15,89	116,12
				Mass (%)	5,99	5,27	15,42	18,53	7,48	18,07	15,57	13,68	
				Cumulative retained (%	5,99	11,26	26,67	45,20	52,68	70,75	86,32	100,00	
				Cumulative passing (%)	94,01	88,74	73,33	54,80	47,32	29,25	13,68	0,00	
		BM 10	Tap 121 (3h)	Mass (g)	0,75	0,42	1,69	17,48	16,14	31,76	41,75	23,61	133,60
				Mass (%)	0,56	0,31	1,26	13,08	12,08	23,77	31,25	17,67	
				Cumulative retained (%	0,56	0,88	2,14	15,22	27,31	51,08	82,33	100,00	
				Cumulative passing (%)	99,44	99,12	97,86	84,78	72,69	48,92	17,67	0,00	
		BM 11	Tap 121 (4h)	Mass (g)	0,45	0,21	1,21	1,36	2,05	18,33	44,31	52,82	120,74
				Mass (%)	0,37	0,17	1,00	1,13	1,70	15,18	36,70	43,75	
				Cumulative retained (%	0,37	0,55	1,55	2,68	4,37	19,55	56,25	100,00	
				Cumulative passing (%)	99,63	99,45	98,45	97,32	95,63	80,45	43,75	0,00	
		SM 3	Tap 121 (2h BM + 1h SM)	Mass (g)	0,78	0,28	3,12	12,14	10,44	29,78	44,01	31,31	131,86
				Mass (%)	0,59	0,21	2,37	9,21	7,92	22,58	33,38	23,74	
				Cumulative retained (%	0,59	0,80	3,17	12,38	20,29	42,88	76,26	100,00	
				Cumulative passing (%)	99,41	99,20	96,83	87,62	79,71	57,12	23,74	0,00	
		SM 4	Tap 121 (2h BM + 2h SM)	Mass (g)	0,31	0,33	1,11	2,22	14,19	19,98	35,09	43,61	116,84
				Mass (%)	0,27	0,28	0,95	1,90	12,14	17,10	30,03	37,32	
				Cumulative retained (%	0,27	0,55	1,50	3,40	15,54	32,64	62,68	100,00	
				Cumulative passing (%)	99,73	99,45	98,50	96,60	84,46	67,36	37,32	0,00	
5	28 rpm	BM 12	Tap 118 (3h)	Mass (g)	0,27	0,17	1,48	4,36	2,49	9,74	14,20	6,11	38,82
				Mass (%)	0,70	0,44	3,81	11,23	6,41	25,09	36,58	15,74	
				Cumulative retained (%	0,70	1,13	4,95	16,18	22,59	47,68	84,26	100,00	
				Cumulative passing (%)	99,30	98,87	95,05	83,82	77,41	52,32	15,74	0,00	
		BM 13	Tap 118 (5h)	Mass (g)	0,04	0,01	0,02	0,12	2,18	3,36	4,55	9,71	19,99
				Mass (%)	0,20	0,05	0,10	0,60	10,91	16,81	22,76	48,57	
				Cumulative retained (%	0,20	0,25	0,35	0,95	11,86	28,66	51,43	100,00	
				Cumulative passing (%)	99,80	99,75	99,65	99,05	88,14	71,34	48,57	0,00	
		SM 5	Tap 118 (3h BM + 2h SM)	Mass (g)	0,27	0,07	0,06	0,10	2,12	0,54	3,02	14,55	20,73
				Mass (%)	1,30	0,34	0,29	0,48	10,23	2,60	14,57	70,19	
				Cumulative retained (%	1,30	1,64	1,93	2,41	12,64	15,24	29,81	100,00	
				Cumulative passing (%)	98,70	98,36	98,07	97,59	87,36	84,76	70,19	0,00	

Table 39: Effect of speed

Speed variation tests													
6	48 rpm	BM 14	Tap 116 (2h)	Mass (g)	0,12	0,06	0,09	0,69	1,82	2,46	3,35	12,67	21,26
				Mass (%)	0,56	0,28	0,42	3,25	8,56	11,57	15,76	59,60	
				Cumulative retained (%	0,56	0,85	1,27	4,52	13,08	24,65	40,40	100,00	
				Cumulative passing (%)	99,44	99,15	98,73	95,48	86,92	75,35	59,60	0,00	
		BM 15	Tap 116 (3h)	Mass (g)	0,04	0,01	0,03	0,29	1,11	1,91	2,09	16,67	22,15
				Mass (%)	0,18	0,05	0,14	1,31	5,01	8,62	9,44	75,26	
				Cumulative retained (%	0,18	0,23	0,36	1,67	6,68	15,30	24,74	100,00	
				Cumulative passing (%)	99,82	99,77	99,64	98,33	93,32	84,70	75,26	0,00	
		BM 16	Tap 116 (4h)	Mass (g)	0,00	0,00	0,00	0,02	0,08	0,35	2,28	19,73	22,46
				Mass (%)	0,00	0,00	0,00	0,09	0,36	1,56	10,15	87,85	
				Cumulative retained (%	0,00	0,00	0,00	0,09	0,45	2,00	12,15	100,00	
				Cumulative passing (%)	100,00	100,00	100,00	99,91	99,55	98,00	87,85	0,00	
		SM 6	Tap 116 (3h BM + 1h SM)	Mass (g)	0,00	0,00	0,00	0,01	0,05	0,08	2,21	25,03	27,38
				Mass (%)	0,00	0,00	0,00	0,04	0,18	0,29	8,07	91,42	
				Cumulative retained (%	0,00	0,00	0,00	0,04	0,22	0,51	8,58	100,00	
				Cumulative passing (%)	100,00	100,00	100,00	99,96	99,78	99,49	91,42	0,00	
7	68 rpm	1BM 17	Tap 116 (2h)	Mass (g)	0,00	0,01	0,02	0,48	1,09	1,95	3,34	15,47	22,36
				Mass (%)	0,00	0,04	0,09	2,15	4,87	8,72	14,94	69,19	
				Cumulative retained (%	0,00	0,04	0,13	2,28	7,16	15,88	30,81	100,00	
				Cumulative passing (%)	100,00	99,96	99,87	97,72	92,84	84,12	69,19	0,00	
		1BM 18	Tap 116 (3h)	Mass (g)	0,00	0,00	0,00	0,12	0,16	0,34	2,69	17,42	20,73
				Mass (%)	0,00	0,00	0,00	0,58	0,77	1,64	12,98	84,03	
				Cumulative retained (%	0,00	0,00	0,00	0,58	1,35	2,99	15,97	100,00	
				Cumulative passing (%)	100,00	100,00	100,00	99,42	98,65	97,01	84,03	0,00	
		1BM 19	Tap 116 (4h)	Mass (g)	0,00	0,00	0,00	0,09	0,13	0,34	1,03	20,72	22,31
				Mass (%)	0,00	0,00	0,00	0,40	0,58	1,52	4,62	92,87	
				Cumulative retained (%	0,00	0,00	0,00	0,40	0,99	2,51	7,13	100,00	
				Cumulative passing (%)	100,00	100,00	100,00	99,60	99,01	97,49	92,87	0,00	
		2BM 1	Tap 116 (2h 1BM + 1h 2BM)	Mass (g)	0,00	0,00	0,00	0,15	0,22	0,41	1,85	18,84	21,47
				Mass (%)	0,00	0,00	0,00	0,70	1,02	1,91	8,62	87,75	
				Cumulative retained (%	0,00	0,00	0,00	0,70	1,72	3,63	12,25	100,00	
				Cumulative passing (%)	100,00	100,00	100,00	99,30	98,28	96,37	87,75	0,00	
		2BM 2	Tap 116 (2h 1BM + 2h 2BM)	Mass (g)	0,00	0,00	0,00	0,10	0,03	0,33	0,73	28,50	29,69
				Mass (%)	0,00	0,00	0,00	0,34	0,10	1,11	2,46	95,99	
				Cumulative retained (%	0,00	0,00	0,00	0,34	0,44	1,55	4,01	100,00	
				Cumulative passing (%)	100,00	100,00	100,00	99,66	99,56	98,45	95,99	0,00	

Table 40: Additional tests for statistics

New additional speed tests for statistical optimization purposes													
change	Speed	Run	Feed	Screen size (µm)	212	180	125	90	75	63	45	-45	Total
8	74 rpm	BM 20	Tap 117 (60 mins)	Mass (g)				3,38	1,77	2,09	3,33	7,65	18,22
				Mass (%)				18,55	9,71	11,47	18,28	41,99	
				Cumulative retained (%)				18,55	28,27	39,74	58,01	100,00	
				Cumulative passing (%)				81,45	71,73	60,26	41,99	0,00	
		BM 21	Tap 117 (120 mins)	Mass (g)				0,37	0,39	2,32	4,64	11,21	18,93
				Mass (%)				1,95	2,06	12,26	24,51	59,22	
				Cumulative retained (%)				1,95	4,01	16,27	40,78	100,00	
				Cumulative passing (%)				98,05	95,99	83,73	59,22	0,00	
		BM 22	Tap 117 (150 mins)	Mass (g)				0,10	0,26	1,62	4,46	8,48	14,92
				Mass (%)				0,67	1,74	10,86	29,89	56,84	
				Cumulative retained (%)				0,67	2,41	13,27	43,16	100,00	
				Cumulative passing (%)				99,33	97,59	86,73	56,84	0,00	
		BM 23	Tap 117 (180 mins)	Mass (g)				0,02	0,04	0,44	1,54	7,91	9,95
				Mass (%)				0,20	0,40	4,42	15,48	79,50	
				Cumulative retained (%)				0,20	0,60	5,03	20,50	100,00	
				Cumulative passing (%)				99,80	99,40	94,97	79,50	0,00	
		BM 24	Tap 117 (240 mins)	Mass (g)				0,01	0,05	0,10	0,57	6,19	6,92
				Mass (%)				0,14	0,72	1,45	8,24	89,45	
				Cumulative retained (%)				0,14	0,87	2,31	10,55	100,00	
				Cumulative passing (%)				99,86	99,13	97,69	89,45	0,00	
9	38 rpm	BM 25	Tap 120 (60 mins)	Mass (g)				6,28	0,70	0,75	1,31	2,28	11,32
				Mass (%)				55,48	6,18	6,63	11,57	20,14	
				Cumulative retained (%)				55,48	61,66	68,29	79,86	100,00	
				Cumulative passing (%)				44,52	38,34	31,71	20,14	0,00	
		BM 26	Tap 120 (120 mins)	Mass (g)				2,31	0,78	1,63	1,53	3,28	9,53
				Mass (%)				24,24	8,18	17,10	16,05	34,42	
				Cumulative retained (%)				24,24	32,42	49,53	65,58	100,00	
				Cumulative passing (%)				75,76	67,58	50,47	34,42	0,00	
		BM 27	Tap 120 (150 mins)	Mass (g)				1,05	0,16	1,61	1,61	2,40	6,83
				Mass (%)				15,37	2,34	23,57	23,57	35,14	
				Cumulative retained (%)				15,37	17,72	41,29	64,86	100,00	
				Cumulative passing (%)				84,63	82,28	58,71	35,14	0,00	
		BM 28	Tap 120 (180 mins)	Mass (g)				0,29	0,29	1,12	2,16	1,99	5,85
				Mass (%)				4,96	4,96	19,15	36,92	34,02	
				Cumulative retained (%)				4,96	9,91	29,06	65,98	100,00	
				Cumulative passing (%)				95,04	90,09	70,94	34,02	0,00	
		BM 29	Tap 120 (240 mins)	Mass (g)				0,22	0,21	1,08	1,39	3,85	6,75
				Mass (%)				3,26	3,11	16,00	20,59	57,04	
				Cumulative retained (%)				3,26	6,37	22,37	42,96	100,00	
				Cumulative passing (%)				96,74	93,63	77,63	57,04	0,00	

Table 41: Effect of milling time-continuation

60 mins & 150 mins tests													
10	28 rpm	BM 30	Tap 123 (60 mins)	Mass (g)				18,11	1,40	3,26	3,11	4,40	30,28
				Mass (%)				59,81	4,62	10,77	10,27	14,53	
				Cumulative retained (%)				59,81	64,43	75,20	85,47	100,00	
				Cumulative passing (%)				40,19	35,57	24,80	14,53	0,00	
		BM 31	Tap 123 (150 mins)	Mass (g)				4,71	1,89	4,15	7,11	4,23	22,09
				Mass (%)				21,32	8,56	18,79	32,19	19,15	
				Cumulative retained (%)				21,32	29,88	48,66	80,85	100,00	
				Cumulative passing (%)				78,68	70,12	51,34	19,15	0,00	
11	48 rpm	BM 32	Tap 123 (60)	Mass (g)				5,08	1,72	3,59	3,37	7,22	20,98
				Mass (%)				24,21	8,20	17,11	16,06	34,41	
				Cumulative retained (%)				24,21	32,41	49,52	65,59	100,00	
				Cumulative passing (%)				75,79	67,59	50,48	34,41	0,00	
		BM 33	Tap 123 (150 mins)	Mass (g)				0,47	1,07	1,98	3,37	15,56	22,45
				Mass (%)				2,09	4,77	8,82	15,01	69,31	
				Cumulative retained (%)				2,09	6,86	15,68	30,69	100,00	
				Cumulative passing (%)				97,91	93,14	84,32	69,31	0,00	
12	68 rpm	BM 34	Tap 123 (60 mins)	Mass (g)				0,83	2,18	2,95	4,02	15,21	25,19
				Mass (%)				3,29	8,65	11,71	15,96	60,38	
				Cumulative retained (%)				3,29	11,95	23,66	39,62	100,00	
				Cumulative passing (%)				96,71	88,05	76,34	60,38	0,00	
		BM 35	Tap 123 (150 mins)	Mass (g)				0,38	0,96	0,74	3,69	17,42	23,19
				Mass (%)				1,64	4,14	3,19	15,91	75,12	
				Cumulative retained (%)				1,64	5,78	8,97	24,88	100,00	
				Cumulative passing (%)				98,36	94,22	91,03	75,12	0,00	

Table 42: Data used for Response Surface Methodology optimization

Std Order	Speed (rpm)	time (min)	% Cumulative passing 90 µm	% Cumulative passing 75 µm	% Cumulative passing 45 µm
1	28	60	70,53	54,65	6,77
2	28	120	74,65	62,91	17,14
3	28	150	86,51	77,10	21,06
4	28	180	85,25	75,99	20,76
5	28	240	97,32	95,63	43,75
6	38	60	44,52	38,34	20,14
7	38	120	75,76	67,58	34,42
8	38	150	84,63	82,28	35,14
9	38	180	95,04	90,09	34,02
10	38	240	96,74	93,63	57,04
11	48	60	75,79	67,59	34,41
12	48	120	95,48	86,92	59,60
13	48	150	97,91	93,14	69,31
14	48	180	98,33	93,32	75,26
15	48	240	99,91	99,55	87,85
16	68	60	96,71	88,05	60,38
17	68	120	97,72	92,84	69,19
18	68	150	98,36	94,22	75,12
19	68	180	99,42	98,65	84,03
20	68	240	99,60	99,01	92,87
21	74	60	81,45	71,73	41,99
22	74	120	98,05	95,99	59,22
23	74	150	99,33	97,59	56,84
24	74	180	99,80	99,40	79,50
25	74	240	99,86	99,13	89,45

Table 43: PSD data of ground granulated slag samples

Size (μm)	PC (%passing)		GGOBFS1 (%)		GGOBFS2 (%)		TKSE (%)		AMSA (%)	
	Normal	Cumulative	Normal	Cumulative	Normal	Cumulative	Normal	Cumulative	Normal	Cumulative
1,096	0	0	0	0	0	0	0	0	0	0
1,259	0	0	0	0	0	0	0	0	0	0
1,445	0	0	0	0	0,01	0,01	0	0	0,01	0,01
1,66	0	0	0	0	0,16	0,17	0	0	0,17	0,18
1,905	0,06	0,06	0,28	0,28	0,49	0,66	0,2	0,2	0,4	0,58
2,188	0,2	0,26	0,54	0,82	0,89	1,55	0,39	0,59	0,65	1,23
2,512	0,39	0,65	0,81	1,63	1,33	2,88	0,58	1,17	0,9	2,13
2,884	0,58	1,23	1,1	2,73	1,78	4,66	0,77	1,94	1,14	3,27
3,311	0,8	2,03	1,37	4,1	2,21	6,87	0,95	2,89	1,37	4,64
3,802	1,07	3,1	1,64	5,74	2,63	9,5	1,13	4,02	1,58	6,22
4,365	1,42	4,52	1,89	7,63	3,02	12,52	1,3	5,32	1,8	8,02
5,012	1,87	6,39	2,14	9,77	3,38	15,9	1,49	6,81	2,04	10,06
5,754	2,46	8,85	2,38	12,15	3,74	19,64	1,7	8,51	2,3	12,36
6,607	3,19	12,04	2,62	14,77	4,07	23,71	1,94	10,45	2,59	14,95
7,86	4,06	16,1	2,85	17,62	4,38	28,09	2,21	12,66	2,94	17,89
8,71	5,07	21,17	3,08	20,7	4,66	32,75	2,52	15,18	3,32	21,21
10	6,14	27,31	3,32	24,02	4,92	37,67	2,88	18,06	3,75	24,96
11,482	7,17	34,48	3,56	27,58	5,13	42,8	3,29	21,35	4,19	29,15
13,183	8,07	42,55	3,83	31,41	5,29	48,09	3,73	25,08	4,65	33,8
15,136	8,71	51,26	4,11	35,52	5,39	53,48	4,2	29,28	5,07	38,87
17,378	8,97	60,23	4,42	39,94	5,41	58,89	4,68	33,96	5,43	44,3
19,953	8,79	69,02	4,74	44,68	5,34	64,23	5,14	39,1	5,69	49,99
22,909	8,13	77,15	5,07	49,75	5,18	69,41	5,56	44,66	5,82	55,81
26,303	7,07	84,22	5,38	55,13	4,93	74,34	5,91	50,57	5,8	61,61
30,2	5,72	89,94	5,64	60,77	4,58	78,92	6,14	56,71	5,62	67,23
34,574	4,26	94,2	5,8	66,57	4,16	83,08	6,24	62,95	5,28	72,51
39,811	2,88	97,08	5,81	72,38	3,68	86,76	6,17	69,12	4,82	77,33
45,709	1,71	98,79	5,65	78,03	3,15	89,91	5,93	75,05	4,28	81,61
52,481	0,86	99,65	5,29	83,32	2,6	92,51	5,51	80,56	3,7	85,31
60,256	0,33	99,98	4,73	88,05	2,04	94,55	4,93	85,49	3,12	88,43
69,183	0,02	100	4,02	92,07	1,5	96,05	4,22	89,71	2,6	91,03
79,433	0	100	3,21	95,28	0,97	97,02	3,43	93,14	2,13	93,16
91,201	0	100	2,37	97,65	0,5	97,52	2,63	95,77	1,74	94,9
104,713	0	100	1,61	99,26	0,21	97,73	1,85	97,62	1,41	96,31
120,226	0	100	0,61	99,87	0,09	97,82	1,15	98,77	1,14	97,45
138,038	0	100	0,11	99,98	0,01	97,83	0,55	99,32	0,89	98,34
158,489	0	100	0,02	100	0	97,83	0,18	99,5	0,67	99,01
181,97	0	100	0	100	0	97,83	0,07	99,57	0,47	99,48
208,93	0	100	0	100	0	97,83	0,03	99,6	0,3	99,78
239,883	0	100	0	100	0,04	97,87	0,02	99,62	0,17	99,95
275,423	0	100	0	100	0,13	98	0,03	99,65	0,05	100
316,228	0	100	0	100	0,24	98,24	0,06	99,71	0	100
363,078	0	100	0	100	0,32	98,56	0,07	99,78	0	100
416,869	0	100	0	100	0,36	98,92	0,08	99,86	0	100
478,63	0	100	0	100	0,36	99,28	0,07	99,93	0	100
549,641	0	100	0	100	0,31	99,59	0,05	99,98	0	100
630,957	0	100	0	100	0,23	99,82	0,02	100	0	100
724,36	0	100	0	100	0,13	99,95	0	100	0	100
831,764	0	100	0	100	0,05	100	0	100	0	100
954,993	0	100	0	100	0	100	0	100	0	100

Table 44: Blaine fineness data

Label	Material type	SSA (m^2/kg)	RD (g/cm^3)
PC	AfriSam CEM I 52.5 R	389,3	3,05
AMSA	ArcelorMittal - Slag	296	2,88
TkSE	Thyssenkrupp - Slag	258,2	2,91
GGOBFS1	Metix 1 - Slag	254,7	2,96
GGOBFS2	Metix 2 - Slag	266,7	2,95

Table 45: BET surface area data

Sample ID	Surface area [m^2/g]	Uncertainty [m^2/g]	Sample mass [g]
PC	1.8154	0.0095	0.2294
TKSE	0.395	0.017	0.224
AMSA	0.571	0.016	0.2106
GGOBFS1	0.529	0.019	0.2358
GGOBFS2	0.537	0.025	0.2136

Table 46: Workability data

Mix ID	Cement blend (grams)			Sand	Water	Measured diameters (mm)						Mould diameter (mm)	Change(%)	Relative to PC	
	PC	Slag	Total			1	2	3	4	Average	Std				error %
100 PC	165	0	165	495	83	193	192	192	194	192,75	0,96	100	92,75	100,00	0,50
85/15 PC/MS1	140	25	165	495	83	191	195	197	196	194,75	2,63	100	94,75	102,16	1,35
85/15 PC/MS2	140	25	165	495	83	193	194	196	195	194,50	1,29	100	94,50	101,89	0,66
85/15 PC/TS	140	25	165	495	83	196	191	195	197	194,75	2,63	100	94,75	102,16	1,35
85/15 PC/AS	140	25	165	495	83	194	190	194	195	193,25	2,22	100	93,25	100,54	1,15
70/30 PC/MS1	116	50	165	495	83	194	195	198	197	196,00	1,83	100	96,00	103,50	0,93
70/30 PC/MS2	116	50	165	495	83	198	196	196	193	195,75	2,06	100	95,75	103,23	1,05
70/30 PC/TS	116	50	165	495	83	196	194	198	197	196,25	1,71	100	96,25	103,77	0,87
70/30 PC/AS	116	50	165	495	83	194	195	197	195	195,25	1,26	100	95,25	102,70	0,64
50/50 PC/MS1	83	83	165	495	83	206	197	201	209	203,25	5,32	100	103,25	111,32	2,62
50/50 PC/MS2	83	83	165	495	83	204	201	203	198	201,50	2,65	100	101,50	109,43	1,31
50/50 PC/TS	83	83	165	495	83	202	207	204	203	204,00	2,16	100	104,00	112,13	1,06
50/50 PC/AS	83	83	165	495	83	201	199	198	196	198,50	2,08	100	98,50	106,20	1,05
Total	**1188**	**297**	**1485**	**4455**	**742,5**										

Table 47: Compressive strength data 1

	2 Days										
ID	Sample	1	2	3	4	AVG. (kN)	AVG. (MPa)	STD. Dev	Confidence interval (95%)		2 Std
100-PC	M1	94,2	92,4	95,4	0,0	94,0	37,6	1,5	40,2	35,0	3,0
15-M1	M6	68,6	68,2	67,6	65,8	68,1	27,3	0,5	28,1	26,4	1,0
15-M2	M7	72,8	74,4	72,3	78,6	73,2	29,3	1,1	31,2	27,4	2,2
15-TK	M8	69,6	66,4	72,4	58,6	69,5	27,8	3,0	33,0	22,6	6,0
15-AM	M9	76,8	74,2	75,2	78,6	75,4	30,2	1,3	32,4	27,9	2,6
30-M1	M10	55,4	58,2	56,4	53,4	56,7	22,7	1,4	25,1	20,2	2,8
30-M2	M11	51,2	53,4	51,0	54,8	51,9	20,7	1,3	23,1	18,4	2,7
30-TK	M12	51,6	52,8	51,8	54,6	52,1	20,8	0,6	21,9	19,7	1,3
30-AM	M13	63,6	61,8	64,2	61,2	63,2	25,3	1,2	27,4	23,1	2,5
50-M1	M2	38,2	42,4	38,8	0,0	39,8	15,9	2,3	19,9	12,0	4,5
50-M2	M3	34,8	39,6	38,4	0,0	37,6	15,0	2,5	19,4	10,7	5,0
50-TK	M4	42,2	41,0	41,6	39,6	41,6	16,6	0,6	17,7	15,6	1,2
50-AM	M5	40,2	38,8	38,2	41,2	39,1	15,6	1,0	17,4	13,8	2,1
15-M1	M6'	90,6	93,6	90,8	97,4	91,7	36,7	1,7	39,6	33,8	
	7 Days										
ID	Sample	1	2	3	4	AVG. (kN)	AVG. (MPa)	STD. Dev	Confidence interval (95%)		2 Std
100-PC	M1	122,4	124,2	124,4	100,4	123,7	49,5	1,1	51,4	47,6	2,2
15-M1	M6	99,2	98,8	98,2	97,8	98,7	39,5	0,5	40,4	38,6	1,0
15-M2	M7	97,4	100,2	101,4	94,8	99,7	39,9	2,1	43,4	36,3	4,1
15-TK	M8	94,6	93,8	97,0	98,8	95,1	38,1	1,7	40,9	35,2	3,3
15-AM	M9	105,4	107,0	106,8	100,4	106,4	42,6	0,9	44,1	41,1	1,7
30-M1	M10	84,8	83,4	85,4	82,6	84,5	33,8	1,0	35,6	32,0	2,1
30-M2	M11	82,6	79,2	82,8	78,4	81,5	32,6	2,0	36,1	29,1	4,0
30-TK	M12	72,2	73,0	71,4	69,2	72,2	28,9	0,8	30,3	27,5	1,6
30-AM	M13	90,2	94,4	93,6	100,2	92,7	37,1	2,2	41,0	33,2	4,5
50-M1	M2	48,9	51,6	51,8	57,2	50,8	20,3	1,6	23,1	17,5	3,2
50-M2	M3	58,2	54,8	57,2	53,4	56,7	22,7	1,7	25,7	19,7	3,5
50-TK	M4	69,2	69,6	70,2	68,4	69,7	27,9	0,5	28,7	27,0	1,0
50-AM	M5	74,4	76,0	75,8	0,0	75,4	30,2	0,9	31,7	28,7	1,7
15-M1	M6'	117,8	115,2	115,6	121	117,45	47,0	1,4	49,4	44,6	
	28 Days										
ID	Sample	1	2	3	4	AVG. (kN)	AVG. (MPa)	STD. Dev	Confidence interval (95%)		2 Std
100-PC	M1	156,8	144,6	142,2	129,6	147,9	59,1	7,8	72,7	45,6	7,8
15-M1	M6	115,0	114,8	115,6	121,6	116,8	46,7	0,4	47,4	46,0	0,8
15-M2	M7	124,2	127,8	126,2	131,4	126,1	50,4	1,8	53,6	47,3	3,6
15-TK	M8	110,8	112,4	112,2	116,2	111,8	44,7	0,9	46,2	43,2	1,7
15-AM	M9	135,4	137,8	137,4	145,4	136,9	54,7	1,3	57,0	52,5	2,6
30-M1	M10	113,4	117,8	115,6	111,2	115,6	46,2	2,2	50,1	42,4	4,4
30-M2	M11	108,6	110,4	106,8	115,8	108,6	43,4	1,8	46,6	40,3	3,6
30-TK	M12	101,2	100,6	103,8	95,6	101,9	40,7	1,7	43,7	37,8	3,4
30-AM	M13	124,4	122,6	122,8	124,8	123,3	49,3	1,0	51,0	47,6	2,0
50-M1	M2	89,8	92,8	95,2	86,6	92,6	37,0	2,7	41,7	32,4	5,4
50-M2	M3	100,4	99,2	100,6	98,6	100,1	40,0	0,8	41,3	38,7	1,5
50-TK	M4	105,2	105,2	108,4	111,4	106,3	42,5	1,8	45,7	39,3	3,7
50-AM	M5	117,2	123,2	115,0	105,6	118,5	47,4	4,2	54,7	40,0	8,5
15-M1'	M6'	163,6	165,6	168,2	177	165,8	66,3	2,3	70,3	62,3	

Table 48: Compressive strength data 2

	56 Days										
ID	Sample	1	2	3	4	AVG. (kN)	AVG. (MPa)	STD. Dev	Confidence interval (95%)		2 Std
100-PC	M1	153,6	149,8	154,6	138,4	152,7	61,1	2,5	65,5	56,7	5,1
15-M1	M6	132,2	131,2	134,6	127,8	132,7	53,1	1,7	56,1	50,0	3,5
15-M2	M7	141,2	140,8	142,2	136,8	141,4	56,6	0,7	57,8	55,3	1,4
15-TK	M8	131,8	133,6	132,4	122,2	132,6	53,0	0,9	54,6	51,5	1,8
15-AM	M9	144,8	142,6	144,4	138,2	143,9	57,6	1,2	59,6	55,5	2,3
30-M1	M10	118,8	118,2	119,8	117,4	118,9	47,6	0,8	49,0	46,2	1,6
30-M2	M11	122,6	117,4	122,8	114,6	120,9	48,4	3,1	53,7	43,1	6,1
30-TK	M12	118,6	115,6	118,8	113,4	116,6	46,6	1,8	49,7	43,5	3,6
30-AM	M13	131,2	132,8	137,2	137,8	134,8	53,9	3,1	59,3	48,5	6,2
50-M1	M2	108,6	110,4	109,8	113,4	109,6	43,8	0,9	45,4	42,3	1,8
50-M2	M3	115,8	116,0	116,4	113,6	116,1	46,4	0,3	47,0	45,9	0,6
50-TK	M4	125,2	126,8	128,8	132,8	126,9	50,8	1,8	53,9	47,6	3,6
50-AM	M5	127,8	129,8	131,2	125,4	129,6	51,8	1,7	54,8	48,9	3,4
15-M1'	M6'	154,8	151,8	153,6	148	153,4	61,4	1,5	64,0	58,7	
84 Days											
ID	Sample	1	2	3	4	AVG. (kN)	AVG. (MPa)	STD. Dev	Confidence interval (95%)		2 Std
100-PC	M1	156,8	155,6	153,2	147,6	155,2	62,1	1,8	65,3	58,9	3,7
15-M1	M6	138,4	139,2	138,8	136,8	138,8	55,5	0,4	56,2	54,8	0,8
15-M2	M7	144,8	145,2	144,4	140,0	144,8	57,9	0,4	58,6	57,2	0,8
15-TK	M8	136,8	137,2	136,4	133,8	136,8	54,7	0,4	55,4	54,0	0,8
15-AM	M9	146,8	147,6	148,4	143,6	147,6	59,0	0,8	60,4	57,7	1,6
30-M1	M10	135,4	134,8	134,6	133,8	134,9	54,0	0,4	54,7	53,3	0,8
30-M2	M11	133,6	135,6	134,8	128,0	134,7	53,9	1,0	55,6	52,1	2,0
30-TK	M12	124,8	123,6	125,4	121,6	124,6	49,8	0,9	51,4	48,3	1,8
30-AM	M13	142,2	139,2	141,4	150,2	140,9	56,4	1,6	59,1	53,7	3,1
50-M1	M2	114,4	115,6	115,8	112,4	115,3	46,1	0,8	47,4	44,8	1,5
50-M2	M3	130,2	134,8	128,8	141,8	131,3	52,5	3,1	57,9	47,1	6,3
50-TK	M4	137,8	132,2	138,2	129,6	136,1	54,4	3,4	60,2	48,6	6,7
50-AM	M5	141,8	154,2	145,8	158,6	147,3	58,9	6,3	69,9	47,9	12,7
168 Days											
ID	Sample	1	2	3	4	AVG. (kN)	AVG. (MPa)	STD. Dev	Confidence interval (95%)		2 Std
100-PC	M1	159,6	159,6	160,6	153,4	159,9	64,0	0,6	65,0	63,0	1,2
15-M1	M6	144,8	142,6	143,8	146,4	143,7	57,5	1,1	59,4	55,6	2,2
15-M2	M7	153,4	152,6	154,8	159,6	153,6	61,4	1,1	63,4	59,5	2,2
15-TK	M8	141,8	142,4	142,6	140,6	142,3	56,9	0,4	57,6	56,2	0,8
15-AM	M9	154,8	153,8	156,2	152,4	154,9	62,0	1,2	64,1	59,9	2,4
30-M1	M10	139,4	140,8	138,6	137,6	139,1	55,6	1,1	57,6	53,7	2,2
30-M2	M11	142,6	141,2	142,4	140,2	141,6	56,6	0,8	58,0	55,3	1,5
30-TK	M12	136,4	136,2	135,4	133,8	135,5	54,2	0,5	55,1	53,3	1,1
30-AM	M13	150,2	149,6	148,2	146,4	148,6	59,4	1,0	61,2	57,7	2,1
50-M1	M2	130,2	130,4	132,4	129,8	131,0	52,4	1,2	54,5	50,3	2,4
50-M2	M3	142,8	141,2	140,4	139,6	141,5	56,6	1,2	58,7	54,5	2,4
50-TK	M4	151,2	148,2	147,4	144,2	148,9	59,6	2,0	63,0	56,1	4,0
50-AM	M5	158,2	155,8	157,4	153,4	157,1	62,9	1,2	65,0	60,7	2,4

Table 49: Summarized cumulative strength data

Mix Proportion	Sample ID	Cumulative strength (Mpa)					
		2 days	7 days	28 days	56 days	84 days	168 days
100-PC	M1	37,6	49,5	59,1	61,1	62,1	64,0
15-M1	M6	27,3	39,5	46,7	53,1	55,5	57,5
15-M2	M7	29,3	39,9	50,4	56,6	57,9	61,4
15-TK	M8	27,8	38,1	44,7	53,0	54,7	56,9
15-AM	M9	30,2	42,6	54,7	57,6	59,0	62,0
30-M1	M10	22,7	33,8	46,2	47,6	54,0	55,6
30-M2	M11	20,7	32,6	43,4	48,4	53,9	56,6
30-TK	M12	20,8	28,9	40,7	46,6	49,8	54,2
30-AM	M13	25,3	37,1	49,3	53,9	56,4	59,4
50-M1	M2	15,9	20,3	37,0	43,8	46,1	52,4
50-M2	M3	15,0	22,7	40,0	46,4	52,5	56,6
50-TK	M4	16,6	27,9	42,5	50,8	54,4	59,6
50-AM	M5	15,6	30,2	47,4	51,8	58,9	62,9

Table 50: Summarized cumulative strength-gain data

Mix Proportion	Sample ID	Cumulative change in strength (Mpa)					
		2 days	7 days	28 days	56 days	84 days	168 days
100-PC	M1	37,6	11,9	9,7	1,9	1,0	1,9
15-M1	M6	27,3	12,2	7,2	6,4	2,5	2,0
15-M2	M7	29,3	10,6	10,6	6,1	1,4	3,5
15-TK	M8	27,8	10,3	6,7	8,3	1,7	2,2
15-AM	M9	30,2	12,4	12,2	2,8	1,5	2,9
30-M1	M10	22,7	11,1	12,4	1,3	6,4	1,7
30-M2	M11	20,7	11,9	10,8	4,9	5,5	2,8
30-TK	M12	20,8	8,1	11,9	5,9	3,2	4,3
30-AM	M13	25,3	11,8	12,2	4,6	2,5	3,1
50-M1	M2	15,9	4,4	16,7	6,8	2,3	6,3
50-M2	M3	15,0	7,7	17,3	6,4	6,1	4,1
50-TK	M4	16,6	11,2	14,6	8,3	3,7	5,1
50-AM	M5	15,6	14,5	17,2	4,5	7,1	3,9

Table 51: Drying shrinkage data 1

100 PC																		
Date	AGE	1		2		3		AGE	1		2		3		Average	Accumulated	Actual strain
	(DAYS)	F	B	F	B	F	B	(DAYS)	F	B	F	B	F	B	strain	strain	strain
	0	949	953	949	942	956	958	0	0	0	0	0	0	0	0	0	0
	1	945	945	945	921	948	948	1	4	8	4	21	8	10	9	9	147
	2	940	942	938	911	944	945	2	5	3	7	10	4	3	5	15	232
	3	938	939	936	908	942	943	3	2	3	2	3	2	2	2	17	269
	4	934	936	933	901	939	940	4	4	3	3	7	3	3	4	21	331
	5	931	933	931	889	936	937	5	3	3	2	12	3	3	4	25	400
	6	931	932	930	886	935	935	6	0	1	1	3	1	2	1	26	421
	13	919	921	918	869	924	923	13	12	11	12	17	11	12	13	39	621
	20	913	916	912	863	919	917	20	6	5	6	6	5	6	6	45	712
	27	909	914	909	859	916	914	27	4	2	3	4	3	3	3	48	763
	55	904	907	903	856	908	907	55	5	7	6	3	8	7	6	54	859
50/50 PC/MS1																		
Date	AGE	1		2		3		AGE	1		2		3		Average	Accumulated	Actual strain
	(DAYS)	F	B	F	B	F	B	(DAYS)	F	B	F	B	F	B	strain	strain	strain
	0	948	959	958	951	920	971	0	0	0	0	0	0	0	0	0	0
	1	942	956	953	947	914	965	1	6	3	5	4	6	6	5	5	80
	2	938	950	949	943	910	960	2	4	6	4	4	4	5	5	10	152
	3	936	949	947	940	906	958	3	2	1	2	3	4	2	2	12	189
	4	932	945	943	937	903	954	4	4	4	4	3	3	4	4	16	248
	5	928	942	939	933	902	951	5	4	3	4	4	1	3	3	19	299
	6	926	941	938	932	899	950	6	2	1	1	1	3	1	2	20	323
	13	915	928	927	920	887	939	13	11	13	11	12	12	11	12	32	509
	20	911	924	923	915	883	935	20	4	4	4	5	4	4	4	36	576
	27	909	920	919	912	879	933	27	2	4	4	3	4	2	3	39	627
	55	905	916	914	908	874	928	55	4	4	5	4	5	5	5	44	699
50/50 PC/MS2																		
Date	AGE	1		2		3		AGE	1		2		3		Average	Accumulated	Actual strain
	(DAYS)	F	B	F	B	F	B	(DAYS)	F	B	F	B	F	B	strain	strain	strain
	0	956	952	949	960	952	1042	0	0	0	0	0	0	0	0	0	0
	1	951	949	945	957	947	1035	1	5	3	4	3	5	7	5	5	72
	2	947	944	942	955	943	1031	2	4	5	3	2	4	4	4	8	131
	3	945	941	937	952	939	1027	3	2	3	5	3	4	4	4	12	187
	4	941	937	935	947	935	1024	4	4	4	2	5	4	3	4	15	245
	5	938	934	931	945	932	1021	5	3	3	4	2	3	3	3	18	293
	6	937	932	930	944	930	1018	6	1	2	1	1	2	3	2	20	320
	13	926	920	917	930	917	1007	13	11	12	13	14	13	11	12	32	517
	20	923	916	913	925	913	1003	20	3	4	4	5	4	4	4	36	581
	27	920	913	910	922	910	999	27	3	3	3	3	3	4	3	40	632
	55	915	909	905	918	905	995	55	5	4	5	4	5	4	5	44	704

Table 52: Drying shrinkage data 2

50/50 PC/TK																			
Date	AGE	1		2		3		AGE	1		2		3		Average	Accumulated	Actual strain
	(DAYS)	F	B	F	B	F	B	(DAYS)	F	B	F	B	F	B	strain	strain	strain
	0	955	525	952	954	954	955	0	0	0	0	0	0	0	0	0	0
	1	950	518	949	952	948	952	1	5	7	3	2	6	3	4	4	69
	2	946	515	945	948	944	947	2	4	3	4	4	4	5	4	8	133
	3	943	511	942	944	940	945	3	3	4	3	4	4	2	3	12	187
	4	938	507	938	939	937	941	4	5	4	4	5	3	4	4	16	253
	5	935	504	935	935	935	938	5	3	3	3	4	2	3	3	19	301
	6	933	503	933	932	932	936	6	2	1	2	3	3	2	2	21	336
	13	921	491	920	920	922	924	13	12	12	13	12	10	12	12	33	525
	20	916	485	915	915	917	920	20	5	6	5	5	5	4	5	38	605
	27	914	483	912	911	914	917	27	2	2	3	4	3	3	3	41	651
	55	907	479	908	905	908	913	55	7	4	4	6	6	4	5	46	733
50/50 PC/AM																			
Date	AGE	1		2		3		AGE	1		2		3		Average	Accumulated	Actual strain
	(DAYS)	F	B	F	B	F	B	(DAYS)	F	B	F	B	F	B	strain	strain	strain
	0	954	949	954	954	996	954	0	0	0	0	0	0	0	0	0	0
	1	947	943	949	950	988	949	1	7	6	5	4	8	5	6	6	93
	2	942	940	945	946	984	944	2	5	3	4	4	4	5	4	10	160
	3	939	938	942	943	982	941	3	3	2	3	3	2	3	3	13	203
	4	935	934	938	939	977	937	4	4	4	4	4	5	4	4	17	269
	5	932	932	935	936	974	935	5	3	2	3	3	3	2	3	20	312
	6	929	930	931	934	973	933	6	3	2	4	2	1	2	2	22	349
	13	918	919	919	922	961	922	13	11	11	12	12	12	11	12	33	533
	20	914	915	914	917	954	916	20	4	4	5	5	7	6	5	39	616
	27	909	912	911	912	952	912	27	5	3	3	5	2	4	4	42	675
	55	903	906	903	907	947	906	55	6	6	8	5	5	6	6	48	771
85/15 PC/MS1																			
Date	AGE	1		2		3		AGE	1		2		3		Average	Accumulated	Actual strain
	(DAYS)	F	B	F	B	F	B	(DAYS)	F	B	F	B	F	B	strain	strain	strain
	0	946	871	991	953	952	949	0	0	0	0	0	0	0	0	0	0
	1	940	865	986	949	947	943	1	6	6	5	4	5	6	5	5	85
	2	937	858	980	945	944	939	2	3	7	6	4	3	4	5	10	157
	3	932	855	978	942	939	935	3	5	3	2	3	5	4	4	14	216
	4	929	852	975	939	937	932	4	3	3	3	3	2	3	3	16	261
	5	928	850	972	936	934	929	5	1	2	3	3	3	3	3	19	301
	6	925	847	970	933	933	926	6	3	3	2	3	1	3	3	21	341
	13	914	835	958	920	919	912	13	11	12	12	13	14	14	13	34	544
	20	909	831	951	915	913	907	20	5	4	7	5	6	5	5	39	629
	27	904	825	946	909	908	902	27	5	6	5	6	5	5	5	45	715
	55	898	818	938	903	904	897	55	6	7	8	6	4	5	6	51	811

Table 53: Drying shrinkage data 3

85/15 PC/MS2																			
Date	AGE	1		2		3		AGE	1		2		3		Average	Accumulated	Actual strain
	(DAYS)	F	B	F	B	F	B	(DAYS)	F	B	F	B	F	B	strain	strain	strain
	0	954	958	951	1081	943	957	0	0	0	0	0	0	0	0	0	0
	1	949	951	947	1077	937	952	1	5	7	4	4	6	5	5	5	83
	2	946	947	943	1071	933	949	2	3	4	4	6	4	3	4	9	147
	3	942	942	938		928	945	3	4	5	5		5	4	5	14	220
	4	939	939	935		925	941	4	3	3	3		3	4	3	17	271
	5	935	937	933		923	937	5	4	2	2		2	4	3	20	316
	6	933	934	931		920	935	6	2	3	2		3	2	2	22	355
	13	921	919	917		907	922	13	12	15	14		13	13	13	36	569
	20	915	913	910		901	916	20	6	6	7		6	6	6	42	668
	27	910	908	904		895	909	27	5	5	6		6	7	6	48	761
	55	905	903	899		890	903	55	5	5	5	0	5	6	4	52	830
85/15 PC/TK																	
Date	AGE	1		2		3		AGE	1		2		3		Average	Accumulated	Actual strain
	(DAYS)	F	B	F	B	F	B	(DAYS)	F	B	F	B	F	B	strain	strain	strain
	0	952	942	950	954	952	946	0	0	0	0	0	0	0	0	0	0
	1	947	937	945	951	947	940	1	5	5	5	3	5	6	5	5	77
	2	944	931	940	948	943	936	2	3	6	5	3	4	4	4	9	144
	3	939	925	937	943	938	932	3	5	6	3	5	5	4	5	14	219
	4	936	923	934	941	936	929	4	3	2	3	2	2	3	3	16	259
	5	932	919	929	936	932	926	5	4	4	5	5	4	3	4	20	325
	6	929	917	927	933	929	923	6	3	2	2	3	3	3	3	23	368
	13	916	901	913	919	915	910	13	13	16	14	14	14	13	14	37	592
	20	910	896	907	914	908	904	20	6	5	6	5	7	6	6	43	685
	27	904	890	901	907	903	899	27	6	6	6	7	5	5	6	49	779
	55	899	885	895	901	897	893	55	5	5	6	6	6	6	6	54	869
85/15 PC/AM																	
Date	AGE	1		2		3		AGE	1		2		3		Average	Accumulated	Actual strain
	(DAYS)	F	B	F	B	F	B	(DAYS)	F	B	F	B	F	B	strain	strain	strain
	0	986	952	963	958	951	505	0	0	0	0	0	0	0	0	0	0
	1	980	947	958	951	944	498	1	6	5	5	7	7	7	6	6	99
	2	976	942	954	947	940	494	2	4	5	4	4	4	4	4	10	165
	3	972	938	949	943	936	490	3	4	4	5	4	4	4	4	15	232
	4	969	935	946	940	933	487	4	3	3	3	3	3	3	3	18	280
	5	965	932	943	937	929	484	5	4	3	3	3	4	3	3	21	333
	6	962	929	941	934	927	481	6	3	3	2	3	2	3	3	24	376
	13	949	916	927	919	912	469	13	13	13	14	15	15	12	14	37	595
	20	945	911	922	913	907	463	20	4	5	5	6	5	6	5	42	677
	27	941	907	917	908	903	457	27	4	4	5	5	4	6	5	47	752
	55	934	902	911	903	897	448	55	7	5	6	5	6	9	6	53	853

Table 54: Drying shrinkage data 4

70/30 PC/MS1																			
Date	AGE	1		2		3		AGE	1		2		3		Average	Accumulated	Actual strain
	(DAYS)	F	B	F	B	F	B	(DAYS)	F	B	F	B	F	B	strain	strain	strain
	0	953	949	953	956	956	952	0	0	0	0	0	0	0	0	0	0
	1	947	944	947	951	950	946	1	6	5	6	5	6	6	6	6	91
	2	941	939	943	946	945	941	2	6	5	4	5	5	5	5	11	171
	3	938	934	939	941	940	936	3	3	5	4	5	5	5	5	15	243
	4	934	932	936	939	938	933	4	4	2	3	2	2	3	3	18	285
	5	931	929	933	936	935	930	5	3	3	3	3	3	3	3	21	333
	6	928	926	929	933	931	926	6	3	3	4	3	4	4	4	24	389
	13	916	914	916	920	919	912	13	12	12	13	13	12	14	13	37	592
	20	911	909	912	915	913	907	20	5	5	4	5	6	5	5	42	672
	27	905	905	906	909	909	902	27	6	4	6	6	4	5	5	47	755
	55	901	899	900	903	903	897	55	4	6	6	6	6	5	6	53	843
70/30 PC/MS2																			
Date	AGE	1		2		3		AGE	1		2		3		Average	Accumulated	Actual strain
	(DAYS)	F	B	F	B	F	B	(DAYS)	F	B	F	B	F	B	strain	strain	strain
	0	965	955	949	943	949	952	0	0	0	0	0	0	0	0	0	0
	1	963	953	948	942	945	950	1	2	2	1	1	4	2	2	2	32
	2	958	950	945	944	942	948	2	5	3	3	-2	3	2	2	4	69
	3	953	947	941	939	937	944	3	5	3	4	5	5	4	4	9	139
	4	950	943	938	936	933	939	4	3	4	3	3	4	5	4	12	197
	5	947	940	935	932	930	936	5	3	3	3	4	3	3	3	16	248
	6	945	937	932	929	926	935	6	2	3	3	3	4	1	3	18	291
	13	933	928	919	917	914	924	13	12	9	13	12	12	11	12	30	475
	20	925	920	913	909	907	916	20	8	8	6	8	7	8	8	37	595
	27	923	918	909	906	903	912	27	2	2	4	3	4	4	3	40	645
	55	917	913	905	902	896	908	55	6	5	4	4	7	4	5	45	725
70/30 PC/TK																			
Date	AGE	1		2		3		AGE	1		2		3		Average	Accumulated	Actual strain
	(DAYS)	F	B	F	B	F	B	(DAYS)	F	B	F	B	F	B	strain	strain	strain
	0	933	947	951	957	950	954	0	0	0	0	0	0	0	0	0	0
	1	930	943	948	954	947	949	1	3	4	3	3	3	5	4	4	56
	2	928	940	945	950	944	945	2	2	3	3	4	3	4	3	7	107
	3	923	935	940	943	938	939	3	5	5	5	7	6	6	6	12	197
	4	916	930	938	940	936	935	4	7	5	2	3	2	4	4	16	259
	5	913	927	934	936	932	932	5	3	3	4	4	4	3	4	20	315
	6	912	925	931	932	928	928	6	1	2	3	4	4	4	3	23	363
	13	904	914	921	922	919	918	13	8	11	10	10	9	10	10	32	517
	20	896	908	914	915	911	910	20	8	6	7	7	8	8	7	40	635
	27	892	905	912	912	907	907	27	4	3	2	3	4	3	3	43	685
	55	886	899	906	906	902	902	55	6	6	6	6	5	5	6	49	776
70/30 PC/AM																			
Date	AGE	1		2		3		AGE	1		2		3		Average	Accumulated	Actual strain
	(DAYS)	F	B	F	B	F	B	(DAYS)	F	B	F	B	F	B	strain	strain	strain
	0	958	952	949	948	950	1189	0	0	0	0	0	0	0	0	0	0
	1	952	947	944	945	946	1185	1	6	5	5	3	4	4	5	5	72
	2	947	942	941	942	942	1179	2	5	5	3	3	4	6	4	9	141
	3	941	937	937	936	937	1174	3	6	5	4	6	5	5	5	14	224
	4	938	935	934	934	934	1172	4	3	2	3	2	3	2	3	17	264
	5	933	930	930	930	930	1168	5	5	5	4	4	4	4	4	21	333
	6	930	927	927	927	927	1165	6	3	3	3	3	3	3	3	24	381
	13	921	918	915	916	917	1155	13	9	9	12	11	10	10	10	34	544
	20	914	912	909	909	911	1147	20	7	6	6	7	6	8	7	41	651
	27	910	907	907	907	907	1144	27	4	5	2	2	4	3	3	44	704
	55	905	902	900	900	902	1139	55	5	5	7	7	5	5	6	50	795

Table 55: Shortened reactivity data - heat released rate

Time	100 PC	50-M1	50-M2	50-TK	50-AM	15-M1	15-M2	15-TK	15-AM	30-M1	30-M2	30-TK	30-AM	Tap 85	Tap 132	Tap 144
hour	watt	watt	watt	watt	watt	watt	watt	watt	watt	watt	watt	watt	watt	watt	watt	watt
4,800	0,421	0,192	0,188	0,183	0,201	0,334	0,315	0,315	0,375	0,288	0,268	0,283	0,291	0,286	0,280	0,278
4,900	0,431	0,198	0,194	0,188	0,205	0,342	0,326	0,326	0,381	0,296	0,278	0,291	0,299	0,294	0,289	0,288
5,000	0,438	0,202	0,199	0,193	0,208	0,349	0,334	0,334	0,385	0,303	0,286	0,298	0,305	0,302	0,296	0,296
5,100	0,443	0,207	0,204	0,196	0,211	0,354	0,341	0,342	0,388	0,308	0,294	0,303	0,310	0,308	0,302	0,303
5,300	0,447	0,212	0,210	0,201	0,214	0,360	0,351	0,351	0,388	0,314	0,303	0,310	0,316	0,316	0,309	0,312
5,500	0,445	0,215	0,213	0,205	0,216	0,362	0,354	0,355	0,383	0,316	0,308	0,312	0,316	0,319	0,312	0,316
6,000	0,436	0,226	0,218	0,216	0,230	0,365	0,345	0,346	0,364	0,307	0,302	0,308	0,306	0,323	0,317	0,312
6,533	0,441	0,250	0,236	0,237	0,278	0,383	0,338	0,337	0,363	0,312	0,298	0,318	0,308	0,343	0,334	0,322
9,317	0,215	0,114	0,123	0,106	0,133	0,180	0,210	0,216	0,205	0,182	0,191	0,178	0,198	0,185	0,182	0,179
12,083	0,113	0,080	0,081	0,077	0,101	0,099	0,109	0,112	0,111	0,093	0,098	0,093	0,103	0,100	0,098	0,093
15,517	0,067	0,057	0,059	0,056	0,074	0,066	0,065	0,069	0,064	0,056	0,059	0,060	0,067	0,070	0,066	0,060
18,933	0,048	0,044	0,046	0,045	0,058	0,049	0,046	0,050	0,047	0,042	0,045	0,046	0,052	0,055	0,052	0,046
32,483	0,030	0,022	0,025	0,026	0,033	0,030	0,029	0,032	0,030	0,024	0,027	0,027	0,031	0,032	0,032	0,027
42,600	0,017	0,016	0,019	0,019	0,023	0,020	0,019	0,021	0,019	0,018	0,020	0,021	0,022	0,021	0,023	0,021
52,667	0,011	0,012	0,015	0,014	0,016	0,013	0,012	0,015	0,013	0,013	0,014	0,015	0,016	0,014	0,016	0,016
62,683	0,007	0,009	0,012	0,010	0,012	0,009	0,009	0,011	0,010	0,009	0,010	0,012	0,012	0,010	0,012	0,013
72,650	0,006	0,008	0,011	0,008	0,010	0,007	0,007	0,009	0,007	0,007	0,008	0,010	0,009	0,007	0,010	0,011
72,667	0,006	0,008	0,011	0,008	0,009	0,007	0,007	0,009	0,007	0,007	0,008	0,010	0,009	0,007	0,010	0,011
72,683	0,006	0,008	0,011	0,008	0,009	0,007	0,007	0,009	0,007	0,007	0,008	0,010	0,009	0,007	0,010	0,011
72,700	0,006	0,008	0,011	0,008	0,009	0,007	0,007	0,009	0,007	0,007	0,008	0,010	0,009	0,007	0,010	0,011
72,717	0,006	0,008	0,011	0,008	0,009	0,007	0,007	0,009	0,007	0,007	0,008	0,010	0,009	0,007	0,010	0,011
72,733	0,006	0,008	0,011	0,008	0,009	0,007	0,007	0,009	0,007	0,007	0,008	0,010	0,009	0,007	0,010	0,011
72,750	0,006	0,008	0,011	0,008	0,009	0,007	0,007	0,009	0,007	0,007	0,008	0,010	0,009	0,007	0,010	0,011

Table 56: Shortened reactivity data - cumulative heat

Time	100 PC	50-M1	50-M2	50-TK	50-AM	15-M1	15-M2	15-TK	15-AM	30-M1	30-M2	30-TK	30-AM	Tap 85	Tap 132	Tap 144
hour	joule	joule	joule	joule	joule	joule	joule	joule	joule	joule	joule	joule	joule	joule	joule	joule
4,80	1866	386	764	514	776	1577	2019	2037	1659	1126	1145	1187	1285	1109	1208	1167
4,90	2019	456	833	580	849	1698	2134	2152	1795	1231	1243	1291	1391	1214	1310	1269
5,00	2175	528	904	649	923	1823	2253	2271	1933	1339	1345	1397	1500	1321	1415	1375
5,10	2334	602	977	719	998	1950	2375	2393	2072	1449	1449	1505	1610	1431	1523	1483
5,30	2655	753	1126	862	1151	2207	2624	2642	2351	1674	1664	1726	1836	1655	1743	1704
5,50	2977	907	1278	1009	1306	2467	2878	2897	2629	1901	1885	1951	2064	1884	1967	1930
6,00	3766	1302	1665	1386	1703	3118	3510	3530	3301	2462	2436	2508	2625	2459	2531	2496
6,53	4611	1757	2099	1817	2181	3838	4161	4182	4001	3054	3007	3109	3211	3100	3157	3104
9,32	8018	3760	4189	3687	4196	6884	7190	7235	7049	5806	5767	5872	6048	6038	5995	5922
12,08	9560	4703	5167	4587	5355	8192	8684	8767	8539	7092	7113	7142	7462	7375	7308	7190
15,52	10626	5534	6015	5397	6415	9180	9720	9848	9576	7972	8039	8046	8471	8391	8287	8094
18,93	11314	6154	6654	6010	7221	9881	10390	10568	10246	8566	8668	8686	9195	9151	9009	8734
32,48	13162	7642	8249	7631	9324	11643	12089	12424	12014	10059	10292	10329	11070	11104	10933	10396
42,60	14005	8328	9028	8433	10314	12556	12948	13384	12902	10837	11162	11209	12030	12070	11923	11286
52,67	14503	8832	9630	9009	11006	13149	13498	14027	13479	11386	11783	11862	12706	12701	12614	11962
62,68	14826	9216	10119	9437	11512	13552	13872	14484	13882	11770	12224	12354	13200	13123	13120	12482
72,65	15056	9518	10531	9763	11900	13848	14147	14832	14185	12052	12551	12747	13581	13424	13511	12911
72,67	15056	9519	10532	9764	11901	13848	14148	14833	14185	12053	12552	12748	13582	13424	13512	12912
72,68	15056	9519	10532	9764	11901	13849	14148	14833	14185	12053	12552	12748	13582	13425	13513	12912
72,70	15057	9520	10533	9765	11902	13849	14148	14834	14186	12053	12553	12749	13583	13425	13513	12913
72,72	15057	9520	10534	9765	11902	13849	14149	14834	14186	12054	12553	12749	13583	13425	13514	12914
72,73	15057	9520	10534	9766	11903	13850	14149	14835	14187	12054	12554	12750	13584	13426	13514	12914
72,75	15058	9521	10535	9766	11903	13850	14150	14835	14187	12055	12554	12751	13585	13426	13515	12915

Table 57: Correlation data - strength to cumulative heat

Proportion	Strength (MPa)		Cumulative heat (j)		Cumulative heat (j)	
	7 days	2 days	24 hours	Heat per gram	146 hours	Heat per gram
15-M1	39,5	27,3	10640	266,0	14950,00	373,75
15-M2	39,9	29,3	11110	277,8	15095,00	377,38
15-TK	38,1	27,8	11359	284,0	16251,00	406,28
15-AM	42,6	30,2	10990	274,8	15299,00	382,48
30-M1	33,8	22,7	9224,7	230,6	12979,00	324,48
30-M2	32,6	20,7	9371,7	234,3	13614,00	340,35
30-TK	28,9	20,8	9407,2	235,2	14428,00	360,70
30-AM	37,1	25,3	10013	250,3	14893,00	372,33
50-M1	20,3	15,9	8616,10	215,4	10576,00	264,40
50-M2	22,7	15,0	9368,20	234,2	12312,00	307,80
50-TK	27,9	16,6	8764,40	219,1	10712,00	267,80
50-AM	30,2	15,6	10013	250,3	13233,00	330,83